Probing atomic and nuclear structure properties of promethium by laser spectroscopy

Dissertation

zur Erlangung des akademischen Grades
„Doktor der Naturwissenschaften“
am Fachbereich Physik, Mathematik und Informatik (FB 08)
der Johannes Gutenberg-Universität Mainz

Dominik Studer
geb. in Wiesbaden

Mainz, den 22. Juni 2020

Tag der Prüfung: 18. Juni 2020

"There is a theory which states that if ever anyone discovers exactly what the Universe is for and why it is here, it will instantly disappear and be replaced by something even more bizarre and inexplicable. There is another theory which states that this has already happened."

Douglas Adams

Dominik Studer
Institut für Physik
Johannes Gutenberg-Universität Mainz
Staudingerweg 7
55128 Mainz
dstuder@uni-mainz.de

Abstract

Laser resonance ionization is a versatile technique for efficient ion source and sensitive spectroscopy applications, based on step-wise optical excitation of atoms by pulsed laser radiation, with the final step ionizing the atom. This work focuses on *in-source* spectroscopy applications, i.e. laser probing directly within the ion source environment, and therefore combines the experimental aspects of spectroscopy and "ion sourcery". In this context atomic and nuclear structure properties of dysprosium and promethium were determined, with a focus on so far widely unknown parameters of the latter. The results are documented in five publications. They can be thematically separated into atomic and nuclear structure research, performed in broadband and high-resolution laser spectroscopic experiments, respectively.

The first part of this thesis aims towards the determination of atomic level energies, efficient resonance ionization pathways and the determination of the first ionization potential. The technique of laser-induced resonant depopulation of excited atomic levels is introduced, offering access to a specific low-lying energy level in Dy. The corresponding ultra-narrow ground-state transition near 1001 nm was located in preparation for high-precision spectroscopy on cold atoms. For the determination of the ionization potential, the techniques of Rydberg-spectroscopy and saddle-point ionization were applied in Dy and Pm, respectively. While the former represents the conventional approach for this task, the sensitivity of the latter was greatly improved and demonstrated in the challenging case of Pm. The extracted values of $\mathrm{IP_{Dy}} = 47\,901.76(5)\,\mathrm{cm}^{-1}$ and $\mathrm{IP_{Pm}} = 45\,020.8(3)\,\mathrm{cm}^{-1}$ improved the precision of $\mathrm{IP_{Dy}}$ by one order of magnitude, while $\mathrm{IP_{Pm}}$ was experimentally determined for the first time.

In the second part, dedicated to high-resolution spectroscopic applications, the long-term stability and accuracy of wavelength meters in precision frequency measurement was characterized as an important aspect for the extraction of reliable spectroscopic data. Systematic patterns in deviations of relative frequency measurements were discovered in comparison to complementary devices. Methods to avoid or at least properly consider these effects in data post-processing are discussed. Lastly, the results of high-resolution spectroscopy on long-lived Pm isotopes are presented, using the novel PI-LIST ion source module. The experiment on cyclotron-produced Pm isotopes demonstrates the capabilities of the PI-LIST and represents a further step towards routine operation at on-line radioactive ion beam facilities. The spectroscopic data obtained allowed for the extraction of several nuclear ground state properties of the isotopic sequence of $^{143-147}$Pm, i.e. magnetic dipole moments, electric quadrupole moments, and changes in mean square charge radii.

List of Included Articles

This cumulative dissertation is based on the five publications [1–5], which are listed below. These articles are chosen to represent the key aspects of this work in a comprehensive way. The author has made significant contributions to each of these articles, which are pointed out in detail in an introductory section preceding each article within this thesis. A complete list of all publications of the author is given in the **??**.

Publication [1] emerged from a collaborative activity within the QUANTUM research group. It describes a specific case of resonance ionization scheme development for the search of a low-lying meta-stable atomic level in dysprosium. The direct ground-state transition to this level, which was also measured in this work, is of high relevance for precision spectroscopy of cold atoms.

Publication [2] also describes the development of ionization schemes, in this case directed towards the achievement of maximum ionization efficiency. In this scope the first ionization potential (IP) of dysprosium was measured. This work exemplarily describes the evaluation of Rydberg convergences in a complex rare-earth atomic system.

Publication [3] rounds up the part on measurements of atomic structure properties. It describes the extensive study of the atomic spectrum of the promethium atom and the determination of its first IP, introducing the approach of electric field ionization as a sensitive and complementary method to the analysis of Rydberg convergences.

Publication [4] is a collaborative work between the University of Jyväskylä, the University of Leuven, GSI Darmstadt and the University of Mainz. Within this network the performance of wavelength meters is characterized, which has important consequences on the accuracy of high-resolution laser spectroscopic studies.

Finally, Publication [5] presents the results of high-resolution spectroscopy on long-lived promethium isotopes. This work concludes this thesis by demonstrating the capabilities of laser resonance ionization spectroscopy for the study of nuclear structure properties on minuit sample amounts of rare radioisotopes, significantly refining and extending literature data.

[1] D. Studer, L. Maske, P. Windpassinger, K. Wendt, *Laser spectroscopy of the 1001-nm ground-state transition in dysprosium*, Phys. Rev. A **98**, 042504 (2018). doi:10.1103/PhysRevA.98.042504.

[2] D. Studer, P. Dyrauf, P. Naubereit, R. Heinke, K. Wendt, *Resonance ionization spectroscopy in dysprosium: Excitation scheme development and re-determination of the first ionization potential*, Hyperfine Interact. **238**, 8 (2017). doi:10.1007/s10751-016-1384-4.

[3] D. Studer, S. Heinitz, R. Heinke, P. Naubereit, R. Dressler, C. Guerrero, U. Köster, D. Schumann, K. Wendt, *Atomic transitions and the first ionization potential of promethium determined by laser spectroscopy*, Phys. Rev. A **99**, 062513 (2019). doi:10.1103/PhysRevA.99.062513.

[4] M. Verlinde, K. Dockx, S. Geldhof, K. König, D. Studer, T. E. Cocolios, R. de Groote, R. Ferrer, T. Kieck, I. D. Moore, W. Nörtershäuser, S. Raeder, P. van den Bergh, P. van Duppen, K. Wendt, *On the reliability of wavelength meters - Part 1: Consequences for medium- to high-resolution laser spectroscopy*, Appl. Phys. B **126**, 85 (2020). doi:10.1007/s00340-020-07425-4.

[5] D. Studer, J. Ulrich, S. Braccini, T. S. Carzaniga, R. Dressler, K. Eberhardt, R. Heinke, U. Köster, S. Raeder, K. Wendt, *High resolution laser resonance ionization spectroscopy of $^{143-147}Pm$*, Eur. Phys. J. A **56**, 69 (2020). doi:10.1140/epja/s10050-020-00061-8.

Contents

Chapter 1

Introduction

Since the first evidence for the existence of an atomic nucleus by Ernest Rutherford, revealed in the famous experiment by scattering α-particles on gold [1], theoretical models for the description of its properties have developed tremendously. The liquid drop model, describing the nucleus as a sphere of uniform density, composed of protons and neutrons bound by the strong force, already allowed a qualitative understanding of binding energy and radioactive decay [2]. Based on experimental evidence for so-called *magic numbers*, i.e. proton- or neutron numbers, at which nuclei of particularly high stability occur, the nuclear shell model was introduced by Maria Goeppert-Mayer and Hans Jensen [3, 4], who were awarded with the physics Nobel Price in 1963 for their discovery. The shell model comprises a quantum-mechanical treatment of the nucleus, resulting in proton- and neutron orbitals similar to electrons in an atom, with the magic numbers corresponding to filled shells. While the shell model successfully describes nuclear spins and electromagnetic moments for spherical nuclei, it does not account for nuclear deformation. Therefore, it was extended by *collective* models in the 1950s, where a collective motion of all nucleons, i.e. vibration and rotation, is considered [5, 6]. This allows for an accurate description of nuclear ground state properties and excited states. However, the predictive power of theory is limited by the complexity in such systems of numerous interacting particles equal to the nucleon number A. Calculations are usually based on mean field approaches and need to be tailored to specific problems. In order to establish benchmarks for theoretical predictions, the objective of experimentalists is to provide nuclear structure data in specific or even exceptional regions of the Nuclear Chart, featuring e.g. extreme or unusual deformation, abrupt shape transitions or shape staggering.

An access to the investigation of nuclear structure is offered indirectly through the study of the atomic shell. Interactions of the nucleus with the surrounding electronic shell manifest as small perturbations in the atomic level structure, known as hyperfine structure and isotope shift. Precise measurements of these effects

allow the extraction of the nuclear spin I, the magnetic dipole moment μ_I, the electric quadrupole moment Q_s and changes in mean square charge radii $\delta\langle r^2\rangle$, all of which are closely related to the nucleus' shape [7]. With energy scales of atomic transitions in the range of few eV, rather than typically keV or MeV in nuclear excitation, they are accessible with lasers. For its versatility, the laser has become the ultimate tool for the study and manipulation of atoms. However, high-precision probing of individual atomic transitions for the study of nuclear effects, with contributions in the order of 10^{-5} eV, requires prior knowledge of the atomic spectrum. Elements with no stable isotopes often exhibit a severe shortcoming in this regard. Spectroscopic studies are impeded by limited availability of samples, together with the necessity of high safety precautions for the handling of radioactive material. One way to overcome these challenges is through an efficient measurement technique, which is capable of analyzing minuscule sample amounts. The method of Resonance Ionization Spectroscopy (RIS) is perfectly suited for this application. It relies on stepwise photoionization of sample atoms by high-power, pulsed laser radiation and subsequent ion counting. This process is highly efficient and inherently element-selective. RIS is usually combined with conventional methods of mass spectrometry allowing the study of a single isotope of interest.

This dissertation deals with the application of RIS for the study of both, atomic and nuclear structure properties, with a special focus on the element promethium (Pm, $Z = 61$) as the main physics case. Correspondingly, it is structured in two parts. The first part describes broadband spectroscopy experiments for the exploration of atomic spectra. In this scope many aspects of broadband RIS were developed and applied in the rare-earth atomic system of dysprosium (Dy, $Z = 66$). This includes the development of ionization schemes aimed towards maximum efficiency, but also covers a rather unusual case where specific ground state transitions are probed indirectly by resonant de-population of excited levels. In addition, the first ionization potential (IP) of Dy was determined via spectroscopy of Rydberg convergences, using the most common and also most precise approach for this task. The Dy experiments therefore offer an ideal overview of the basics and concepts of RIS for atomic structure research in the rare-earth region. Afterwards, the challenging case of Pm is addressed. Pm has an extraordinarily rich atomic spectrum, which on the one hand makes it easy to develop a laser ionization scheme, but on the other hand complicates the determination of the IP, as all Rydberg-series are obscured or strongly perturbed. An alternative approach, based on DC electric field ionization of weakly bound states, is introduced, which benefits from the high atomic level density and remains applicable with extremely small sample amounts. In addition to the first measurement of the IP of Pm, this experiment also represents an important methodical preparation for IP measurements in the region of medium mass to heavy actinides, where complex atomic systems are likewise expected and only very limited atom numbers are accessible, resulting in

low measurement statistics.
The second part of this work is dedicated to high-resolution spectroscopy in the Pm isotopic chain. This experiment marks the first high-precision spectroscopy measurements in the Pm atom, based on the ionization schemes developed earlier within this work. It serves as an important test and preparation step for on-line[1] experiments, pushing further away from the valley of β-stability, towards very short-lived Pm isotopes. In this context the experimental challenges of high-precision experiments on exotic nuclei are discussed. As a basic prerequisite this task specifically addresses precise absolute laser frequency measurements and ion source developments, which are tailored for sensitive spectroscopy studies.

1.1 Promethium

The exclusively radioactive element promethium has been subject to an interesting history of discovery, including the proposals of the names *florentium* and *illinium* for the missing element between neodymium and samarium [8, 9]. In 1945, based on research in the framework of the Manhattan project, Marinsky *et al.* successfully separated ^{147}Pm from uranium fission products by means of ion exchange chromatography [10], finally marking the discovery of element 61. Together with technetium (Tc, $Z = 43$), Pm is one of two cases on the Periodic Table where an element with an atomic number below $Z = 83$ has no stable isotope. An explanation for this exceptional situation can be found in the liquid drop model of the atomic nucleus, or more specifically the Bethe-Weizsäcker mass formula [2]. It describes parabola-like curves of nuclear mass for isobaric nuclei of a given number of nucleons A, where the mass minimum (i.e. maximum binding energy) can be reached through radioactive β-decay. The consequence, that no neighboring stable isobars can exist, is formulated in Mattauch's isobar rule [11]. Accordingly, any stable Pm isotopes are ruled out by the existence of the large number of stable Nd and Sm isotopes, as shown in the Nuclear Chart section in Fig. 1.1. Even the longest-lived Pm isotopes ^{145,146,147}Pm have half-lives in the order of only few years, making Pm extremely rare in nature. Practical applications of Pm are based on its radioactivity. ^{147}Pm ($T_{1/2} = 2.62\,\mathrm{y}$), the most easily accessible isotope in terms of production, is used in nuclear batteries [13] or β-thickness gauges [14]. Some shorter-lived isotopes, i.e. ^{142}Pm ($T_{1/2} = 40.5\,\mathrm{s}$) and ^{149}Pm ($T_{1/2} = 2.21\,\mathrm{d}$) are promising candidates for medical imaging techniques [15, 16]. The synthesis of weightable amounts of Pm is possible using nuclear reactors. ^{147}Pm can be produced by neutron activation of ^{146}Nd, where the reaction product ^{147}Nd decays with a half-life of 11 days to ^{147}Pm (cf. Fig. 1.1). Alternatively, it can be extracted from fission products within nuclear reactor waste [17]. A different pro-

[1] In this context, *on-line* means the experiment is coupled to a production site of radioactive isotopes. In contrast, experiments which rely on externally introduced samples are referred to as *off-line*.

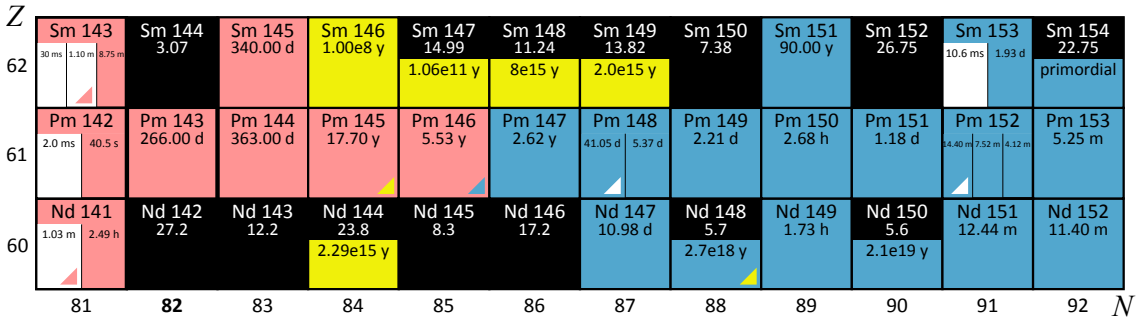

Figure 1.1.: Section of the Nuclear Chart in the Pm region close to the valley of β-stability. The underlying data is taken from [12].

duction route is offered by cyclotrons, where stable Nd isotopes can be irradiated with high-energy protons. Through (p, xn)-reactions (at a suitable proton energy of some ten MeV) a large number of Pm isotopes can be accessed (cf. Fig. 1.1). However, at reasonable irradiation times the amounts produced are usually small. As a consequence of the generally low availability of Pm, accompanied by the high specific radioactivity, some fundamental atomic and nuclear properties of Pm have not been studied until today, although fundamental research interests in Pm are quite strong. Pm marks the last element below $Z = 100$ where no experimental value for the first ionization potential (IP) is available. The first IP specifies the energy required to remove one valence electron from the neutral atom and is closely linked to an element's chemical behavior. Closing this gap in the Periodic Table is a very timely endeavor specifically in the year 2019, which has been declared the International Year of the Periodic Table of Elements for the 150th birthday of Mendeleev's discovery[2]. As a mid-f-shell element Pm exhibits a particularly complex atomic structure. Its ground-state configuration is [Xe]$4f^5 6s^2$. Already at moderate excitation energies the $6p$ and $5d$ orbitals are populated, leading to a system with four open shells and consequently forming an extraordinarily rich atomic spectrum.

From a nuclear physics point of view, Pm with its 61 protons lies in an interesting region with regard to nuclear shapes. ^{143}Pm possesses a filled neutron shell ($N = 82$) and thus is expected to exhibit a rather spherical shape, as no valence neutrons contribute to its electromagnetic properties. Towards neutron deficient isotopes, at $N \approx 75$, a particularly sharp transition to strongly quadrupole deformed nuclei is predicted by Leander *et al.* [18]. In Nd ($Z = 60$) already clear evidence for strong deformation was found at $N < 76$ [19]. On the neutron rich side one can push towards the well-known region of shape transition between $N = 86 - 90$, which has been observed in several other lanthanide elements. The characteristic of this transition, being either gradual (Ce [20], Nd [21, 22]) or abrupt

[2]Official website of the International Year of the Periodic Table of Elements: https://iypt2019.org/ Accessed 12/2019.

(Sm [23], Eu [24]), is largely dependent on the element. This behavior can be related to the $Z = 64$ proton subshell closure [25]. The fact that Pm lies exactly at the border between those two characteristics makes it a particularly interesting case.

1.2 Resonance ionization techniques for mass separators

In the 1970s the concept of step-wise photo-ionization by laser radiation was first introduced as a highly selective ion source [26, 27]. This technique, today commonly known as Resonance Ionization (RI), exploits each element's unique atomic structure to achieve an inherent elemental selectivity in the ionization process. A sketch of the RI principle is given on the left side in Fig. 1.2. Atoms are successively excited along strong optical dipole transitions, with the final step leading to ionization. This process is not only selective, but also highly efficient in most cases. Moreover, with the use of tunable laser systems, the adjustment of laser ion sources to different elements is possible within a short period of time. The elemental selection (respectively the atomic number Z) is often combined with conventional mass spectrometry techniques, which allow an additional selection of one set of isobars (nuclides of equal mass number A). As a result, one nuclide of interest can be selectively addressed in the experiment, as illustrated in the Nuclear Chart section on the right side in Fig. 1.2 for the specific case of ^{147}Pm. For its high versatility, the RI technique has evolved in different directions and is used today for a wide variety of applications. Terminologies for the Resonance Ionization principle vary dependent on the application case. A general distinction is often made between Resonance Ionization Spectroscopy (RIS) and Resonance Ionization Mass Spectrometry (RIMS), although the former usually relies on mass separation, too. It should also be noted that laser ion sources are often referred to as RILIS (Resonance Ionization Laser Ion Source), which strictly speaking does not include the subsequent mass separation step. Most laser ion sources are based on the hot-cavity approach, i.e. a resistively heated metal or graphite tube furnaces, where the sample material is atomized at temperatures of up to 2500 °C. Atoms in the source are resonantly ionized by the laser radiation and extracted with high-voltage electrodes. Alternative atomization approaches are e.g. sputtering [28, 29] or laser ablation [30, 31].

The RI technique, with its multitude of applications, is the field of expertise of the LARISSA group (Laser Resonance Ionization Spectroscopy for Selective Applications) at Mainz University. Apart from dedicated off-line RIMS projects, such as implantation of ^{163}Ho in metallic micro-calorimeters for the ECHo-project (Electron Capture in ^{163}Ho) [32–34], or trace analysis of actinide elements within the SIRIUS project (Secondary Ionisation of Radioactive Isotopes for Ultra trace analysis) [35, 36], the group is closely collaborating with the laser ion source teams at on-line radioactive ion beam (RIB)-facilities, e.g. ISOLDE at CERN, ISAC at TRIUMF or IGISOL at JYFL. Related activities include fundamental research, e.g.

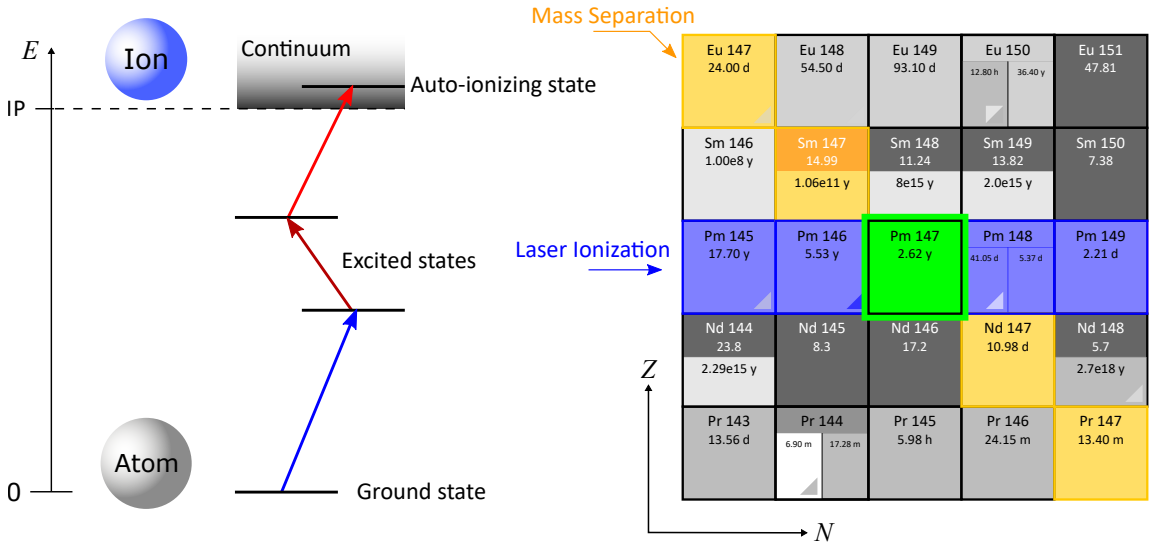

Figure 1.2.: Left: Resonance Ionization scheme. The arrows indicate the step-wise optical excitation from the atomic ground state to ionization. A detailed description of different ionization mechanisms in the final excitation step is given in section 3.4. Right: Selection principle of RIMS. The laser ionization scheme selectively ionizes one chemical element (blue). A following mass separation of the produced ion beam allows the selection of one set of isobars (orange). In combination, one nuclide of interest is selected.

measurement of atomic properties of radioactive species , or high-resolution spectroscopy on long isotopic chains for nuclear structure research.
The major part of this dissertation was carried out within the *Resonance Ionization Techniques for Separators* (RESIST) project, which is part of the Horizon 2020 research initiative of the European Commission. The main goals of this project are the refinement of laser RI techniques for applications at European on-line mass separator facilities. This includes specifically

- **Ionization scheme development:** The applicability of RI depends on optical excitation pathways populating excited atomic levels and leading to ionization through the final step. Since these schemes are specific to each element, extensive spectroscopic studies are necessary in order to make an element accessible for laser ion sources. The efficiency of these schemes can be determined in dedicated measurements with calibrated samples. A compilation of available ionization schemes is given in [37]. Since these schemes are the key to RIS itself, it is of high relevance to extend such databases, in particular towards previously unavailable elements.

- **Ion source development:** Although the RI process is fully element-selective, it often competes with other ionization mechanisms in the hot ion source environment, predominantly surface ionization. Isobaric species, which cannot be mass-separated, may consequently introduce significant contamination to

the ion beam and and impede on the experiment. In some extreme cases this contamination might surpass the species of interest by several orders of magnitude. Consequently, the feasibility and success of many experiments depends on a stringent suppression of this contamination. A well-established approach is the separation of the laser-atom interaction region from the hot atomization region [38–40]. This technique has recently been refined to allow high-resolution in-source spectroscopy through a perpendicular geometry between atomic beam and probing laser beam [41]. This approach is complementary to state-of-the-art spectroscopy techniques, e.g. collinear spectroscopy in fast beams, and needs to be well established thoroughly tested before being used on-line on a routine basis.

- **Laser development:** Sensitive RI in hot cavities usually relies on pulsed, high-repetition rate tunable laser systems. Almost twenty years ago, the Mainz Ti:sapphire laser system has been developed specifically for this application and is today in use at the majority of on-line laser ion sources worldwide [42–44]. Based on the original design, specialized variants emerged over the years. In particular pulsed narrow-bandwidth lasers are being requested within the RIS community for use in high-resolution spectroscopy. As part of the high-resolution capabilities of a laser system comes the challenge of precise laser wavelength measurement. In RIS, this is usually done with wavelength-meters, which allow for absolute wavelength measurements. With the steadily increasing precision in laser spectroscopy, it is important to develop techniques to characterize and verify the accuracy of such devices.

In conclusion, techniques of and around RI represent the methodical foundation of this dissertation. In the following chapter, related instrumentation is introduced as a basis for developments and experiments which were performed in this framework. Afterwards, specific chapters on atomic- and nuclear structure studies are presented, including the related publications as the central pillars of this thesis work. In order to establish a basis for the presented laser spectroscopy experiments and to improve readability without the need to consult supplementary literature, the publications are preceded by brief theory sections. Note that the primary purpose of these sections is not to elaborate on basic textbook theory, but rather to summarize the most important facts, equations and notations. For details the reader is referred to the cited textbooks and articles.

Chapter 2

Experimental instrumentation

2.1 Pulsed tunable laser systems

Hot cavity laser ion sources have special requirements for suitable laser systems. In terms of efficiency, pulsed lasers have clear advantages over continuous wave (cw) laser systems for several reasons. The peak power in pulsed laser radiation is much higher compared to cw, on one side allowing for straightforward frequency conversion using non-linear optics without dedicated resonators. On the other side, the high power density also renders the saturation of relatively weak transitions possible, which is often the bottleneck in the ionizing step (for details see section 3.4). Moreover, considering the state population transfer in the step-wise excitation, it is important to avoid optical pumping into states which are not part of the excitation ladder. After typically 1 ns a population equilibrium between the lower and the upper state is reached as long as the external laser field is sufficiently intense [45]. However, through additional loss channels the population may be quenched into inaccessible states, which are not part of the excitation ladder. These losses can be dramatically reduced by a laser pulse length shorter than the excited state lifetime, which is typically in the order of some ten nanoseconds [46]. Additional requirements on the laser system are introduced by the thermal conditions within the ion source. At a typical temperature of $T = 2000\,^{\circ}\mathrm{C}$ the most probable velocity in the Maxwell-Boltzmann distribution of a medium-mass-particle with mass $m = 100\,\mathrm{u}$ is $\hat{v} = \sqrt{2k_BT/m} = 615\,\mathrm{m\,s^{-1}}$. Considering a two-dimensional tubular atomizer of about 4 cm length (which is the case at ISOLDE), a particle with a velocity vector pointing towards the exit will require 60 µs to leave the tube (while strictly speaking still being exposed to the collinearly entering laser radiation). At exemplary angles of 45° (75°) towards the exit, this time is extended to 90 µs (250 µs). As the release of atoms is continuous, a high laser pulse repetition rate is mandatory. Only in this case every atom experiences at least one laser pulse before leaving the laser interaction re-

gion. At a repetition rate of 10 kHz, which is typically used at the majority of laser ion sources (e.g. ISOLDE, ISAC and RISIKO), a sample atom is exposed to 1 to 3 laser pulse sequences, resulting in a high ionization probability. The thermal movement of the atoms also causes a spectral Doppler broadening which is, depending on atomic mass, laser wavelength and temperature, and lies in the order of 1 to 5 GHz (for details see section 3.3). In order to achieve maximum ionization efficiency, the spectral laser profile has to match the Doppler distribution. Note that in dedicated high-resolution spectroscopy experiments, Doppler broadening is greatly reduced, e.g. by a perpendicular laser-atom beam interaction geometry [41] or by Doppler compression in accelerated beams [47, 48]. Naturally these experiments rely on narrow-band laser radiation, raising the demand for different and more complex laser types. Finally, and most essential, RIS depends on the availability of tunable lasers with a wide spectral coverage as basis for a versatile and universal ion source. Laser media fulfilling all the requirements are laser dyes or, alternatively, titanium-doped sapphire (Ti:sapphire) crystals. All laser systems in laser ion sources are based on these two types. Although dye and Ti:sapphire are widely complementary with regard to their emission wavelength range, they are rarely used in combination (with a prominent exception being the RILIS at CERN-ISOLDE), since most elements can be reliably accessed by a laser system of either type. Consequently, and for the sake of simplification of the experimental expenditure, most ionization schemes rely on a single laser type rather than using a mixed laser system. Dye lasers usually have a higher output power (≈10 W) and a short pulse length (≈5 ns) [44] as laser dyes have high gain compared to Ti:sapphire. However, they require high maintenance and degrade quickly during operation due to break-up of dye molecules by the pump laser radiation. Particularly in the case of UV-pumped dye lasers, a dye change may be required every 6 to 10 h. The Mainz University laser system is based on home-built Ti:sapphire lasers, which are widely maintenance free and provide a stable power output over hours to days without readjustment. A commercial frequency doubled Nd:YAG laser emitting at 532 nm serves a a pump source for the Ti:sapphire. Typical specifications for the pump laser are 10 kHz repetition rate, 150 ns pulse width and 40 to 200 W output power. One pump laser is usually used for pumping a number of Ti:sapphire lasers, each with 10 to 20 W. An output pulse synchronization can either be achieved by Q-switches (Pockels-cells) within the Ti:sapphire resonator based on the linear electro-optical effect or by proper adjustment of the pump power distribution.

2.1.1 Standard Laser

The basic Mainz University Ti:sapphire laser design was developed in 2003 by R. Horn [42] and underwent constant refinement ever since. It is based on a Z-pinch standing wave cavity with a Brewster-cut Ti:sapphire crystal in the central arm.

Two curved mirrors ($r_{\mathrm{curv}} = 75\,\mathrm{mm}$) focus the resonator mode inside the crystal at a folding angle of 17.4° to compensate for the astigmatism induced by the Brewster-cut of the crystal. The outer arms of the cavity are almost parallel beam propagation and are terminated by a high-reflective end mirror and an output coupler ($R = 0.8$), respectively. The latter has a slight wedge to avoid unwanted etalon effects. The resonator layout is shown in Fig. 2.1 (a). The spectral bandwidth of the laser output is given by two frequency selective elements, namely a Lyot-Filter (LF) and a Fabry-Pérot-Etalon (FPE). The LF is based on a birefringent material of thickness L. A sketch of the LF principle is given in Fig 2.2 (a). The electric field components E_y, E_z of an incident beam are subject to a phase shift

$$\delta_{\mathrm{LF}}(\lambda, L) = \frac{2\pi}{\lambda}(n_0 - n_e)L, \tag{2.1}$$

where n_0 and n_e denote the ordinary and extraordinary refractive indices of the birefringent material, respectively [49]. Generally this results in an elliptical polarization of transmitted light. Brewster surfaces within the laser resonator cause high losses for the s-polarized component (normal to the plane of the resonator). Considering a p-polarized beam traveling in the resonator, the phase shift δ_{LF} has to match multiples of 2π for minimal losses. The transmission function is given by

$$T_{\mathrm{LF}}(\lambda, L) = T_0 \cos^2\left(\frac{\pi(n_0 - n_e)L}{\lambda}\right) \tag{2.2}$$

[49]. Since the bandwidth (full width at half maximum (FWHM)) $\delta\nu$ scales with L, but the free spectral range (FSR) with L^{-1}, multiple plates are often combined in order to achieve a high finesse $\mathcal{F} = \mathrm{FSR}/\delta\nu$. The Mainz Ti:sapphire laser uses a set of three quartz plates of thickness $L_1 = 0.3\,\mathrm{mm}$, $L_2 = 4L_1$, $L_3 = 16L_1$, resulting in a transmission profile of $\delta\nu \approx 250\,\mathrm{GHz}$. The transmitted wavelength can be tuned by rotation of the LF optical axis with respect to the propagation vector of the incident beam, causing a change in n_e.
The spectral profile of the laser is further narrowed by a solid intra-cavity FPE. The principle is depicted in Fig. 2.2 (b). Subsequent reflection orders between the plane parallel surfaces within the material are phase-shifted by

$$\delta_{\mathrm{FPE}}(\lambda, d) = \frac{4\pi}{\lambda} n_2 d \cos(\beta). \tag{2.3}$$

Depending on the wavelength λ and the thickness of the substrate d, constructive or destructive interference occurs. The transmission fringes of an FPE are described by an Airy-function

$$T_{\mathrm{FPE}}(\lambda, d, R) = T_0 \frac{(1-R)^2}{(1-R)^2 + 4R\sin^2(\delta/2)} \tag{2.4}$$

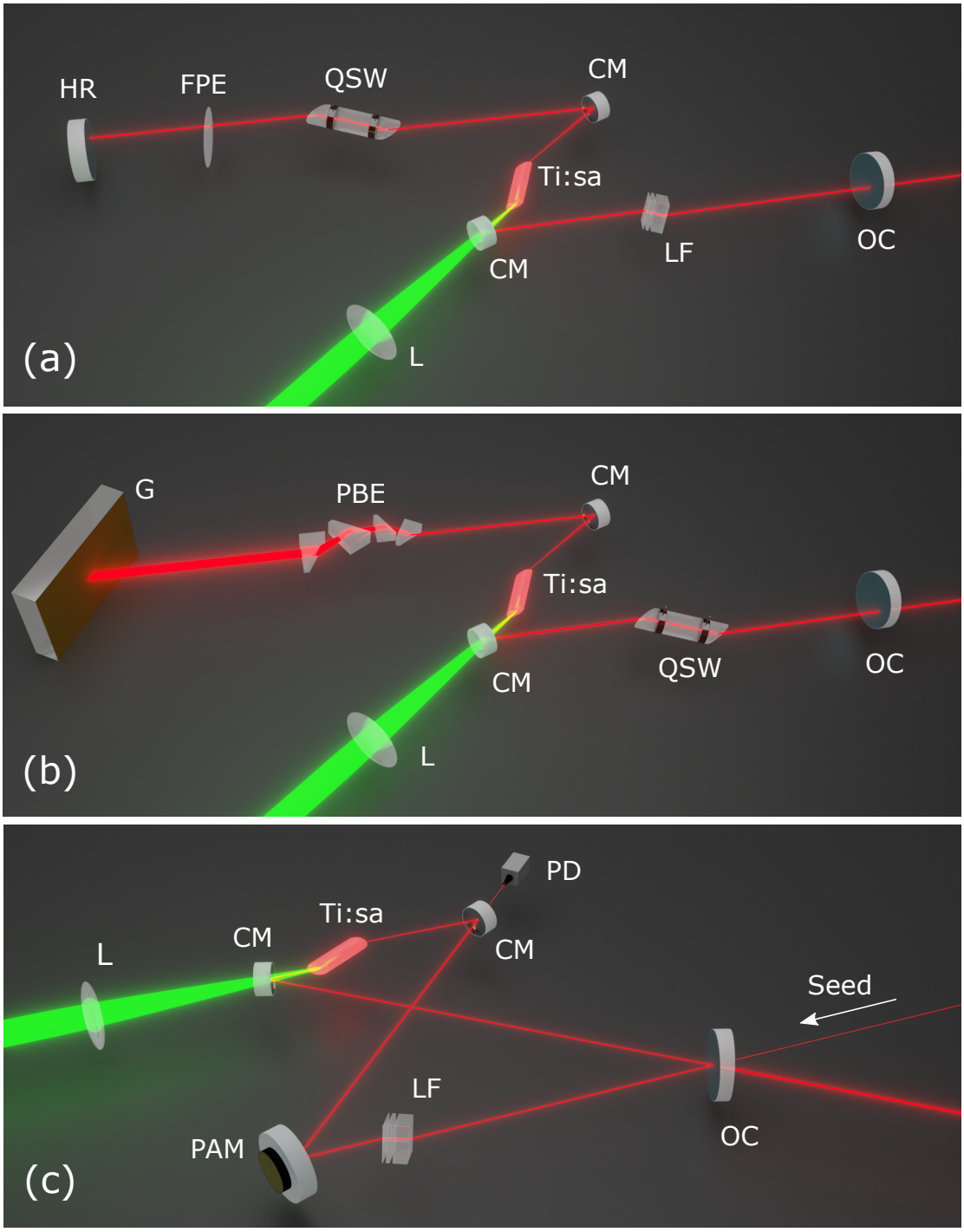

Figure 2.1.: Layout of the different Mainz University Ti:sapphire laser types. (a) Standard laser. (b) Grating-tuned laser. (c) Injection-seeded laser. For details see text. **HR:** high reflector; **FPE:** Fabry-Pérot etalon; **QSW:** Q-switch; **CM:** curved mirror; **Ti:sa:** Ti:sapphire crystal; **LF:** Lyot-filter; **OC:** output coupler; **L:** (biconvex) lens; **G:** reflective diffraction grating; **PBE:** prism beam expander: **PD:** photodiode; **PAM:** piezo-actuated mirror.

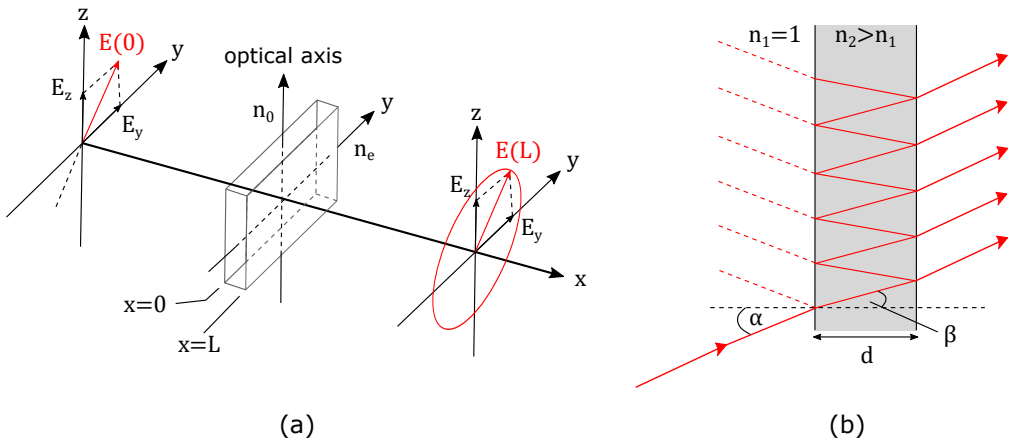

Figure 2.2.: Frequency Selection principles in a (a) Lyot-Filter and (b) Fabry-Pérot-Etalon. Figures adapted from [49].

[49]. Similar to the LF, the finesse $\mathcal{F}$ is defined as the FSR to bandwidth $\delta\nu$ ratio of a transmission fringe. It scales with the parallelism of the surfaces and their reflectivity R. In standard configuration the Mainz Ti:sapphire laser design uses a FPE with $d = 0.3\,\text{mm}$ and $R = 0.4$. This results in $\text{FSR}_{\text{FPE}} = c/2nd = 345\,\text{GHz}$ and a finesse of $\mathcal{F}_{\text{FPE}} = \pi\sqrt{R}/(1-R) = 3.3$. The bandwidth of this etalon is $\delta\nu = \text{FSR}/\mathcal{F} \approx 100\,\text{GHz}$, however, depending on the number of round-trips in the resonator during pulse build-up (typically ≈ 100), the resulting laser bandwidth is 3 GHz to 10 GHz, properly matching typical Doppler ensembles, as discussed above. Note that the laser bandwidth can be further reduced to ≈1 GHz by using an additional FPE (uncoated YAG, $d = 6\,\text{mm}$, $R = 0.08$) [50]. Furthermore, with a length of $\approx 450\,\text{mm}$ the resonator itself acts as a FPE with $\mathcal{F}_{\text{cavity}} \approx 0.8$ and $\text{FSR}_{\text{cavity}} \approx 330\,\text{MHz}$. Nonetheless, since the laser is running on multiple longitudinal modes, the effective bandwidth is given by the FPE fringe which lies within the LF transmission maximum. Fine-tuning of the emission wavelength is performed through careful adjustment of the FPE tilting angle α. The output characteristics are summarized in Table 2.1.

2.1.2 Grating-tuned laser

Although wide range spectroscopy can be performed using the standard resonator geometry, frequency scanning is a tedious procedure, as the transmission peaks of LF and FPE always have to be matched. Mode hops can often not be avoided. Nonetheless, a continuous scanning operation can be realized by using a reflective diffraction grating as frequency-selective element, replacing LF and FPE. The principle is depicted in Fig. 2.3. The grating has sawtooth-like grooves perpendicular to the plane of incidence. Light reflected from two neighboring grooves features an optical path difference Δs. When the relation $\Delta s = m\lambda$ is satis-

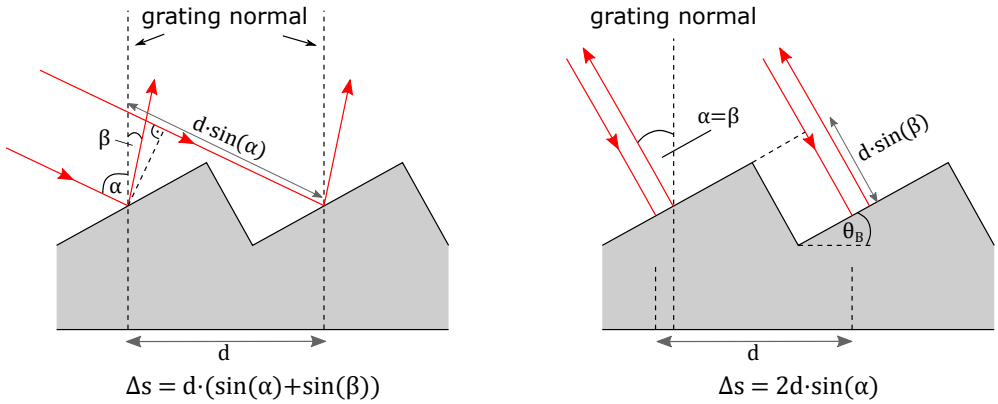

Figure 2.3.: Operation principle of a reflective diffraction grating. Left: general case at an arbitrary angle of incidence α. Right: Littrow configuration. The angle of incidence α equals the reflection angle β. Constructive interference can be optimized for certain wavelengths with the so-called blaze angle θ_B. Figure adapted from [49].

fied, where m denotes the interference order, constructive interference occurs. In Littrow-configuration, shown on the right side in Fig. 2.3, the grating is used as a wavelength-selective retro-reflector, which is particularly useful in lasers. Usually the $m = 1$ interference order is coupled back to the resonator. The resolving power of a diffraction grating scales with the number of illuminated grooves N according to

$$\frac{\lambda}{\delta\lambda} = mN. \tag{2.5}$$

In the grating-tuned Ti:sapphire laser, a reflective grating with 1740 grooves/mm (blazed for 800 nm) replaces the end mirror. A prism beam expander (PBE) is used in front of the grating to horizontally widen the beam to 3 mm ($1/e$ radius). This laser type was developed in 2010 at Mainz University and TRIUMF [51, 52]. It is shown in Fig. 2.1 (b). Tuning of the grating angle on a rotation stage allows continuous frequency scanning. The grating-tuned laser features a more narrow bandwidth than the standard design in the order of 1 to 3 GHz, which is favorable in spectroscopy applications. However, it suffers from a lower output power by a factor of ≈ 2. The output characteristics are summarized in Table 2.1.

2.1.3 Injection-seeded laser

In terms of spectral linewidth and stability, cw lasers are clearly superior to pulsed lasers. Indeed, tunable cw Ti:sapphire lasers with linewidths of < 100 kHz and output powers of few W are commercially available, although at relatively high costs. Laser diodes can be used as an economical low-power alternative over a limited wavelength range (typically ± 10 nm around the specified emission wavelength λ_c). Nonetheless, since the RI process highly benefits from pulsed laser radiation, as discussed above, the advantages of cw and pulsed lasers have to be

combined. This can be achieved by *seeding* a pulsed amplifier cavity (slave) with a cw laser (master or seed). This concept was applied to the Mainz Ti:sapphire laser system in 2010 [51], and refined in a collaboration with the University of Jyväskylä [53, 54]. The layout is shown in Fig. 2.1 (c). A bowtie-shaped cavity is designed to avoid spatial hole burning, which would prevent single-mode operation [55]. Standing waves are stationary, resulting in non-collected inversion in the laser medium at the spatial nodes of the main resonator mode m. Consequently, the $m \pm 1$ side-modes, which have their anti-nodes located at the nodes of the main mode, are amplified. The bowtie-shaped design allows for a traveling wave and thus avoids this effect. Selective amplification of the desired longitudinal mode is achieved by proper focusing of stabilized cw light into the amplifier (slave) cavity. Upon built-up of population inversion in the laser medium by injection of the pump pulse, the seed light is already present in the resonator, strongly promoting the corresponding longitudinal mode by stimulated emission. As a constructive interference condition, the optical path length within the cavity needs to be matched to multiples of λ_{seed}. Although the slave laser has a rugged design, it is prone to temperature drifts and vibrations on the desired level of precision and requires continuous active stabilization. For this purpose, one cavity mirror is mounted on a piezo actuator, allowing for fast adjustments of the cavity length in the order of few micrometers. A sensitive fast photodiode placed behind one of the curved mirrors collects leaking cw light from the cavity and provides the stabilization signal to a fast lock-in voltage supply (TEM Laselock 3.0) controlling the piezo-actuated mirror. The photodiode amplifier is blanked during pulse build-up preventing disturbance from the high-intensity Ti:sapphire fluorescence and scattered pump light. The electronic layout of the photodiode amplifier circuitry can be found in [53]. Usually no frequency-selective elements are placed within the resonator, however, at wavelengths far from the Ti:sapphire gain maximum Brewster-plates or a LF may be required. Provided the seed laser is sufficiently stable and the amplifier properly locked, the linewidth of the pulsed laser radiation can reach the Fourier-limit of $\delta\nu = \text{TDP}/\delta t \approx 11\,\text{MHz}$ (with a time-to-bandwidth product of $\text{TDP} = 0.44$ for a Gaussian pulse shape and a pulse width of $\delta t = 40\,\text{ns}$), while the other characteristics are similar to the standard laser, as comprised in Table 2.1. At Mainz University, an external cavity diode laser (ECDL) with sophisticated stabilization electronics and monitoring is used as master laser. For a description of the cw laser system see Publication IV or [56, 57].

Note that two bowtie-resonator laser prototypes were designed in the scope of this dissertation: a compact-footprint injection-seeded laser and an unseeded bowtie-resonator laser with a dual-etalon configuration. The resonator geometry is based on calculations using the Gaussian ray transfer matrix analysis, or ABCD formalism, which is described e.g. in [58]. The optimized geometry results are directly transferred to a paper-printed layout, which can be fixed to an optical breadboard allowing for easy assembly and testing. The compact-footprint injection-

seeded laser is now in use at the ISOLDE-RILIS and is presented in [59]. The unseeded bowtie-resonator laser development was later abandoned due to unstable single-mode operation and high spectral jitter. It is now being replaced by a cw Ti:sapphire laser with a similar resonator geometry [60, 61], which can then be used for seeding another pulsed Ti:sapphire amplifier. Since these prototypes are widely unrelated to the spectroscopy results presented in this thesis (with the exception of the 741 nm transition in Publication I, where the unseeded bowtie-resonator laser was used), they are only briefly described in the appendix A.1.

Table 2.1.: Specifications for the output of the different Ti:sapphire laser types. The values are based on the references [44, 51–54, 62], as well as measurements which were performed in the scope of this dissertation. The given specifications correspond to 10 kHz repetition rate. For the injection-seeded laser, values marked with an asterisk are directly transferred from the master laser. In this case typical values for an ECDL, as used in Publication V, are given.

	Standard	Grating-tuned	Injection-seeded
Repetition rate	7 to 15 kHz		
Pulse width	40 to 60 ns		
Average Power	3 to 5 W	1 to 2 W	3 to 5 W
Output range	700 to 1020 nm		$\lambda_c \pm 10$ nm*
Tuning range	100 GHz	700 to 1020 nm	10 to 20 GHz*
Spectral bandwidth	1 to 10 GHz	1 to 3 GHz	20 MHz
Beam quality (M^2)	< 1.3		

2.1.4 Frequency conversion

The fundamental emission range of Ti:sapphire of 700 to 1020 nm corresponds to photon energies of 1.22 to 1.77 eV. With ionization potentials between 5 to 9 eV for most metallic elements, typically 4 to 6 photons would thus be required for ionization. Apart from the fact that a six-photon ionization scheme would be rather impractical, most atomic ground state transitions can simply not be accessed by the fundamental Ti:sapphire radiation. The atomic level density roughly scales with the square of the principal quantum number n (for single-electron excitations). Consequently, ground-state transitions in many elements lie in the blue or ultraviolet (UV) wavelength regime. They can be accessed by higher harmonics, i.e. multiples of the fundamental laser frequency. In this process a wave $\mathbf{E}$ is passed through a so-called non-linear optical medium, which in response is polarized. The electric polarization density $\mathbf{P}$ of the material can be expressed by the

Taylor-series

$$P_i = \epsilon_0 \left(\chi_{ij}^{(1)} E_i + \chi_{ijk}^{(2)} E_j E_k + \chi_{ijkl}^{(3)} E_j E_k E_l + ... \right), \tag{2.6}$$

where ϵ_0 is the electric field constant and $\chi^{(n)}$ the electric susceptibility tensor [63]. Considering a non-vanishing $\chi^{(2)}$ and a plane wave $\mathbf{E} = E_z = E_0 \cos(kz - \omega t)$ of frequency ω traveling in z direction, the polarization density is given by

$$P_{z,\mathrm{SHG}} = \epsilon_0 \chi_{zz}^{(1)} E_0 \cos(kz - \omega t) + \epsilon_0 \chi_{zzz}^{(2)} E_0^2 \cos^2(kz - \omega t) \tag{2.7}$$

$$= \epsilon_0 \chi_{zz}^{(1)} E_0 \cos(kz - \omega t) + \epsilon_0 \chi_{zzz}^{(2)} \frac{E_0^2}{2} (1 + \cos(2kz - 2\omega t)). \tag{2.8}$$

Obviously, the non-linear polarization generates a new wave with frequency 2ω, referred to as the second harmonic of the incident wave, as well as a zero-frequency component. This process is called second harmonic generation (SHG) and represents the simplest case of non-linear frequency conversion. The more general case with two different waves $E_1(k_1, \omega_1)$ and $E_2(k_2, \omega_2)$ interacting within the medium results in a polarization of the form

$$P = P^{(0)} + P^{(\omega_1)} + P^{(\omega_2)} + P^{(2\omega_1)} + P^{(2\omega_2)} + P^{(\omega_1+\omega_2)} + P^{(|\omega_1-\omega_2|)}, \tag{2.9}$$

which includes sum-frequency and difference-frequency terms. Independent of the specific process, the phase-matching condition

$$\frac{n_3\omega_3}{c} = \frac{n_1\omega_1}{c} + \frac{n_2\omega_2}{c} \tag{2.10}$$

has to be met, where n_i are the wavelength-specific refractive indices of the material. It is based on the fact that incident and generated waves should constructively interfere along the entire length of the medium to achieve maximum intensity in the corresponding term. Since non-linear media are often birefringent crystals, where the refractive indices depend on direction and polarization of incident waves, phase-matching can be achieved by a suitable crystal orientation with respect to the optical axis (type I phase matching) or alternatively by temperature adjustment (type II phase matching) [64].

SHG is routinely used as part of the Mainz Ti:sapphire laser system. The simplest approach is focusing the fundamental output of a Ti:sapphire laser into a beta-barium borate (BBO) crystal in single-pass geometry. The conversion efficiency of this process is 10 to 20 %. Alternatively, the BBO is placed directly inside the Ti:sapphire laser resonator. In this configuration the output coupler is replaced by a broadband high-reflective mirror. As a result the cavity is completely closed for the fundamental wave, leading to high power density within the cavity and an efficient SHG process with $\approx$ 50 % conversion efficiency. The second harmonics is coupled out with a dichroic mirror. A photograph of this configuration, as was

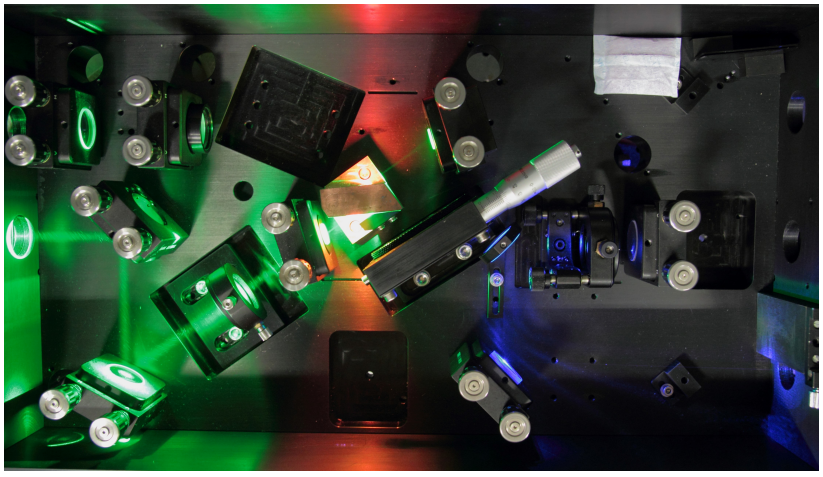

Figure 2.4.: Photograph of the standard Ti:sapphire resonator with intra-cavity SHG, as used in [65]. A BBO crystal within the laser cavity generates the second harmonic at $\lambda^{(2)} = 470\,\text{nm}$. In this configuration the output coupler is replaced by a broadband high reflective mirror. The second harmonic is coupled out with a dichroic mirror.

used in the work [65], is presented in Fig. 2.4.

Other processes employed at the Mainz laser setup are sum frequency generation and difference frequency generation [66]. The former is usually applied for production of the third harmonic by mixing the fundamental and SHG waves. A dedicated frequency tripling unit has been designed for this purpose, where a conversion efficiency of $\approx 3\,\%$ can be achieved [44]. Moreover, the fourth harmonic can be generated in a two-stage SHG process. However, wavelengths below 215 nm cannot be reached as BBO absorbs light in this range, resulting in low output intensity possible damage of the crystal.

Using non-linear frequency conversion, laser ionization schemes usually rely on two to three photons, where higher harmonics are predominantly used for ground-state transitions, which require high photon energies but relatively low laser power for saturation.

2.2 Wavelength measurement

In laser spectroscopy an accurate frequency measurement is as important as the bandwidth and stability of the probe laser. In particular the RIS technique depends on reliable absolute frequency measurements, since usually several excitation steps are involved and have to be added in order to extract high-lying level energies. Even for relative frequency measurements, e.g. for the study of hyperfine spectra or isotope shifts, reproducibility has to be ensured since RIS most often relies on the measurement of one isotope at a time. For this task usually commercial wavelength meters are used, which are convenient in operation and

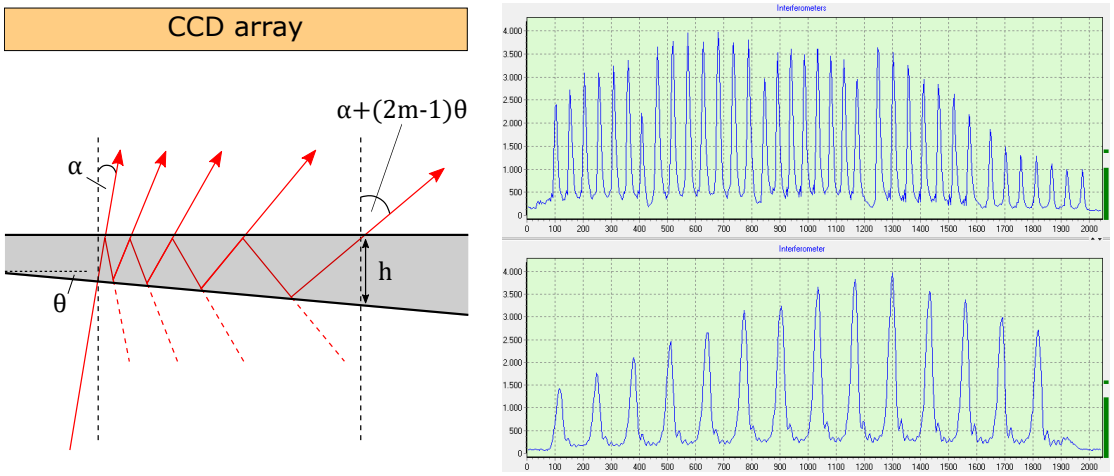

Figure 2.5.: Left side: sketch of the Fizeau interferometer principle for use in a wavelength meter. The interference creates a line pattern along the axis of the wedge, which can be captured on a CCD array. Right side: fringe pattern of a narrow-linewidth diode laser in the WSU-30 wavelength meter. The spectrum is plotted as intensity vs. pixel number on the CCD array. The lower graph shows the pattern of the thickest interferometer with a FSR of $\approx 2\,\mathrm{GHz}$.

easily meet the required specifications in broadband spectroscopy experiments. However, with increasing precision in high-resolution experiments, the accuracy and long-term stability of such devices needs to be verified and, in specific cases, extended by complementary measurements. This task was tackled by a collaboration of European RIS groups and is presented in Publication IV. In the following, the underlying basics of laser frequency measurement are briefly introduced.

2.2.1 Wavelength meters

Wavelength meters (or Lambdameters) are commercially available since many years. Modern high-end devices reach an accuracy of few MHz in absolute frequency measurement. The LARISSA lab uses two different commercial devices: a High Finesse WS6-600 and a High Finesse WSU-30 with specified absolute 3σ accuracy of 600 MHz and 30 MHz, respectively. The wavelength measurement is based on the evaluation of fringe patterns from a set of Fizeau interferometers. Since the exact assembly of the device is not known, only the basic principle is discussed here. Disassembly and upgrade of a similar, but also rather old wavelength meter is presented in [67].

A Fizeau interferometer (FI) is very similar to a plane Fabry-Pérot interferometer (FPI, see Fig. 2.2), except that the surfaces of the cavity are inclined at a small angle θ (in the order of 10^{-5} rad [68]) to each other. A sketch is given on the left side in Fig. 2.5. The phase shift of the m-th reflection order is given by

$$\delta_{\mathrm{FI}}^{m}(\lambda, h, \theta, \alpha) = \frac{2\pi}{\lambda} \frac{h}{\tan\theta} \left(\sin\left[\alpha + 2(m-1)\theta\right] - \sin\alpha\right), \tag{2.11}$$

where α is the angle of incidence and h the distance of the reflecting surfaces [68, 69]. Rather than a circular fringe pattern as obtained from a FPI, a FI forms a line pattern along the axis of the wedge, which can be captured on linear CCD sensor arrays. Note that the interferometer is often formed by two air-spaced reflecting surfaces rather than a solid wedged substrate. Since the two partly reflecting mirrors have to be wedged themselves in order to avoid etalon effects, this may lead to confusion in some cases. However, the substrate wedge angle is much larger than the actual Fizeau wedge. The free spectral wavelength range of $\mathrm{FSR}_{\mathrm{FI}} = \lambda^2/2h$ depends on the plate separation h and the wavelength λ [68, 69]. Combining multiple FI of different FSR and evaluating the fringe patterns with a previously recorded calibration pattern allows for a precise frequency measurement within few milliseconds. The right side of Fig. 2.5 shows a measured sample pattern of a diode laser close to 780 nm in the WSU-30 wavelength meter. According to the data sheet, the FSR of the two finest (thickest) interferometers in the WSU-30 are 2 GHz and 15 to 20 GHz, whereas the design of the WS6-600 omits the finest interferometer with a dedicated CCD array. However, the specified accuracy of 600 MHz is sufficient for all kinds of broadband spectroscopic experiments.

2.2.2 Absolute references

As mentioned in the previous section, wavelength meters rely on external absolute references. Although commercial devices are initially calibrated, frequent re-calibration is necessary to account for temperature, pressure or mechanical influences. A prerequisite for reference sources is the precise knowledge of the absolute frequency as well as long-term stability. Suitable options are e.g. frequency combs, stabilized single-frequency lasers or tunable lasers locked to an atomic transition. From an economical point of view the former is undue for the sole use as wavelength meter calibration source. The LARISSA lab formerly used a stabilized HeNe laser (SIOS SL03) with a specified wavelength of 632.991 040(25) nm as absolute reference. Despite offering a suitable stability of $\Delta\nu = 2.5$ MHz over 24 h, the absolute frequency uncertainty of 19 MHz exceeds the 1σ accuracy of the WSU-30 wavelength meter. Moreover, the HeNe emission is relatively far away from the Ti:sapphire laser output between 700 and 1000 nm, making it rather unsuitable for calibration in that range, as the wavelength meter accuracy is specified for a calibration within ± 200 nm of the wavelength to be measured. For these reasons a Rb saturated absorption spectroscopy (SAS) setup was recently installed as replacement for the HeNe laser. A schematic view of the setup is shown in Fig. 2.6. As laser source an external cavity diode laser (Toptica DL Pro 780) is used, which is coupled to a Rb spectroscopy assembly (TEM CoSy 4.0). SAS is based on a pump-probe scheme. The laser beam is split into three beams: a reference

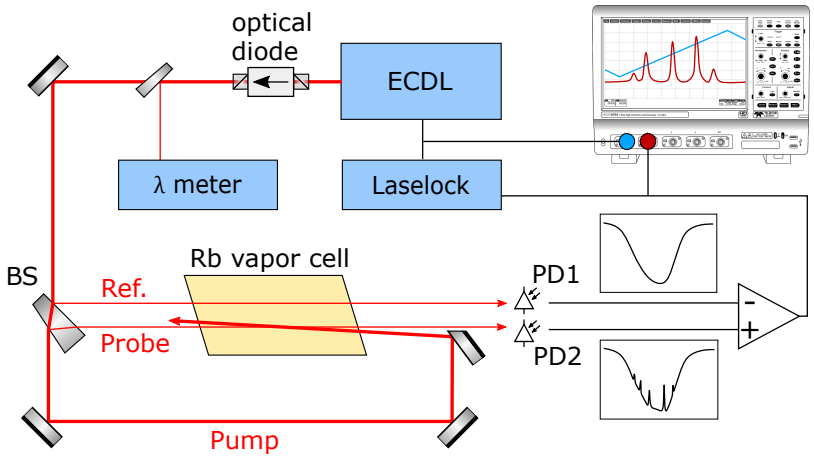

Figure 2.6.: Schematic of the Rb saturated absorption spectroscopy setup. **ECDL:** external cavity diode laser; **BS:** beam splitter; **PD:** photodiode. Note that the actual design of the commercial Rb spectroscopy module may differ slightly.

beam, a probe beam and a high intensity pump beam. The reference beam simply passes through the Rb vapor cell, whereas the pump and the probe beam are counter-propagating within the cell. Both, the reference beam and the probe beam are separately captured on photodiodes after transmission through the cell. The difference signal can be monitored with an oscilloscope. The feedback signal from the photodiodes is sent to an electronic laser stabilization system (TEM LaseLock 3.0), which controls a current offset for the ECDL, enabling fast frequency scanning within a range of few GHz. Since the atomic transition frequency ν of moving atoms at a velocity v in the Rb gas is shifted according to $\nu = \nu_0(1 + v/c)$, where ν_0 is the frequency at rest, the reference beam imprints a Doppler-broadened absorption profile on the photodiode upon scanning[1]. The absorption of the probe laser, on the other hand, shows additional features. For $\nu = \nu_0$ both, the probe and the pump beam address the same velocity class of atoms, i.e. $v = 0$. In this case the high intensity pump beam burns a hole into the atomic ground state population, thus lowering the absorption of the probe beam. This effect is visible as narrow dip in the absorption structure, also known as Lamb-Dip. For multiple transitions which are separated by less than the Doppler width, a number of Lamb-Dips plus additional lines are visible. These so-called crossover lines occur at laser frequencies exactly between the two transition frequencies. In this case the probe and the pump beam address different transitions for atoms moving at velocities $\pm v$ and $\mp v$, respectively [70].

For wavelength meter calibration in the Ti:sapphire output range the D2 line in the Rb atom at 780 nm was chosen, which is close to the Ti:sapphire gain maximum. The level scheme and recorded spectrum of the multiplet starting from the $F = 2$ ground state is shown in Fig. 2.7. For reasons of a larger line separa-

[1]For details on atomic transitions and Doppler broadening see sections 3.2 and 3.3.

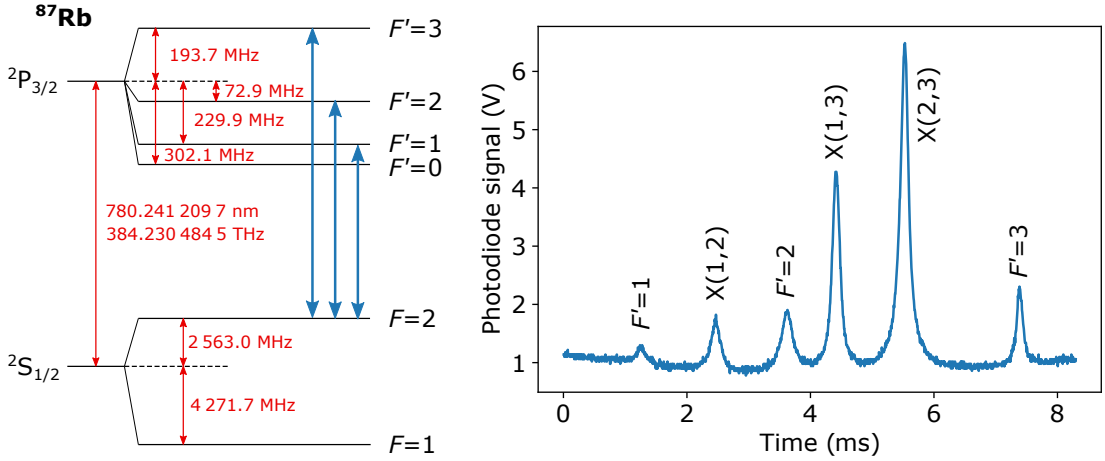

Figure 2.7.: Left: level scheme for the D2 line in ^{87}Rb. Data is taken from [71], where also higher precision numbers and uncertainties can be found. Right: saturated absorption spectrum for $F = 2$ in ^{87}Rb, corresponding to the transitions shown as blue arrows in the level scheme. Crossover lines are denoted by an X with the participating F' levels in brackets. The baseline structure is caused by slight imperfections in the gain adjustment of the two photodiodes. The horizontal axis gives the timescale at which the ECDL is scanned over the structure (i.e. the progress of the diode current offset sweep).

tion ^{87}Rb was chosen over ^{85}Rb and the $F = 2$ over the $F = 1$ ground state. The $F = 2 \rightarrow F' = 3$ line is of advantage for fast re-locking. Upon losing the lock, the laser approaches the structure from the high-frequency side. Stabilization is based on a top-of-fringe dither lock. The $F = 2 \rightarrow F' = 3$ transition in ^{87}Rb is located at 780.246 020 886(22) nm (= 384.228 115 203(11) THz) [71]. This precision of 11 kHz in literature exceeds by far the long-term stability of the SAS setup, which is specified as $\Delta\nu = 2$ MHz and acts as the limiting factor in calibration accuracy. Since drifts in the wavelength meter readout may reach up to 5 MHz per hour (see Publication IV), an automated re-calibration was implemented into the LabVIEW data acquisition. The cycle can be set to a fixed time interval or to a number of recorded data points.

2.2.3 Fringe-offset technique

In addition to laser frequency measurement using wavelength meters, a scanning Fabry-Pérot interferometer (SFPI) offers a complementary, *relative* measurement. It is based on a comparison of transmission fringes of a laser under investigation with those of a reference laser of known wavelength and high stability. In the LARISSA lab this complementary measurement is only applied to the master ECDL used for seeding of the injection-locked Ti:sapphire laser (see Sec. 2.1.3), where highest accuracy is required. At the same time this technique is used for (slow) stabilization and scanning of the the master ECDL. An additional fast stabi-

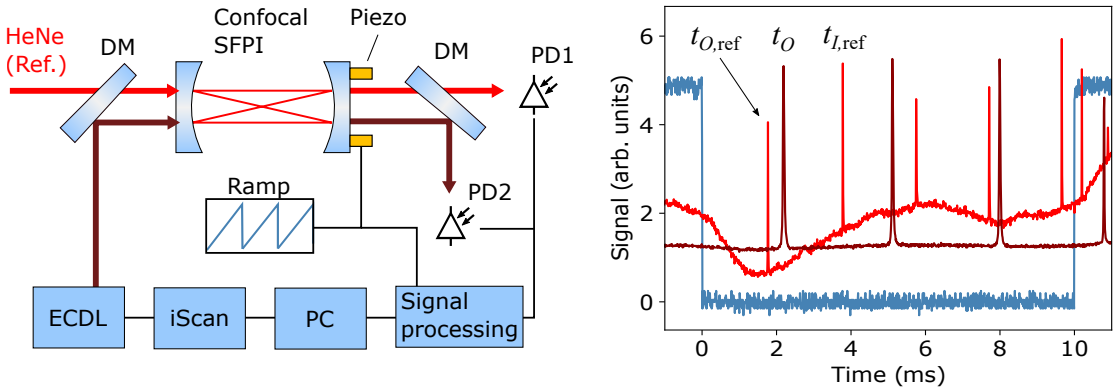

Figure 2.8.: Left: Schematic layout of relative frequency measurement with a confocal scanning FPI. The feedback signal can be used for slow stabilization of the ECDL. **DM:** dichroic mirror; **PD:** photodiode. Right: Signal readout recorded with an oscilloscope. Signals are scaled for better visibility. The blue envelope marks one piezo ramp. The photodiode signal of HeNe and ECDL (near 930 nm) are plotted in the colors corresponding to the sketch. The HeNe signal is generally low and features some electronic baseline noise, however, fringes are clearly visible. Fringes are marked according to Eq. 2.12. A detailed descriptiopn of the signal processing is given in [56].

lization is provided by a quadrature interferometer coupled to a fast electronic lock-box (TEM iScan). For a technical description of the locking see [56]. A schematic layout of the fringe-offset measurement setup is shown in Fig. 2.8. The ECDL and a HeNe reference laser (SIOS SL03) are transmitted through a confocal SFPI. A confocal FPI features curved mirrors, which are spaced at a distance d corresponding to the mirror radius of curvature. In contrast to the plane-parallel FPI, the free spectral range is $\mathrm{FSR}_{\mathrm{FPI,conf}} = c/4nd$ [49]. Using a piezo-actuated mirror, the cavity length is periodically changed on a micrometer scale, so that each ramp covers several transmission fringes of both lasers. After passing the cavity, the two laser beams are separated with a dichroic mirror and the intensities are captured by fast photodiodes. From the fringe time differences, measured from the start of the piezo ramp, the relative frequency ν_{rel} of the ECDL to an arbitrary anchor point can be determined. The first and second fringes (offsetfringe and interfringe) of the HeNe reference laser act as a kind of ruler in this measurement. The frequency change of the ECDL between two piezo ramps is given by

$$\nu_{\mathrm{rel}} = n\mathrm{FSR}\frac{(t'_O - t'_{O,\mathrm{ref}}) - (t_O - t_{O,\mathrm{ref}})}{t_{I,\mathrm{ref}}} \cdot \frac{\lambda_{\mathrm{ref}}}{\lambda}, \tag{2.12}$$

where t_O and t_I mark the timings of the offset- and interfringe, respectively. Primed symbols refer to fringe timings in a different piezo ramp [57]. From Eq. 2.12, it is obvious that the wavelength of both lasers and the FSR of the SFPI have to be known. The latter was measured as FSR = 299.721 MHz [72]. With the spec-

ified wavelength of the HeNe of $\lambda_{\text{ref}} = 632.991\,040(25)\,\text{nm}$, a precision of λ in the range of 0.1 nm is sufficient to reach $\Delta\nu_{\text{rel}} < 40\,\text{kHz}$ [57], so that in practice the uncertainty of the master ECDL is dominated by the laser frequency jitter of few MHz.

2.3 RISIKO

The RISIKO mass separator is the heart of the LARISSA lab at Mainz. It is an exemplary apparatus for RIMS applications. Regarding its key features, i.e. a hot-cavity laser ion source coupled to a magnetic mass separation, it is very similar to the RIB facility ISOLDE at CERN. Obviously, with the main difference being that ISOLDE is directly coupled to the radioactive isotope production site (*on-line* method), whereas RISIKO uses externally introduced samples (*off-line* method), but nonetheless acts as RIB facility with operation permission for a variety of long-lived radionuclides.
The RISIKO separator was originally designed by K. Zimmer [73] for trace analysis of strontium radioisotopes in environmental samples, following the disaster of the Chernobyl nuclear power plant in 1986. Today the main applications of RISIKO are isotope separation and ion beam implantation into collector foils or calorimetric detectors, most prominently within the ECHo project [32–34], or laser spectroscopy of stable and long-lived isotopes [74–76], as e.g. funded within the RESIST project. In this context, RISIKO is also used as an off-line research & development laboratory for novel developments and refinements of the ISOLDE laser ion source RILIS (see section 2.5).
The combined vacuum chambers of the separator have a total length of $\approx 7\,\text{m}$ on a pressure in the range of 10^{-7} to $10^{-8}\,\text{mbar}$. Some parts of RISIKO are modular and can be replaced depending on the current application. Since this work is focused on laser spectroscopy, the apparatus is presented in the corresponding configuration if not explicitly noted. An overview of the setup is given in Fig. 2.9. It can be divided into four main parts: ion source, ion beam extraction and shaping, mass separation and ion detection.

2.3.1 Ion source

The hot-cavity ion source of RISIKO is depicted in Fig. 2.10. The central parts are the sample reservoir (also referred to as *mass marker*[2]) and the atomizer (also referred to as *hot-cavity* or *line*[2]), both made of tantalum. The atomizer is a tubular oven with 2.5 mm inner diameter, 1 mm wall thickness and 35 mm length, mounted between a water-cooled multi-layer Ta spring and a water-cooled Ta panel, featur-

[2]The terms *mass marker* and *line* refer to the corresponding components at ISOLDE's ion source, where the line acts as transfer tube between target and ion beam extraction and the mass markers as independent reservoirs, containing stable samples which can be used for mass calibration.

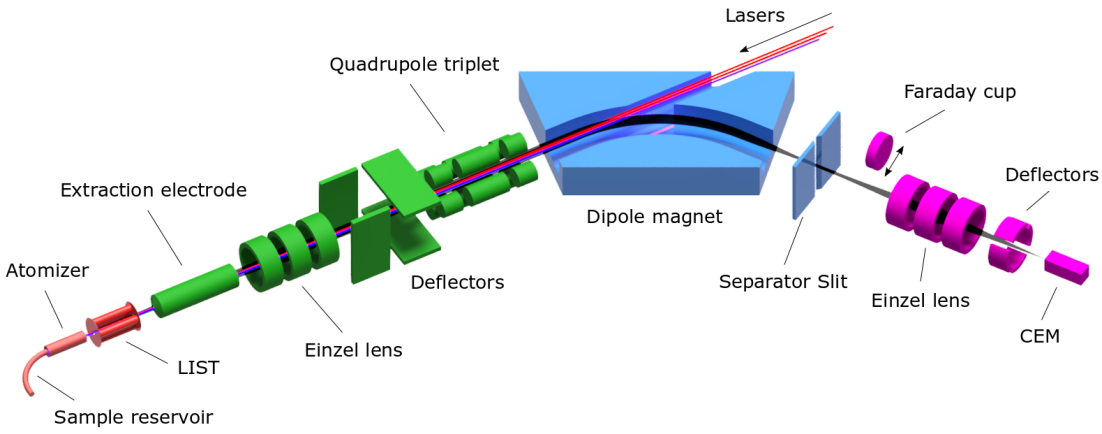

Figure 2.9.: Overview of the RISIKO mass separator setup. Red: Ion source; green: Ion beam extraction and shaping; blue: Mass separation; magenta: Ion detection. Parts are not to scale for better visualization. For details see text. Figure adapted from [34].

ing four through-holes to minimize heat dissipation. The sample reservoir is a bent capillary with an inner diameter of 1 mm, a wall thickness of 0.5 mm and 165 mm length, which is connected to the back side of the atomizer through a conical push-in assembly. The atomizer mount is fixed to the Ta spring by a molybdenum washer and nut, preventing irreversible welding of the connection surfaces.
Usually the sample material is dissolved in nitric acid (HNO_3) and afterwards dropped on a $\approx 5 \times 5$ mm backing foil. The solution is dried on the foil, which is then folded like an envelope and introduced into the sample reservoir. A photograph of a 5 µL sample solution droplet on a 5×5 mm Ti foil, as well as a folded "envelope" is shown on the right side of Fig. 2.10, with an atomizer for comparison. The choice of backing material depends on the ion source chemistry. Since the dried sample is usually oxidized, the backing should act as a reduction agent as the sample diffuses through the foil. Titanium, Zirconium or Hafnium are often used as backing material, depending on the required source temperature and *a priori* thermal equilibrium simulations[3]. Atomizer and sample reservoir can be heated resistively with a currents of up to 400 A and 150 A, respectively, allowing operation at temperatures of up to 2500 °C. While the atomizer is always operated at a sufficiently high temperature for atomization, the temperature of the sample reservoir is carefully ramped up for a controlled release of the sample into the atomizer, where resonance ionization by the incident laser beams occurs. A uniform temperature distribution in the whole assembly is crucial for sensitive studies on limited sample amounts. Cold spots lead to adsorption of sample atoms on walls, lowering the effective ionization efficiency. On the other hand, excessive heating

[3]HSC Outotec Chemistry 9.

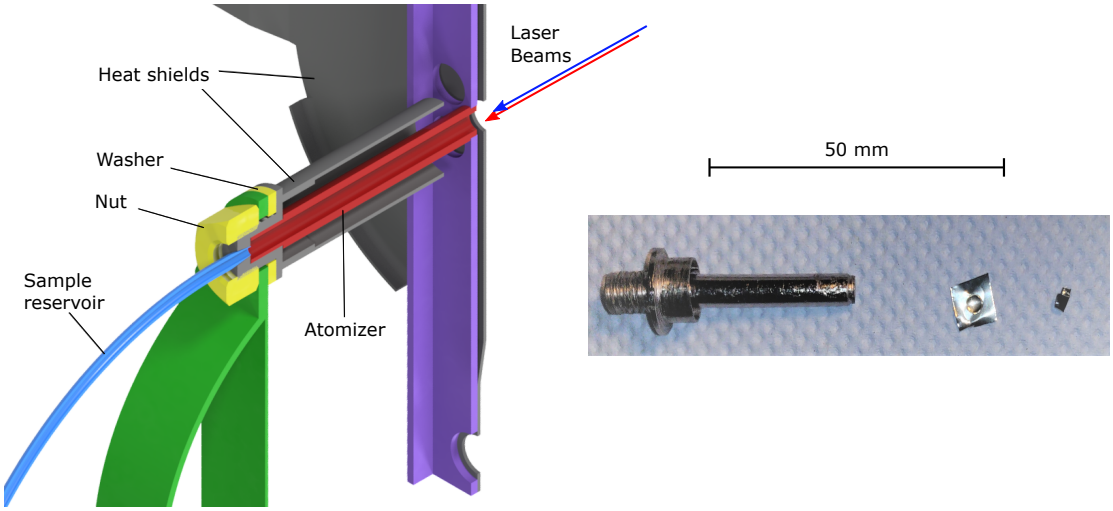

Figure 2.10.: Left: Cross section of the hot-cavity ion source assembly of the RISIKO mass separator (CAD drawing). The sample is placed in the sample reservoir, which can be heated independently of the atomizer. The incident laser beams resonantly ionize sample atoms within the atomizer tube. Ions are extracted with 30 kV upon leaving the atomizer. Right: Photograph of a 5 µL sample solution droplet on a 5 × 5 mm Ti foil and a folded sample "envelope", with the 35 mm long atomizer tube for scale.

enhances surface ionization, as described by the Saha-Langmuir equation

$$\frac{n_+}{n_0} = \frac{g_+}{g_0} \exp\left(\frac{e(W - \mathrm{IP})}{k_B T}\right), \tag{2.13}$$

where n_+ and n_0 denote the flux of ions and neutral atoms with their respective statistical weights g_+ and g_0 (the atomic and ionic ground state degeneracy), e the elemental charge, W the work function of the ion source material and IP the ionization potential of the sample atoms [77].
Obviously the hot-cavity can act as a surface ion source by itself. However, in most cases the efficiency is comparatively low and a very limited elemental selection is only provided by the respective ionization potentials of the different species within the ion source. Therefore surface ion source operation is avoided for most elements, with an exception in the groups of the alkaline and alkaline-earth elements due to their low ionization potentials.
In laser ion source operation, the effect of surface ionization introduces unspecific contamination in the extracted ion beam, therefore reducing the selectivity of the ion source. In order to keep the effect of surface ionization at minimum while maintaining high efficiency, an optimization of the ion source temperature distribution was recently performed and is described in [33]. With typical operation parameters for rare-earth samples, the ion source temperature is between 1500 °C to 2200 °C. Nonetheless, specific experiments can be impeded or even prevented

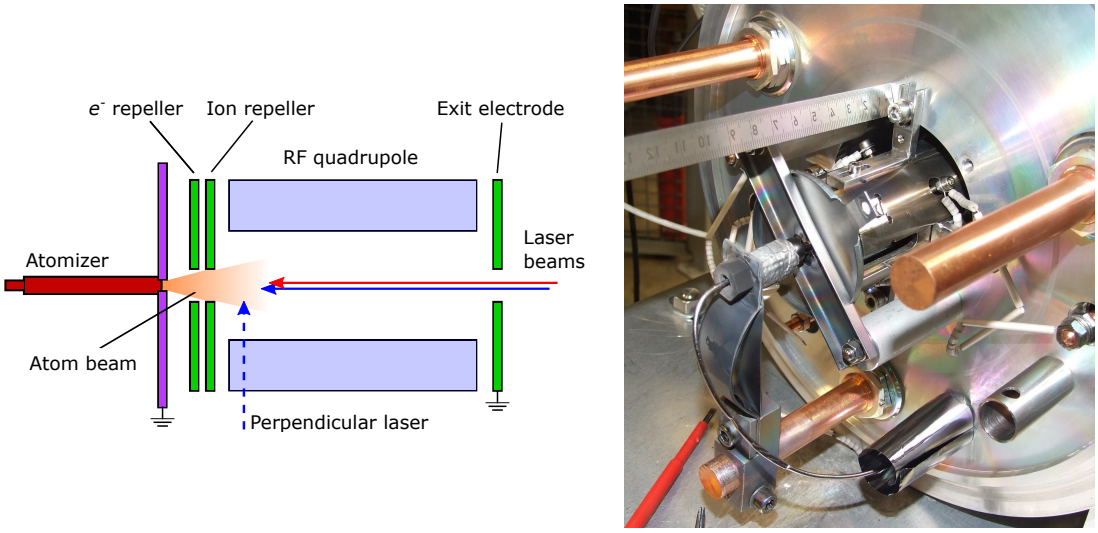

Figure 2.11.: Left: Schematic layout of the Laser Ion Source and Trap LIST. The dashed line indicates the perpendicular laser-atom interaction geometry (PI-LIST mode). Right: Photograph of the ion source region with an installed (PI-)LIST module.

by ion beam impurities from surface ionization. Such cases are, for example, when a low-IP element has stable isobars to the nuclide of interest, or simply when the number of sample atoms is so small that even surface ionization of metallic elements is in the order of the laser ion signal. Approaches for further reduction of the surface ion contribution are the use of low-workfunction materials within the ion source [78], or a separation of the laser-atom interaction region from the hot atomization region. This latter concept is implemented in the Laser Ion Source and Trap LIST [79–81].

The LIST is an optional ion source module, which can be installed directly in front of the atomizer. A schematic view is shown in Fig. 2.11. It features two repeller electrodes facing the atomizer, a radio frequency (RF) quadrupole structure and an exit electrode. Like the Ta panel holding the atomizer, the exit electrode is set to the local ground potential of 30 kV. The voltages applied to the two electrodes facing the atomizer define the mode of operation: In **Ion-Guide mode** both electrodes are set to a negative potential of -20 V. Ions generated within the atomizer are extracted, guided by the 1.2 MHz RF field towards the exit electrode, and are extracted from the source region with 30 kV. This configuration resembles operation of the ion source in standard RILIS mode, i.e. without a LIST module, with an efficiency loss factor of < 2 [40]. In **LIST mode**, the second electrode is set to $+20$ V, thus acting as an ion repeller. Surface ions from the atomizer are suppressed and only laser-ionized species from the atomic beam effusing to the LIST volume are extracted. In this case the first (negative) electrode acts as an electron repeller, preventing electron-impact ionization within the LIST volume through electrons emitted from the hot atomizer. Typical suppression factors in LIST mode are in

the order of 10^3 [76, 81]. However, LIST operation also introduces a loss factor, as all charged species (including laser ions) within the atomizer are suppressed. Typical loss factors lie between 20 and 50 [76, 81]. Therefore LIST operation is only advisable if an experiment depends on additional isobar suppression.
The most recently introduced mode of operation, the PI-LIST-mode, is described in detail in Publication V, as well as in the references [41, 74, 76]. Therefore it is only mentioned here for the sake of completeness. As the name suggests, the *perpendicularly illuminated* (PI) LIST features a different laser-atom interaction geometry. Instead of guiding all laser beams directly into the atomizer, i.e. anti-collinearly to the ion beam axis, one laser beam perpendicularly intersects the atomic beam effusing from the atomizer. This geometry offers greatly reduced spectral Doppler broadening. Some quantitative considerations about expected Doppler linewidths in perpendicular laser-atom interaction are given in section 3.3.

2.3.2 Ion beam extraction and shaping

The RISIKO ion optics consists of an extraction electrode, an einzel lens, a set of horizontal and vertical deflector plates and a quadrupole triplet, as schematically depicted in Fig. 2.9 by the green parts. The ion beam is extracted in two stages from the ion source region, which is set to a potential of +30 kV. The extraction electrode, located 40 mm downstream of the LIST exit electrode (or the atomizer outlet in standard RILIS operation) acts as a pre-acceleration stage, with a potential of typically +20 kV. The tip of the extraction electrode features a conical shape in order to counteract beam expansion due to space-charge effects. The full beam energy of 30 keV is reached at the grounded first electrode of the einzel lens, located 400 mm downstream of the extraction electrode. The einzel lens assembly consists of three ring electrodes, with the outer two sitting on ground potential and the middle electrode at typically +10 kV. Through deceleration and subsequent acceleration of the ion beam, a focusing effect can be achieved without changing the beam energy. Together with the two-stage extraction, this configuration acts as a telescope, allowing careful adjustment of beam size and divergence. For minor corrections of the ion beam direction, which can be traced back to slight misalignment of the atomizer, two sets of 140 mm long deflector plates are installed downstream of the einzel lens, with an offset of ± 50 mm to the ion beam axis. In order to preserve the on-axis potential, opposite sign voltages of identical absolute value are applied to facing plates. Typically low voltages $|U_{\mathrm{defl}}| < 50$ V are needed for optimal transmission. Note that the deflector plates can also be used as *kickers* for active ion beam gating. Since the ion beam has a pulsed time-structure, following the 10 kHz laser repetition rate, the continuously extracted surface ion contribution can be actively suppressed by a factor of > 2 by fast switching of the deflector plates to a higher potential of e.g. ≈ 300 V [76, 81, 82]. Finally, an electrostatic quadrupole triplet allows for compensation of an astigmatism in the

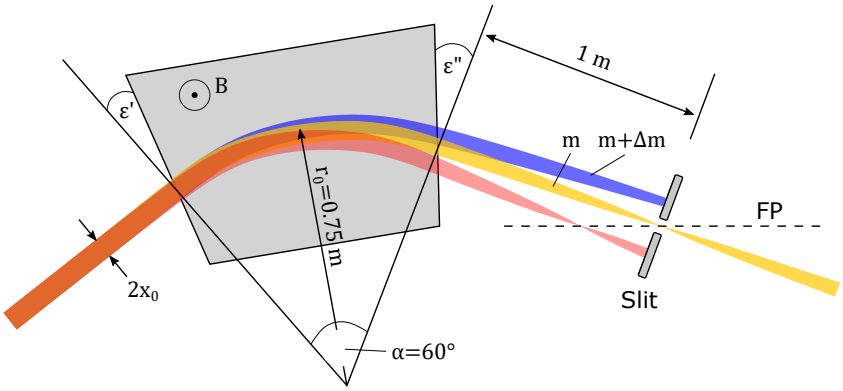

Figure 2.12.: Sketch of the mass separation principle with a focusing dipole magnet. For details see text. $\mathbf{x_0}$: beam offset; $\boldsymbol{\epsilon'/\epsilon''}$ **:** entrance/exit angle; **B** : magnetic field; $\mathbf{r_0}$: nominal radius; $\boldsymbol{\alpha}$ **:** nominal deflection angle; **m** : mass; $\boldsymbol{\Delta m}$ **:** mass difference; **FP:** focal plane. Figure adapted from [73].

ion beam. Ideally, after passing the quadrupole triplet, the ion beam is adjusted for optimal parallelism in both axes.

2.3.3 Mass separation

Magnetic mass separation is based on the circular deflection of charged particles traveling in a magnetic field B. A sketch of the dipole magnet mass separation principle is given in Fig. 2.12. With a fixed kinetic energy of $eU_0 = 30\,\mathrm{keV}$ of the incident ion beam, the deflection radius r is given by the equilibrium of Lorentz force and centrifugal force as

$$r = \frac{1}{B}\sqrt{\frac{2mU_0}{e}}, \tag{2.14}$$

where m denotes the particle mass. A beam of finite width $2x_0$ is focused upon passing the magnet, with the focal length exclusively depending on the geometric parameters $r, \alpha, \epsilon', \epsilon''$ (cf. Fig 2.12) and the particle mass m. With a proper shape of the magnet yoke in y-direction, as well as the angles ϵ' and ϵ'', the foci in x and y direction can be matched. At the focal plane of the nominal trajectory with $r = r_0$ a slit aperture is placed. In order to achieve a separation of two neighboring masses m and $m + \Delta m$, their geometric splitting at the position of the slit has to be greater than the beam spot size. In case of a parallel beam, the mass resolution can be expressed as

$$\frac{m}{\Delta m} = x_0 \frac{D_m}{k\epsilon}, \tag{2.15}$$

where $D_m(r_0, \alpha, \epsilon', \epsilon'')$ is the mass dispersion, ϵ the emittance representing the beam quality, and k an imaging parameter [73]. Under optimal conditions the RISIKO magnet reaches a resolving power of $\frac{m}{\Delta m} \approx 700$. Obviously the magnet

can be tuned to transmit a mass of choice according to Eq. 2.14 by adjusting the magnetic field. The maximum field strength of the RISIKO magnet is 0.62 T [73]. According to Eq. 2.14, the maximum mass is ≈ 350 u at 30 keV beam energy.

2.3.4 Ion detection

The ion detection region is shown in Fig. 2.9 (magenta). After passing the slit aperture, ions can be detected either with a Faraday cup (FC) or a channel electron multiplier (CEM). The home-built FC essentially consists of a conducting plate for charge collection and an electron repeller. Implanted ions induce a current flow from the plate, which can be measured with a sensitive electrometer. Since an impinging particle may also release several electrons, an aperture set to -100 V is placed 20 mm upstream, deflecting electrons back to the plate. The sensitivity of the FC is limited by electrical noise on a level of $\approx$ 50 fA, corresponding to $\approx 3 \times 10^5\, e\, s^{-1}$. On the other hand, the FC has practically no upper limit for the ion beam load. Typical peak currents that can be achieved at RISIKO are some hundred nA. For very low-intensity beams, as usually the case in spectroscopy of radioactive species, the CEM offers a more sensitive measurement. In order to guide the ions to the CEM, the FC is retracted from the beam axis with a pneumatic piston. The diverging ion beam passes an einzel lens for post-focalization and a set of deflectors for beam steering. Finally, ions reach the CEM. It consists of a front aperture, a conversion electrode, installed at an angle of $\approx 30°$ to the beam axis, and a conical insulating channel, which is layered with a high-resistance material on the inside. By applying a potential to the front of the channel, an electric field gradient is created towards the grounded electrode on the back side. The RISIKO CEM is operated with -1 kV on the front aperture, -3 kV on the conversion electrode and -2.5 kV on the front of the channel. Upon ion impact on the conversion electrode, secondary electrons are released and guided into the channel, where an electron avalanche is created through several wall collisions towards the grounded electrode. The signal is converted to a TTL pulse by a discriminator and acquired with an Arduino MCU. The dead time of an identical CEM was measured in [83] as $\tau = 398(50)$ µs, allowing single ion counting up $10^5\, s^{-1}$ with losses < 4 %. Higher counting rates should be avoided anyway to prevent damage of the detector.
Data acquisition and storage is performed with a modular LabVIEW interface on a personal computer. The data acquisition cycle is 300 ms.

2.4 MABU

The Mainz Atomic Beam Unit (MABU) is a compact laser ion source coupled to a quadrupole mass spectrometer. This tabletop setup has a footprint of $< 1\, m^2$. Since it is similar to RISIKO in many aspects, a detailed description is not given

here to avoid repetition. The setup is briefly described in Publication I, Publication II and Publication III. For details the reader is referred to [83, 84], where the design, construction and characterization of the apparatus was performed.
The main differences to RISIKO are the low beam energy of $\approx$ 200 eV and the use of a quadrupole mass filter (QMF) instead of a magnet. An in-depth treatise of the QMF mass separation principle and a characterization of the same type quadrupole as used in the MABU system (ABB Extrel) is given in [85]. The MABU setup is coupled to a dedicated Ti:sapphire laser system and can thus be operated independently of RISIKO. The main drawback is its relatively low ion transmission efficiency through the apparatus, which is in the range of 10^{-3} and thus about one to two orders of magnitude lower compared to RISIKO. In addition, the MABU system only features ion detection by a CEM, so it can be operated only at low ion currents. Therefore it is mainly used for laser spectroscopy applications, e.g. ionization scheme development [36, 86], measurement of ionization potentials [87, 88], or high-resolution spectroscopy on stable isotopes or long-lived radioisotopes [89–91].

2.5 ISOLDE

The ISOLDE facility is the on-line mass separator at CERN. The original facility, located at the synchrocyclotron, started operation in 1967 and was moved to the proton synchrotron booster (PSB) in 1992 [92]. A recent technical overview is given in [93]. ISOLDE delivers radioactive ion beams for fundamental atomic and nuclear physics research to currently ten fixed experimental setups[4], as well as a number of temporary setups, such as the GANDALPH spectrometer [94, 95]. The production of radioisotopes is achieved using the ISOL technique. Protons are accelerated to an energy of 1.4 GeV in the PSB and impinge on a massive target, formed e.g. by uranium carbide (UC_x), producing a wide range of short lived nuclei all over the Nuclear Chart through spallation, fission and fragmentation processes [96]. The reaction products effuse out of the target unit through a transfer line into the ion source. Ions are extracted with 60 kV, followed by magnetic mass separation and delivery to an experiment. ISOLDE uses different types of ion sources, based on surface ionization, plasma ionization or resonance laser ionization (RILIS). The latter has been producing the majority of beams in recent years due to its high selectivity and efficiency. The target and ion source in RILIS configuration is shown in Fig. 2.13. Obviously, this configuration is very similar to the RISIKO ion source (cf. Fig. 2.10 and Fig. 2.11), so that both facilities directly benefit from the close collaboration. Moreover, the RILIS is using the Mainz type Ti:sapphire lasers as part of their laser system [44]. Consequently, the LARISSA group and the RILIS team are working on similar developments. This includes upgrades to the laser

[4] http://isolde.web.cern.ch/experimental-setups. Accessed 12/2019.

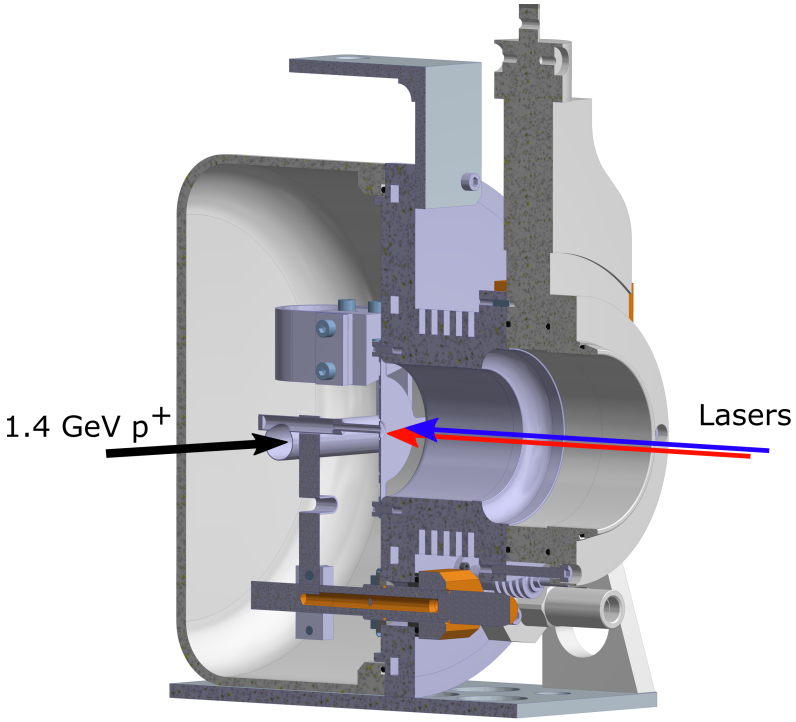

Figure 2.13.: Layout of the ISOLDE target and ion source unit (CAD drawing). The many common features to the RISIKO ion source are obvious (cf. Fig. 2.10 and Fig. 2.11). For details see text.

system, new laser ionization schemes, measurement of ionization efficiencies for different elements [97, 98] or technical ion source developments, e.g. the LIST [79–81]. Many successful in-source spectroscopy experiments were performed with the RILIS technique [99, 100]. However, the resolution that can be achieved is limited by spectral Doppler broadening within the hot ion source. High-resolution in-source spectroscopy techniques, such as the PI-LIST [41, 76] or Doppler-free two-photon spectroscopy [59], are coming up only recently. In this context, it should be noted that there are two fixed experiments at ISOLDE focusing on high-resolution laser spectroscopy, namely COLLAPS [101, 102] and CRIS [48, 103, 104]. Both setups rely on collinear laser spectroscopy of fast atom or ion beams. The initial energy distribution of atoms in the ion source is conserved during the extraction of ions by 60 keV, resulting in a strongly compressed Doppler broadening, to the order of the natural linewidth of strong atomic transitions [47, 48]. Like this hyperfine splittings and isotope shifts in long isotopic chains can be measured and may be used to extract nuclear structure parameters. A compilation of radioisotopes that have been subject to laser spectroscopy studies is given in Fig. 2.14. A similar overview is given in [7]. Note that the presented data was not exclusively taken at ISOLDE. Other facilities that should be mentioned in this context are ISAC at TRIUMF or IGISOL at JYFL, among others[5]. In order to expand this chart of nuclear structure data, is it important to provide suitable laser ionization

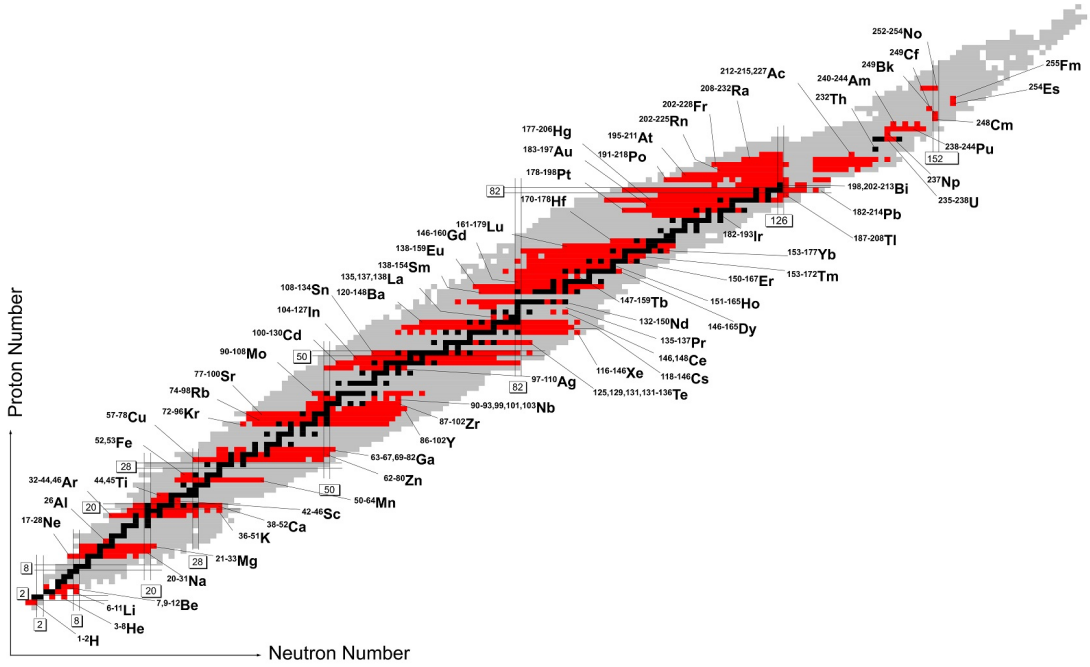

Figure 2.14.: An overview of the status of laser spectroscopy on radioactive isotopes. This figure was taken from an online database maintained by the group of W. Nörtershäuser at TU Darmstadt. Black tiles mark stable isotopes, red tiles mark radioactive isotopes which have been studied by laser spectroscopy with the results published in peer reviewed articles. References are given on the website[5].

schemes for previously inaccessible elements, both for ion beam production and probing of individual transitions. Additionally, the extension of high-resolution in-source spectroscopy capabilities is of high relevance as complementary technique to collinear laser spectroscopy. The benefits of in-source techniques are the independence from dedicated beam lines, laser systems or charge exchange processes for re-neutralization of ions, greatly reducing the complexity of the experiment.

[5] https://www.ikp.tu-darmstadt.de/gruppen_ikp/ag_noertershaeuser/research_wn/exotic_nuclei_wn/uebersicht_2/laserspectroscopy_survey.de.jsp. Accessed 12/2019.

Chapter 3

Atomic structure and the ionization potential

3.1 Atomic energy levels

As a starting point for the treatment of many-electron systems we first consider a simple atomic system with a single electron orbiting a nucleus with Z protons. The quantum-mechanical energy levels of such a hydrogen-like system are given by the solution of the time-independent Schrödinger equation $H|\psi\rangle = E'|\psi\rangle$. In polar coordinates (r, θ, ϕ) and with the center of mass of the system as origin of coordinates it can be written as

$$-\frac{\hbar^2}{2\mu}\Delta\psi(r,\theta,\phi) + V_C(r)\psi(r,\theta,\phi) = E'\psi(r,\theta,\phi), \tag{3.1}$$

where $\mu = m_e M/(m_e + M)$ is the reduced mass of the system and $V_C(r) = -\frac{Ze^2}{4\pi\epsilon_0 r}$ the Coulomb potential [105]. By double separation of variables the solution, i.e. the wave function, can be expressed as

$$\psi_{nlm}(r,\theta,\phi) = R_{nl}(r)Y_l^m(\theta,\psi), \tag{3.2}$$

where the quantum numbers n, l and m can assume the values

$$\begin{aligned} n &\in \mathbb{N} && \text{(Principal quantum number)} \\ l &= 0, 1, ..., (n-1) && \text{(Angular momentum quantum number)} \\ m &= -l, -(l-1), ..., l && \text{(Magnetic quantum number).} \end{aligned}$$

In spectroscopic notation $l = 0, 1, 2, 3, 4, ...$ is written as $s, p, d, f, g, ...$ The spherical harmonics $Y_l^m(\theta, \psi)$ completely describe the angular dependence of Eq. 3.2. They are tabulated and can be found in common atomic physics textbooks, e.g. [105,

106]. The differential equation for the radial wave function R_{nl} has a similar form to Eq. 3.1, but is only one-dimensional. With the substitution $R_{nl}(r) = u_{nl}(r)/r$ it can be written as

$$-\frac{\hbar^2}{2\mu}\frac{\mathrm{d}^2 u_{nl}}{\mathrm{d}r^2} + V_{\mathrm{eff}} u_{nl} = E'_{nl} u_{nl}, \tag{3.3}$$

introducing the *effective potential* $V_{\mathrm{eff}} = \frac{\hbar^2 l(l+1)}{2\mu r^2} + V_C$ [107]. For a state with principal quantum number n the energy eigenvalue is given by

$$E'_{nl} \equiv E'_n = -\frac{\mu Z^2 e^4}{8\epsilon_0^2 h^2 n^2} = -\frac{Z^2 R_\mu}{n^2}, \tag{3.4}$$

where R_μ is the reduced Rydberg energy [106]. In the case of hydrogen, it corresponds to $R_{\mathrm{H}} = 13.6\,\mathrm{eV}$, the binding energy of the atomic ground state. The energy in 3.4 only depends on n, leading to a $\sum_{l=0}^{n-1}(2l+1) = n^2$-fold degeneracy of each state.
Note that in 3.4, $n \to \infty$ corresponds to a binding energy of $E'_\infty = 0$. In order to go along with the notation in the publications presented within this work, we define the atomic ground state as the zero-point energy. Consequently, E_n describes an excitation energy rather than a binding energy and E_∞ corresponds to the ionization potential (IP), i.e. the energy required to lift the electron from the atomic ground state to the ionization continuum. Accordingly, Eq. 3.4 is modified to

$$E_n = \mathrm{IP} - \frac{Z^2 R_\mu}{n^2}. \tag{3.5}$$

3.1.1 Fine structure

Relativistic corrections to the energy eigenvalues derived from the Schrödinger equation 3.1 are summarized under the term *fine structure* (FS). The consideration of these effects partly lifts the above mentioned degeneracy. The individual contributions to the fine structure are

- The increase in mass of the electron by taking into account the relativistic energy $E = \sqrt{m_0^2 c^4 + p^2 c^2} - m_0 c^2 + V$.
- Non-localization of the electron within the volume λ_c^3, where $\lambda_c = \hbar/m_e c$ is the Compton wavelength of the electron, leading to a shift in s-wave energies.
- The spin-orbit interaction, based on the coupling of the electron spin moment to the magnetic field caused by its orbital motion. The parallel or anti-parallel orientation of the spin $\boldsymbol{s}$ to the orbital angular momentum $\boldsymbol{l}$ leads to a splitting of energy levels into doublets. The *total angular momentum* $\boldsymbol{j} = \boldsymbol{l} + \boldsymbol{s}$ is introduced, with a new quantum number $j = l \pm 1/2$ (or more generally

$j = |l - s|, .., l + s$). Note that, analogous to l, s and j have associated magnetic quantum numbers m_s and m_j.

Finally, taking into account the FS corrections, the excited energy levels of hydrogen-like atoms are given by

$$E_{nj} = \mathrm{IP} - E'_n \left[1 + \frac{Z^2\alpha^2}{n}\left(\frac{1}{j+1/2} - \frac{3}{4n}\right)\right], \tag{3.6}$$

where E'_n denotes the energy from Eq. 3.4 and $\alpha = e^2/4\pi\epsilon_0\hbar c$ is the *fine structure constant* [106]. In hydrogen the FS corrections are in the order of 10^{-4} eV, however, the FS contribution scales with Z^2, which leads to a relatively large effect in heavy atoms.

3.1.2 Multi-electron systems

The exact calculation of energy levels in a multi-electron system is not possible anymore, since the mutual Coulomb repulsion of each individual electron has to be considered, leading to an N-particle problem. In practice one has to rely on mean-field approaches, treating the individual electrons as independent particles in an effective potential. Depending on the level of precision and the complexity of the atomic system, theoretical calculation may become computationally very intensive. The common approximation methods shall not be discussed here and can be found e.g. in [107, 108]. As established above, each single-particle state is fully characterized by a set of quantum numbers (n, l, m_l, m_s). In a multi-electron system, two electrons may not share the same set of quantum numbers due to the Pauli exclusion principle. The individual angular momentum quantum numbers in multi-electron systems may couple in different ways to a total angular momentum $\boldsymbol{J}$. In light atoms the single-electron orbital angular momenta $\boldsymbol{l}_i$ and the spins $\boldsymbol{s}_i$ couple through the exchange interaction to a total orbital angular momentum $\boldsymbol{L}$ and a total spin $\boldsymbol{S}$, respectively, which in turn couple to the total angular momentum

$$\boldsymbol{J} = \boldsymbol{L} + \boldsymbol{S} \quad \text{with} \quad \boldsymbol{L} = \sum_{i=1}^{N} \boldsymbol{l}_i \quad \text{and} \quad \boldsymbol{S} = \sum_{i=1}^{N} \boldsymbol{s}_i. \tag{3.7}$$

This is referred to as ***LS*-coupling**. The state is described with a term symbol according to

$$^{2S+1}L_J^{\pi}, \tag{3.8}$$

where $L = 0, 1, 2, ...$ is written as $S, P, D, ...$ in analogy to the lowercase letters for single particles. The parity π is omitted for even parity states and denoted with a superscript 'o' for odd parity states.
In heavy atoms, where the spin-orbit interaction dominates the exchange interaction, individual electron spins and orbital angular momenta couple to single-

particle total angular momenta $\boldsymbol{j}_i$, which then couple to the total angular momentum

$$\boldsymbol{J} = \sum_{i=1}^{N} \boldsymbol{j}_i \quad \text{with} \quad \boldsymbol{j}_i = \boldsymbol{l}_i + \boldsymbol{s}_i. \tag{3.9}$$

This is referred to as ***jj*-coupling**. The term symbol of a state is written as

$$(j_1, j_2, ...)^{\pi}_{J} \tag{3.10}$$

[107]. For example, the notation for the atomic ground state in dysprosium is [Xe]$4f^{10}6s^2\ {}^5I_8$. The preceding [Xe] denotes the full electron configuration of xenon, which, as a noble gas configuration, need not be considered further ($L = 0, S = 0$). Similarly, the $6s$ shell is completely filled by the two electrons and may be disregarded. The ten $4f$ valence electrons couple to a ${}^5I_8$ term via LS-coupling. Particularly in excited states, one may also find couplings of a collective electronic core to excited electrons. As an example, the excited state in Dy at 9991 cm^{-1} with a configuration of $4f^9({}^6H^o)5d6s^2\ {}^7I^o_9$ [109], which is subject to spectroscopy studies in Publication I, can be considered. Like the atomic ground state, it is described in LS-coupling. The total spin and the total orbital angular momentum of the electronic core term ${}^6H^o$ couple with the outer $5d$ electron to a ${}^7I^o_9$ term. As another example, the excited state in Dy at 24 709 cm^{-1} with a configuration $4f^{10}({}^5I_8)6s6p({}^1P^o_1)\ (8,1)^o_7$ [109], as addressed in Publication II, exhibits LS-coupling in an inner and an outer part of the electronic shell, which then couple to a term of $(8,1)^o_7$ via jj-coupling (or strictly speaking JJ-coupling).
Note that there are also the possibilities of J_1K-coupling or LK-coupling, which are rather rare and not of relevance for this work. A brief description is given e.g. on the NIST Atomic Spectra Database website[1].

3.1.3 Rydberg atoms

An atom with one electron excited to a high principal quantum number state is referred to as a Rydberg atom - and correspondingly the excited state as Rydberg state. Some atomic properties exhibit a strong n dependence, as tabulated e.g. in [110], leading to the extraordinary nature of Rydberg atoms. Particularly interesting for RI applications are the low binding energy, accompanied by long radiative lifetimes and large collisional ionization cross sections. Moreover, Rydberg atoms can be easily ionized with electric fields in the order of 100 V cm^{-1} [110] or by blackbody radiation, e.g. within a hot-cavity ion source, rendering laser excitation to high-lying Rydberg-states an efficient ionization method [111]. Another peculiar property of Rydberg atoms is their similarity to a hydrogenic atomic system due to the low overlap of the excited electron wave function with the electronic

[1] www.nist.gov/pml/atomic-spectroscopy-compendium-basic-ideas-notation-data-and-formulas/atomic-spectroscopy-2. Accessed 12/2019.

core. The nuclear charge of Ze is effectively screened by the $-(Z-1)e$ charge of the electronic core. Accordingly, the potential acting on the outer electron can be well approximated with a Coulomb potential of $Z_{\text{eff}} = 1$. Similar to Eq. 3.5, the energy levels can be calculated with

$$E_n = \text{IP} - \frac{R_\mu}{(n^*)^2} = \frac{R_\mu}{(n-\delta(n))^2}, \tag{3.11}$$

introducing the *effective* principal quantum number n^* and the quantum defect $\delta(n)$ [112]. Obviously, this rather simple relation can be used to determine the IP in any atomic system by measuring excitation energies for a series of Rydberg states, provided $\delta(n)$ can be described conclusively. This approach, together with the underlying theory, is presented in Publication II, where the IP of dysprosium was determined by evaluation of Rydberg convergences. For more details the reader is referred to [113, 114], where the analysis of perturbed Rydberg series is discussed and alternative fitting functions are compared.

3.2 Electronic transitions

Optical spectroscopy is all about the interactions of light with the atomic shell. Considering the two states $|i\rangle$ and $|k\rangle$ with energies $E_i > E_k$ of an atom within an external light field, one can distinguish between three basic interaction processes:

- A photon is absorbed by the atom, changing its energy from E_k to $E_i = E_k + h\nu$, where ν is the frequency of the photon (**absorption**).
- A photon may induce the excited atom to emit an identical photon under relaxation to a lower state $E_k = E_i - h\nu$ (**stimulated emission**).
- The atom with excitation energy E_i may spontaneously relax to a lower energy state E_k under emission of a photon with the energy $h\nu = E_i - E_k$ (**spontaneous emission**).

The rates for absorption and stimulated emission

$$\begin{aligned} W_{ki} &= B_{ki} u(\nu) \text{ and} \\ W_{ik} &= B_{ik} u(\nu) \end{aligned} \tag{3.12}$$

depend on the spectral energy density of the external light field $u(\nu)$, where the proportionality constants B are called *Einstein coefficients* for absorption and stimulated emission. Their relation $B_{ik} = \frac{g_k}{g_i} B_{ki}$ only depends on the statistical weights of the states $|i\rangle$ and $|k\rangle$, meaning that the maximum population transfer from $|k\rangle$ to $|i\rangle$ is 50 % for $g_i = g_k$ [106]. In practice, the cross section σ is more commonly used to

express the proportionality between the intensity of the light field $I(\nu) = u(\nu)/c\nu$ and the transition rate as

$$W = \frac{\sigma I}{h\nu} \tag{3.13}$$

[107]. The Einstein coefficient A_{ik} describes the probability for spontaneous emission, related to B_{ik} via

$$A_{ik} = \frac{8\pi h\nu^3}{c^3} B_{ik}. \tag{3.14}$$

It can be calculated from the expectation value of the transition dipole moment $\langle \boldsymbol{p}_{ik} \rangle = M_{ik}$ according to

$$A_{ik} = \frac{16\pi^3 \nu_{ik}^3}{3\epsilon_0 c^3 h} |M_{ik}|^2 = \frac{16\pi^3 e^2 \nu_{ik}^3}{3\epsilon_0 c^3 h} \left| \int \psi_i^* \boldsymbol{r} \psi_k d\tau \right|^2, \tag{3.15}$$

where $\boldsymbol{r}$ is position of the electron and M_{ik} the so-called transition matrix element [106]. From the properties of $\langle \boldsymbol{p}_{ik} \rangle$ selection rules for atomic dipole transitions can be derived, which are comprised in Table 3.1. Note that in pure LS-coupling $\Delta S = \pm 1$ is forbidden. In heavy atoms, however, S is not a good quantum number due to the strong spin-orbit interaction and inter-combination lines with $\Delta S = \pm 1$ can be observed, although they are strongly suppressed [106]. Atomic dipole transitions are also referred to as E1-transitions, denoting a first order electric multipole transition. Similarly, E2, E3,... denote electric quadrupole, octupole and higher order transitions, while M1, M2,... refer to different magnetic multipole transitions. Higher order transitions exhibit different selection rules as those in Table 3.1. However, they are strongly suppressed and usually not considered in RIS.

General
$\pi = -\pi'$
$\Delta J = 0, \pm 1;\ J = 0 \nrightarrow J' = 0$
$\Delta m_J = 0, \pm 1;\ m_J = 0 \nrightarrow m'_J = 0$ if $\Delta J = 0$
LS-coupling
$\Delta S = 0$
$\Delta L = 0, \pm 1;\ L = 0 \nrightarrow L' = 0$
$\Delta l = \pm 1$ for the transition electron
Intermediate coupling
$\Delta S = \pm 1$
$\Delta L = 0, \pm 1, \pm 2$
jj-coupling
$\Delta j = 0, \pm 1$ for one electron
$\Delta j = 0$ for all other electrons

Table 3.1.: Selection rules for electronic dipole transitions [105, 106]. Primed symbols refer to the final state quantum numbers.

3.3 Spectral lineshapes

3.3.1 Natural linewidth

The minimum spectral width of an atomic transition is given by the natural linewidth. In consideration of Heisenberg's uncertainty principle, the finite lifetime τ of an atomic state leads to an energy uncertainty of $\Delta E = \hbar/\tau$. The natural linewidth $\Delta\nu$ of an atomic transition between two excited levels $|i\rangle$ and $|k\rangle$ is determined by the lifetimes of both states, resulting in

$$\Delta\nu = \frac{1}{h}\left(\Delta E_i + \Delta E_k\right) = \frac{1}{2\pi}\left(\frac{1}{\tau_i} + \frac{1}{\tau_k}\right). \tag{3.16}$$

The intensity distribution $I(\omega)$ of the spectral line follows a Lorentzian profile

$$I(\omega) = I_0 \frac{\gamma^2/2\pi}{(\omega - \omega_0)^2 + (\gamma/2)^2} \tag{3.17}$$

around the center frequency ω_0, with $\omega = 2\pi\nu$. The natural linewidth corresponds to the FWHM of the Lorentzian profile, i.e. $\Delta\nu = \gamma/2\pi$ [49, 106]. Excited level lifetimes and respectively natural linewidths of atomic transitions span many orders of magnitude. For example, the lifetime of the excited state of the 1001 nm ground-state transition in atomic dysprosium (Dy I), presented in Publication I, was later determined as $\tau \geq 82.2(6.7)$ ms [115], which corresponds to $\Delta\nu \lessapprox 2$ Hz. On the other hand, the excited state of the 405 nm ground-state transition in Dy I, presented in Publication II, has a lifetime of $\tau \approx 5$ ns, corresponding to a natural

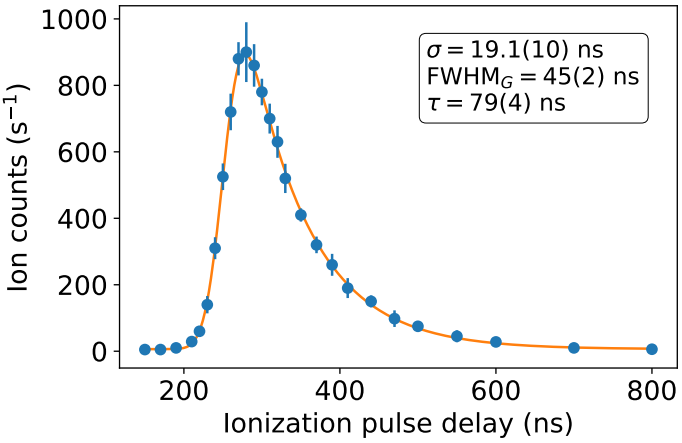

Figure 3.1.: Lifetime measurement of the excited state at 23 083.3 cm^{-1} in Cm I. The orange curve shows a fit according to Eq. 3.18.

linewidth of $\Delta\nu \approx 30$ MHz [116]. Note that both of these examples are electronic dipole transitions (E1) according to the selection rules in Table 3.1. Nonetheless, the former is a very uncommon case in RIS as one usually aims for high excitation probability.

3.3.2 Lifetime measurement

Although the natural linewidth can often not be resolved in RIS due to several line broadening effects, as will be discussed in the following sections, the lifetime τ of excited states can be measured. In the experiment this is performed by a temporal delay of the ionization laser(s) with respect to the excitation laser, so that the ion count rate is a function of the population decay. For short lifetimes, which are in the order of the laser pulse length, one has to consider a convolution of the approximately Gaussian temporal laser profile with an exponential decay law, which can be expressed as

$$n(t) = A \cdot \left[1 + \mathrm{erf}\left(\frac{t - t_0}{\sigma\sqrt{2}} - \frac{\sigma}{\tau\sqrt{2}}\right)\right] \exp\left(\frac{\sigma^2}{2\tau^2} - \frac{t - t_0}{\tau}\right) + n_0, \tag{3.18}$$

where t_0 and σ are the center and the standard deviation of the Gaussian distribution, τ the lifetime and erf the Gaussian error function. Additionally, the function features an amplitude A and an offset n_0 [117]. An example lifetime measurement of the excited state at 23 083.3 cm^{-1} in neutral Cm is shown in Fig. 3.1. Obviously, for very short lifetimes the exponential decay may be obscured by the laser pulse width, as seen in Publication V. Moreover, an upper limit of ≈ 3 µs for the measured lifetime is given by the experimental conditions in the hot ion source environment, related to the mean free path of excited atoms. This was observed in Publication I and is supported by a similar lifetime measurement of a meta-stable

state in neutral Ra [118].

3.3.3 Doppler broadening

For an observer in the lab frame, the Doppler effect shifts the frequency ν of light emitted or absorbed by atoms moving at a speed v towards the light source according to

$$\nu = \nu_0(1 + v/c), \tag{3.19}$$

where ν_0 denotes the resonance frequency for a particle at rest. If we consider an atomic vapor at a temperature T, the velocities follow a Boltzmann distribution

$$p(v)\mathrm{d}v \;\propto\; \exp\left(-\frac{mv^2}{2k_BT}\right)\mathrm{d}v = \exp\left(-\frac{v^2}{\hat{v}^2}\right)\mathrm{d}v, \tag{3.20}$$

where $p(v)\mathrm{d}v$ is the probability to find a particle in the velocity interval $[v, v + \mathrm{d}v]$ and $\hat{v} = \sqrt{2k_BT/m}$ gives the most probable velocity [107]. Inserting Eq. 3.19 into Eq. 3.20 yields a Gaussian line profile of the form

$$I(\nu) = I_0 \exp\left(-\frac{mc^2(\nu-\nu_0)^2}{2k_BT\nu_0^2}\right) = I_0 \exp\left(-\frac{c^2(\nu-\nu_0)^2}{\nu_0^2\hat{v}^2}\right) \tag{3.21}$$

with a FWHM Doppler linewidth of

$$\Delta\nu = \nu_0\sqrt{\frac{8k_BT\ln 2}{mc^2}} = \frac{2\nu_0\hat{v}}{c}\sqrt{\ln 2}. \tag{3.22}$$

Let us reconsider the back-of-the-envelope example calculation from Sec. 2.1, i.e. an ensemble of particles with $m = 100\,\mathrm{u}$ and a Boltzmann velocity distribution at $T = 2000\,^\circ\mathrm{C}$. At an arbitrary resonance frequency of $\nu_0 = c/400\,\mathrm{nm}$, the Doppler width of the resonance line is $\Delta\nu \approx 2.5\,\mathrm{GHz}$. The mass and temperature dependence of $\Delta\nu$ is visualized in Fig. 3.2. In crossed-beam geometry, as is the case with the PI-LIST ion source, we consider the conical atom beam effusing from the atomizer at an opening angle β, which is perpendicularly intersected by the probe laser beam and collinearly overlapped with an ionizing laser beam. The situation is schematically depicted in Fig. 3.3. The original velocity distribution is now constrained by the opening angle β of the atomic beam. It was assessed as close to 45° in [119] for the RISIKO ion source. However, due to the finite cross section of the ionizing laser, which limits the effective laser-atom interaction region radially, it is further constrained to β_{eff}. As a consequence, the velocity classes which are addressed by the laser are limited to

$$v_\perp = v/\sin(\beta_{\mathrm{eff}}). \tag{3.23}$$

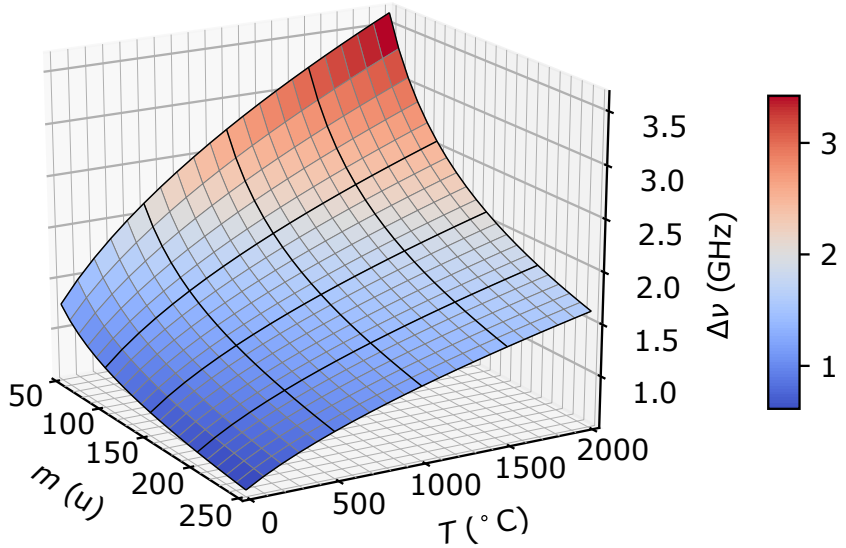

Figure 3.2.: Mass and temperature dependence of spectral Doppler broadening according to Eq. 3.22, plotted for $\nu_0 = c/400\,\mathrm{nm}$. Obviously $\Delta\nu$ scales linearly with ν_0.

With this, Gaussian linewidths of $\Delta\nu < 100\,\mathrm{MHz}$ could be demonstrated in Tc ($m = 99\,\mathrm{u}$) at a transition frequency of $\nu_0 \approx c/425\,\mathrm{nm}$ [74]. Since this is already in the order of the natural linewidth for strong transitions, one has to consider a convolution

$$I_V(\nu) = (I_G * I_L)(\nu) = \int_{-\infty}^{\infty} I_G(\nu') I_L(\nu - \nu') \mathrm{d}\nu' \tag{3.24}$$

of a Lorentzian profile $I_L(\nu)$ with a Gaussian profile $I_G(\nu)$. This is referred to as a *Voigt profile*. It expresses the fact that the spectral line shape of each velocity class within the Boltzmann distribution follows a Lorentzian profile. For fitting purposes Eq. 3.24 is not practical, since there is no analytical solution to the integral. A popular approximation for rapid calculation is given by

$$\begin{aligned} I_V(\nu) =& \frac{2\sqrt{\ln 2}}{\sqrt{\pi}\Delta\nu_G} \mathrm{Re}\left[w(z)\right] \\ \text{with} \quad z =& \sqrt{\ln 2}\left(\frac{2(\nu-\nu_0)}{\Delta\nu_G} + i\frac{\Delta\nu_L}{\Delta\nu_G}\right), \end{aligned} \tag{3.25}$$

where $\Delta\nu_G$ and $\Delta\nu_L$ are the Gaussian and Lorentzian full widths, respectively, and $w(z) = e^{-z^2}\mathrm{erfc}(-iz)$ the Faddeeva function [120]. The FWHM of the Voigt profile $I_V(\nu)$ can be calculated as

$$\Delta\nu_V = 0.535\Delta\nu_L + \sqrt{0.2166\Delta\nu_L^2 + \Delta\nu_G^2} \tag{3.26}$$

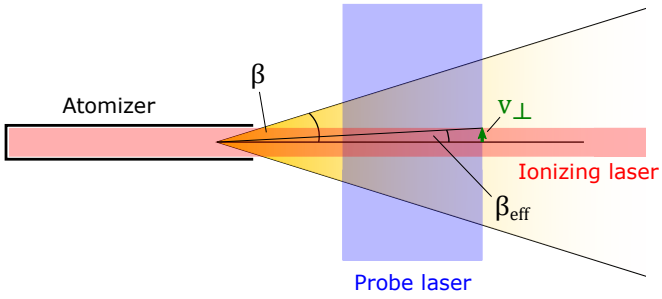

Figure 3.3.: Laser-atom interaction in crossed-beam geometry. $v_\perp$ denotes the perpendicular velocity component of effusing atoms, i.e. on the axis of the probe laser.

[49]. An approximation of the form 3.25 is also used in the SATLAS python package [121], which was used for fitting of hyperfine structures in Publication IV and Publication V.

3.3.4 Saturation and power broadening

As discussed in Sec. 3.2, the maximum population transfer from a state $|k\rangle$ to $|i\rangle$ in a two-level system is 50 % for equal statistical weights of both states. A transition is saturated when the excitation probability corresponds to the relaxation probability. In this context, a saturation parameter $S = W_{ki}/R_i$, given by the ratio of excitation rate W_{ki} to relaxation rate R_i, can be defined [106]. It can be understood as an intensity ratio of an external light field to a saturation intensity I_{sat}, with

$$S = \frac{W_{ki}}{R_i} = \frac{I}{I_{\text{sat}}} \tag{3.27}$$

[72, 74]. Obviously, $S(I = I_{\text{sat}}) = 1$ expresses that excitation and relaxation are in equilibrium. The frequency-dependent absorption cross section α, describing the spectral line profile, is modified through the saturation parameter to

$$\alpha(\nu) = \frac{S\alpha_0(\nu)}{1 + S\alpha_0(\nu)}, \tag{3.28}$$

where α_0 is the unmodified cross section, i.e. without consideration of saturation effects [72]. An experimental access to the saturation intensity is possible by monitoring the absorption cross section on resonance (i.e. the ion rate in RIS) as a function of laser intensity. Similar to Eq. 3.28, it can be expressed as

$$\alpha(I) = a\frac{I/I_{\text{sat}}}{1 + I/I_{\text{sat}}} + bI + c, \tag{3.29}$$

where the linear contribution accounts for non-resonant ionization processes and the constant term considers any background signal [74]. The saturation intensity is an important parameter in RIS experiments. In ion source applications, where the highest possible ionization rate is desired, all transitions in the excitation scheme should be driven with sufficient laser power to ensure saturation. Correspondingly, strong dipole transitions and high power laser radiation are used. As an example, the reader is referred to Fig. 2 in Publication II or Fig. 4 in Publication III, where the saturation behavior of RIS schemes is studied in detail. Saturation effects involve a spectral line broadening, which can be observed in the same figures as mentioned above (particularly distinct in the latter). A typical feature of transitions driven by a laser with $I \gg I_{\mathrm{sat}}$ is the flat-top line profile. Upon reaching the excitation-relaxation rate equilibrium at the resonance frequency, i.e. for $I(\nu_0) = I_{\mathrm{sat}}$, the absorption cross section for slightly detuned frequencies still rises with increasing intensity, effectively lifting the edges of the profile while the center is unaffected. In case of a Lorentzian profile, the modified linewidth corresponds to $\Delta\nu = \nu_0\sqrt{1+S}$ [49].
On the other hand, in high-resolution spectroscopy experiments the effect of saturation broadening has to be avoided in order to achieve highest possible spectral resolution. The laser intensity is correspondingly kept slightly below I_{sat} as a reasonable trade-off between linewidth and efficiency. Nonetheless, when the linewidth of a probed transition is small, broadening effects from other transitions in the excitation scheme may become significant. This can be understood by an effective shortening of the excited state lifetime through a transfer of the population to the ionization continuum. In order to minimize this effect, the ionization step may be de-coupled from the probed transition by a temporal delay. This effect was studied qualitatively in Publication V. An in-depth treatise of power broadening in pulsed laser RIS on the high-precision level can be found in [122].

3.4 Ionization scheme development

As described in the introduction, the method of resonance ionization is based on step-wise excitation and finally photo-ionization of sample atoms. Due to their unique atomic structure, resonance ionization (RI) schemes are specific for each chemical element. On the one hand this renders the RI process highly selective, but on the other hand demands for extensive spectroscopic studies in order to make an element accessible to RI. A database comprising available ionization schemes for different elements can be found on the web presence of the RILIS group [37]. Depending on their application, ionization schemes have different figures of merit. Most commonly, for the application in laser ion sources, one aims to achieve maximum efficiency in the ionization process. This is closely linked to saturation of all

involved transitions. Combining Eqs. 3.13 and 3.27 yields

$$I_{\text{sat}} = \frac{R_i h\nu}{\sigma_{ki}}, \tag{3.30}$$

meaning that the required laser intensity for saturation of a transition $|k\rangle \rightarrow |i\rangle$ is proportional to the relaxation rate R_i and to the inverse of the absorption cross section σ_{ki}. The latter can also be related to the Einstein A_{ik} coefficient via Eqs. 3.12, 3.13 and 3.14, resulting in

$$\sigma_{ki} = \frac{g_i}{g_k} \frac{c^2}{8\pi\nu^3} A_{ik}. \tag{3.31}$$

From the relations introduced so far one can already establish rate equations to calculate ionization rates in a multi-step scheme, as presented e.g. in [111, 123]. However, this requires knowledge about natural linewidths, decay channels of excited states and the ion source temperature to estimate Doppler broadening. A simpler approach is the qualitative assessment of ionization rates by the dependencies 3.30 and 3.31, followed by experimental determination of the ionization efficiency. Firstly, transitions in an ionization scheme should be chosen with respect to σ_{ki}. An example scheme, similar to the one depicted in [111], is shown in Fig. 3.4. It shows a three step excitation with the wavelengths $\lambda_1, \lambda_2, \lambda_3$ and typical excitation cross sections for the individual steps. Obviously, the bottleneck of a RI scheme is usually the final transition, with an excitation cross section of up to 7 orders of magnitude lower than strong transitions between bound atomic levels. In some cases a non-resonant final excitation step is driven by a high-power fixed frequency laser, e.g. one of the harmonics of an Nd:YAG laser (1064 nm, 532 nm, 355 nm, 266 nm). However, high-power laser radiation may introduce undesired background through non-linear multi-photon processes. This effect can only somewhat be reduced by choosing the lowest possible harmonics for reaching the ionization potential, but in most cases not completely eliminated. Consequently, non-resonant ionization is avoided whenever possible. The preferable ionization mechanisms, i.e. transitions to auto-ionizing states (AIS) or high-lying Rydberg states, require far less laser power for saturation. High-lying Rydberg states, as discussed in Sec. 3.1.3, exhibit a very low binding energy and can be efficiently ionized by collisions, external electric fields, an additional photon from any laser in the excitation scheme or simply by blackbody radiation from the hot atomizer, even in the far infrared (FIR) regime [111]. As indicated by the statistical weight term in Eq. 3.31, excitation to Rydberg states can often be advantageous, since the fine structure interval scales with n^{-3} and high-lying Rydberg-states may be degenerate [110]. Lastly, there is the possibility of a resonant ionization process via auto-ionizing states (AIS). An AIS is a collective excitation with the total energy lying above the ionization potential. Rather than undergoing radiative decay to a

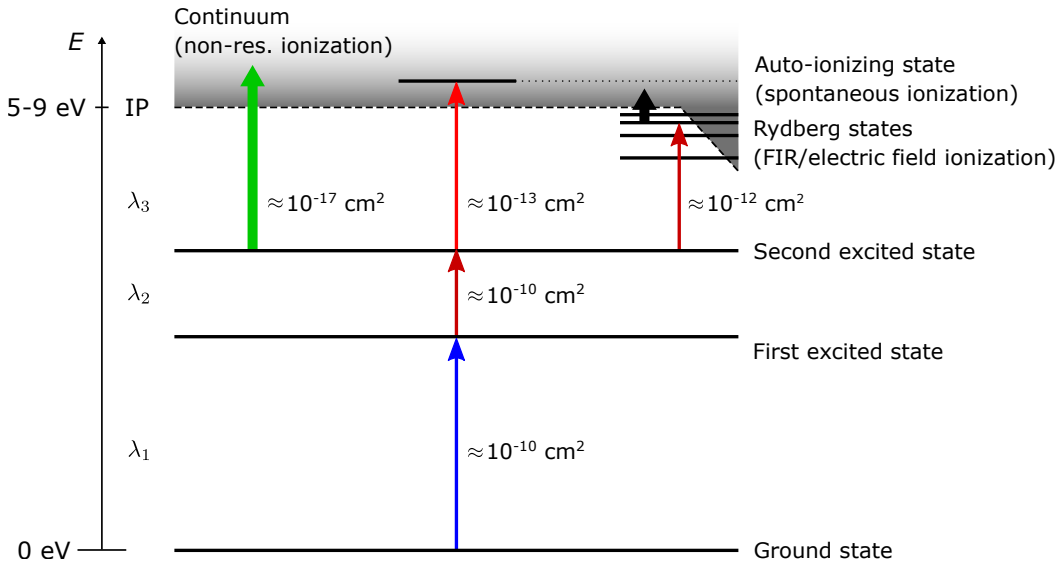

Figure 3.4.: Schematic description of Resonance Ionization Spectroscopy. The arrows indicate the step-wise optical excitation from the atomic ground state to ionization. The ionization efficiency crucially depends on the final excitation step, which may address the continuum, Rydberg-states or auto-ionizing states. The lowered IP on the right indicates an electric field, which effectively reduces the ionization threshold. Approximate excitation cross sections are given. Figure adapted from [111]. For details see text.

bound atomic state, AIS preferably decay into an ion-electron pair with lifetimes in the order of well below nano- down to picoseconds, which can be verified by the huge natural linewidths of tens or even hundreds of GHz. The absorption cross section of auto-ionizing transitions follows a Fano-profile of the form

$$\alpha(E) = \alpha_0 \frac{(\epsilon + q)^2}{1 + \epsilon^2} + \alpha_b \quad \text{with} \quad \epsilon = \frac{E - E_R}{\Gamma/2}, \tag{3.32}$$

where E_R is the resonance energy, $\Gamma = 1/\tau$ the resonance FWHM, and q the Fano-parameter, describing the asymmetry of the line profile [107, 124]. Since the ionization of AIS is independent of experimental circumstances, i.e. the presence of an electric field or the temperature of the atomizer, they are the most universal choice for an efficient ionization scheme.

From a practical point of view, atomic transitions have to be accessible with the laser system at hand. For the Mainz Ti:sapphire laser system, as described in Sec. 2.1, the fundamental wavelength range is $700\,\text{nm} < \lambda < 1020\,\text{nm}$ (see Table 2.1), with a decreased output power towards the edges of the gain profile. This range can be extended by second, third and fourth harmonic generation. Due to the relatively high level spacing and high absorption cross section for ground-state transitions or transitions between low-lying states, they are often driven by a second or third harmonic laser output. Ionizing transitions, on the other hand, are preferably

driven by the fundamental output in order to obtain maximum laser power. The pulse length of the lasers of ≈ 50 ns is in the order of the lifetime of excited states, so that the loss channel of spontaneous relaxation to inaccessible states, described via R_i, is minimized. However, it can not always be avoided completely and strong radiative decay channels to meta-stable states, as observed e.g. in Ra [118], can lower the overall ionization efficiency. A similar effect is much stronger present in a buffer-gas environment. Depending on the pressure, collisional quenching to meta-stable states can be observed, e.g. in No [125] or Pu [126]. In such cases one tends to prefer two-step ionization schemes over three-step ionization schemes in order to keep the number of intermediate levels at minimum. Recently two-step schemes are becoming more popular even in hot-cavity ion sources for the sake of simplification and reliability. However, a potentially lower selectivity due to the additional high-power, high-energy laser radiation required for the ionization step has to be considered. Naturally, radiative de-excitation can also be induced by a resonant laser through stimulated emission. Such a case is presented in Publication I, where resonant de-excitation was utilized to observe a meta-stable state in dysprosium.
Lastly, one should keep in mind that the highest possible Einstein A_{ik} factors, representing shortest excited state lifetimes, might not be ideal for high-resolution spectroscopy applications. As discussed in Sec. 3.3.4, the probed transition has to be de-coupled from all other excitation steps to achieve highest spectral resolution [122]. This can only be achieved if the excited state lifetime is longer than the laser pulse length.

3.5 Determination of the ionization potential

One of the fundamental properties of each chemical element is the first ionization potential (IP), specifying the binding energy of the outermost electron in the neutral atom. It is closely related the chemical properties of an element, e.g. the electronegativity, which is defined as $\chi_M = (\mathrm{IP} - \mathrm{EA})/2$ on the Mulliken scale, where EA is the electron affinity [127]. Today the IP is precisely known for all stable elements, with experimental precision in the order of μeV, apart from very few exceptions (cf. Fig. 1 in Publication III). For radioactive elements the situation is different, due to the challenges in experiments on radioactive species, i.e. small sample amounts and high safety precautions. Methods for the determination of the IP are, for example, measurement of ionization rates from a well defined and controlled surface ion source, which can be used to deduce the IP via the Saha-Langmuir equation 2.13, or alternatively spectroscopic methods, i.e. evaluation of Rydberg convergences using Eq. 3.11. The latter usually offers the highest precision and can be perfectly realized in RIS due to the straightforward ionization of Rydberg states. Moreover, RIS is highly sensitive and thus still applicable with low sample amounts, making spectroscopy studies on rare radioactive species feasible.

Such studies for the determination of the IP were successfully performed within the LARISSA group, including measurements on exclusively radioactive elements, e.g. Tc or Ac [87, 88] among others. In this context one should also mention on-line RIS experiments on very-short lived species, e.g. At or No, where off-line studies are not feasible [100, 125]. Additionally, the RIS method can be used in more sophisticated approaches for IP measurement, which become important in complex spectra where a straightforward identification of Rydberg convergences is not possible anymore. An extensive treatise on methods for the determination of the IP, demonstrated on stable elements of the lanthanide series, is given in the dissertation of T. Gottwald [128]. This includes the methods of isolated core excitation and delayed field ionization for the identification of Rydberg states, which are not subject of this work.

3.5.1 Rydberg convergences

The analysis of Rydberg convergences relies on the measurement of level energies close to the IP. Within an easily realizable laser scanning range of $\approx 1000\,\mathrm{cm}^{-1}$ below the IP, corresponding to $\approx 70\,\mathrm{nm}$ in the fundamental Ti:sapphire laser output, a high number of Rydberg states can be localized. In Publication II, principal quantum numbers of $20 < n < 60$ could be covered within this range. Higher n-states can most often not be resolved in broadband RIS and would require high resolution techniques involving narrow bandwidth cw lasers, as demonstrated in Gd and Sm [129]. The usually large amount of data points obtained from Rydberg convergences leads to a precise result for the IP when fitting the energy positions E_n with Eq. 3.11. However, Rydberg series in rare-earth or actinide spectra are often subject to strong perturbations due to the high number of open shells and interacting valence electrons. In this case a shift in the Rydberg level energies under the influence of an interloper state formed by a collective excitation can be described in the framework of multichannel quantum defect theory [124, 130]. The application to perturbed Rydberg series is presented in Publication II, or similarly in [88], and will not be explained here in detail. For the sake of completeness just the final fitting function for a perturbed Rydberg series with interloper states at energies $E_{R,i}$ and of width $\Gamma_{R,i}$ is given here as

$$E_n = \mathrm{IP} - R_\mu \left[n - \left(\delta_0 + \frac{\delta_1}{(n-\delta_0)^2} - \frac{1}{\pi} \sum_i \arctan\left(\frac{\Gamma_{R,i}/2}{\mathrm{IP} - \frac{R_\mu}{(n-\delta_0)^2} - E_{R,i}} \right) \right) \right]^{-2}, \tag{3.33}$$

where δ_0 and δ_1 are the zero- and first order terms in the Ritz expansion of the quantum defect [114].

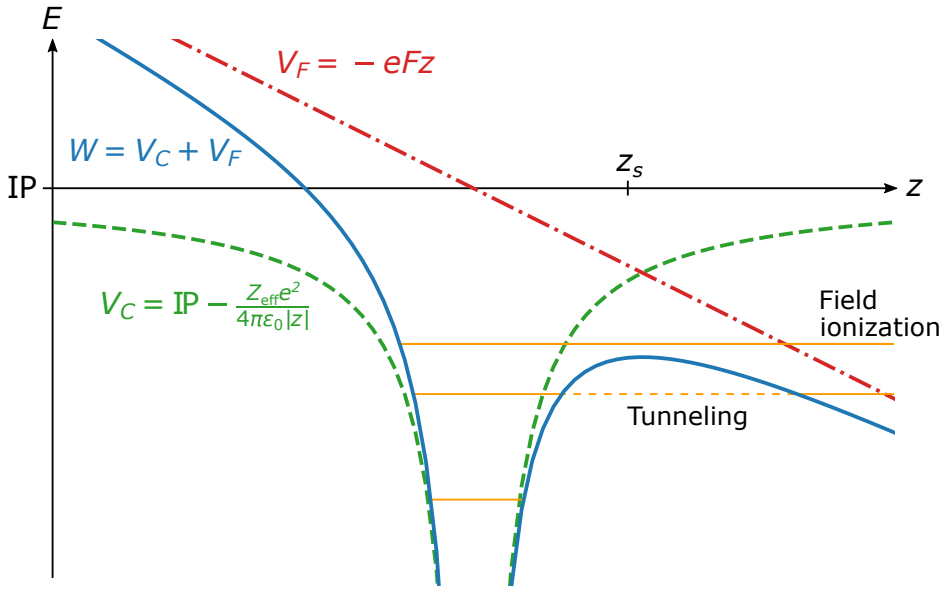

Figure 3.5.: Graphical representation of electric field ionization. The external electric field F along the z-axis distorts the Coulomb potential. Excited atomic states (orange lines) with an energy E_n greater than the saddle-point of the potential $W(z_S)$ are field-ionized. Meta-stable states may also tunnel through the potential barrier.

3.5.2 Saddle-point ionization

An alternative approach for the determination of the IP is found by applying DC electric field ionization. This method does not rely on an assignment of specific states and benefits from high level density in the region close to the IP. Thus, it is perfectly suited for the extraction of the IP from complex atomic spectra, where the analysis of Rydberg convergences fails. The principle of electric field ionization, or classically speaking saddle point ionization, is depicted in Fig. 3.5. Considering an atom within a homogeneous electric field F along the z-axis, the Coulomb potential is superimposed by an electric potential $V_F = -eFz$, resulting in an effective potential of the form

$$W(\mathrm{r}, F) = \mathrm{IP} - \frac{Z_{\mathrm{eff}}e^2}{4\pi\epsilon_0|\boldsymbol{r}|} - eFz \tag{3.34}$$

[107]. By solving $\partial/\partial z\, W(z_S) = 0$, the potential at the location of the saddle point z_S can be written as

$$W(z_S, F) \equiv W_S(F) = \mathrm{IP} - 2\sqrt{\frac{Z_{\mathrm{eff}}e^3F}{4\pi\epsilon_0}}, \tag{3.35}$$

where the effective charge of the nucleus is $Z_{\mathrm{eff}} \approx 1$ for highly excited states, resulting in $W_S = \mathrm{IP} - \mathrm{const} \cdot \sqrt{F}$. This simple relation can be used to determine

the IP by measurement of several field ionization thresholds and extrapolation to zero field strength. Note that Eq. 3.35 is purely classical and does not account for tunneling, which leads to ionization already at field strengths lower than the classical saddle point, as indicated in Fig. 3.5 by a dashed lined. However, since the experiment relies on the measurement of a sharp increase in the ionization rate upon reaching the saddle point, rather than a gradual increase as expected from tunneling [131], the latter can be disregarded from our experimental point of view. Another effect to keep in mind is the increased ionization threshold for states with a magnetic quantum number $m \neq 0$. This additional centrifugal barrier

$$W_m \propto |m| F^{3/4} + \frac{3}{16} m^2 F \tag{3.36}$$

leads to additional ionization thresholds with $W = W_S + W_m$ [131–133]. If the experiment relies only on the first increase in the ionization rate, Eq. 3.35 is sufficient for data evaluation. However, this only holds valid when m-states are not selectively populated, i.e. through specific laser polarization with the corresponding selection rules for Zeeman sublevels.

3.6 Publication I: Laser spectroscopy of the 1001-nm ground-state transition in dysprosium

The following work was published as a regular article in Physical Review A **98**, 042504 (2018) DOI 10.1103/PhysRevA.98.042504. The experiment addressed a request from the group of Prof. Dr. Patrick Windpassinger to determine the ground state transition wavelength to the low-lying excited state at 9991 cm^{-1}. From theoretical calculations in [134], this state is predicted to have an exceptionally long lifetime of 3 ms, which makes it highly interesting for precision studies and quantum-optical engineering. According to the selection rules presented in Sec. 3.2, this ground-state transition falls in the category of an intercombination line with $\Delta S = +1$. Correspondingly, it features an ultra-narrow linewidth in the range of $\Delta\nu_{\text{theo}} \approx 50$ Hz, making it a perfect candidate for high precision spectroscopy within the magneto-optical trap (MOT) setup of the Windpassinger group. However, since the transition could not be observed by another group with a similar setup [135], and because the laser scanning capability of the laser system coupled to the MOT is limited to few GHz, a pre-search of the atomic level at 9991 cm^{-1} was undertaken in the LARISSA group using RIS method. This task was particularly challenging due to the extremely low absorption cross section in the transition under investigation, together with the required wavelength of 1001 nm, close to the edge of the Ti:sapphire gain profile. Therefore, in the first phase of the experiment the transition was searched and observed by resonant de-excitation of a higher excited level, which was to our knowledge applied for the first time in the context of RIS. Subsequently direct excitation spectroscopy was successfully performed, including measurements in the 741 nm ground-state transition, which is a promising candidate for high-resolution RIS.
Based on the results from this publication, the Windpassinger group succeeded in spectroscopy of the 1001 nm-transition on cold atoms within a MOT [115]. The excited state lifetime was measured as $\tau \geq 82.2(6.7)$ ms, even surpassing the predictions from theory.
Note that this article was published together with a supplemental data table, which is given in the appendix A.2.

Author contribution

The author contributed to this work by preparing the experimental setup for the measurements, i.e. complete set-up of the laser system and optimization of the experimental apparatus towards dysprosium spectroscopy. Data taking, evaluation and preparation of the manuscript was done jointly with the master student Lena Maske from the group of Prof. Dr. Patrick Windpassinger, who also presented this work as part of her master thesis [136].

Laser spectroscopy of the 1001-nm ground-state transition in dysprosium

D. Studer, L. Maske, P. Windpassinger, and K. Wendt
Institut für Physik, Johannes Gutenberg-Universität Mainz, 55128 Mainz, Germany

(Received 20 July 2018; published 10 October 2018)

We present a direct excitation of the presumably ultranarrow 1001-nm ground-state transition in atomic dysprosium. By using resonance ionization spectroscopy with pulsed Ti:sapphire lasers at a hot cavity laser ion source, we were able to measure the isotopic shifts in the 1001-nm line between all seven stable isotopes. Furthermore, we determined the upper level energy from the atomic transition frequency of the ^{164}Dy isotope as 9991.004(1) cm^{-1} and confirm the level energy listed in the NIST database. Since a sufficiently narrow natural linewidth is an essential prerequisite for high-precision spectroscopic investigations for fundamental questions, we furthermore determined a lower limit of 2.9(1) μs for the lifetime of the excited state.

DOI: 10.1103/PhysRevA.98.042504

I. INTRODUCTION

Narrow-linewidth atomic transitions can serve as highly sensitive probes for various inner and outer atomic interaction potentials and respective forces, and have become a general-purpose tool in the field of quantum many-body physics [1,2]. In addition, narrow linewidth is usually accompanied with long lifetimes of the excited states, such that these transitions offer precise, coherent control over metastable state populations and therefore allow for, e.g., the study of quantum gas mixtures and Kondo-type physics [3,4] or the implementation of qubits [5,6]. Beyond that, precision isotope shift measurements [7] have been suggested as a vehicle to reveal high-energy physics contributions to atomic spectra and search for physics beyond the standard model [8–10]. Various atomic species possess ultranarrow transitions; however, dysprosium is a particularly interesting case. Because of its high magnetic moment and consequent anisotropic long-range interaction, dysprosium is highly attractive for quantum many-body physics. On the other hand, many high-energy effects scale with atomic mass. Thus, dysprosium, with about 160 nucleons and seven stable isotopes, is an ideal study case. Finding and characterizing a particularly narrow optical transitions in this system therefore is of high relevance.

Some promising narrow-linewidth transitions are discussed in Ref. [11], including calculated level energies and lifetimes which are compared to experimental values, if available. One is the 1001-nm $4f^{10}6s^2(^5I_8) \rightarrow 4f^9(^6H^o)5d6s^2(^7I_9^o)$ ground-state transition with a theoretically predicted linewidth of 53 Hz [11]. It was first observed indirectly in the spectrum of an induction lamp filled with ^{162}Dy [12]. The NIST database [13] reports an energy of 9990.97(1) cm^{-1} for the upper level, which corresponds to a transition wavelength of 1000.904(1) nm. In contrast, calculations using the configuration interaction (CI) method yield a value of 9944 cm^{-1} (corresponding to 1005.6 nm) [11]. This and the fact that the transition at 1001 nm could not be detected via fluorescence laser spectroscopy in an atomic beam [14] motivate the verification of either result.

In order to detect this weak transition, we use the highly efficient technique of laser resonance ionization spectroscopy (RIS) [15]. The aims of this work are to (i) determine the exact transition frequency and extract first values for the isotope shifts of all stable isotopes and (ii) give a lower limit for the lifetime of the excited state, since a sufficiently narrow natural linewidth is a prerequisite for precision spectroscopy.

II. EXPERIMENTAL

A. Setup

Laser resonance ionization is based on multistep photoionization via characteristic transitions of the element under investigation. Because of the typically high efficiency and selectivity, this technique is often applied at radioactive ion beam facilities, such as ISOLDE at CERN, both for ion beam production [16,17] and spectroscopy of short-lived radioisotopes [18–20].

Similarly, our setup is optimized with respect to high sensitivity and relies on the hot-cavity laser ion source technique, combined with a low-energy quadrupole mass spectrometer. Figure 1 shows a sketch of the apparatus. A detailed description is given in Ref. [21]. In our experiment, we use a sample of $\approx 10^{15}$ Dy atoms, prepared from a standard nitric acid solution,[1] which is enclosed in a 3×3 mm^2 Zr carrier foil and introduced into a tantalum oven 35 mm long with an inner diameter of 2 mm. Dysprosium atoms are ionized by three properly synchronized laser pulses at a repetition rate of 10 kHz. The laser beams are overlapped anticollinearly with the ion beam axis, so that ionization takes place directly inside the atomizer oven. Alternatively, one may guide the laser beams through a side window of the vacuum chamber, perpendicularly intersecting the effusing atomic beam in front of the oven. This significantly reduces spectral Doppler broadening at the cost of approximately two orders of magnitude in ionization efficiency.

[1] Alfa Aesar Dysprosium AAS.

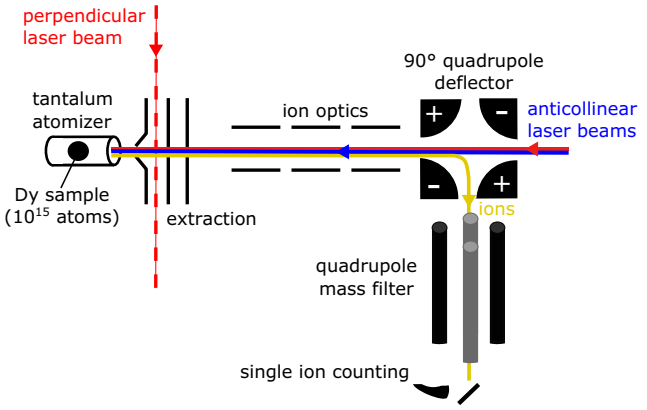

FIG. 1. Sketch of the atomic beam mass spectrometer with ion flight path (yellow) and laser beams in anticollinear (solid red, solid blue) and perpendicular, crossed beam (dashed red) geometry. In the latter case, the first extraction electrode is put on a positive voltage to act as an ion repeller.

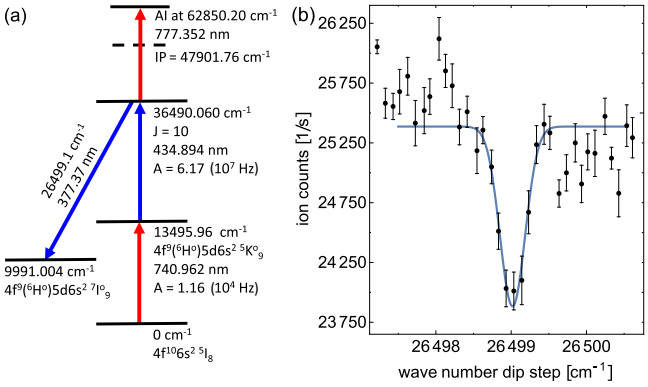

FIG. 2. Indirect measurement of the upper energy level belonging to the 1001-nm transition. (a) Measurement scheme consisting of a three-step resonant excitation, addressing an autoionizing state (AI) above the first ionization potential IP = 47901.76 cm^{-1} of dysprosium [28], together with the additional dip step. (b) Ion counts as a function of the dip-step wave number.

The laser system consists of up to four pulsed Ti:sapphire lasers, each of them pumped with 12 to 18 W of average power of a commercial 532-nm pulsed Nd:YAG laser.[2] The Ti:sapphire lasers have pulse lengths of typically 50 ns with up to 4 W average output power. They can be tuned from about 680 to 940 nm and have a spectral linewidth of 1–10 GHz depending on the specific resonator components used. The tuning range can be extended with second, third, and fourth harmonic generation. Details of the laser system are given in Refs. [22–24]. For wide-range scans, we use a modified laser design, featuring a diffraction grating in Littrow configuration for frequency selection [25]. This laser type has an output power of up to 2 W and can be tuned mode-hop-free from 700 to 1020 nm. Under optimal conditions the linewidth is 1.5 GHz; however, at wavelengths far from the Ti:sapphire gain maximum the pump power and the Ti:sapphire crystal position in the resonator have to be adjusted specifically so that the linewidth increases to 5 GHz. The fundamental output of each laser is measured with a wavelength meter.[3]

B. Spectroscopic technique

Spectroscopy is performed by detuning one laser in the excitation scheme while monitoring the ion count rate. Since this requires a photoionization scheme to begin with, the initial measurements were carried out with a scheme based on the $4f^{10}6s^2(^5I_8) \rightarrow 4f^9(^6H^o)5d\,6s^2(^5K^o_9)$ ground-state transition at 741 nm. The excited state has a configuration similar to the one at 1001 nm, but the line intensity is a factor of ≈50 higher [11,26]. This enormously facilitates the development of a full resonant three-step ionization scheme. Starting from the excited state of the 741-nm transition, a wide range spectrum of high-lying states was accessed by scanning the second harmonics of a grating-assisted Ti:sapphire laser between 401 and 437 nm. A third laser at 780 nm (the gain maximum of Ti:sapphire) is used for nonresonant ionization of excited atoms. The spectrum shows over 100 lines, with some of the upper states known in literature [13]. A complete list of recorded lines is given in the Supplementary Material [27]. In most cases, a resonant third excitation step to an autoionizing state can be easily found in the dense spectrum of dysprosium by detuning the ionization laser output by few nanometers.

To connect our photoionization scheme to the 1001-nm transition, we use a fourth laser to de-excite atoms from the second excited state into the $4f^9(^6H^o)5d\,6s^2(^7I^o_9)$ state. When the laser is resonant to the transition, the de-excitation competes with the ionization and a dip in the ion signal can be observed, as shown in Fig. 2.

The rather weak dip signal of less than 10% of the total ion counts may be related to the fact that the specifically induced de-excitation competes with a number of loss channels through spontaneous decay into other lower lying levels. With the dip technique, we cannot only indirectly measure the level energy of the excited state but also prepare for a full-resonant three-step ionization scheme for the direct excitation of the 1001-nm ground-state transition. To further reduce the uncertainty of the $4f^9(^6H^o)5d\,6s^2(^7I^o_9)$ level energy, which depends on three wavelengths in the dip measurements, we proceed by using the settled ionization scheme involving the direct excitation of the 1001-nm transition.

III. DIRECT EXCITATION SPECTROSCOPY

A. The 1001-nm transition

In this section, we discuss a direct excitation of the 1001-nm ground-state transition. For the measurements, all laser beams are oriented anticollinearly to the atom beam (see Fig. 1). A perpendicular geometry does not lead to an improvement at this point, since the expected Doppler broadening of ≈600 MHz within the tantalum oven is in the order of the laser linewidth. The beam diameter at atom position is about 2 mm which corresponds to the inner diameter of the oven. For the photoionization a Ti:sapphire laser with

[2]Photonics Industries DM100-532.

[3]High Finesse WS6-600 for wide-range scans and High Finesse WSU-30 for isotope shift measurements.

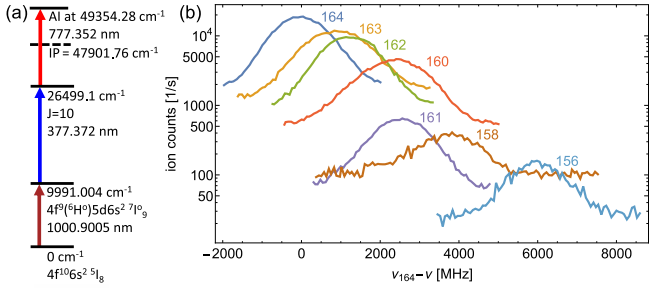

FIG. 3. Isotope shift measurement for the 1001-nm ground-state transition. (a) Excitation scheme. (b) Ion counts as a function of first excitation step frequency ν relative to the atomic transition frequency $\nu_{164} = 299.5228(1)$ THz of the ^{164}Dy isotope.

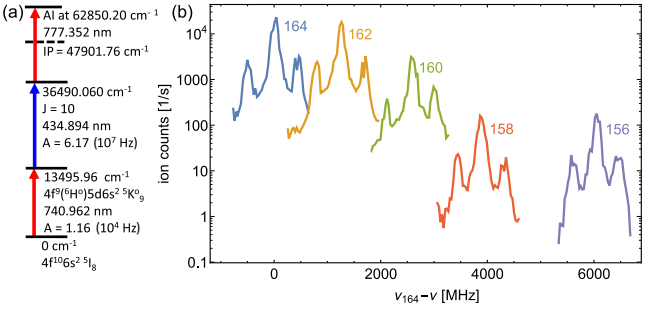

FIG. 4. Isotope shift measurement for the 741-nm ground-state transition. (a) Excitation scheme. (b) Ion counts as a function of first excitation step frequency ν relative to the atomic transition frequency $\nu_{164} = 404.5990(1)$ THz of the ^{164}Dy isotope. Laser side modes are clearly visible.

a wavelength of 1001 nm first excites the atoms into the $4f^9(^6H^o)5d\,6s^2(^7I^o_9)$ state. From this state, the atoms are resonantly excited to the second excited state with an energy of 26499.1 cm^{-1} with a wavelength of 377 nm by using a second, this time frequency-doubled, Ti:sapphire laser. In the last step, a third laser with a wavelength of 777 nm addresses an autoionizing state to resonantly ionize the atoms. The complete excitation scheme is shown in Fig. 3(a).

While the frequencies of the upper two steps are fixed for the whole measurement, the frequency of the first step is scanned. Because of its wide tuning range, the grating assisted laser, as described in Sec. II A, was used to probe the 1001-nm transition, while an additional etalon ($d = 2$ mm, $R = 0.4$) was inserted to reduce the linewidth to 1 GHz. Figure 3(b) shows the resulting direct excitation of all seven stable dysprosium isotopes. For the individual isotopes, we adapted the mass spectrometer setting accordingly.

From the measurement, we calculated the isotopic shifts in the 1001-nm transition, which are listed in Table I.

The specified error corresponds to the sum of the fit error and an estimated error of 30 MHz for the drift of the wavelength meter during the measuring time. Any other systematics are comparatively small and were neglected. The error estimation is based on later measurements in which we determined the drift as ≈10 MHz per hour as well as the long measuring time due to the individual mass spectrometer setting for each isotope. Furthermore, we determined the upper level energy from the atomic transition frequency of the ^{164}Dy isotope as 9991.004(1) cm^{-1}. Taking the isotope shift into account, the latter is in good agreement with the value listed in the NIST database [13].

TABLE I. Isotope shift in the 1001-nm transition in Dy, relative to the isotope 164.

	Isotope shift $\delta\nu$ [MHz]
$\delta\nu_{164–163}$	907(36)
$\delta\nu_{164–162}$	1233(35)
$\delta\nu_{164–161}$	2337(37)
$\delta\nu_{164–160}$	2566(36)
$\delta\nu_{164–158}$	3685(45)
$\delta\nu_{164–156}$	5976(39)

B. The 741-nm transition

In the course of the indirect detection of the upper energy level belonging to the 1001-nm transition, we were also able to measure the isotope shift in the first excitation step along the 741-nm ground-state transition. These data were measured with a different implementation of the standard Ti:sapphire laser featuring a bow-tie resonator design. Similar to the standard laser, frequency selection is achieved by a combination of a birefringent filter and a solid etalon ($d = 0.3$ mm, $R = 0.4$), but with the option to add an additional piezo-actuated air-spaced etalon ($d = 12$ mm, $R = 0.4$). This potentially allows operation on a single longitudinal mode; however, since the cavity lacks active stabilization at this stage, it suffers from an occasional rise of side modes, which appear at $\delta\nu = \pm 443$ MHz and are suppressed by only about a factor of ≈10.

Figure 4 shows the direct excitation of the five stable bosonic isotopes and Table II shows the resulting isotope shifts. Since the isotope shifts of the stable odd-mass isotopes with nonzero nuclear spin I as well as the isotope shifts of the three stable even-mass isotopes ($I = 0$) with highest abundance are already given in Ref. [26], we omitted a re-measurement of the odd-mass isotopes at this point. The isotope shifts obtained here for the even-mass isotopes with highest abundance are in accordance with Ref. [26]. However, here we have also provided an isotope shift measurement in this line for the two rarest stable isotopes, ^{158}Dy and ^{156}Dy.

IV. LIFETIME MEASUREMENTS

Lower limits for the lifetimes of the excited states at 9990.96 and 13495.96 cm^{-1} can be determined by

TABLE II. Isotope shift in the 741-nm transition in Dy for the five isotopes with even mass number.

	Isotope shift $\delta\nu$ [MHz]
$\delta\nu_{164–162}$	1245(32)
$\delta\nu_{164–160}$	2583(32)
$\delta\nu_{164–158}$	3874(32)
$\delta\nu_{164–156}$	6042(32)

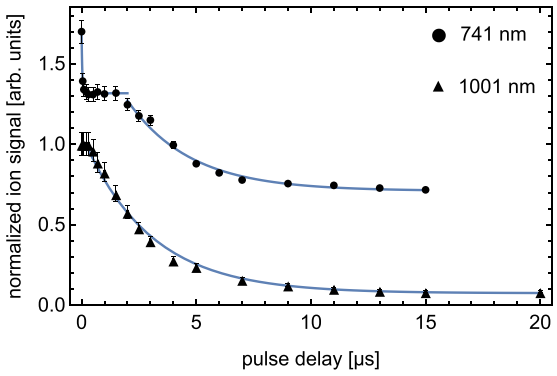

FIG. 5. Lifetime measurements in the 741- and 1001-nm transitions obtained by delaying the ionization laser pulse. For better readability, we added a random offset to the ion signal of the 741-nm transition.

investigating the population decay after the pulsed laser excitation. The population is probed by delayed ionization laser pulses, according to the excitation schemes in Secs. III A and III B, and subsequent ion counting. The temporal profiles and delays between the individual Ti:sapphire laser pulses are captured by fast photodiodes and monitored with an oscilloscope. In order to maintain stable laser power during the measurement, the first excitation step laser is pumped by a separate Nd:YAG laser[4] and pulse delays are controlled by means of shifting the pump laser trigger accordingly. Figure 5 shows the excited-state population decay at oven temperatures of 700(100) °C and 950(100) °C for the states at 9990.96 and 13495.96 cm^{-1}, respectively. The excited state at 9990.96 cm^{-1} shows an exponential decay with a lifetime of 2.9(1) μs, whereas the 13495.96 cm^{-1} state clearly features two components with lifetimes of 32(2) ns and 2.8(3) μs. The short-lived contribution is an artifact, which is related to the ionization scheme for the 741-nm transition where the first excitation step has enough energy to ionize atoms parasitically from the second excited state. This effect is completely suppressed by a delayed second excitation pulse; thus, the 32(2)-ns lifetime corresponds to the laser pulse length. Nonetheless, lifetimes of the investigated states are orders of magnitude shorter than theoretical values [11], which actually was expected due to the experimental circumstances. De-excitation of atoms within the hot atomic vapor may occur by collisions with the oven wall or other atoms. In comparison to an experimental value for the lifetime of the 13495.96 cm^{-1} excited state of 89.3(8) μs [26] and the fact that both of our measured values agree with each other we can conclude that, in our experiment, the extracted lifetimes predominantly depend on the mean free path of the hot atoms within the atomic beam oven cavity. Consequently, the 2.9(1) μs lifetime for the 9990.96 cm^{-1} excited state should be treated as a very conservative lower limit, which corresponds to an upper limit for the 1001-nm transition linewidth of 55(2) kHz.

[4]Quantronix Hawk-Pro 532-60-M.

V. CONCLUSION

We presented a direct excitation of the 1001-nm ground-state transition for all seven stable dysprosium isotopes for the first time by applying high-repetition-rate pulsed laser resonance ionization. Furthermore, we measured the isotopic shift in the 1001-nm transition and determined the upper level energy from the atomic transition frequency of the ^{164}Dy isotope as 9991.004(1) cm^{-1}, which is in accordance with the value listed in the NIST database [13]. We obtain an upper limit of 55(2) kHz for the transition linewidth of the excited state. Our results open the route toward investigation of physics beyond the standard model of particle physics and enable the study of many-body physics with magnetic quantum gases by atomic high-resolution spectroscopy within the 1001-nm transition.

ACKNOWLEDGMENTS

The authors would like to point out that this work is part of the M.Sc. thesis of L. Maske, who not only contributed to the experimental activities but also did a major part of the data evaluation. We thank N. Petersen and F. Mühlbauer for their ideas and fruitful discussions. We gratefully acknowledge the financial support of the EU through ENSAR2-RESIST (Grant No. 654002) and DFG Großgerät: DFG FUGG (INST 247/818-1).

[1] A. Yamaguchi, S. Uetake, S. Kato, H. Ito, and Y. Takahashi, New J. Phys. **12**, 103001 (2010).
[2] M. J. Martin, M. Bishof, M. D. Swallows, X. Zhang, C. Benko, J. von Stecher, A. V. Gorshkov, A. M. Rey, and J. Ye, Science **341**, 632 (2013).
[3] M. Foss-Feig, M. Hermele, and A. M. Rey, Phys. Rev. A **81**, 051603(R) (2010).
[4] L. Riegger, N. Darkwah Oppong, M. Höfer, D. R. Fernandes, I. Bloch, and S. Fölling, Phys. Rev. Lett. **120**, 143601 (2018).
[5] A. J. Daley, M. M. Boyd, J. Ye, and P. Zoller, Phys. Rev. Lett. **101**, 170504 (2008).
[6] A. V. Gorshkov, A. M. Rey, A. J. Daley, M. M. Boyd, J. Ye, P. Zoller, and M. D. Lukin, Phys. Rev. Lett. **102**, 110503 (2009).
[7] W. H. King, J. Opt. Soc. Am. **53**, 638 (1963).
[8] V. V. Flambaum, A. J. Geddes, and A. V. Viatkina, Phys. Rev. A **97**, 032510 (2018).
[9] J. C. Berengut, D. Budker, C. Delaunay, V. V. Flambaum, C. Frugiuele, E. Fuchs, C. Grojean, R. Harnik, R. Ozeri, G. Perez, and Y. Soreq, Phys. Rev. Lett. **120**, 091801 (2018).
[10] C. Delaunay, R. Ozeri, G. Perez, and Y. Soreq, Phys. Rev. D **96**, 093001 (2017).
[11] V. A. Dzuba and V. V. Flambaum, Phys. Rev. A **81**, 052515 (2010).
[12] J. G. Conway and E. F. Worden, J. Opt. Soc. Am. **61**, 704 (1971).

[13] A. Kramida, Y. Ralchenko, J. Reader, and the NIST ASD Team, NIST Atomic Spectra Database, https://www.nist.gov/pml/atomic-spectra-database.
[14] M. Lu, N. Q. Burdick, S. H. Youn, and B. L. Lev, Phys. Rev. Lett. **107**, 190401 (2011).
[15] V. S. Letokhov and V. I. Mishin, Opt. Commun. **29**, 168 (1979).
[16] V. N. Fedosseev, Y. Kudryavtsev, and V. I. Mishin, Phys. Scr. **85**, 058104 (2012).
[17] J. Lassen, P. Bricault, M. Dombsky, J. P. Lavoie, C. Geppert, and K. Wendt, Hyperfine Interact. **162**, 69 (2006).
[18] T. E. Cocolios, H. H. Al Suradi, J. Billowes, I. Budinčević, R. P. de Groote, S. de Schepper, V. N. Fedosseev, K. T. Flanagan, S. Franchoo, R. F. Garcia Ruiz *et al.*, Nucl. Instrum. Methods Phys. Res., Sect. B **317**, 565 (2013).
[19] S. Rothe, A. N. Andreyev, S. Antalic, A. Borschevsky, L. Capponi, T. E. Cocolios, H. de Witte, E. Eliav, D. V. Fedorov, V. N. Fedosseev *et al.*, Nat. Commun. **4**, 1835 (2013).
[20] R. P. de Groote, M. Verlinde, V. Sonnenschein, K. T. Flanagan, I. Moore, and G. Neyens, Phys. Rev. A **95**, 032502 (2017).
[21] V. Sonnenschein, S. Raeder, A. Hakimi, I. D. Moore, and K. Wendt, J. Phys. B: At., Mol. Opt. Phys. **45**, 165005 (2012).
[22] S. Rothe, B. A. Marsh, C. Mattolat, V. N. Fedosseev, and K. Wendt, J. Phys.: Conf. Ser. **312**, 052020 (2011).
[23] V. Sonnenschein, I. D. Moore, H. Khan, I. Pohjalainen, and M. Reponen, Hyperfine Interact. **227**, 113 (2014).
[24] S. Wolf, D. Studer, K. Wendt, and F. Schmidt-Kaler, Appl. Phys. B **124**, 412 (2018).
[25] A. Teigelhöfer, P. Bricault, O. Chachkova, M. Gillner, J. Lassen, J. P. Lavoie, R. Li, J. Meißner, W. Neu, and K. D. A. Wendt, Hyperfine Interact. **196**, 161 (2010).
[26] M. Lu, S. H. Youn, and B. L. Lev, Phys. Rev. A **83**, 012510 (2011).
[27] See Supplemental Material at http://link.aps.org/supplemental/10.1103/PhysRevA.98.042504 for list of atomic transitions starting from the 13495.96 cm^{-1} excited state.
[28] D. Studer, P. Dyrauf, P. Naubereit, R. Heinke, and K. Wendt, Hyperfine Interact. **238**, 02A916 (2017).

3.7 Publication II: Resonance ionization spectroscopy in dysprosium: Excitation scheme development and re-determination of the first ionization potential

The following article was published in Hyperfine Interactions **238**, 8 (2017) DOI 10.1007/s10751-016-1384-4. It is part of the Topical Collection on Proceedings of the 10th International Workshop on Application of Lasers and Storage Devices in Atomic Nuclei Research: "Recent Achievements and Future Prospects" (LASER 2016) Poznan, Poland. It comprises the results of a series of spectroscopic experiments of the element dysprosium. New three-step laser ionization schemes were assessed as alternatives to previously used schemes, relying on dye lasers or non-resonant ionization steps [37]. This included extensive spectroscopy in various three-step excitation ladders and measurements of saturation powers for individual transitions. A series of dedicated efficiency measurements was performed for a suitable ionization scheme, where all transitions could be saturated with the available laser power. This scheme was used later on to determine isotope ratios of a Dy contamination in holmium samples produced for the ECHo project [137]. The second part of the article presents spectroscopy of Rydberg states, accessed in a two-step excitation scheme. The analysis of perturbed Rydberg convergences is presented and a value for the ionization potential of $\mathrm{IP}^{\mathrm{Ryd}}_{\mathrm{Dy}} = 47\,901.76(5)\,\mathrm{cm}^{-1}$ is extracted. Note that this value is in perfect agreement with results from electric field ionization, where $\mathrm{IP}^{\mathrm{SP}}_{\mathrm{Dy}} = 47\,901.8(3)\,\mathrm{cm}^{-1}$ was measured [128, 138]. This confirms the accuracy of the classical saddle point model, which is used in Publication III for the determination of the IP of promethium.

Author contribution

Part of the data for this work, i.e. the two-step spectroscopy of Rydberg convergences, was jointly measured with Patrick Dyrauf, who presented the respective results in his master thesis [113]. These results were later re-evaluated by the author in preparation for publication. The three-step spectroscopy measurements were partly presented in the diploma thesis of the author [114], and then further extended in the scope of this dissertation. After the assessment of an optimal ionization scheme, the author performed efficiency measurements. P.D. is listed as second author for the experimental work and data evaluation during his master thesis. The other co-authors, P.N. and R.H. contributed to the experimental work. The author presented this data on the International Conference on Application of Lasers and Storage Devices in Atomic and Nuclei Research (Poznan, Poland) and prepared the manuscript as conference proceeding.

Hyperfine Interact (2017) 238: 8
DOI 10.1007/s10751-016-1384-4

Resonance ionization spectroscopy in dysprosium

Excitation scheme development and re-determination of the first ionization potential

D. Studer[1] · P. Dyrauf[1] · P. Naubereit[1] · R. Heinke[1] · K. Wendt[1]

Published online: 19 December 2016

Abstract We report on resonance ionization spectroscopy (RIS) of high-lying energy levels in dysprosium. We developed efficient excitation schemes and re-determined the first ionization potential (IP) via analysis of Rydberg convergences. For this purpose both two- and three-step excitation ladders were investigated. An overall ionization efficiency of 25(4) % could be demonstrated in the RISIKO mass separator of Mainz University, using a three-step resonance ionization scheme. Moreover, an extensive analysis of the even-parity 6s*n*s- and 6s*n*d-Rydberg-series convergences, measured via two-step excitation was performed. To account for strong perturbations in the observed s-series, the approach of multichannel quantum defect theory (MQDT) was applied. Considering all individual series limits we extracted an IP-value of 47901.76(5) cm^{-1}, which agrees with the current literature value of 47901.7(6) cm^{-1}, but is one order of magnitude more precise.

Keywords Resonance ionization spectroscopy · Ionization potential · Ionization scheme development · Dysprosium

1 Introduction

Resonance ionization spectroscopy has been proven to be a most versatile experimental technique with a wide range of applications in both atomic and nuclear research. The stepwise excitation and ionization using strong optical dipole transitions provides excellent

This article is part of the Topical Collection on *Proceedings of the 10th International Workshop on Application of Lasers and Storage Devices in Atomic Nuclei Research: "Recent Achievements and Future Prospects" (LASER 2016), Poznań, Poland, 16–19 May 2016*
Edited by Krassimira Marinova, Magdalena Kowalska and Zdzislaw Błaszczak

✉ D. Studer
dstuder@uni-mainz.de

[1] Institut für Physik, Johannes Gutenberg-Universität Mainz, 55099 Mainz, Germany

elemental selectivity by utilizing each elements unique atomic structure, while being highly efficient at the same time. In particular on-line mass separators, such as ISOLDE at CERN and others, benefit from laser ion sources and related spectroscopic work. The production of high-purity radioactive ion beams (RIBs) is achieved by applying resonance ionization in combination with mass spectrometers (RIMS) and enables research on shortest lived exotic radioisotopes far off stability [1, 2]. In addition to fundamental research, practical applications of RIMS span from ultratrace analysis [3] to the production of medically relevant radioisotopes, where highest purity against any radioactive interference is mandatory to meet ethical standards [4].

While laser ion sources have undergone constant development in the last decades, their efficiency is finally determined by the sequence of transitions used for resonant ionization process. Optimum ionization schemes have to be theoretically prepared from literature data and experimentally developed individually for each element. In complex atomic systems like the lanthanide and actinide elements, reliable spectroscopic data towards higher excitation energies is most often rather scarce or incomplete in literature. In particular high-lying Rydberg-states and auto-ionizing states (AI) are often unknown but of primary interest, since they represent promising candidates for strong ionizing transitions, as required to maximize ionization efficiency.

Besides scheme development, the spectroscopic data obtained is useful for the analysis of Rydberg convergences, which allows for a detailed study of the atomic system and for a precise determination of the first ionization potential. This fundamental quantity is closely linked to the chemical behavior of each element and can be used for the identification of various trends across the periodic table [5]. Due to their complex electronic structure, theoretical estimates of the IP for lanthanide elements can even today just be computed with precisions several orders of magnitude below experimental uncertainties [6]. Correspondingly, precise experimental data serves also as a valuable reference for optimizing calculations.

The rare earth element dysprosium ($Z = 66$) has been subject to a number of RIS studies in the past, during which different excitation schemes were developed and utilized. Worden et al. used two-step excitation schemes with first excitation steps between 456 and 461 nm for spectroscopy of auto-ionizing Rydberg-series [7]. A similar approach was applied by Zhou et al. [8], using a different first step at 554.7 nm. Both bound and auto-ionizing Rydberg-series were studied in that publication. By minimization of variations in the quantum defect for individual series (for details see Section 4), a value for the first ionization potential of $\mathrm{IP_{Dy}} = 47901.7(6)\ \mathrm{cm}^{-1}$ was determined. Excitation scheme development for efficient ionization of Dy was carried out by Fedosseev et al. [9]. An overall efficiency of 20 % was measured using a three-step scheme. Two dye lasers at 625.9 nm and 607.5 nm were used for the first and the second excitation step, respectively, and the 510.6 nm component of a copper vapor laser for non-resonant ionization.

The work presented here aims to refine these previous approaches. Excitation scheme development is primarily oriented for the production of the radioisotopes ^{152}Dy and ^{155}Dy, which are used for medical imaging in the framework of the CERN-MEDICIS-project [4]. In the course of spectroscopy of high-lying states, so far unknown Rydberg series were discovered and convergences are analyzed to improve the accuracy of the first ionization potential.

2 Experimental

The laser system used here for resonance ionization consists of two to three high-power pulsed Ti:sapphire lasers, pumped by a commercial frequency doubled Nd:YAG laser (Photonics DM100-532). They are operated at a repetition rate of 10 kHz with typical pulse lengths of 50 ns. With an accessible spectral range of 690 to 960 nm and the option of higher harmonic generation, the ionization of 38 elements with Ti:sapphire lasers could be demonstrated so far [10]. Output powers of up to 4 W in the fundamental wavelength range and about 1 W in the second harmonics are achieved. For wide range scans a grating-assisted resonator in Littrow geometry is used, which allows mode-hop free tuning over the whole Ti:sapphire range. Linewidths for the standard- and the grating Ti:sapphire laser are in the range of 5 GHz and 1 GHz, respectively. The wavelength of the fundamental laser beam is measured using a High Finesse WS6-600 wavelength meter with a specified 1σ-uncertainty of 200 MHz. For the studies of two step excitation schemes the grating-laser was frequency doubled with an extra-cavity BBO crystal. During scanning operation the crystal angle was manually tuned to maintain phase matching, while the blue laser power was constantly monitored with a sample beam reflected from a wedged glass plate. Walkoff effects due to crystal angle adjustment were compensated with a commercial TEM Aligna Beamlock system.

The spectroscopic measurements were carried out at the Mainz Atomic Beam Unit (MABU), a compact low-energy quadrupole mass spectrometer, combined with a laser ion source. The mass spectrometer is a commercial device by ABB Extrel, including the quadrupole mass filter and the detection system. For a detailed description see [11, 12]. A sketch of the apparatus is given in the upper left of Fig. 1. The sample material is atomized in a resistively heated graphite tube at approximately 1500 °C. Resonance ionization of the atomic vapor occurs directly inside the atomizer cavity by irradiating the lasers in anti-collinear geometry to the extracted ion beam. The ions are accelerated by a three-stage extraction electrode, followed by an Einzel-lens and a telescopic lens for focusing and beam shaping. All ion optics components operate with low voltages < 1 kV. Suppression of neutral species is ensured by a 90° quadrupole deflector. The isotope of interest is selected with a quadrupole mass filter, operated at 1.2 MHz. Transmitted ions are detected with a channel electron multiplier in single ion counting mode.

While the MABU is a reliable instrument for spectroscopy, it is unfavorable for a quantification of the ionization efficiency due to its low acceleration voltage and ion transmission through the apparatus (which is primarily limited by the QMF settings). A more suitable apparatus for efficiency measurements is found in the RISIKO mass separator (see lower part of Fig. 1). Here the sample reservoir and the atomizer cavity can be heated independently, allowing a well controlled release of the sample material. Laser ions are accelerated to 30 keV before entering a 60° sector field magnet for mass separation. Depending on the intensity of the beam, ions are detected with a Faraday cup (FC) or a secondary electron multiplier (SEM) just behind the focal plane of the magnet. The RISIKO mass separator has a resolving power of $M/\Delta M > 500$.

3 Excitation scheme development and efficiency measurements

The strongest transition probability into a suitable first excited state (FES) in dysprosium is predicted for $4f^{10}6s^2(^5I_8) \rightarrow 4f^{10}(^5I_8)6s6p(^1P_1)_{7,8,9}$ [13]. A-values are in the order

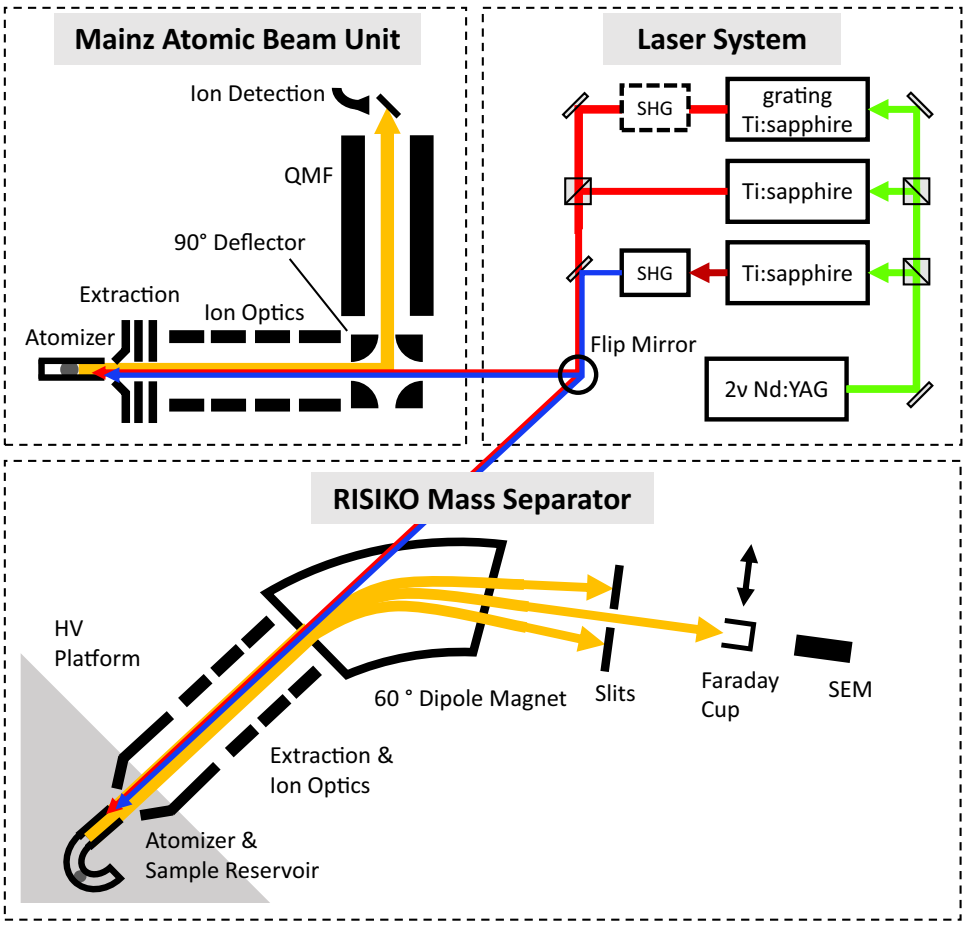

Fig. 1 Schematic view of the experimental setup, divided into the laser system (*upper right*), the Mainz Atomic Beam Unit MABU (*upper left*) and the RISIKO mass separator (*bottom*). Abbreviations: QMF - quadrupole mass filter, SHG - second harmonic generation, SEM - secondary electron multiplier. The *dashed* SHG-unit represents the option to frequency-double the grating laser as well

of 10^8 s^{-1} [14]. With 404 nm, 418 nm and 421 nm they are accessible with a frequency doubled Ti:sapphire laser. From the FES, one can either directly ionize the atom with an additional blue laser photon or populate a second excited state (SES) to subsequently ionize with a third excitation step, both in the fundamental wavelength regime. Two-step schemes were successfully used for spectroscopy in [7] and [8]. A three-step scheme for dysprosium was proposed by T. Gottwald et al. [15], but the ionizing transition was not specified. Based on these transitions known from literature, several two- and three-step excitation ladders were developed and tested. A summary of all utilized schemes with the respective transition wavenumbers and configurations of the intermediate steps, as well as the scanning range of the ionizing laser, is given in Table 1. Schemes #1 to #3 represent three-step ladders, where the third laser excitation is scanned for odd-parity AI- or Rydberg-states, while schemes #4 to #6 are two-step ladders with scanning in the second step for even-parity states. Regarding relative intensities and laser power requirements to saturate each transition, the three-step scheme #1, aiming for an auto-ionizing state at $E = 49101.8$ cm^{-1} was chosen for a series of efficiency measurements. Line profiles and saturation curves were measured at the MABU with a laser beam diameter of approximately 2 mm, which corresponds to the inner diameter of the atomizer tube of 2.2 mm. The obtained graphs for the individual transitions are shown in Fig. 2. The intermediate steps were saturated with few mW laser power, while

Table 1 Summary of all studied excitation schemes, starting from the atomic ground state $4f^{10}6s^2(^5I_8)$

	$\tilde{\nu}_1$ [cm^{-1}]	FES	$\tilde{\nu}_2$ [cm^{-1}]	SES	$\tilde{\nu}_{\text{scan}}$ [cm^{-1}]
1	24708.97	$4f^{10}(^5I_8)6s6p(^1P_1^o)(8,1)_7^o$	12454.20	$J = 6$	11080 – 12450
2	23877.74	$4f^{10}(^5I_8)6s6p(^1P_1^o)(8,1)_8^o$	12882.89	$J = 8$	11040 – 13640
3	23877.74	$4f^{10}(^5I_8)6s6p(^1P_1^o)(8,1)_8^o$	12721.70	$J = 8$	11200 – 13800
4	23877.74	$4f^{10}(^5I_8)6s6p(^1P_1^o)(8,1)_8^o$	–	–	22800 – 25130
5	23832.07	$4f^9(^6H^o)5d^2(^3F)(^8K^o)_8$	–	–	23150 – 25200
6	23736.60	$4f^{10}(^5I_8)6s6p(^1P_1^o)(8,1)_9^o$	–	–	23640 – 25420

The level energies and the configurations of the FES and SES are taken from [16]. For the SES only a J value is given since the configurations are not known, with the exception of the SES in scheme #2, where the configuration $4f^{10}6s6d$? $J = 8$ is given in NIST. The question mark indicates a doubtful configuration assignment

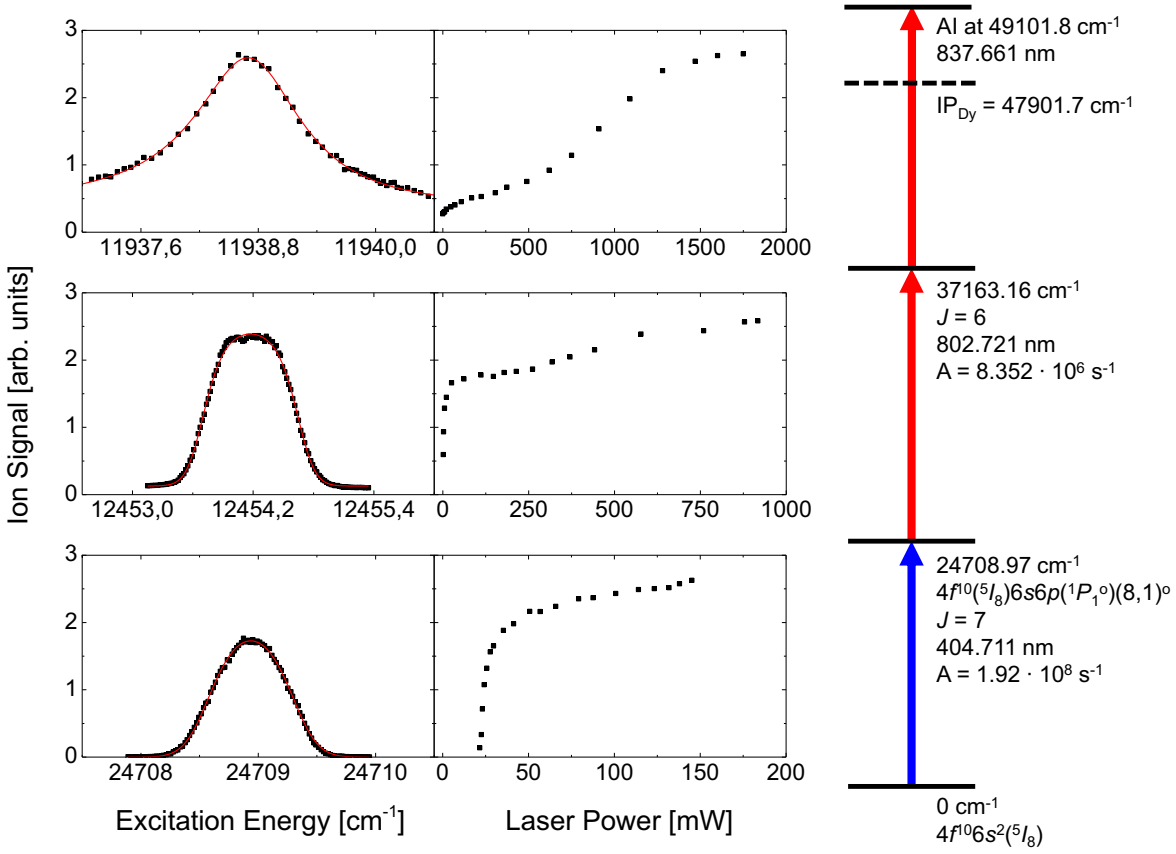

Fig. 2 Line profiles and saturation curves for the three-step excitation scheme used for efficiency measurements. The peaks from the first step and second step are fitted with power-broadened Gaussian profiles. The peak from the third step is fitted with a Fano profile [17]

the ionizing transition showed saturation at approximately 1.5 W, which was reached easily with the available laser system.

Quantification of the ionization efficiency was achieved by complete exhaustion of a calibrated sample and integration over the ion current. For singly charged ions, as obtained with the employed excitation scheme, the overall efficiency is given by Q/eNA, where Q

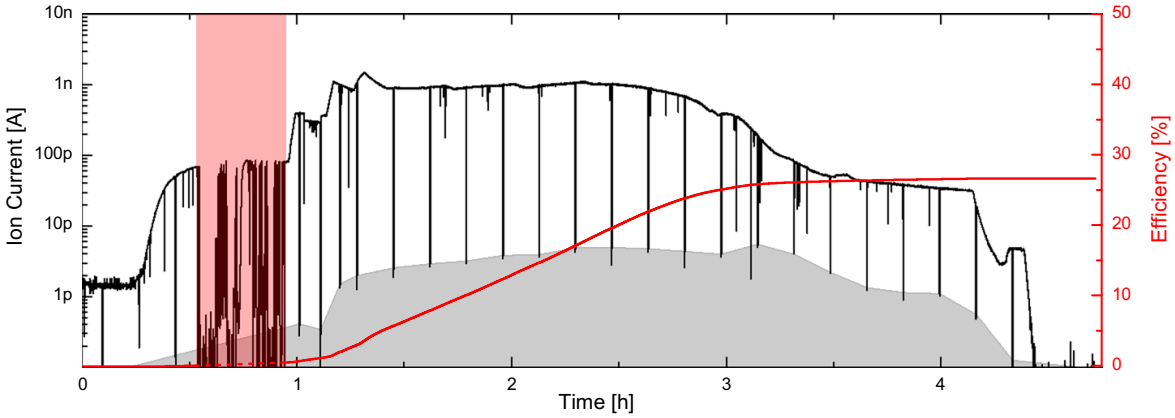

Fig. 3 Typical course of an efficiency measurement at the RISIKO mass separator. The *black curve* shows the measured ion current for mass 164. The optimization phase of the apparatus (mass scans, adjustment of temporal and spatial laser overlap) is indicated by the red area. The *gray area* marks the background due to surface ionized species, which is determined by interpolation over the shutter phases (sharp signal drops). The measurement was stopped shortly after 4 hours of accumulation time at low ion signal

is the total accumulated charge in the detector (minus the laser-independent background signal), e the elemental charge, N the number of sample atoms and A the isotopic abundance. For sample preparation dysprosium atomic absorption standard solution (Dy_2O_3 in 5 % HNO_3) with 997(5) μg/ml, supplied from Alfa Aesar, was used. Samples with a total of $5 \cdot 10^{14}$ atoms for all natural Dy isotopes were produced by applying and heating the solution on a 3x3 mm^2 piece of zirconium foil until the nitric acid and any water were completely vaporized. The left over dysprosium oxide is enclosed in the Zr-foil, which serves as a reduction agent. For further details on the efficiency measurement process at RISIKO see [18].

A typical efficiency measurement is shown in Fig. 3. Most of the sample is evaporated over a period of about two hours. The ion current is stabilized at approximately 1 nA by gradual heating of the sample reservoir until the sample is exhausted. This measurement was repeated four times, yielding values of 28.3 %, 18.0 %, 26.6 % and 27.5 %. Even though one of the values is significantly lower, which can be caused by an improper alignment of the ion source, the obtained values show an overall good reproducibility. In conclusion we can extract a value of 25(4) % by averaging over the series of measurements. The uncertainty is given by the standard deviation of the set of efficiency values.

4 Analysis of Rydberg series

An extensive analysis of Rydberg-convergences was carried out for bound even-parity Rydberg-states populated in three different two-step excitation schemes (schemes #4, #5 and #6 in Table 1), starting from the atomic ground state $4f^{10}6s^2(^5I_8)$. All three scans cover a wide spectral range of up to 2300 cm^{-1} around the IP, so that Rydberg-series converging to the ionic ground state $4f^{10}(^5I_8)6s_{1/2}(8, 1/2)_{17/2}$ and the higher lying fine-structure component $4f^{10}(^5I_8)6s_{1/2}(8, 1/2)_{15/2}$ located 828.314 cm^{-1} above the ionic ground state can be observed [16]. The obtained spectra are shown in Fig. 4. An assignment of resonances to Rydberg series is achieved by identification of trends in the quantum defect $\delta(n)$, which can be calculated using the Rydberg-Ritz formula

$$E_n = E_\infty - \frac{R_\mu}{(n - \delta(n))^2} = E_\infty - \frac{R_\mu}{(n^*)^2} \quad (1)$$

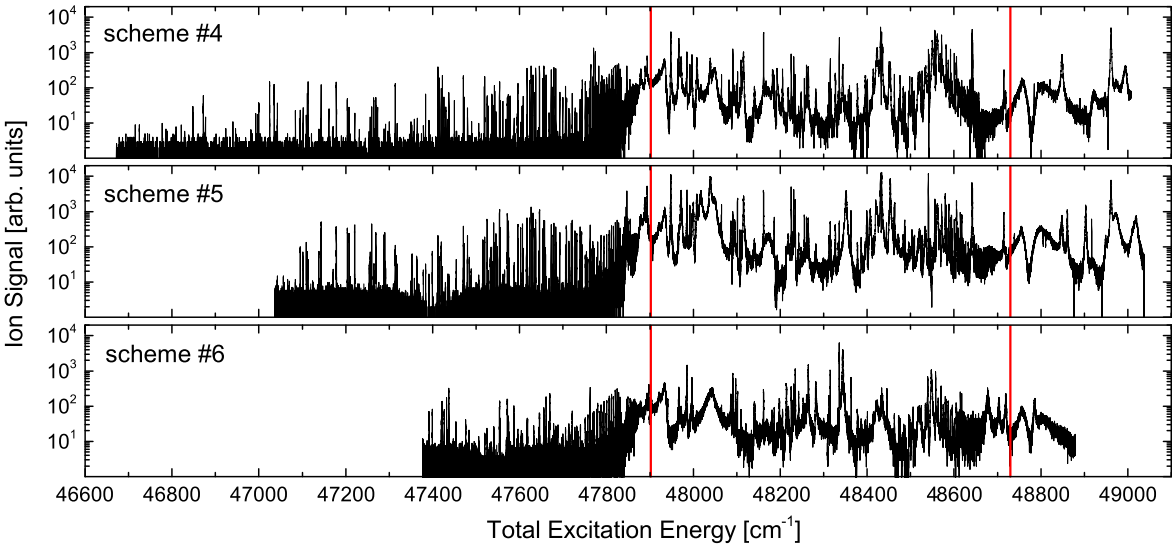

Fig. 4 Measured spectra of the ionization step of the excitation schemes given in Table 1. The *vertical red lines* mark the series limits, i.e. the ionic ground state $4f^{10}(^5I_8)6s_{1/2}(8, 1/2)_{17/2}$ and the higher lying fine-structure component $4f^{10}(^5I_8)6s_{1/2}(8, 1/2)_{15/2}$, located at 828.314 cm^{-1}

where n is the principal quantum number, E_∞ the series limit (e.g. the IP) and R_μ the mass reduced Rydberg constant. Unless a principal quantum number n can be assigned to the measured resonances, it is sufficient to consider the remainder of the quantum defect $\delta' = \mathrm{mod}_1(\delta(n)) = \mathrm{mod}_1(-n^*)$ since a shift of a series by an integer number does not influence its convergence. For $E_\infty \approx$ IP, high-lying Rydberg-states of one series possess a nearly constant quantum defect, as described by the Ritz expansion [19]

$$\delta(n) \approx \delta_0 + \frac{\delta_1}{(n-\delta_0)^2} + \frac{\delta_2}{(n-\delta_0)^4} + [...] \tag{2}$$

where δ_0 is expected to be in the range of $0 < \delta_0 < 6$ [20] and the higher order δ_i parameters in the range of 10^{-3} to 10^1 [21]. Therefore the IP can be coarsely approximated by minimizing the overall slope of $\delta(n)$ [7]. In Fig. 5 the spectrum obtained through excitation scheme #6 is plotted against the effective principal quantum number n^* for the literature value $\mathrm{IP_{Dy}} = 47901.7$ cm^{-1} [8], with the corresponding values of δ' for each individual resonance peak extracted into the graph above the spectrum. Three Rydberg-series can be distinguished, together with some unassigned peaks. The series at $\delta' \approx 0.35$ and $\delta' = 0.8$ are identified as the 6sns (red) and 6snd-series (blue), by comparing the respective δ' with the calculations of Fano et al. [20]. The high-intensity series, which approaches $\delta' = 0.2$ towards high n, could not be identified due to its unexpected steady and strong variation of the quantum defect all along the measured series for $25 < n^* < 45$. Nevertheless above $n^* = 55$ a stable value of δ' is approached, which supports the IP determination via the other two identified series.

For the 6snd-series we observe a fine structure splitting, which cannot be resolved above $n^* = 33$ due to the experimental linewidth of > 5 GHz and the decreasing splitting between individual fine structure components according to $\Delta E_{\mathrm{FS}} \propto n^{-3}$ [22]. To extend the series towards lower n, the center of gravity of each fine structure multiplet is taken from $n^* = 28$ to 33. Below $n^* = 28$ peak intensities are too low for reliable assignment. For a fit of this series we neglect second and higher order terms of the Ritz expansion, as the variations in $\delta(n)$ are expected to lie well within the experimental uncertainty for the considered n-interval.

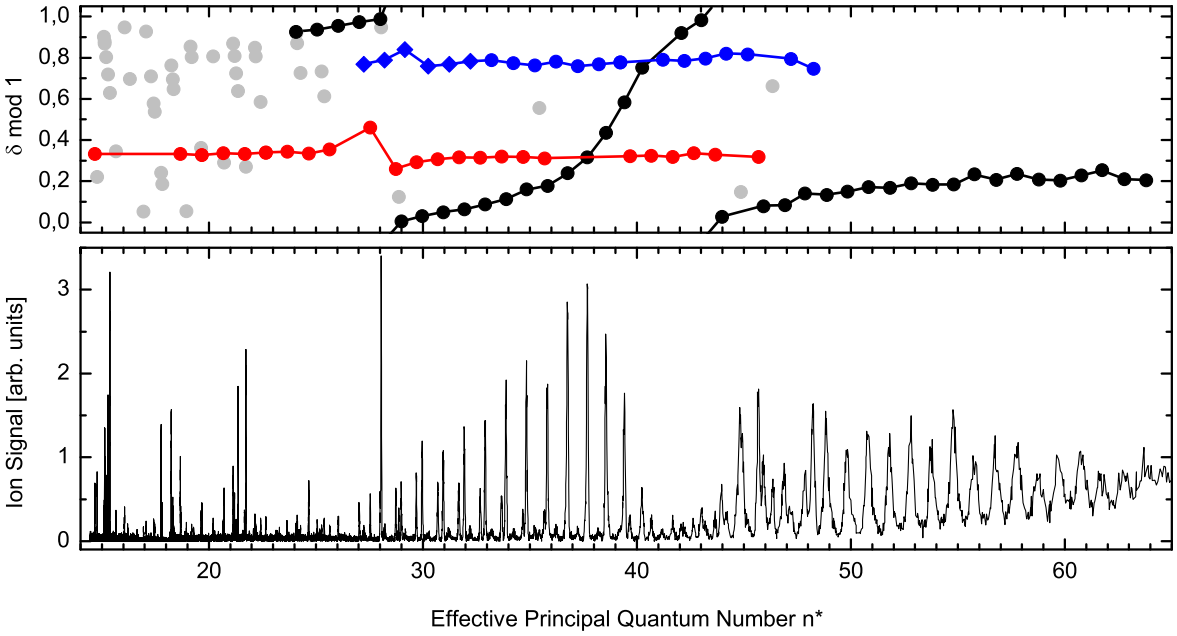

Fig. 5 Rydberg spectrum obtained through excitation scheme #6, plotted against the effective principal quantum number n^* as calculated from $E_\infty = 47901.7\ \mathrm{cm}^{-1}$. The corresponding value of $\delta' = \mathrm{mod}_1(\delta(n))$ for each resonance is shown in the upper part. Three series can be distinguished: the 6s*n*s-series (*red*), the 6s*n*d-series (*blue*) and an unidentified series (*black*). Diamond signs on the lower part of the d-series mark the center of gravity of a fine-structure multiplet. Individual components in that range are not shown for the sake of clarity. Points of the same series are interconnected by lines to guide the eye. Grey points are unassigned peaks

The other series in Fig. 5 show some distinct deviations from a constant quantum defect, which are accompanied by strong fluctuations in peak intensities. For the 6s*n*s-series the very obvious perturbation around $n^* = 28$ can be described within the framework of multi-channel quantum defect theory (MQDT) [23]. Rydberg-states in the vicinity of an interloper state with energy E_I and width Γ_I are shifted away from the interloper according to

$$\delta_{\mathrm{shift}}(n) = \delta(n) - \frac{1}{\pi} \arctan\left(\frac{\Gamma_I/2}{E_n - E_I}\right). \tag{3}$$

The perturbation in the s-series, which is observed in the spectra of all three excitation schemes, can be accurately considered through this modification of the quantum defect. A fit of this series is shown in Fig. 6, including the Ritz expansion to the second order term. Towards lower n the course of the series is predominantly governed by δ_1. The fitting errors of this parameter are in the order of the value itself, yet the much higher consistency in the values observed for all three spectra (see Table 2) leads to the assumption that the fit is indeed very accurate. Even under consideration of the entire error range of δ_1 only two levels at 30560.56 cm^{-1} and 30979.53 cm^{-1} with the configuration $4f^{10}(^5I_8)6s7s(^3S_1)\ (8,\ 1)_{8,9}$ [16] represent possible band heads for the series. By using either one of these states as anchor point for the series, the integer digit of the quantum defect can be determined. As a result we obtain $\delta \approx 4.33$ for high n, which is in good agreement with calculations of Fano et al. [20].

The unidentified series, represented by the black points in Fig. 5, is subject to quantum defect variations over an extended range, which cannot be described with Eq. 3. The attempt of fitting this series even with up to fourth order corrections from Eq. 2 is possible, however resulting parameters for δ_1 and δ_2 are in the range of 10^2 and 10^5, respectively, which does not seem appropriate. For this reason the series was excluded from evaluation.

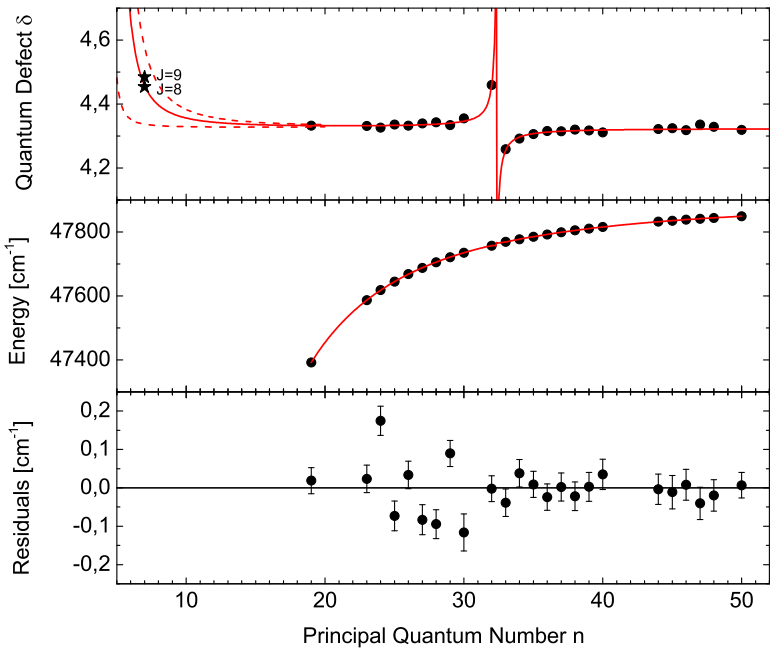

Fig. 6 Rydberg-Ritz fit of the 6s*n*s-series (excitation scheme #6) in the energy representation (*middle*) and the quantum defect representation (*top*). *Dashed lines* indicate the error range of δ_1. The stars at $n = 7$ represent possible series heads with the configuration $4f^{10}(^5I_8)6s7s(^3S_1)\ (8,1)_J$ [16]. The lower graph shows the fit residuals

Table 2 Summary of the IP values obtained from Rydberg-Ritz fits of the 6s*n*s and 6s*n*d-series with the respective statistical uncertainties

scheme #	series	n^*-interval	#peaks	E_∞[cm^{-1}]	δ_0 mod 1	δ_1
4	6s*n*d	27 – 45	20	47901.81(5)	0.749(9)	–
	6s*n*s	12 – 47	14	47901.81(7)	0.329(9)	1.1(1.0)
5	6s*n*d	25 – 40	16	47901.55(22)	0.69(2)	–
	6s*n*s	12 – 48	23	47901.79(10)	0.33(1)	1.0(1.5)
6	6s*n*d	28 – 49	20	47901.77(5)	0.766(7)	–
	6s*n*s	15 – 46	24	47901.71(4)	0.327(5)	0.95(86)

Taking the weighted average yields a value of $E_\infty = 47901.76(2)_{\text{stat}}$

A summary of all series limits obtained from the different excitation schemes is given in Table 2. The large deviation of value from the 6s*n*d-series in scheme #5 is most likely a consequence of missing fine structure components within the fitted n-interval, which were not observed due to the low intensity of this series. Correspondingly the uncertainty of this series limit is comparatively high, which is also a result of the limited n-interval and the number of fitted peaks.

Taking the weighted average yields a value of $E_\infty = 47901.76(2)$ cm^{-1}. Uncertainties in the energy position of the FES, as well as systematic errors in the wavelength measurement linearly propagate to E_∞ and are thus added as a systematic uncertainty to the error of the IP. In comparison to this, stark shifts are neglectable due to the low electric field of < 1 V/cm inside the atomizer cavity. In conclusion we extract a final value of $\text{IP}_{\text{Dy}} = 47901.76(2)_{\text{stat}}(3)_{\text{sys}}$ cm^{-1}, which is in good agreement with the results from Zhou et al. [8].

5 Conclusion

The spectra of altogether six different excitation schemes, covering spectral ranges of up to 2500 cm^{-1} around the first ionization potential of Dy, were studied. In the spectra obtained from two-step excitation we observed the bound $4f^{10}6sns$ and $4f^{10}6snd$ Rydberg-series as well as a so far unidentified series, all of them converging to the ionic ground state. Considering the second-order Ritz expansion and an approach from MQDT for the characterization of a strong perturbation of the s-series around $n = 32$, we could re-determine the first ionization potential of dysprosium. With the obtained value of $IP_{Dy} = 47901.76(5)$ cm^{-1} we can confirm the literature value of Zhou et al. [8] and improve the precision by about one order of magnitude. Auto-ionizing Rydberg-series converging to the level $4f^{10}(^5I_8)6s_{1/2}(8, 1/2)_{15/2}$ at 828.314 cm^{-1} were observed but not studied in detail due to high non-resonant background and strong perturbing interactions of the Rydberg-states with broad continuum states.

Spectroscopic data obtained in three-step excitation schemes was primarily used for scheme development. Bound Rydberg-series could not be observed, most likely due to unfavorable experimental conditions of low accessible laser power for the required third step wavelengths of >931 nm as well as high background from additional photons of the second excitation step laser. For scheme development several high-intensity auto-ionizing resonances were studied with respect to their saturation power and laser ion signal intensity. Utilizing the excitation scheme given in Fig. 2 an ionization efficiency of 25(4) % could be reproducibly demonstrated at the RISIKO mass separator at JGU Mainz.

References

1. Lecesne, N.: Laser ion sources for radioactive beams (invited). Rev. Sci. Instrum. **83**, 02A916 (2012)
2. Fedosseev, V.N., Kudryavtsev, Y., Mishin, V.I.: Resonance laser ionization of atoms for nuclear physics. Phys. Scrip. **85**, 58104 (2012)
3. Trautmann, N., Passler, G., Wendt, K.D.A.: Ultratrace analysis and isotope ratio measurements of long-lived radioisotopes by resonance ionization mass spectrometry (RIMS). Anal. Bioanal. Chem. **378**, 348 (2004)
4. dos Santos Augusto, R., Buehler, L., Lawson, Z., Marzari, S., Stachura, M., Stora, T.: CERN-MEDICIS collaboration: CERN-MEDICIS (medical isotopes collected from ISOLDE): A new facility. Appl. Sci. **4**, 265 (2014)
5. Wendt, K., Gottwald, T., Mattolat, C., Raeder, S.: Ionization potentials of the lanthanides and actinides – towards atomic spectroscopy of super-heavy elements. Hyp. Inter. **227**, 55 (2014)
6. Liu, W., Dolg, M.: Benchmark calculations for lanthanide atoms: Calibration of ab initio and density-functional methods. Phys. Rev. A **57**, 1721 (1998)
7. Worden, E.F., Solarz, R.W., Paisner, J.A., Conway, J.G.: First ionization potentials of lanthanides by laser spectroscopy*. J. Opt. Soc. Am. **68**, 52 (1978)
8. Zhou, H.J., Xu, X.Y., Huang, W., Chen, D.Y.: Study of high-lying excited states of rare-earth element Dy by laser resonance ionization spectroscopy. Acta Physica Sinica (Overseas Edn), 19 (1992)
9. Fedosseev, V.N., Marsh, B.A., Fedorov, D.V., Köster, U., Tengborn, E.: Ionization scheme development at the ISOLDE RILIS. Hyp. Inter. **162**, 15 (2006)
10. Rothe, S., Marsh, B.A., Mattolat, C., Fedosseev, V.N., Wendt, K.: A complementary laser system for ISOLDE RILIS. J. Phys. Conf. Ser. **312**, 52020 (2011)
11. Blaum, K., Geppert, C., Müller, P., Nörtershäuser, W., Otten, E.W., Schmitt, A., Trautmann, N., Wendt, K., Bushaw, B.A.: Properties and performance of a quadrupole mass filter used for resonance ionization mass spectrometry. Int. J. Mass Spectrom. **181**, 67 (1998)
12. Blaum, K., Geppert, C., Müller, P., Nörtershäuser, W., Wendt, K., Bushaw, B.A.: Peak shape for a quadrupole mass spectrometer: Comparison of computer simulation and experiment. Int. J. Mass Spectrom. **202**, 81 (2000)
13. Cowan, R.D.: The theory of rare earth energy levels and spectra. Nucl. Instrum. Methods **110**, 173 (1973)

14. Wickliffe, M., Lawler, J., Nave, G.: Atomic transition probabilities for Dy I and Dy II. J. Quant. Spectros. Rad. Transfer **66**, 363 (2000)
15. Gottwald, T., Lassen, J., Liu, Y., Mattolat, C., Raeder, S., Wendt, K.: Laser resonance ionization spectroscopy of the lanthanides Tb, Dy and Ho as homologues to actinides and super heavy elements. AIP Conf. Proc., 138 (2009)
16. Kramida, A.E., Ralchenko, Y., Reader, J.: NIST ASD Team. NIST Atomic Spectra Database (ver. 5.3). (2016). http://physics.nist.gov/asd
17. Fano, U.: Effects of configuration interaction on intensities and phase shifts. Phys. Rev. **124**, 1866 (1961)
18. Kron, T., Liu, Y., Richter, S., Schneider, F., Wendt, K.: High efficiency resonance ionization of palladium with Ti: Sapphire lasers. J. Phys. B: Atom. Molec. Opt. Phys. **49**, 185003 (2016)
19. Ritz, W.: Zur Theorie der Serienspektren. Annalen der Physik **317**, 264 (1903)
20. Fano, U., Theodosiou, C.E., Dehmer, J.L.: Electron-optical properties of atomic fields. Rev. Modern Phys. **48**, 49 (1976)
21. Weber, K.H., Sansonetti, C.J.: Accurate energies of nS, nP, nD, nF, and nG levels of neutral cesium. Phys. Rev. A **35**, 4650 (1987)
22. Harvey, K.C., Stoicheff, B.P.: Fine Structure of the nD2 Series in Rubidium near the Ionization Limit. Phys. Rev. Lett. **38**, 537 (1977)
23. Seaton, M.J.: Quantum defect theory. Reports Progress Phys. **46**, 167 (1983)

3.8 Publication III: Atomic transitions and the first ionization potential of promethium determined by laser spectroscopy

The following work was published as a regular article in Physical Review A **99**, 062513 (2019) DOI 10.1103/PhysRevA.99.062513. It presents extensive laser spectroscopy studies on a sample of 15 ng ^{147}Pm, which was produced by neutron activation of enriched ^{146}Nd in a nuclear reactor. In the course of ionization scheme development for this previously inaccessible element by RIS, several regions in the atomic spectrum were studied, including high-lying levels close to the IP. The new ionization schemes pave the way for laser ion sources applications and high-resolution spectroscopy on atomic Pm, as presented in Publication V.
For the determination of the IP, the approach of Rydberg convergences, as used for Dy in Publication II, was not applicable due to the high complexity of the spectrum. Instead, electric field ionization thresholds of weakly bound states were measured to determine the IP using the classical saddle point model (see Sec. 3.5.2). This technique was used earlier by T. Gottwald [128] in the precursor of the MABU setup for the study of several lanthanide elements. The results from these experiments are published in [138]. The study of Pm was deemed not feasible at the time due to low sample availability and comparatively low efficiency in the required perpendicular ionization geometry. In fact, in the experiment presented here atom numbers are a factor of 10^3-10^4 lower than in earlier experiments on stable species. This challenge was overcome by refining the measurement procedure. Scanning the electric field strength while keeping the ionization laser wavelength on resonance allows for higher counting statistics, but introduces some experimental complications, in particular maintaining high ion transmission through the apparatus. Comparing the IP values for Dy from Publication II of $\mathrm{IP}^{\mathrm{Ryd}}_{\mathrm{Dy}} = 47\,901.76(5)\,\mathrm{cm}^{-1}$ with the one of $\mathrm{IP}^{\mathrm{SP}}_{\mathrm{Dy}} = 47\,901.8(3)\,\mathrm{cm}^{-1}$ [128] confirms the excellent agreement of the results obtained from Rydberg analysis and the saddle point model.
Note that this article was published together with supplemental data tables, which are given in the appendix A.3.

Author contribution

This project was proposed by the author as part of a series of measurements on the element Pm. The enriched ^{146}Nd sample was provided by C.G. and irradiated at ILL by U.K. Chemical purification of the sample was performed at PSI by S.H., R.D. and D. Schumann. Laser spectroscopy was carried out by the author, R.H. and P.N. Data evaluation and the manuscript draft were prepared by the author. This work was supervised by K.W.

Atomic transitions and the first ionization potential of promethium determined by laser spectroscopy

Dominik Studer,[1,*] Stephan Heinitz,[2] Reinhard Heinke,[1] Pascal Naubereit,[1] Rugard Dressler,[3] Carlos Guerrero,[4] Ulli Köster,[5] Dorothea Schumann,[3] and Klaus Wendt[1]

[1]*Institut für Physik, Johannes Gutenberg-Universität Mainz, 55128 Mainz, Germany*
[2]*Belgian Nuclear Research Centre, SCK-CEN, 2400 Mol, Belgium*
[3]*Paul-Scherrer Institut, 5232 Villigen, Switzerland*
[4]*Departamento de Física Atómica, Molecular y Nuclear, Universidad de Sevilla, 41012 Sevilla, Spain*
[5]*Institut Laue-Langevin, 38042 Grenoble, France*

(Received 19 March 2019; published 26 June 2019)

The atomic spectrum of neutral promethium has been studied extensively by laser resonance ionization spectroscopy. We report on more than 1000 atomic transitions in the blue and near infrared spectral ranges, most of them between high excited energy levels. As Rydberg convergences could not be assigned unambiguously in the dense spectrum at high excitation energies, the first ionization potential (IP) was determined via field ionization of weakly bound states within a static electric field. By applying the saddle-point model, a value of $\mathrm{IP}_{(\mathrm{Pm})} = 45\,020.8(3)\ \mathrm{cm}^{-1}$ [5.58188(4) eV] was derived, which confirms previous expectations of 45 027(80) and 44 985(140) cm^{-1}, which were obtained indirectly from lanthanide IP systematics.

DOI: 10.1103/PhysRevA.99.062513

I. INTRODUCTION

The year 2019 has been declared the International Year of the Periodic Table of Chemical Elements for the 150th anniversary of Mendeleev's discovery, which today comprises 118 elements. While most stable species are studied thoroughly, for a number of elements, which either have no stable isotopes or are produced only artificially, still today fundamental atomic properties have not been determined with satisfying precision or are entirely missing. These deficits also include the ionization potential (IP), i.e., the energy required to remove one electron from the neutral atom. In this sense we aim to shed light on the promethium case (Pm, $Z = 61$), which is the only exclusively radioactive lanthanide element. The longest-lived isotope of this element is ^{145}Pm with a 17.7-yr half-life; however, the more commonly used isotope in the few practical applications of this element is ^{147}Pm with a half-life of 2.6 yr. ^{147}Pm is used in nuclear batteries [1], e.g., for space missions and as a β source for thickness gauges [2]. ^{142}Pm ($T_{1/2} = 40.5$ s) in a so-called ^{142}Sm/^{142}Pm *in vivo* generator had been used for preclinical positron emission tomography at a Geneva hospital [3]. ^{149}Pm ($T_{1/2} = 2.2$ days) is a promising radiolanthanide for receptor-targeted radiotherapy [4] due to its emission of medium-energy β rays and only a few disturbing gamma rays. It can be produced via neutron activation in non-carrier-added form [5,6].

First spectroscopy studies of promethium were performed with milligram samples of ^{147}Pm, corresponding to an activity in the terabecquerel range. These measurements revealed numerous resonance lines in the spectra of neutral (Pm I) and singly charged (Pm II) promethium [7,8], as well as hyperfine splittings of ^{147}Pm [9]. The most comprehensive works on Pm I energy levels and transitions to date are [7,10], which also account for the major part in spectroscopic data compilations, such as [11,12]. However, one should note that only well-assigned atomic transitions from the low-lying $^6\mathrm{H}^o$ and $^6\mathrm{F}^o$ fine-structure multiplets with excitation energies of $E < 10\,000\ \mathrm{cm}^{-1}$[1] are given in literature, leaving almost the upper half of the spectrum unexplored. Moreover, the first ionization potential of Pm has never been determined experimentally. Worden *et al.* [13] and Wendt *et al.* [14] report values of 45 027(80) cm^{-1} and 44 985(140) cm^{-1}, respectively. Both of these results were obtained from a systematic interpolation of the IPs of all lanthanide elements. A direct measurement could confirm the underlying assumption of a linear trend in the IPs of lanthanide atoms above and below the half-filling of the $4f$ shell. Considering that the IP has recently been measured up to $Z = 103$ [15,16], it is even more remarkable that this fundamental property of Pm remains unknown. Figure 1 gives an overview of the present situation regarding the experimental uncertainties in the first ionization potential across the Periodic Table. With the exception of the transactinide elements, Pm marks the last gap where no experimental result is listed. Apart from the high specific radioactivity of Pm isotopes, this is a consequence of the

*dstuder@uni-mainz.de

[1]As commonly used in spectroscopy, we give energies (and IP values) in units of cm^{-1}, which can be converted to actual energy values by multiplication with hc. Here 1 cm^{-1} corresponds to 1.24×10^{-4} eV.

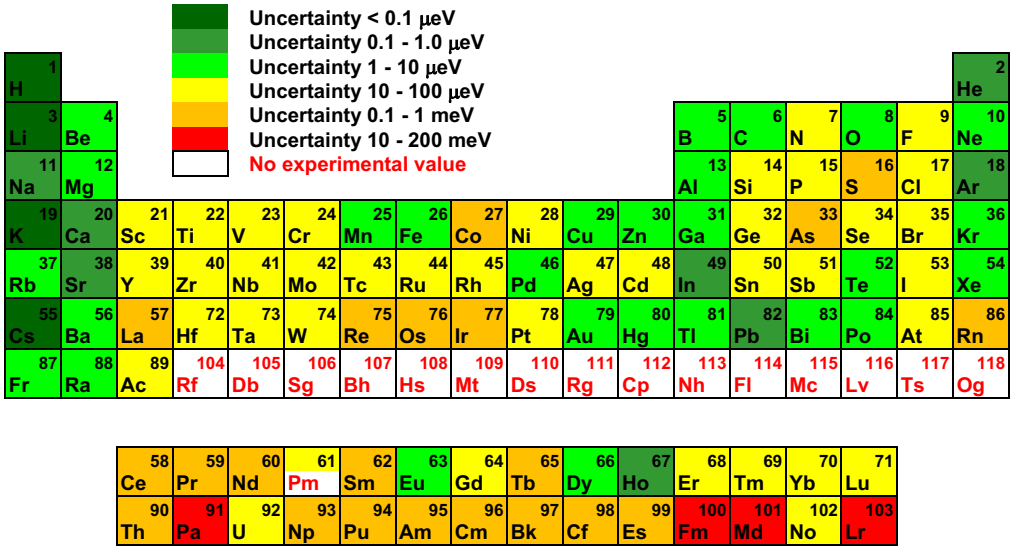

FIG. 1. Periodic Table of Chemical Elements with a color coded display of the experimental uncertainty in the value of the first ionization potential for each element. In the case of Pm the upper half of the tile corresponds to the achieved precision in this work. A complete list of all values, uncertainties, and corresponding references is given in the Supplemental Material [17].

complex atomic spectra of midshell elements, most notably in the lanthanide and actinide series with an additional open f subshell. Usually the analysis of Rydberg series allows a determination of the ionization potential with a precision in the range of 10^{-5} eV, as demonstrated for a number of radioactive elements, e.g., Tc [18], Ac [19], Po [20,21], At [22], or No [23]. However, the identification of Rydberg states becomes increasingly difficult with the occurrence of strong configuration mixing in complex atomic systems, up to a point where an unambiguous level assignment is not possible anymore. The spectrum may even exhibit chaotic behavior, as recently observed in Pa [24,25]. In this work we apply a complementary approach for the IP determination, based on dc electric field ionization of highly excited levels, which even benefits from high level density. The method was utilized by Köhler *et al.* [26] and Erdmann *et al.* [27] for the measurement of IPs of several actinide elements. We refined this approach for applicability at even lower counting statistics without a loss in precision.

II. EXPERIMENTAL SETUP

Our experiment is based on resonance ionization spectroscopy (RIS), which offers an excellent sensitivity for the investigation of minuscule sample amounts. The method relies on a stepwise photoionization process by pulsed laser radiation, providing an inherent elemental selectivity together with usually high efficiency.

For our measurements we used a sample of approximately 6×10^{13} atoms of ^{147}Pm (corresponding to 15 ng or 500 kBq). It was produced in the high-flux reactor at ILL Grenoble by neutron activation of highly ^{146}Nd-enriched neodymium. The produced ^{147}Nd decays with a half-life of 11 days to ^{147}Pm. The irradiated sample was dissolved in 7M HNO_3 and underwent chemical purification via ion exchange chromatography at PSI Villigen in order to remove the macroscopic Nd component, as described in Ref. [28]. Part of this batch was repurified from the ^{147}Sm decay product using extraction chromatography. The purified ^{147}Pm solution was shipped to Mainz University for the spectroscopy measurements. The experimental apparatus is shown in Fig. 2. The principle of RIS is implemented with a hot cavity laser ion source coupled to a compact quadrupole mass spectrometer. The Pm solution is heated and crystallized on a 3×3 mm^2 titanium carrier foil (also serving as a reduction agent), which is then folded and introduced into a tubular graphite furnace with 37 mm length and 2.2 mm inner diameter. The furnace can be heated resistively with a current of up to 100 A. At a temperature of approximately 850 °C the Pm is atomized [according to chemical equilibrium simulation (Outotec HSC Chemistry)] and irradiated by pulsed laser light. Laser-ionized species are extracted and accelerated by a set of three extraction electrodes (U_1, U_2, and U_3). The ion beam is guided through a 90° electrostatic quadrupole deflector to remove

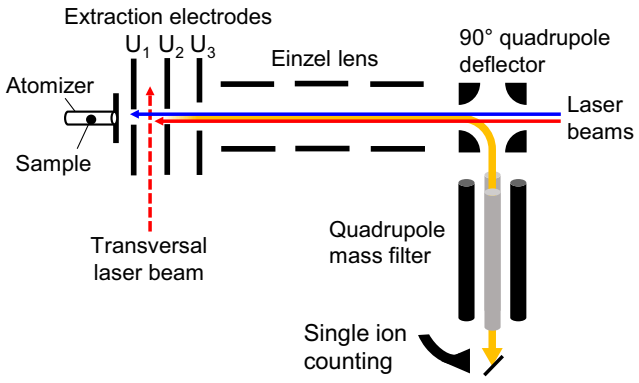

FIG. 2. Sketch of the atomic beam mass spectrometer with ion flight path (yellow) and laser beams in anticollinear (solid red and solid blue) and perpendicular crossed-beam (dashed red) geometry. The latter offers a spatially-well-defined laser-atom interaction region inside a homogeneous electric field between U_1 and U_2.

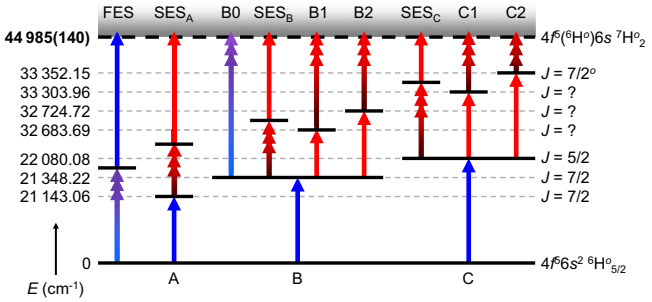

FIG. 3. Overview of investigated excitation schemes in Pm I. The respective scanning excitation step is indicated by a series of arrows. The notation for every scheme is given on top. The letters A, B, and C below define the schemes in a more general sense, referring to the respective first excitation step. The level energies for the first excited states are taken from the NIST database [11].

unspecific neutral background components and directed into an rf quadrupole mass filter. Singly charged ions of the desired mass are finally detected with a channel electron multiplier in single-ion-counting mode.

In standard operation all lasers are guided along the ion beam axis, ionizing the sample directly within the atomizer cavity. The alternative, transversal ionization geometry is discussed in Sec. IV. The laser system consists of three pulsed Ti:sapphire lasers. Each laser is pumped with 13–18 W of a 10-kHz repetition rate Nd:YAG laser at 532 nm (Photonics Industries DM100-532). Under optimal conditions the average fundamental output of each Ti:sapphire laser reaches up to 5 W, with a pulse length of 40–60 ns and a spectral linewidth of 5–8 GHz so that all Doppler classes within the hot atomic vapor are addressed. This type of laser system is also in operation at the majority of on-line radioactive ion beam facilities worldwide (for details see [29,30]). In our setup we extend the fundamental tuning range of 680–960 nm by second harmonic generation in an external beta barium borate (BBO) single-pass assembly with a conversion efficiency of approximately 10%. Wide-range scans are performed with a dedicated spectroscopy Ti:sapphire laser. It is based on a diffraction grating for frequency selection, allowing mode-hop-free scanning operation by angle tuning of the grating. This laser type has an output power of approximately 2 W and a spectral linewidth of 2–5 GHz. A similar laser design is described in [31]. Scanning of the second harmonic is performed by manual phase-matching adjustment via the BBO tilting angle, while spatial beam walk-off is compensated with a system of position sensitive detectors and motorized mirrors (TEM Aligna Beamlock 2D). The fundamental frequency of each laser is monitored with a wavelength meter during all measurements (High Finesse WS6-600).

III. BROADBAND LASER SPECTROSCOPY

Several optical excitation ladders were investigated in order to probe the spectrum of Pm I and for the development of resonance ionization schemes. An overview of all schemes is given in Fig. 3, where a series of arrows indicates the scanned excitation step. In the following these schemes are abbreviated with the notation given on top in Fig. 3. Initially, a search for first excited states (scheme FES) was performed by scanning one laser from 408 to 473 nm, along with a second laser at a fixed wavelength for nonresonant ionization from excited states. The spectrum contains 196 lines. In an independent scan with a sample of natural Sm we could identify 43 of those lines as parasitic resonances from the isobaric ^{147}Sm daughter nuclide of ^{147}Pm, which cannot be separated in our mass filter. Most of the recorded Pm lines can be found in [10]. Our data show a systematic deviation of $\Delta\tilde{\nu}_{\mathrm{Pm}} = (-0.12)_{\mathrm{sys}}(4)_{\mathrm{stat}}$ cm^{-1} from Pm literature values (the statistical error is inferred from the standard deviation). In the case of the observed Sm lines this deviation is $\Delta\tilde{\nu}_{\mathrm{Sm}} = (-0.11)_{\mathrm{sys}}(4)_{\mathrm{stat}}$ cm^{-1} when comparing our results to energies given in the NIST database [11]. This systematic shift is well understood and arises from an imperfect synchronization in the data acquisition process, depending on the laser scan speed. In independent scans of the ground-state transitions in schemes B and C we could perfectly reproduce the literature values. Therefore, a correction of the shifts mentioned above was applied to the recorded data. In the Supplemental Material [17] we list the 32 previously unknown transitions. We refrain from giving associated energy levels in this case, as we cannot clearly determine the lower level energy. This is due to a thermal population of low-energy states, thus observed lines are not necessarily ground-state transitions. In fact, when comparing our spectrum with literature data, we find that the whole ^{6}H^o multiplet of altogether six levels with $5/2 \leqslant J \leqslant 15/2$ is considerably populated in the hot atomizer. At an average operating temperature of 1200 °C, the relative $^6\mathrm{H}^o_{5/2}$ ground state population is at approximately 55%. However, one should note that this state maintains leading percentage in the ensemble even at high temperatures of 2000 °C, making it the initial state of choice for efficient photoionization. As first excited states we chose the three odd-parity levels at 21 143.06, 21 348.22, and 22 080.08 cm^{-1} for further investigation, because there are strong ground-state transitions leading to these levels. Moreover, these transitions fulfill the condition $2\tilde{\nu} <$ IP, preventing a one-color, two-photon ionization process which would induce background in further spectroscopy measurements.

Second excitation steps (schemes SES$_A$, SES$_B$, and SES$_C$) were measured in the same manner, i.e., with the first excitation step fixed on the respective resonance and with the addition of a third, nonresonant step. We recorded 157 lines and 126 associated even-parity energy levels. Possible values for the total angular momentum are constrained by the selection rule $\Delta J = 0, \pm 1$ for dipole transitions and may be further restricted whenever a state is visible in more than one excitation scheme. In the case of the excited state at 33 352.15 cm^{-1} the total angular momentum was determined as $J = 7/2$ by a measurement of the hyperfine structure of the 22 080.08 cm^{-1} $\rightarrow$ 33 352.15 cm^{-1} transition. Details on these measurements are beyond the scope of the present work.

Some first and second step transitions were also analyzed with respect to their saturation behavior. Figure 4 shows the laser power influence on the line shape and the ion signal in excitation scheme C2. In the region of strong saturation the ion signal is almost independent of the laser power and the line profile is significantly broadened. The saturation power P_{sat} is defined as the laser power where half of the

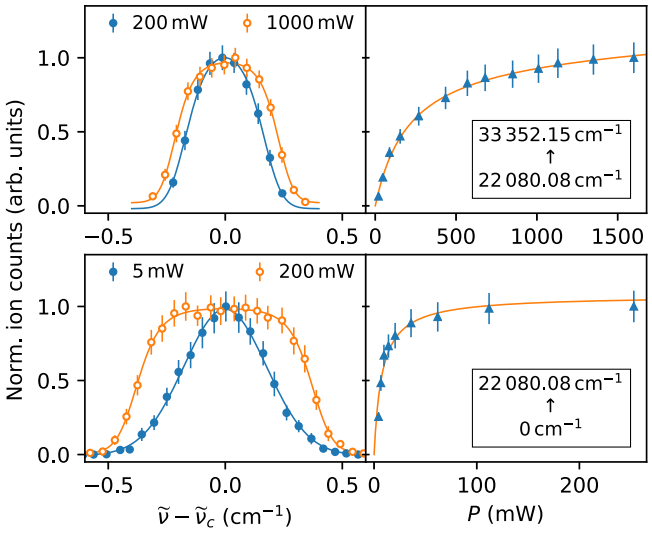

FIG. 4. Shown on the left are line profiles of the first step (bottom) and second step (top) transitions in excitation scheme C2 for different laser powers. Ion counts are normalized in order to emphasize the saturation broadening. Shown on the right is the laser power dependence of the ion signal.

maximum ion signal is reached. The saturation curve fit for the determination of P_{sat} and the broadened line shape are discussed in detail in [32]. All saturation power measurements are summarized in Table I. For reasons of time, only a limited number of transitions could be investigated; however, it is clear that all these transitions can be easily saturated with the available laser power, which is favorable with regard to the ionization efficiency.

Finally, ionizing transitions were measured in the excitation schemes B0, B1, B2, C1, and C2. The high level density is similar in all spectra and only slightly varies with the signal-to-background ratio in the different scans. A sample spectrum from excitation scheme C2 is shown in Fig. 5, containing 342 lines in a range of approximately 800 cm^{-1}. An increase in the overall ion signal can be observed in the regions of the expected IP [13,14], which suggests that the linear trend in lanthanide IPs is indeed accurate. However, a more precise IP value may not be readily determined from these spectra. The nonresonant photoionization threshold is obscured due to the high level density and Rydberg states converging to the $^7\text{H}_3^o$ ionic ground state may not be assigned unambiguously. Low-lying excited states in Pm II from the NIST database [11] were also considered as Rydberg-series limits, most importantly the $^7\text{H}_3^o$ state at 446.45 cm^{-1}, representing the state in Pm II with the lowest excitation energy. In this case too, no clear assignment could be made, rendering the method of Rydberg convergences inapplicable. On the other hand, many strong autoionizing transitions can be observed, which may serve as final excitation steps for efficient photoionization of Pm, e.g., for high-resolution spectroscopy on the nuclear structure in the Pm isotopic chain.

TABLE I. Saturation powers P_{sat} for several investigated transitions with lower energy level E_l and upper level E_u.

Scheme	E_l (cm^{-1})	E_u (cm^{-1})	P_{sat} (mW)
A	0	21 143.06	3(1)
B	0	21 348.22	10(5)
C	0	22 080.08	7(4)
B1	21 348.22	32 683.69	140(50)
C2	22 080.08	33 352.15	200(40)

All recorded transitions and energy levels are listed in the Supplemental Material [17]. We included a data table for each excitation scheme, where all lines are listed by wavelength in descending order. The uncertainties are stated in the table captions. The above-mentioned systematic deviation in the measured ground-state transitions was eliminated in the spectra of the second excitation steps by performing scans in both directions. For the ionizing transitions, comparatively slow scanning speeds were chosen, so the systematic effect is estimated to be well below the statistical uncertainty.

Associated energy levels for the transitions are given whenever possible. We also inferred line intensities from the ion count rate on resonance. However, these should be considered as rough guidelines, as intensities in RIS are prone to interference from all involved excitation lasers. In the schemes SES_A, SES_B, and SES_C, where we use an arbitrary-wavelength third step for ionization, this is particularly striking because the third step may be resonant to an autoionizing transition. In order to counteract this to some extent we repeated each scan in these schemes with a different ionization laser wavelength for a more reliable estimation of the transition intensity. In the data tables we state the mean value of both intensities. The second part of the Supplemental Material comprises excited

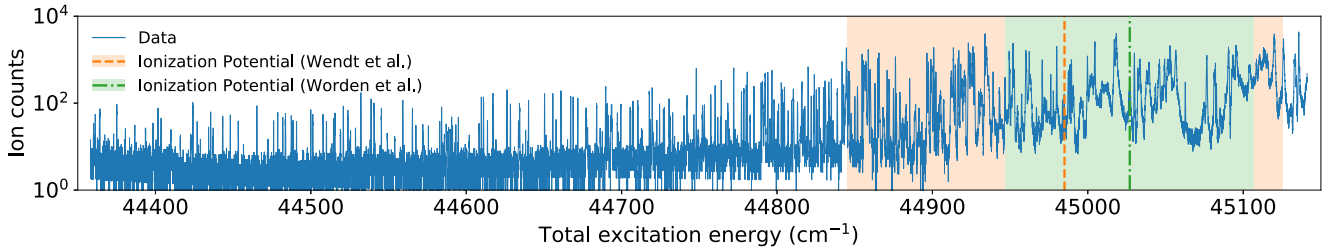

FIG. 5. Spectrum obtained from scanning the third excitation step in scheme C2. The literature values of the first ionization potential of 44 985(140) cm^{-1} [14] and 45 027(80) cm^{-1} [13] are shown by the orange dashed and green dash-dotted vertical lines, respectively. The shaded regions indicate the uncertainty. The ion counts are linearly scaled with respect to the laser power in the final excitation step (which varies between 0.5 and 1.3 W over the scan range).

levels, sorted by energy in ascending order. The level energies were derived from the recorded transitions according to the rules stated in [24]. As discussed above, possible values for the total angular momentum J are included in the data tables.

IV. IONIZATION POTENTIAL

Our approach for the IP measurement is based on a dc electric field ionization of highly excited states. The underlying concepts, namely, tunneling of the electron through the potential barrier along the electric field axis and the classical view of the so-called saddle-point model, are discussed and compared in detail by Littman *et al.* [33]. With increasing field strengths tunneling leads to an exponential increase of ionization rates of excited atoms and is most notably observed through a gradual broadening of Stark sublevels into a continuum. Saddle-point ionization, on the other hand, manifests as a sharp increase of ionization rates at excitation energies greater than the saddle-point of the effective Coulomb potential, which can be written as

$$W_s = \mathrm{IP} - 2\sqrt{\frac{Z_{\mathrm{eff}} e^3 F}{4\pi\epsilon_0}}, \tag{1}$$

with the effective charge of the atomic core Z_{eff} and the external electric field F. A precise measurement of several electric field ionization thresholds allows an extrapolation to zero-field strength, thus yielding the ionization potential. From the experimental point of view, tunneling can be neglected in this case, as ionization rates are very small at moderate electric fields and do not significantly influence the sharp saddle-point threshold. After inserting values for the constants, this law simplifies to $W_s = \mathrm{IP} - 6.12\ (\mathrm{V\,cm})^{-1/2}\sqrt{F}$ (assuming $Z_{\mathrm{eff}} = 1$ for high excited states). At this point one should note that Eq. (1) requires a modification in the form of additional terms proportional to $|m_F|F^{3/4} + \frac{3}{16}m_F^2 F$ (note that the subscript F does not denote the electric field, but the total angular momentum) for states with nonzero magnetic quantum numbers [33,34]. A simple explanation is that energy which is stored in angular momentum perpendicular to the axis of the electric field cannot contribute to the escape of the electron over the potential barrier. Consequently, states of high $|m_F|$ require significantly stronger electric fields for ionization. Gallagher *et al.* observed this effect for Rydberg states in sodium [35]. In our experiment all laser beams are polarized perpendicular the direction of the electric field, while the first excitation step laser is also polarized perpendicular with respect to the second and third excitation step lasers. We do not selectively excite certain m_F sublevels and thresholds are dominated by the $m_F = 0$ contribution.

For this experiment we operate the laser ion source slightly differently than described in Sec. II. Instead of guiding all lasers along to the ion beam axis, we cross the lasers between the two flat electrodes U_1 and U_2, as depicted in Fig. 2 by a transversal laser beam. In this geometry laser ionization no longer takes place inside the atomizer. Neutral Pm atoms effuse from the furnace and the laser-atom interaction region is spatially well defined within a static electric field generated by U_1 and U_2. The electrodes are set 1 cm apart and have central holes of 2 mm diameter. In order to suppress surface ionized

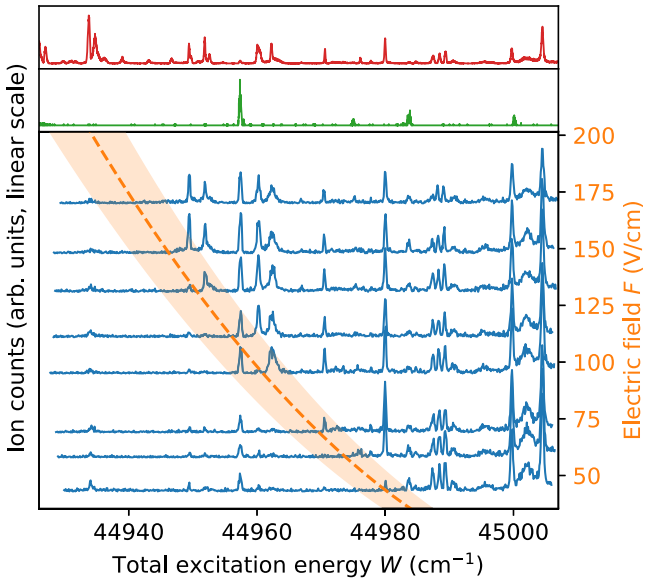

FIG. 6. Determination of ionization thresholds from scans of the final laser excitation step in scheme C2. The upper trace shows the full resonant in-source laser scan (red), the middle trace the in-source laser scan with detuned second excitation step, revealing parasitic resonanes (green); and the lower trace the laser ionization scans with external electric field (blue). The ion count offset for each scan is scaled with the corresponding electric field strength. The orange dashed line illustrates the electric field ionization threshold, with the shaded region indicating the uncertainty.

species from the furnace, U_1 is set on a positive voltage. Because saddle-point ionization is very similar to the mechanism of autoionization, states above the threshold ionize almost instantaneously and independently of the absolute field strengths (in contrast to tunneling). As a consequence, ions are generated with a relatively small spatial spread around the laser-atom interaction region, which is advantageous in terms of the ion beam energy spread. Nevertheless, as we tune the electric field, the voltages on the extraction electrode U_3 and the quadrupole deflector have to be adjusted in order to guarantee optimal transmission through the apparatus.

Initially we recorded the highly excited spectrum by scanning the wave number of the laser used in the final excitation step in the presence of a constant electric field, similar to the approach of Köhler *et al.* [26] and Erdmann *et al.* [27] in the actinide series.

Figure 6 shows the results for laser scans with excitation scheme C2 over a range of approximately 6 nm in the region slightly below the expected ionization potential. The upper trace shows the relevant region of the spectrum obtained from ionization inside the atomizer furnace (see Fig. 5), i.e., containing all resonances independent of the electric field. The spectra from transversal laser-atom interaction inside the electric field are presented in the lower trace. For the sake of clarity we added an offset proportional to the electric field strength. In comparison to the full spectrum, one can clearly observe that the spectra are subsequently cut off towards lower excitation energies. Strong resonances below the threshold (e.g., at approximately 44 930 cm^{-1}) may

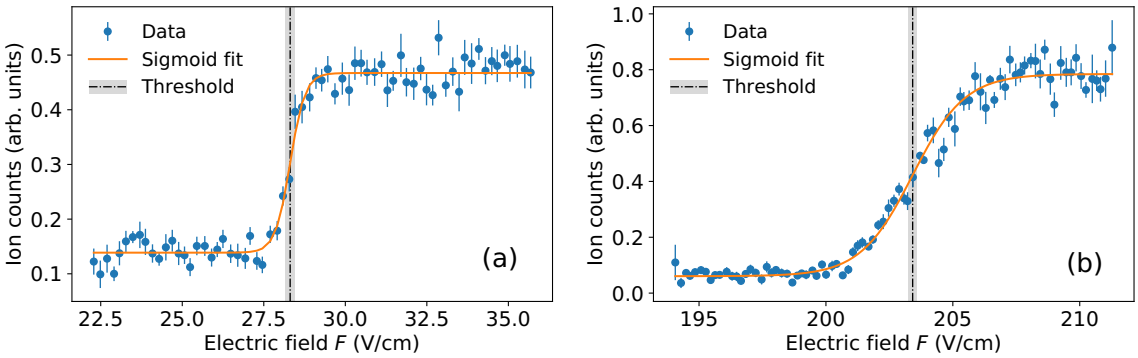

FIG. 7. Electric field ionization threshold for the energy levels at (a) 44 989.3 cm^{-1} and (b) 44 933.8 cm^{-1}. The threshold corresponds to the turning point of the sigmoid fit. The shaded region indicates the uncertainty.

remain visible, albeit strongly suppressed, due to nonresonant photoionization or collisional ionization of the excited atoms. One resonance slightly below 44 960 cm^{-1} is hardly affected by the electric field. Here the scanned third laser excites the 22 080.08 $\mathrm{cm}^{-1} \rightarrow$ 33685.3 cm^{-1} transition, followed by nonresonant ionization ($\nu_1 + \nu_3 + \nu_3$). These parasitic resonances can be identified by means of a scan with an off-resonant second step, which in this case corresponds to excitation scheme $\mathrm{SES_C}$. The relevant region of this scan is plotted in the middle trace of Fig. 6. At this energy scale, all peaks in this spectrum correspond to artifacts in scheme C2 and may be ignored with regard to ionization thresholds.

Because no clear nonresonant ionization onset can be observed, thresholds can only be constrained by the presence or absence of resonances for given electric field strengths. By comparing two data sets, we estimate the photoionization threshold as the mean value of the energy of a peak which disappeared and the next higher energy peak, with an error range spanning to either side. Depending on the local spectral level density, this leads to rather unprecise results, but nonetheless allows a first direct IP determination. With Eq. (1) we derive[2]

$$W_s^{\lambda} = 45\,020.2(6)\ \mathrm{cm}^{-1} - 6.07(6)\ (\mathrm{V\,cm})^{-1/2}\sqrt{F}.$$

The corresponding curve and error range are included in Fig. 6. The extracted IP law meets the expectation of $W_s \propto 6.12\ (\mathrm{V\,cm})^{-1/2}\sqrt{F}$; however, the achieved precision in the IP value is not satisfactory due to the strong dependence on the spectral level density. This can be improved by turning around the measurement procedure: Instead of scanning the final laser excitation step, we keep the laser on resonance and vary the electric field strength. Naturally this method does not rely on a nonresonant ionization onset and therefore counting statistics benefit from the resonant ionization process. Energy levels can be precisely assigned to electric field thresholds, determined from a sharp increase in the ion count rate. However, the improved precision comes at the cost of increased complexity in the measurement process, since knowledge of the atomic spectrum in the relevant range is a prerequisite for the applicability of this method. Moreover, the scanning procedure is not trivial as the voltages U_1 and U_2 significantly influence the ion beam transmission through the ion optics downstream. For this reason we performed reference scans on the energy level at 45 005 cm^{-1} (which is above threshold for all investigated values of F) for relevant voltage sets. Ionization thresholds were measured for 11 energy levels in the range from 44 930 to 44 990 cm^{-1} with electric fields between 25 and 205 V/cm. All data sets were corrected for the ion beam transmission loss with the corresponding reference scans. The resulting saddle-point ionization thresholds for the highest and lowest investigated level energies are presented in Figs. 7(a) and 7(b), respectively. The data can be well described with a sigmoid function

$$S(F) = A_0 + \frac{A_1}{1 + e^{-k(F-F_T)}}, \tag{2}$$

with an offset A_0, amplitude A_1 and turning point F_T. The turning point can be identified as the electric field threshold for the corresponding resonance. For $F < F_T$ the high-energy tail of the resonance is gradually ionized and for $F > F_T$ the low-energy tail, respectively. Consequently, for symmetric line shapes F_T corresponds to an ionization rate of $A_0 + A_1/2$. The obtained values F_T with the associated energies W_s are displayed in Fig. 8. A fit with Eq. (1) yields the IP law

$$W_s^{F} = 45\,020.8(3)\ \mathrm{cm}^{-1} - 6.08(1)\ (\mathrm{V\,cm})^{-1/2}\sqrt{F}. \tag{3}$$

The extracted value of $\mathrm{IP_{(Pm)}} = 45\,020.8(3)\ \mathrm{cm}^{-1}$ is more than one order of magnitude more precise than the one derived from W_s^{λ} thresholds. The line slopes in the W_s^{λ} and W_s^{F} IP laws are in perfect agreement with each other; however, at higher precision we observe a significant deviation from the expected value of $6.12\ (\mathrm{V\,cm})^{-1/2}$. Moreover, one could argue about a minor systematic trend in the fit residuals, which are presented in the insets of Fig. 8. While this does not necessarily require a modification to our fitting function (as the data are still within a 1σ range), it motivates a careful consideration of possible systematic effects in our measurements. Merkt *et al.* report similar deviations (i.e., lower than expected slopes) for field ionization of Rydberg states in argon [36], which become more significant towards lower electric field strengths. They attribute this observation to electric field inhomogeneities. For our setup we simulated electric fields in the ion source region for each set of applied voltages, using the IBSIMU C++ library [37]. The simulations yield a constant

[2]With W_s^{λ} we refer to thresholds obtained from scanning the photon energy at a fixed electric field strength, whereas W_s^{F} are fixed energies used for scans of the electric field strength.

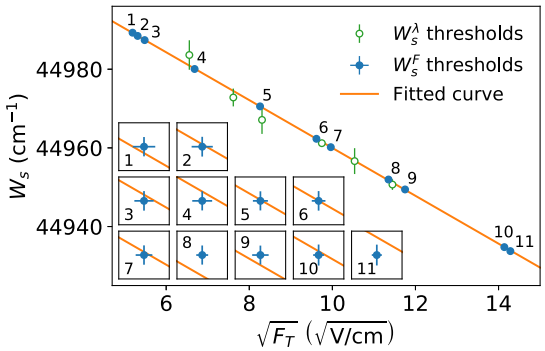

FIG. 8. Overview of all extracted ionization thresholds. The open green circles are the photoionization thresholds obtained from wavelength scans at a fixed electric field (see Fig. 6), whereas the closed blue circles are obtained from the electric field scans at a given level energy (see Fig. 7). The linear fit for the extraction of the ionization potential (solid orange line) corresponds to the latter. The insets display the deviation of the fitted curve to the data points (labeled 1–11) with a magnification factor of 27.

shift of approximately −0.3% from the nominal field, i.e., $(U_1 - U_2)$ cm^{-1}. This shift is already considered in the data presented above. A displacement of the laser-atom interaction region, e.g., through misalignment of the transversal laser, would induce an additional field offset due to minor electric field inhomogeneities. A shift towards the lower field region would explain the observed deviation. Further effects can be recognized in the threshold widths. We included the spectral widths ΔW in Table II, which were calculated from widths with respect to the electric field, using Eq. (3). The ΔW widths are relatively constant except for the two highest field thresholds. Three effects play a role in our observation. (i) The finite size of the laser-atom interaction region within the field gradient forces a lower limit on the width of field-induced thresholds. (ii) A slightly off-resonant excitation laser will cause a broadening and shift the threshold energy towards the excitation energy. (iii) The Stark effect causes a level splitting which broadens the thresholds at high fields. Possibly this effect can be observed in the two highest field thresholds. We expect the influence of the Stark effect to be somewhat limited to the laser linewidth, since in our measurement we use fixed wavelength lasers and have to consider a convolution of the approximately Gaussian spectral laser profile and the Stark manifold as excited states. From our data we do not find a maximum width limit ΔW of the thresholds, which could be associated with the laser linewidth (which is on the order of 10 GHz). We expect saturation effects from the high-power pulsed excitation to extend this beyond the laser linewidth.

TABLE II. Electric field ionization thresholds F_T for given excitation energies W_s, with corresponding spectral threshold widths ΔW.

W_s (cm^{-1})	F_T (V/cm)	ΔW (cm^{-1})
44 989.29(9)	26.94(10)	0.6(2)
44 988.46(9)	28.23(10)	0.5(2)
44 987.40(9)	30.05(9)	0.4(1)
44 980.06(9)	44.68(12)	0.5(2)
44 970.55(9)	68.22(11)	0.4(1)
44 962.31(9)	92.48(12)	0.4(1)
44 960.18(9)	99.24(15)	0.6(2)
44 951.96(9)	128.85(12)	0.5(2)
44 949.43(9)	138.06(17)	0.6(2)
44 934.77(10)	199.92(14)	0.8(2)
44 933.75(10)	204.03(13)	1.0(3)

In addition to threshold broadening, the Stark effect may also induce systematic shifts. In the case of a hydrogenic system, blueshifted levels ionize at field strengths far beyond the saddle point, as they are located on the high-energy side of the potential [38]. Although this restriction is lifted in complex atomic systems and blueshifted states may autoionize over the underlying redshifted continuum, they require higher fields than the classical saddle-point limit for ionization (for details see [36] and references therein). This results in an offset of field-induced thresholds towards higher fields strengths. Note that states which show no splitting may also be affected by a Stark shift, which is magnified by avoided crossings of strongly interacting neighboring states [38]. A conclusive analysis of these effects is hampered by the experimental resolution in our setup and the lack of knowledge about the configuration of the investigated states. However, as one aims to push towards higher precision, all the aspects mentioned above should be taken into account.

V. CONCLUSION

We have presented an extensive study in the spectrum of neutral promethium. The data cover 126 odd energy levels, 546 even energy levels, and more than 1000 transitions, which add to the knowledge about Pm atomic structure and provide a considerable contribution to its atomic spectra database. The data may give valuable input for the study of such phenomena as quantum chaos in the exceptionally dense atomic spectrum, as recently investigated in Pa [25].

We developed photoionization schemes for Pm, which pave the way for efficient production of high-purity Pm ion beams. Possible applications include, e.g., fundamental nuclear physics research on the Pm isotopic chain or isobar-free ultratrace analysis via resonance ionization mass spectrometry.

The precisely measured value of the first ionization potential serves as a valuable benchmark for *ab initio* atomic physics and quantum chemistry calculations. Our findings confirm the predictions of Worden *et al.* [13] and Wendt *et al.* [14], which were assuming a linear trend in the ionization potentials of light lanthanide elements below the half-filling of the $4f$ shell. Our measured value of $\text{IP}_{(\text{Pm})} = 45\,020.8(3)$ cm^{-1} perfectly fits into this trend (which is tantamount to the good agreement with the interpolation values). The improved precision of a factor of 270 or 470 compared to the previous estimates of Worden *et al.* and Wendt *et al.*, respectively, could be achieved with the measurement of electric field ionization thresholds, which proves to be a powerful method for the IP determination in complex spectra. The use of narrow linewidth laser systems or dedicated field ionization ion sources, allowing for stronger and more homogeneous fields, could push the precision even further. In this case systematic influences from the Stark effect must be analyzed and considered carefully.

ACKNOWLEDGMENTS

D. Studer gratefully acknowledges financial support from the EU through ENSAR2-RESIST (Grant No. 654002). R.H. acknowledges financial support from the Bundesministerium für Bildung und Bundesministerium fr Bildung und Forschung (BMBF Germany) under Grant No. 05P15UMCIA. The open access fee was covered by FILL2030, an European Union project within the European Commission's Horizon 2020 Research and Innovation Programme under Grant Agreement No. 731096.

[1] H. Flicker, J. J. Loferski, and T. S. Elleman, IEEE Trans. Electron **11**, 2 (1964).

[2] M. Kumar, J. Udhayakumar, J. Nuwad, R. Shukla, C. G. S. Pillai, A. Dash, and M. Venkatesh, Appl. Radiat. Isotopes **69**, 580 (2011).

[3] G. J. Beyer and T. J. Ruth, Nucl. Instrum. Methods Phys. Res., Sect. B **204**, 694 (2003).

[4] H. Mohsin, F. Jia, J. N. Bryan, G. Sivaguru, C. S. Cutler, A. R. Ketring, W. H. Miller, J. Simón, R. K. Frank, L. J. Theodore, D. B. Axworthy, S. S. Jurisson, and M. R. Lewis, Bioconjugate Chem. **22**, 2444 (2011).

[5] F. Rösch, Radiochimica Acta **95**, 303 (2009).

[6] H. Uusijärvi, P. Bernhardt, F. Rösch, H. R. Maecke, and E. Forsell-Aronsson, J. Nucl. Med. **47**, 807 (2006).

[7] W. F. Meggers, B. F. Scribner, and W. R. Bozman, J. Res. Natl. Bur. Stand. **46**, 85 (1951).

[8] P. Klinkenberg and F. S. Tomkins, Physica **26**, 103 (1960).

[9] J. Reader and S. P. Davis, J. Opt. Soc. Am. **53**, 431 (1963).

[10] J. Reader and S. P. Davis, J. Res. Natl. Bur. Stand. A **71A**, 587 (1967).

[11] A. Kramida and Y. Ralchenko, *NIST Atomic Spectra Database, NIST Standard Reference Database 78* (National Institute of Standards and Technology, Gaithersburg, 2018), Version 5.6.

[12] J. E. Sansonetti and W. C. Martin, J. Phys. Chem. Ref. Data **34**, 1559 (2005).

[13] E. F. Worden, R. W. Solarz, J. A. Paisner, and J. G. Conway, J. Opt. Soc. Am. **68**, 52 (1978).

[14] K. Wendt, T. Gottwald, C. Mattolat, and S. Raeder, Hyperfine Interact. **227**, 55 (2014).

[15] T. K. Sato, M. Asai, A. Borschevsky, T. Stora, N. Sato, Y. Kaneya, K. Tsukada, C. E. Düllmann, K. Eberhardt, E. Eliav *et al.*, Nature (London) **520**, 209 (2015).

[16] T. K. Sato, M. Asai, A. Borschevsky, R. Beerwerth, Y. Kaneya, H. Makii, A. Mitsukai, Y. Nagame, A. Osa, A. Toyoshima *et al.*, J. Am. Chem. Soc. **140**, 14609 (2018).

[17] See Supplemental Material at http://link.aps.org/supplemental/10.1103/PhysRevA.99.062513 for a complete list of measured transition wavelengths, level energies and uncertainties, as well as values and corresponding references for the Periodic Table in Fig. 1.

[18] C. Mattolat, T. Gottwald, S. Raeder, S. Rothe, F. Schwellnus, K. Wendt, P. Thörle-Pospiech, and N. Trautmann, Phys. Rev. A **81**, 052513 (2010).

[19] J. Roßnagel, S. Raeder, A. Hakimi, R. Ferrer, N. Trautmann, and K. Wendt, Phys. Rev. A **85**, 012525 (2012).

[20] S. Raeder, H. Heggen, A. Teigelhöfer, and J. Lassen, Spectrochim. Acta B **151**, 65 (2019).

[21] D. A. Fink, K. Blaum, V. N. Fedosseev, B. A. Marsh, R. E. Rossel, and S. Rothe, Spectrochim. Acta B **151**, 72 (2019).

[22] S. Rothe, A. N. Andreyev, S. Antalic, A. Borschevsky, L. Capponi, T. E. Cocolios, H. de Witte, E. Eliav, D. V. Fedorov, V. N. Fedosseev *et al.*, Nat. Commun. **4**, 1835 (2013).

[23] P. Chhetri, D. Ackermann, H. Backe, M. Block, B. Cheal, C. Droese, C. E. Düllmann, J. Even, R. Ferrer, F. Giacoppo *et al.*, Phys. Rev. Lett. **120**, 263003 (2018).

[24] P. Naubereit, T. Gottwald, D. Studer, and K. Wendt, Phys. Rev. A **98**, 022505 (2018).

[25] P. Naubereit, D. Studer, A. V. Viatkina, A. Buchleitner, B. Dietz, V. V. Flambaum, and K. Wendt, Phys. Rev. A **98**, 022506 (2018).

[26] S. Köhler, R. Deissenberger, K. Eberhardt, N. Erdmann, G. Herrmann, G. Huber, J. V. Kratz, M. Nunnemann, G. Passler, P. M. Rao, J. Riegel, N. Trautmann, and K. Wendt, Spectrochim. Acta B **52**, 717 (1997).

[27] N. Erdmann, M. Nunnemann, K. Eberhardt, G. Herrmann, G. Huber, S. Köhler, J. V. Kratz, G. Passler, J. R. Peterson, N. Trautmann, and A. Waldek, J. Alloys Compd. **271-273**, 837 (1998).

[28] S. Heinitz, E. A. Maugeri, D. Schumann, R. Dressler, N. Kivel, C. Guerrero, U. Köster, M. Tessler, M. Paul, and S. Halfon, Radiochim. Acta **105**, 155 (2017).

[29] S. Rothe, B. A. Marsh, C. Mattolat, V. N. Fedosseev, and K. Wendt, J. Phys.: Conf. Ser. **312**, 052020 (2011).

[30] V. Sonnenschein, I. D. Moore, H. Khan, I. Pohjalainen, and M. Reponen, Hyperfine Interact. **227**, 113 (2014).

[31] A. Teigelhöfer, P. Bricault, O. Chachkova, M. Gillner, J. Lassen, J. P. Lavoie, R. Li, J. Meißner, W. Neu, and K. D. A. Wendt, Hyperfine Interact. **196**, 161 (2010).

[32] F. Schneider, K. Chrysalidis, H. Dorrer, C. Düllmann, K. Eberhardt, R. Haas, T. Kieck, C. Mokry, P. Naubereit, S. Schmidt, and K. Wendt, Nucl. Instrum. Methods Phys. Res. Sect. B **376**, 388 (2016).

[33] M. G. Littman, M. M. Kash, and D. Kleppner, Phys. Rev. Lett. **41**, 103 (1978).

[34] W. E. Cooke and T. F. Gallagher, Phys. Rev. A **17**, 1226 (1978).

[35] T. F. Gallagher, L. M. Humphrey, W. E. Cooke, R. M. Hill, and S. A. Edelstein, Phys. Rev. A **16**, 1098 (1977).

[36] F. Merkt, A. Osterwalder, R. Seiler, R. Signorell, H. Palm, H. Schmutz, and R. Gunzinger, J. Phys. B **31**, 1705 (1998).

[37] T. Kalvas, O. Tarvainen, T. Ropponen, O. Steczkiewicz, J. Arje, and H. Clark, Rev. Sci. Instrum. **81**, 02B703 (2010).

[38] T. F. Gallagher, Rep. Prog. Phys. **51**, 143 (1988).

Chapter 4

High-resolution spectroscopy as a probe for nuclear structure

The evolution of nuclear ground state properties across the chart of nuclei is of high relevance for a basic understanding of nuclear structure and as a test for theoretical models. Several observables, i.e. nuclear spin, electromagnetic moments and mean square charge radii, are directly or indirectly linked to the ground state configuration, size and deformation of the nucleus and thus offer valuable information on its many-body character, where simple shell model considerations fail. The experimental access to these properties through their interaction with the atomic shell is discussed in Sec. 4.4. As start, basics of the shell model and nuclear deformation are established and linked to observable nuclear properties.

4.1 The shell model

The discovery of *magic numbers*, representing proton- or neutron numbers at which nuclei of particularly high natural abundance or long half-life occur, motivated the development of a theoretical model capable of explaining this observation. Introducing a quantum mechanical treatment of the atomic nucleus, it was found that magic numbers correspond to closed shells in the arrangement of nucleons, somewhat similar to a noble gas configuration of the electronic shell in an atom [139, 140]. In analogy to Sec. 3.1, the Schrödinger equation acts as starting point for the calculation of energy levels. For the atomic nucleus, a common choice of the binding potential is

$$V_{\mathrm{WS}}(r) = -V_0 \left[1 + e^{(r-R)/a}\right]^{-1}, \tag{4.1}$$

which is referred to as Woods-Saxon potential, with $V_0 \approx 40\,\mathrm{MeV}$ as the depth of the potential well, $R \approx 1.2\,\mathrm{fm} \cdot A^{1/3}$ as the nuclear radius and $a \approx 0.5\,\mathrm{fm}$ as

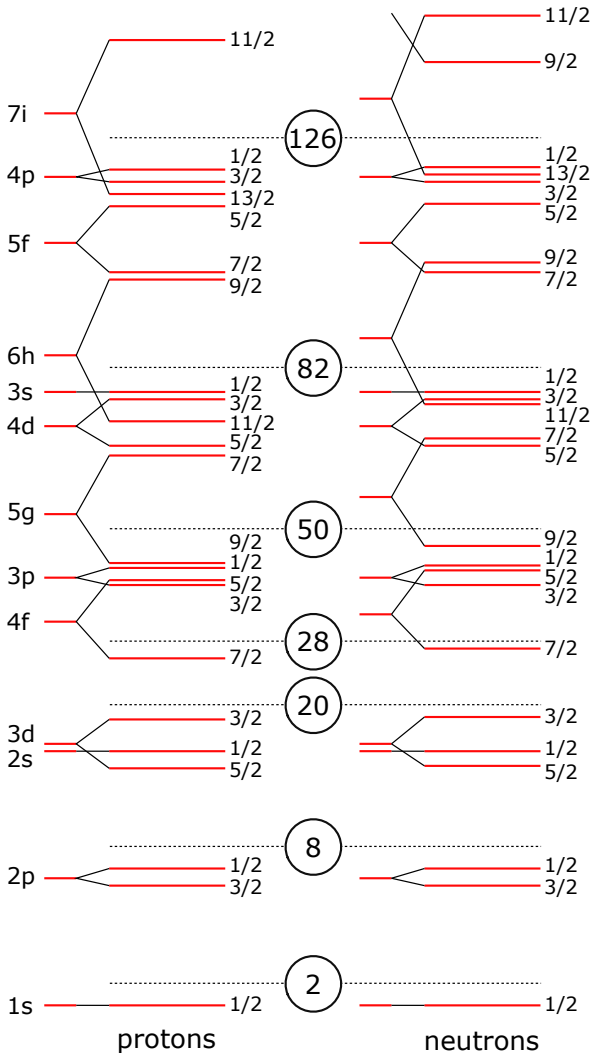

Figure 4.1.: Nuclear energy level diagram of the single particle shell model for protons (left) and neutrons (right). The left side of each column shows the level structure without consideration of spin-orbit coupling (nl quantum numbers), while the right side includes the spin-orbit term (j quantum numbers). Magic numbers are indicated by dotted lines. Figure adapted from [143].

the surface diffuseness parameter [141, 142]. Naturally, for protons the Coulomb repulsion has to be considered, too, and correspondingly different shell structures are found for protons and neutrons. As solution for single valence nucleons one obtains the energy level structure depicted on the left side in the two columns of Fig. 4.1. Additionally, nucleons possess spin of $|\boldsymbol{s}| = 1/2$ which couples to the orbital angular momentum $\boldsymbol{l}$, introducing the total angular momentum $\boldsymbol{j} = \boldsymbol{l} + \boldsymbol{s}$. Similar to atomic fine structure, the relative orientation of $\boldsymbol{l}$ and $\boldsymbol{s}$ leads to a level splitting, as depicted on the right side of each column in Fig. 4.1. However, unlike the atomic fine structure splitting, which is rather small in most cases, nucleon spin-orbit coupling is a major contribution to the level structure and, at least

partly, rearranges the level order. The maximum population of each level is $2j+1$ nucleons. As a result, magic numbers are given by the large gaps between excited levels, indicated by the dotted lines in Fig. 4.1. The total angular momentum J of the nucleus results from jj-coupling. Considering the fact that nucleons form pairs of opposite spin orientation, J and the parity π can have the values

$$J = |j_p - j_n|, |j_p - j_n| + 1, ..., j_p + j_n \quad \text{and} \quad \pi = (-1)^{l_p + l_n}, \tag{4.2}$$

where the subscripts p and n denote the single proton and neutron quantum numbers. In spherical nuclei J directly corresponds to the nuclear spin I. For even-even nuclei the spin is always equal to zero.

4.2 Nuclear moments

4.2.1 Magnetic dipole

The spin of the charged nucleus induces a magnetic dipole moment

$$\mu_I = g_I \frac{e\hbar}{2m_p} I = g_I \mu_N I, \tag{4.3}$$

where g_I is the Landé g-factor, m_p the proton mass and $\mu_N = e\hbar/2m_p$ the nuclear magneton [144]. From a simplistic point of view one can directly derive the nuclear magnetic moments for even-odd or odd-even nuclei, i.e. featuring an unpaired single proton or neutron, respectively, from the considerations made so far. Depending on the spin orientation of the unpaired nucleon, there are only two possible values of μ_I. In units of the nuclear magneton, they can be calculated with

$$\mu_I^S = I \left(g_l \pm \frac{g_s - g_l}{2l+1} \right) \quad \text{for} \quad I = j = l \pm \frac{1}{2}, \tag{4.4}$$

where g_l and g_s are the orbital and spin g-factors of the unpaired nucleon, given by

$$\begin{aligned} g_s^p &= +5.586, \quad g_l^p = 1 \quad \text{for protons} \\ \text{and} \quad g_s^n &= -3.826, \quad g_l^n = 0 \quad \text{for neutrons} \end{aligned} \tag{4.5}$$

[144]. These so-called *Schmidt moments* are rather accurate for "close-to magic nuclei", which exhibit a spherical shape. Magnetic moments of mid-shell nuclei, however, might differ significantly from the Schmidt moments. They may even exhibit a spin which differs from the shell model prediction. This behavior arises from the effects introduced by nuclear deformations. In sufficiently strong deformed nuclei, an axially symmetric harmonic oscillator can be used as nuclear

potential, where the deformation parameter

$$\epsilon = \frac{\omega_\perp - \omega_z}{\omega_0} \tag{4.6}$$

is defined via the oscillator frequency ω_0 of the corresponding spherical potential and the frequencies ω_z and $\omega_\perp$ parallel and perpendicular to the symmetry axis, respectively [145]. Note that sometimes in literature, ϵ is referred to as δ. For large deformations J, L, S are no good quantum numbers anymore, but rather their projections on the symmetry axis Ω, Λ, Σ, with $\Omega = \Lambda + \Sigma$ [145]. Additionally, the principal quantum number is defined as the sum $N = n_z + n_\perp$ of the oscillator quantum numbers parallel and perpendicular to the symmetry axis. A common notation for such states is $\Omega[Nn_z\Sigma]$, often referred to as asymptotic quantum numbers or Nilsson quantum numbers [145]. The energetic evolution of single particle shell model states with increasing deformation is shown in the so-called Nilsson diagram Fig. 4.2. Each shell model states splits into $j + 1/2$ levels, which exhibit a two-fold degeneracy for the different signs of Ω [142]. Generally the nuclear spin of deformed nuclei is given by the sum of total angular momentum and a collective rotational angular momentum $\boldsymbol{R}$. However, in the special case of the nuclear ground state, which is exclusively considered here, $I = \Omega$ is expected [144]. Naturally, the determination of magnetic moments is less conclusive than in the simple spherical case. The vicinity of several levels of one parity may lead to level admixtures, which strongly influence μ_I [144]. Nonetheless, experimental values close to the Schmidt moment may give hints on the ground state configuration of the nucleus and thus the deformation parameter. Figure 6 in Publication V shows the trend of $g_I = \mu_I / I$ for several Pm nuclei. As deformation increases with the neutron number, the nuclear ground state changes from a $d_{5/2}$ to Nilsson states belonging to the $g_{7/2}$ shell model state.

4.2.2 Electric quadrupole

Considering a deformed nucleus as an ellipsoid with a charge density $\rho(\boldsymbol{r})$, the quadrupole moment Q is defined as

$$Q = \int d^3r \rho(\boldsymbol{r})(3z^2 - r^2), \tag{4.7}$$

where z is the symmetry axis [147]. Neglecting higher order terms in ϵ (octupole ϵ_3, hexadecapole ϵ_4), the quadrupole moment can be related to the deformation parameter ϵ via

$$Q = \frac{4}{5} Z R_0^2 \epsilon, \tag{4.8}$$

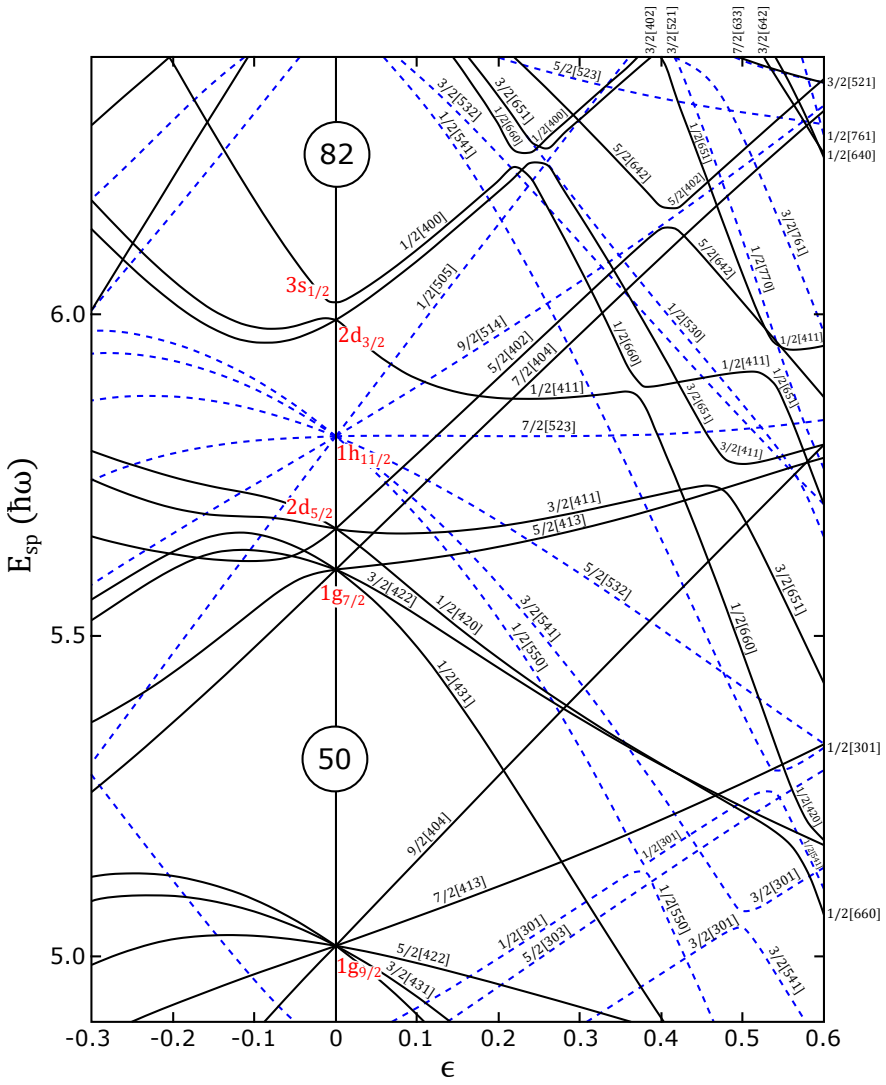

Figure 4.2.: Nilsson diagram for $40 < Z < 82$. The single particle energy is plotted as function of the deformation parameter ϵ. Solid black lines mark even parity bands and dashed blue lines odd parity bands. The respective single particle shell model configuration is given in red at the $\epsilon = 0$ line, where also the magic numbers at $Z = 50$ and $Z = 82$ are indicated in circles. Nilsson quantum numbers are given as $\Omega[Nn_z\Sigma]$. Figure adapted from [146].

with $R_0 \approx 1.2\,\text{fm}$ [142, 147]. From the definitions of Eq. 4.6 and Eq. 4.7 one can conclude that $\epsilon > 0$ (or $Q > 0$) corresponds to prolate deformation, i.e. elongation along the symmetry axis, and $\epsilon < 0$ (or $Q < 0$) to oblate deformation, i.e. compression along the symmetry axis. In this sense Q is a more direct probe for nuclear deformation than the quantity μ_I. However, in a measurement the quadrupole moment manifests as the component along the I-axis Q_s, rather than the *intrinsic quadrupole moment* Q along the symmetry axis. Q_s is referred to as *spectroscopic*

quadrupole moment and can be related to Q with

$$Q_s = Q\frac{3\Omega^2 - I(I+1)}{(I+1)(2I+3)} \overset{I=\Omega}{=} Q\frac{I}{I+1}\frac{2I-1}{2I+3} \tag{4.9}$$

[144]. Note that according to Eq. 4.9, $Q_s(I = 1/2) = 0$ even for $Q \neq 0$.

4.3 Mean square charge radius

A property which is directly linked to the size and deformation of the nucleus is the nuclear charge radius. Although it is only sensitive to the radius of the proton distribution, which may differ from the neutron distribution (in the order of 0.1 to 0.2 fm [148]), it is a sensitive probe for relative nuclear sizes and shapes. In the following, only the charge radius is considered and differences to the nuclear matter radius are neglected. In the liquid drop model, the nuclear radius is described by $R_{\text{sph}} = R_0 A^{1/3}$, with $R_0 = 1.2\,\text{fm}$ and A the number of nucleons [149]. A more commonly used parameter is the mean square charge radius

$$\langle r^2\rangle_{\text{sph}} = \frac{\int \rho(r) r^2 \,\mathrm{d}^3 r}{\int \rho(r)\,\mathrm{d}^3 r} \approx \frac{3}{5} R_0 A^{2/3}, \tag{4.10}$$

where the charge density $\rho(r)$ is of the form of Eq. 4.1 [149]. Considering deformed nuclei, the angle-dependent radius can be expressed as

$$R_{\text{def}}(\theta) = R_0(1 + \beta_2 Y_{20}(\theta))/N, \tag{4.11}$$

where β_2, as coefficient of the quadrupolar spherical harmonic Y_{20}, describes the deformation and N acts as a normalization parameter [150]. Similar as in the previous section, higher order deformations and associated spherical harmonics are neglected. The corresponding mean square charge radius is given by

$$\langle r^2\rangle_{\text{def}} = \langle r^2\rangle_{\text{sph}} \left(1 + \frac{5}{4\pi}\langle\beta_2\rangle\right) \tag{4.12}$$

[150]. A link between β_2 and the previously introduced deformation ϵ, as well as the electric quadrupole moment Q, can be established with

$$\epsilon \approx \frac{3}{2}\sqrt{\frac{5}{4\pi}}\beta_2 \tag{4.13}$$

$$Q = \frac{3ZR_0^2}{\sqrt{5\pi}}\beta_2 \tag{4.14}$$

[142, 151]. From Eqs. 4.10 and 4.12 it becomes obvious that a measurement of changes in mean square charge radii $\delta\langle r^2\rangle^{A,A'} = \langle r^2\rangle^{A'} - \langle r^2\rangle^{A}$ can be used to track

nuclear deformation along a series of isotopes. Discontinuities in $\delta\langle r^2\rangle^{A,A'}$ are considered as indicators for nuclear sub-shell closures [152]. A phenomenon which is sometimes observed in $\delta\langle r^2\rangle^{A,A'}$ along an isotopic chain is the so-called odd-even staggering (OES). With few exceptions odd neutron number (odd-N) isotopes exhibit slightly smaller radii relative to their even-N neighbors. To some extent this effect has been understood and related to pairing effects, resulting in less pronounced deformation for odd-N nuclei and correspondingly smaller $\langle r^2\rangle$ [153–155]. Just in some exceptional cases an inverted OES is observed, most prominently reported for neutron deficient Hg isotopes, where it is linked to the coexistence of prolate and oblate deformed ground states (see e.g. [156]). Inverted OES has also been interpreted as an indicator for octupole deformation [153, 157, 158]. Quantitatively, OES can be described with the staggering parameter

$$\gamma_A = \frac{\delta\langle r^2\rangle^{A-1,A}}{\delta\langle r^2\rangle^{A-1,A+1}} \tag{4.15}$$

where A is the mass number of an odd-N isotope [149]. For no staggering, $\gamma_A = 1$, for normal OES $\gamma_A < 1$ and for inverted OES $\gamma_A > 1$.

4.4 Probing nuclear structure by laser spectroscopy

In the previous section the nuclear spin I, the magnetic dipole moment μ_I, the electric quadrupole moment Q and changes in mean square charge radii $\delta\langle r^2\rangle$ were introduced as fundamental nuclear properties. Together they form a conclusive picture of the evolution of nuclear ground states and their deformation across the chart of nuclei. All these parameters can be probed by laser spectroscopy through the interactions of the nucleus with the surrounding electronic shell, namely the hyperfine structure (HFS) and the isotope shift (IS). Since laser spectroscopic experiments usually focus on one or more atomic lines of a given chemical element, nuclear properties are often studied for extended isotopic chains. The contribution of HFS and IS to the atomic transition frequency are typically in the order of 0.1 to 10 GHz $\widehat{=}$ 10^{-5} to 10^{-7} eV, i.e. much smaller than FS splittings, which are in the order of 10^{-1} eV in the medium mass range of $Z \approx 50$ (cf. the NIST database [109]). Correspondingly, the experimental resolution has to be in the order of 10^7 and beyond for a conclusive analysis of these effects. Radioactive species far off the valley of β-stability are of highest interest as end points of isotopic chains, often exhibiting extreme ground state properties. Such experiments are particularly challenging, since high precision has to be combined with highest sensitivity.

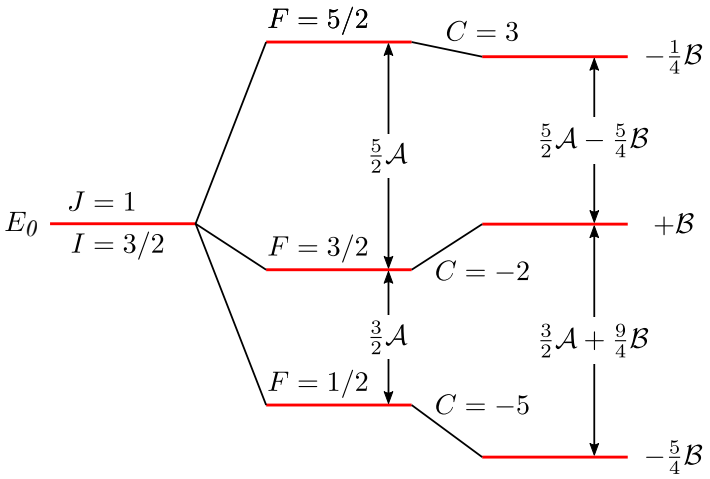

Figure 4.3.: Exemplary hyperfine level scheme for $J = 1$, $I = 3/2$ and $\mathcal{B} < 0$. Figure adapted from [144].

4.4.1 Hyperfine structure

Hyperfine structure arises from coupling of the total angular momentum of the atomic shell $\boldsymbol{J}$ with the nuclear spin $\boldsymbol{I}$. The resulting angular momentum

$$\boldsymbol{F} = \boldsymbol{I} + \boldsymbol{J} \tag{4.16}$$

and its projection on the z-axis F are introduced. The magnetic field induced by the electronic shell at the location of the nucleus $\overline{H(0)}$ interacts with the nuclear magnetic dipole moment μ_I and leads to a splitting of spectral lines into multiplets. Depending on the orientation of $\boldsymbol{I}$ and $\boldsymbol{J}$, this splitting is given by

$$\Delta E_\mu = \frac{\mathcal{A}C}{2} \quad \text{with} \quad C = F(F+1) - I(I+1) - J(J+1), \tag{4.17}$$

where $\mathcal{A} = \mu_I \overline{H(0)}/IJ$ is referred to as magnetic hyperfine coupling constant or simply $\mathcal{A}$-factor [144, 159]. Similarly, the electric field gradient $\overline{\phi_{zz}(0)} = \langle \partial^2\phi(0)/\partial z^2 \rangle$ interacts with the nuclear electric quadrupole moment, introducing an energy shift of

$$\Delta E_Q = \frac{\mathcal{B}}{4} \frac{3/2C(C+1) - 2I(I+1)J(J+1)}{I(2I-1)J(2J-1)}, \tag{4.18}$$

where $\mathcal{B} = eQ_s\overline{\phi_{zz}(0)}$ is the electric hyperfine coupling constant or $\mathcal{B}$-factor [144, 159]. Neglecting higher orders, the total hyperfine splitting is given by $\Delta E_{\mathrm{HFS}} = \Delta E_\mu + \Delta E_Q$. An example energy level scheme is shown in Fig. 4.3, where E_0 corresponds to the unperturbed atomic level energy. As mentioned above, the energy difference between two levels F and F' is often in the order of GHz and transitions between sublevels of an atomic state can be driven by microwave ra-

diation. In order to use laser light, one has to consider an atomic transition from a state $|l\rangle \rightarrow |u\rangle$, more specifically between the respective F and F' levels. The hyperfine pattern is given by the sum over

$$E_{F\rightarrow F'} = E_0 + \Delta E_{\mathrm{HFS}}(\mathcal{A}_u, \mathcal{B}_u, F', I, J_u) - \Delta E_{\mathrm{HFS}}(\mathcal{A}_l, \mathcal{B}_l, F, I, J_l) \tag{4.19}$$

for all allowed transitions $F \rightarrow F'$, where the subscripts denote parameters of the $|l\rangle$ and $|u\rangle$ states, respectively. The selection rule for hyperfine transitions is $\Delta F = 0, \pm 1$ with $F = 0 \nrightarrow F' = 0$ [144]. Line intensities follow the coupling of angular momenta, which can be expressed as

$$I_{F\rightarrow F'} \propto (2F+1)(2F'+1) \begin{Bmatrix} J_u & F' & I \\ F & J & 1 \end{Bmatrix}^2, \tag{4.20}$$

where the curly bracket denotes the Wigner $6j$-symbol [159, 160]. As a rule of thumb, for transitions between high J-states, the components with $\Delta F = \Delta J$ have the highest intensity [144]. However, one should note that in RIS the intensities predicted from Eq. 4.20 cannot always be reproduced for several reasons. This includes limited spectral overlap of the secondary laser for further excitation or ionization with the excited state HFS, resulting in reduced intensities for transitions addressing the outermost F' states, as well as saturation effects which promote the relative intensities of weak transitions, or simply depletion of the sample over the duration of the measurement.

From Eqs. 4.17 and 4.18, it is obvious that HFS patterns contain a great deal of information on the atomic nucleus, i.e. the spin I and, through the $\mathcal{A}$ and $\mathcal{B}$ factors, the magnetic dipole and electric quadrupole moment, respectively. With known total angular momenta of the involved atomic transitions, I can simply be derived from the number of observed peaks. Although this method strictly speaking only allows for an extraction of a lower limit for I, since peaks may be obscured or unresolved, it usually gives conclusive results since fits only converge well for a correct spin assignment. With this, $\mathcal{A}$ and $\mathcal{B}$ are the only parameters describing the relative energetic positions of all observed resonances and can thus be extracted with high precision. When fitting HFS patterns, it is convenient to use the SATLAS python package [121], where Eq. 4.19 and Eq. 4.20, as well as the constraints through selection rules, are implemented. The intensities are not necessarily fixed to Eq. 4.20, however, this choice usually provides good starting parameters. In Publication V fits were performed with the help of this tool, using Voigt line profiles to account for residual Doppler broadening in the perpendicular laser-atom interaction geometry (see Sec. 3.3). Deriving μ_I and Q_s from the $\mathcal{A}$ and $\mathcal{B}$ fit parameters requires knowledge of the magnetic field $\overline{H(0)}$ and the electric field gradient $\overline{\phi_{zz}(0)}$ at the location of the nucleus, which can be extracted

from sophisticated theoretical calculations. In case nuclear moments are already known for a reference isotope, $\mathcal{A}$ and $\mathcal{B}$ ratios can be used for the determination of previously unknown moments with

$$\mu_I = \frac{\mathcal{A}}{\mathcal{A}_{\text{ref}}} \frac{I}{I_{\text{ref}}} \mu_{I,\text{ref}} \tag{4.21}$$

$$Q_s = \frac{\mathcal{B}}{\mathcal{B}_{\text{ref}}} Q_{s,\text{ref}} \tag{4.22}$$

[7]. Note that Eq. 4.21 is only accurate to a limited precision due to omission of the so-called hyperfine anomaly. It arises from the Breit-Rosenthal-Crawford-Schawlow correction ϵ_{BR} for the diffuse nuclear charge distribution, and the Bohr-Weisskopf effect ϵ_{BW} for magnetism distribution over the nuclear sphere, resulting in a modification of the form $\mathcal{A} = \mathcal{A}_{\text{point}}(1+\epsilon_{BR})(1+\epsilon_{BW})$. The hyperfine anomaly ${}^{A}\Delta^{A'}$ between two isotopes is specific to an atomic transition and can be expressed as

$$\frac{\mathcal{A}^A}{\mathcal{A}^{A'}} = \frac{g_I^A}{g_I^{A'}}(1 + {}^{A}\Delta^{A'}). \tag{4.23}$$

Usually it is in the order of 10^{-3} to 10^{-4} and requires very high precision to be observed or conclusively analyzed [159, 161]. A table of measured hyperfine anomalies is given in [161].

4.4.2 Isotope shift

Istopes are distinguished by the number of neutrons within the nucleus, which is accompanied by a change of nuclear mass and volume. Both of these small changes lead to a shift in atomic transition frequencies $\delta\nu$, which is in the order of the HFS. The effects of mass shift $\delta\nu_M^{A,A'}$ and field (or volume) shift $\delta\nu_F^{A,A'}$ between two isotopes with mass numbers A and A' are comprised under the term isotope shift (IS), which is defined as

$$\delta\nu^{A,A'} = \nu^A - \nu^{A'} = \delta\nu_M^{A,A'} + \delta\nu_F^{A,A'} \tag{4.24}$$

$$= K\frac{1}{\mu^{A,A'}} + F\delta\langle r^2\rangle^{A,A'}, \tag{4.25}$$

where $\mu^{A,A'}$ is the reduced mass and K and F the mass and field shift constant, respectively [150, 159]. For isotopes exhibiting HFS, the transition frequency ν^A is given by the center of gravity of all transitions $F \rightarrow F'$. From a measurement of $\delta\nu^{A,A'}$ for a series of isotopes, changes in mean square charge radii $\delta\langle r^2\rangle^{A,A'}$ can be determined with Eq. 4.25. Obviously, this requires knowledge of the mass and field shift constants. A discussion on the separation of mass and field shift using systematic trends in neighboring elements, as well as the so-called King-plot

analysis is subject of Publication V. Therefore, a detailed discussion is not given here to avoid repetition.

4.5 Publication IV: On the reliability of wavelength meters - Part 1: Consequences for medium- to high-resolution laser spectroscopy

The following manuscript was published as a regular article in Applied Physics B: Lasers and Optics **126**, 85 (2020) DOI 10.1007/s00340-020-07425-4. The presented work focuses on the characterization of the performance of wavelength meters, specifically in applications of high-resolution laser spectroscopy. Shortcomings in long-term stability of wavelength meters are a known issue and can be linked to temperature or pressure fluctuations in the laboratory. Usually such drifts remain within the specified accuracy of the device, however, in relative frequency measurements, where one aims for higher precision this becomes a limiting factor. This limitation was already noticed in the isotope shift measurements in Publication I, where the uncertainty in $\delta\nu^{A,A'}$ is ultimately dominated by the absolute accuracy of the wavelength meter, despite the data being of higher quality. Consequently, prior to data taking for Publication V, the laser setup was extended by a Rb SAS setup as absolute wavelength reference. In combination with relative frequency measurement using a SFPI, the setup allowed for frequent calibration and characterization of the used WSU-30 wavelength meter (see Sec: 2.2). The author presented these results on the EMIS conference in 2018 at CERN, where other laboratories reported similar issues. Finally, the submission of a joint publication with the laboratories at the University of Jyväskylä, KU Leuven, GSI Darmstadt and the University of Mainz was concluded and resulted in the following manuscript. Note that this article features a second part *"On the reliability of wavelength meters – Part 2: Frequency-comb based characterization revealing their relative limitations and offering opportunities for more accurate absolute wavelength determinations"*, submitted by Kristian König *et al.* to the same journal. This connected work mainly comprises the test of wavelength meters using frequency combs as reference and thus also allows for a characterization of their absolute accuracy, whereas the work at hand is mainly focused on the more economic alternative of SFPIs and compact atomic spectroscopic setups.

Author contribution

The following article has five main authors: M.V., K.D. (KU Leuven), S.G. (Univ. of Jyväskylä), K.K. (GSI Darmstadt) and D.S. (Mainz Univ.). Each of them contributed the major part of the measurements performed at the respective institute and prepared a part of the manuscript describing the corresponding setup, measurement protocol and data evaluation. The final manuscript was then compiled and structured by the first author, M.V. Specifically for the part of Mainz University, D.S. installed the SAS setup and data acquisition and performed the wavelength meter characterization, with support from T.K. Similarly, the corresponding sections and plots (Fig. 3 and Fig. 8) for the manuscript draft were prepared by D.S.

Applied Physics B (2020) 126:85
https://doi.org/10.1007/s00340-020-07425-4

Applied Physics B
Lasers and Optics

On the performance of wavelength meters: Part 1—consequences for medium-to-high-resolution laser spectroscopy

M. Verlinde[1] · K. Dockx[1] · S. Geldhof[2] · K. König[3] · D. Studer[4] · T. E. Cocolios[1] · R. P. de Groote[2] · R. Ferrer[1] · Yu. Kudryavtsev[1] · T. Kieck[4] · I. Moore[2] · W. Nörtershäuser[3] · S. Raeder[5,6] · P. Van den Bergh[1] · P. Van Duppen[1] · K. Wendt[4]

Received: 30 August 2019 / Accepted: 20 March 2020 / Published online: 21 April 2020

Abstract

Present-day laser-spectroscopy experiments increasingly rely on modern commercial devices to monitor, stabilize, and scan the wavelength of their probe laser. Recently, new techniques are capable of achieving unprecedented levels of precision on atomic and nuclear observables, pushing these devices to their performance limits. Considering the fact that these observables themselves are deduced from the frequency difference between specific atomic resonances, in the order of MHz–GHz, the uncertainty on the output of the device measuring the wavelength is often directly related to the final systematic uncertainty on the experimental results. Owing to its importance, the performance of several commercial wavelength meters was compared against different reference sources, including a Scanning Fabry–Pérot Interferometer (SFPI) and a frequency comb. Reproducible, wavelength- and device-dependent disagreements are observed, potentially skewing the experimental output at high precision. In this paper, a practical and relatively inexpensive wavelength meter characterization procedure is presented and validated. This method is capable of improving the precision on wavelength differences considerably depending on the device, while together with a second investigation that is published separately, (König et al., in Appl Phys B, 2020), it offers a full description of the expected wavelength meter performance for users.

1 Introduction

To run modern laser-spectroscopy experiments, the probe laser requires means to monitor, stabilize, and/or scan the wavelength during operation. These tasks are often realized using state-of-the-art commercial wavelength meters, which are capable of performing a wavelength determination for a variety of optical radiation sources ranging from deep UV to infrared in relatively short time scales (> 1 kHz), ideal for fast correction feedback loops. The performance of these wavelength meters has already been the topic of several studies, mainly focused on their performance stability (see, e.g., [2–6]).

A specific field of use of these devices is the study of exotic radionuclides at radioactive ion beams (RIB) facilities via hyperfine laser spectroscopy. This technique provides information on the electromagnetic structure of the nucleus by offering a nuclear-model independent window to the nuclear spin, nuclear moments, and differences in mean-square charge radii, for a range of isotopes [7, 8]. The hyperfine structure, carrying the nuclear information imprinted in the form of frequency differences between specific closely spaced resonances in the atomic spectrum (MHz–GHz energy scale), can be uncovered with varying degrees of precision (defined here via the full-width-at-half-maximum (FWHM), Δf_{FWHM}, of the obtained resonance). As the production rate of nuclei decreases as one pushes to more exotic species, resonant ionization spectroscopy (RIS), whereby the number of ions produced as a function

✉ M. Verlinde
Matthias.Verlinde@kuleuven.be

[1] KU Leuven, Instituut voor Kern-en Stralingsfysica, Celestijnenlaan 200D, 3001 Leuven, Belgium

[2] Department of Physics, University of Jyväskylä, 40014 Jyväskylä, Finland

[3] Institut für Kernphysik, TU Darmstadt, 64289 Darmstadt, Germany

[4] Institut für Physik, Johannes Gutenberg-Universität, 55099 Mainz, Germany

[5] Helmholtz-Institut Mainz, 55128 Mainz, Germany

[6] GSI Helmholtzzentrum für Schwerionenforschung GmbH, 64291 Darmstadt, Germany

of laser wavelength is monitored, is the technique of choice due to the high efficiency of counting ions or detecting the radioactive decay signal. A number of RIS techniques exist, adapted to the environment in which the atomic species of interest are probed, which eventually defines the achievable precision [9]. These techniques are, for example: RIS in a hot-cavity source or in a gas cell (3 GHz $< \Delta f_{\mathrm{FWHM}} <$ 10 GHz [10, 11]), RIS in a perpendicular geometry, which can be realized in a gas jet or within the PI-LIST ion source (0.1 GHz $< \Delta f_{\mathrm{FWHM}} <$ 1 GHz [11, 12]) and with collinear techniques on fast ion/atom beams ($\Delta f_{\mathrm{FWHM}} \approx$ natural linewidth [13]). To reduce the linewidth of the hyperfine resonances, and, hence, to provide higher precision data on the nuclear observables, the latter two techniques are pushing the limits on accurate frequency determination using commercial wavelength meters for monitoring, stabilizing, and potentially scanning the probe laser [6].

As the final hyperfine observables of interest are directly related to the ill-defined uncertainty of the readout of this wavelength meter, it is important to understand its performance in determining frequency differences $\nu_{\alpha\beta} = \nu_\beta - \nu_\alpha$ of the order ~ MHz/GHz over the complete operational spectral range. Additionally, as the isotopes of interest are becoming increasingly exotic and, thus, only produced in minute quantities, the performance stability over longer periods of time, required to obtain sufficient statistics, is crucial. Moreover, RIS most often relies on the measurement of one isotope at a time, so that the accurate determination of isotope shifts strongly depends on the comparability of the data and, thus, the reproducibility of the frequency determination. In this paper, we report on a reliability study performed in different laboratories using different wavelength ranges, different wavelength meters, and different measuring protocols with the goal to provide an easy, cost-friendly, widely applicable and potentially performance-increasing, wavelength meter characterization procedure. The wavelength meters of interest in this paper and [1] belong to the WS series from HighFinesse GmbH. These devices consist of beam optics coupling the laser light, entering the device via an optical fiber, into Fizeau interferometers. The induced interference pattern is imaged on a CCD photodiode array. The obtained spectrum is fitted and compared to the calibration pattern resulting in a wavelength determination. Here, we will concentrate on the accuracy of relative frequency measurements, while in a second study, the focus will lie on the accuracy of absolute frequency determinations [1].

To determine the precision on $\nu_{\alpha\beta}$, $\Delta\nu_{\alpha\beta}$, for different wavelength meters in different wavelength ranges, the readout of these devices was compared to another reference. To summarize the tests, the paper is structured as follows. In Sect. 2, the capabilities of several wavelength meters (WS series HighFinesse GmbH, when no specific type is specified the notation WSX is used) to accurately measure frequency differences, $\nu_{\alpha\beta} = \nu_\beta - \nu_\alpha$, in a range of ~ 10 GHz is investigated with the aid of a Scanning Fabry–Pérot Interferometer (SFPI), a frequency comb, and an ionic resonance. Section 3 contains a description of the temporal stability of these devices and different solutions on how to improve it. Several measurement methods are combined to give a comprehensive overview for a number of devices over a large spectral range. In Sect. 4, a validation of the results from Sect. 2 is done by performing laser spectroscopy on ^{63,65}Cu isotopes in an Atomic-Beam Unit (ABU) and in a gas-jet environment, confirming the necessity of a proper wavelength meter characterization.

2 Determination of $\Delta\nu_{\alpha\beta}$(WSX)

2.1 WSX–SFPI comparison

The first series of tests were performed at the In-Gas Laser and Ionization Spectroscopy (IGLIS) laboratory at KU Leuven, Belgium. This facility has been built to carry out a full characterization, validation, and optimization of the in-gas-jet spectroscopy for its later implementation in a number of online accelerator facilities (S3 LEB, MARA LEB, and GSI), to study, amongst others, the heavy and super heavy elements [11]. In the in-gas-jet method, the atoms of interest are embedded in a low-density and low-temperature gas jet environment, minimizing the spectral pressure and temperature broadening mechanisms, while still offering high selectivity, short extraction time (< 0.5 s), high efficiency, and an independence to the chemical nature of the species of interest [14]. To probe the hyperfine structure of the atoms embedded in the gas jet, high-repetition rate, high-power dye lasers are available, supported by a pulsed dye amplifier system seeded with a cw single-mode diode laser for high-resolution laser operation [15].

A second set of characterization tests were performed in the RISIKO laboratory at Johannes Gutenberg-University (JGU) Mainz, Germany. This facility is in use for studies on beams of stable or long-lived radioactive ions, in combination with related development on hot cavity laser ion sources, dedicated laser systems, and spectroscopic techniques. The laser ion source here is based on high-repetition rate pulsed Ti:sapphire lasers specifically developed for this application [16]. While these lasers provide high output power required for efficient ionization, a complementary cw laser system provides the stability and narrow linewidth necessary for ultra-trace analysis applications [17, 18] and high-resolution spectroscopy [19–21]. The benefits of both systems can be combined using a cw external cavity diode laser (ECDL) as master laser for seeding of a pulsed injection-locked Ti:sapphire laser (slave). This combination

provides both, high-power pulsed laser radiation and a narrow spectral linewidth of ≈ 20 MHz with appropriate stability [22, 23], well suited for sensitive RIS studies.

2.1.1 Measurement protocol

The tests at the IGLIS laboratory were done by studying, simultaneously, the readout of a wavelength meter (WS7-60, acquired in 2012), which has a quoted accuracy of 60 MHz (according to the 3σ criterion) in the range 420–1100 nm, and a Scanning Fabry–Pérot Interferometer (SFPI, Toptica FPI-100-0500-1) with a Free Spectral Range (FSR) of 4 GHz. A schematic overview of the setup is given in Fig. 1a. The IGLIS control software performs a stepwise frequency scan of a diode laser (TA:pro, TOPTICA Photonics AG) by applying a DC voltage to the DC 110 diode laser driver, a component of the Diode Laser Driver Electronics (Sys DC 110, TOPTICA Photonics AG), via a pulse generator (PicoScope 5000a, Pico Technology). This voltage is amplified in the DC110 diode laser driver and applied to a piezo actuator in the diode laser for accurate control of the laser wavelength. The TA:pro laser, lasing around 654.9 nm, is stabilized relative to the WS7-60's readout of either a 770.108796 nm diode reference laser (DL pro 780, TOPTICA Photonics AG), frequency locked to a potassium cell (CoSy, TEM Messtechnik GmbH), or a 632.991026 nm frequency-stabilized HeNe laser (Model 32734, Research Electro-Optics, Inc.) during a laser scan, see [15]. For the wavelength determination via the SFPI, both TA:pro and HeNe laser beams are overlapped in the SFPI. In this way, both wavelength measuring devices contain a reference source for calibration and stabilization purposes. A finesse, $\mathcal{F} \approx 300$, is obtained in the SFPI for both TA:pro and HeNe laser light. To provide optimal working conditions for the SFPI, a scanning range of its piezo actuator is chosen, such that a previously optimized number of fringes (≈ 10) of both lasers is visible in one single voltage ramp. At each wavelength step of the TA:pro, one or more traces of the SFPI's diode sensor are recorded. Off-line, all data are analyzed with a Python-based algorithm. This program uses peak finder and peak tracker algorithms to identify HeNe and TA:pro fringes, fitting each with Gaussian profiles. The fringe positions of the HeNe laser are used as a ruler to accurately transform the time positions of each fringe into a frequency value via the known FSR. After this procedure, the average position of the TA:pro fringes of each trace in the frequency domain is saved together with their standard deviation. In case higher precision is required, multiple traces can be extracted at each wavelength, providing a final value as the weighted average with corresponding uncertainty, taking into account the reduced χ^2.

At the RISIKO laboratory, a similar comparison was performed between a wavelength meter (WSU-30, acquired in 2003) and a home-made SFPI. The WSU-30(UV) wavelength meter has an accuracy of 30 MHz in the range 248–1180 nm. The scanning ECDL consists of a custom-built mount with

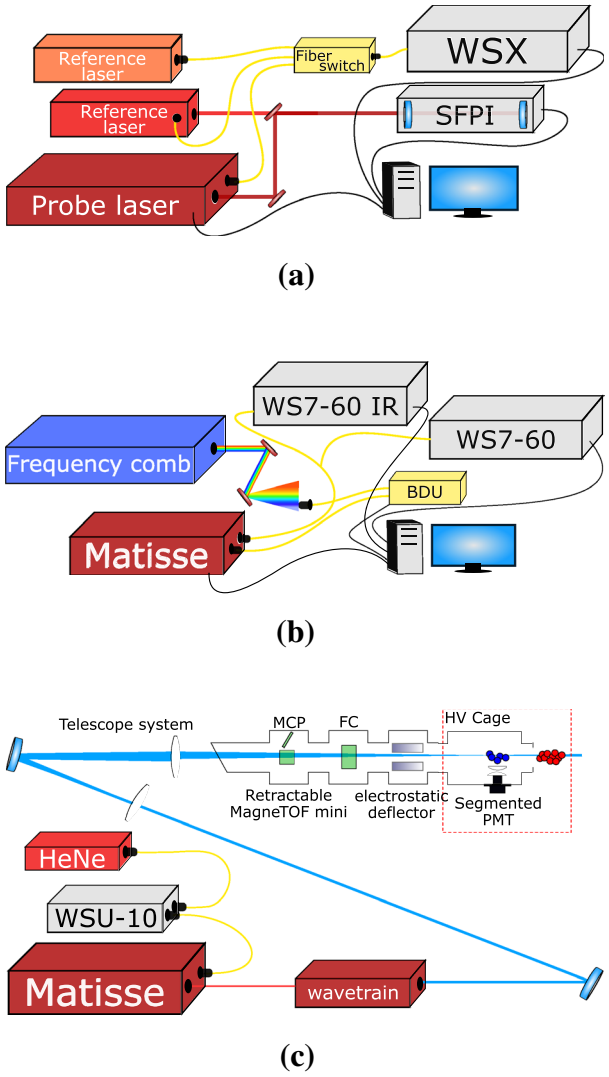

Fig. 1 Experimental techniques used in this work. (**a**) Simplified schematic layout of a general setup used to compare the output of an SFPI with that of a specific wavelength meter. The probe laser is measured by a specific WSX wavelength meter together with a reference laser. The wavelength scan of the probe laser is controlled externally by a feedback loop, based on the readout of the WSX. One reference laser is also overlapped with the probe laser and directed to the SFPI. For details, see text. (**b**) Simplified schematic layout of the continuous wave (cw) laser setup at TU Darmstadt. The Matisse 2 TS laser frequency, locked to both reference cavity and FC1500 frequency comb, is monitored during a wavelength scan by the WS7-60 wavelength meters and by the comb itself via a Beat Detection Unit (BDU). For details, see text. (**c**) Schematic view of the light collection region and laser systems of the collinear beamline at IGISOL for the measurements on 89Y. The ion beam enters the beamline from the right side. The laser interaction region is monitored by a segmented Photo-Multiplier Tube (PMT) for resonance fluorescence detection

a piezo-actuated grating for external feedback, and a Peltier element for temperature stabilization, supplied by commercial laser driver electronics (LDC202, Thorlabs Inc.). In total, two different laser diodes were used in this setup (RWE-920, RWE-980, Eagleyard Photonics GmbH). Fast stabilization and scanning operation are performed with a quadrature interferometer, (iScan, TEM Messtechnik GmbH). The long-term and accurate stabilization of the ECDL set frequency is obtained from an SFPI via a fringe off-set locking (FOL) technique [24]. More information on the laser setup can be found in [25]. Here, the light from the probe ECDL and from a stabilized HeNe laser (SL-03, SIOS Messtechnik GmbH) is overlapped in a custom-built confocal SFPI, with a piezo-actuated mirror. The SFPI has a free spectral range of FSR = 298.721 MHz and a Finesse of $\mathcal{F} \approx 400$. Depending on the wavelength, the piezo ramp covers 2–3 fringes. The transmission of the probe ECDL and the HeNe fringes are separated by a dichroic mirror and detected with separate photodiodes. The time difference of the first ECDL fringe after the start of the voltage ramp is measured with respect to the fringe from the reference HeNe laser via a counter card and the frequency change is evaluated using an Arduino MCU, via the precisely known FSR and HeNe wavelengths. To ensure proper single-mode operation of the ECDL, the time between the first and the second fringe is in addition evaluated. Values of the mean relative frequency and frequency jitter within a time of ≈ 50 ms (matched to the data acquisition cycle of the wavelength meter) are sent to a LabVIEW interface, used for controlling, monitoring, and recording. An absolute frequency measurement is provided by the WSU-30, where both the probe ECDL and the stable HeNe output are measured through a multichannel switch (HighFinesse GmbH). The absolute reference and calibration source for the wavelength meter is an additional ECDL (DL pro 780, Toptica Photonics AG), coupled to a compact rubidium saturated absorption spectroscopy setup (SAS) (CoSy 4.0, TEM Messtechnik GmbH). Using a dither-lock stabilization (LaseLock 3.0, TEM Messtechnik GmbH), it is locked to the $F = 2 \rightarrow F = 3$ transition in the D2 line of ^{87}Rb at 780.24602 nm. A schematic overview of this setup is shown in Fig. 1a.

To compare the relative performance of both SFPI and wavelength meter during a frequency scan, the magnitude of each laser step with respect to the starting point of the scan is monitored for both devices. Finally, the difference in the step size as measured by the SFPI and wavelength meter, respectively, is subtracted to obtain a relative result. Mathematically, the final output $\Delta_{\mathrm{SFPI-WSX}}(\nu)$ for a random wavelength meter WSX, reads as follows:

$$\begin{aligned}\Delta_{\mathrm{SFPI-WSX}}(\nu) &= \Delta_{\mathrm{SFPI}}(\nu) - \Delta_{\mathrm{WSX}}(\nu) \\ &= \left(\nu_{\mathrm{SFPI}} - \nu_{0,\mathrm{SFPI}}\right) - \left(\nu_{\mathrm{WSX}} - \nu_{0,\mathrm{WS}X}\right).\end{aligned} \tag{1}$$

In Eq. (1), ν_{WSX} represents the frequency readout at a certain moment during a laser scan, while $\nu_{0,\mathrm{WSX}}$ represents a reference point within the scan.

2.1.2 Results

The procedure described for the IGLIS laboratory, using the setup in Fig. 1a, was applied to a number of scan ranges. The results for $\Delta_{\mathrm{SFPI-WS7}}(\nu)$, defined in Eq. (1), in the 654.9570–654.9969 nm range (spanning roughly 28 GHz in total) are shown in Fig. 2. These results show that the WS7-60 and SFPI disagree reproducibly on the step size taken by the TA:pro laser with a maximum of 8 MHz, with an additional degree of periodicity. To map this periodicity, a triangular wave form was fitted to the data of Fig. 2 without any prior knowledge on the underlying mechanism:

$$\begin{aligned}\Delta_{\mathrm{triangle}}(\nu) = &\frac{4A}{T}\left((\nu+S) - \frac{T}{2}\left\lfloor\frac{2(\nu+S)}{T} + \frac{1}{2}\right\rfloor\right) \\ &\cdot (-1)^{\left\lfloor\frac{2(\nu+S)}{T}+\frac{1}{2}\right\rfloor}.\end{aligned} \tag{2}$$

This function of the frequency ν has three parameters; the amplitude, A, period, T and shift, S, of the triangular wave. The fitting procedure reveals a peak-to-peak amplitude $A_{655}^{\mathrm{WS7}} = 8.2(2)$ MHz and a period $T_{655}^{\mathrm{WS7}} = 3.871(10)$ GHz for Eq. (2). The period matches closely to the FSR of the most precise interferometer of the WS7-60 wavelength meter (≈ 4 GHz). To understand the behavior of the WS7-60 in more detail, the wavelength range 654.973–654.985 nm was scanned with higher resolution (≈ 10 traces per wavelength step were combined). The results of this measurement are shown in yellow in Fig. 2 with a magnified region shown in Sect. 4, Fig. 10. The finer details observed in Fig. 10 show

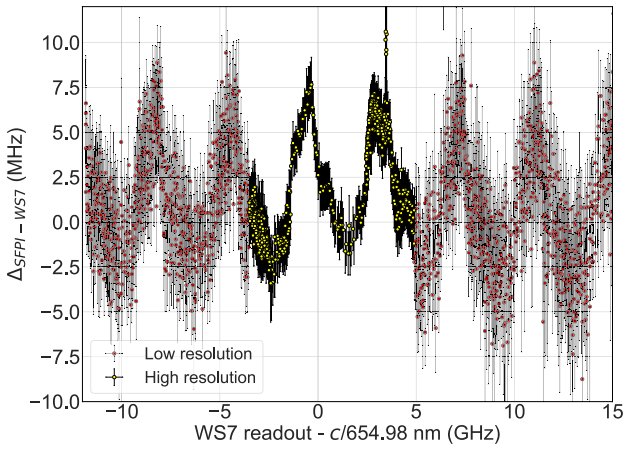

Fig. 2 Results for $\Delta_{\mathrm{SFPI-WS7}}(\nu)$, defined in Eq. (1), recorded at the IGLIS laboratory. The results presented here combine multiple scans taken at different times to prove the reproducibility of the data. For details, see text. c represents the speed of light in m/s

that the underlying mechanism, causing the disagreement between the WS7-60 and SFPI, is of a more complex nature than a simple triangular waveform. However, the general features of the disagreement between both devices are clear. The data of Fig. 2 present multiple measurements confirming the reproducibility of the results. Additionally, the structure obtained for Fig. 2 is independent of the calibration laser. The specific calibration tool only causes an absolute offset, not visible in these measurements.

The comparison between the WSU-30 wavelength meter and the home-made SFPI at the RISIKO laboratory is presented in Fig. 3 (middle and bottom panel). The data in Fig. 3 show also a periodic deviation of the WSU-30 readout with respect to the SFPI, calculated according to Eq. (1), with $\nu_{0,\mathrm{WSU30}} = c/905.795\,\mathrm{nm}$ and $\nu_{0,\mathrm{WSU30}} = c/938.853\,\mathrm{nm}$ for

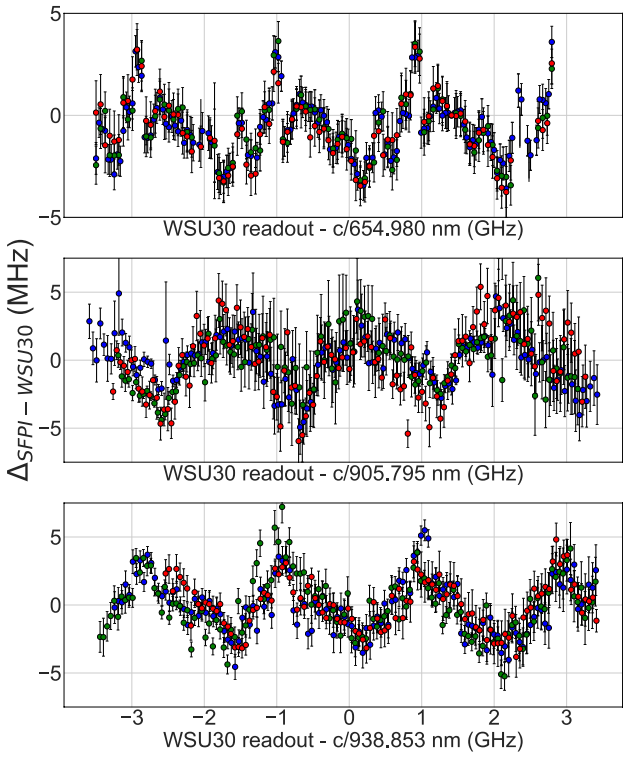

Fig. 3 Results for $\Delta_{\mathrm{SFPI-WSU30}}$, measured for three different laser wavelength ranges. The upper panel at 654.980 nm was obtained at the IGLIS laboratory. Each data point of the upper panel is taken as the weighted average with corresponding uncertainty of the results from 10 SFPI traces, obtained via Eq. (1), at a distinct frequency. Around ten consistent measurements were taken, from which three are shown in the upper panel. The other panels, scanned at 905.795 nm and 938.853 nm, respectively, were measured at the RISIKO laboratory in Mainz. The results are obtained with a similar analysis to the one in the IGLIS laboratory, and the final data points represent the average and standard deviation of all SFPI results taken within one wavelength bin. 11 and 8 consistent measurements were taken for the 905 nm and 938 nm cases, respectively, from which again three full range results are shown in both panels. All three measurements for $\Delta_{\mathrm{SFPI-WSU30}}$ show the same period in their structure

middle and lower graph, respectively ($\nu_{0,\mathrm{SFPI}} = 0$). In both measurements, a calibration of the wavelength meter was performed after each data point, to exclude any time-dependent drifts of the wavelength meter performance, as discussed in the next section. The rather large scatter in the scan at 905 nm arises from stability issues of the probe ECDL, which may be caused by internal feedback in the laser diode, owing to an inferior anti-reflection coating of the front window. The different colors represent measurements performed on different days over the same frequency range and underline the reproducibility of the periodic pattern. Minor shifts may be caused by drifts of the HeNe laser (i.e., the SFPI reference), but still lie within the specified stability. Fitting all datapoints of one frequency range with the triangular pattern from Eq. (2) yields a period of $T_{905}^{\mathrm{WSU30}} = 1.923(14)\,\mathrm{GHz}$ and $T_{938}^{\mathrm{WSU30}} = 1.912(12)\,\mathrm{GHz}$, close to the FSR of the final WSU-30 interferometer of $\approx 2\,\mathrm{GHz}$. The peak-to-peak deviation is $A_{905}^{\mathrm{WSU30}} = 5.1(3)\,\mathrm{MHz}$ and $A_{938}^{\mathrm{WSU30}} = 5.3(2)\,\mathrm{MHz}$, respectively. To confirm both the IGLIS and RISIKO data acquisition and, in general, the SFPI measurement procedure, the WSU-30 wavelength meter was remeasured at the IGLIS laboratory in the wavelength range around 654.980 nm. The results are shown in Fig. 3 (top panel) and they confirm both the $\approx 2\,\mathrm{GHz}$ period for this WSU-30 and the smaller amplitude compared to the WS7-60 ($A_{655}^{\mathrm{WSU30}} \approx 5\,\mathrm{MHz}$). While the 'global' periodicity of the signal is easily distinguished, extra structures are clearly visible. The obtained results for $\Delta_{\mathrm{SFPI-WSU30}}$, also, clearly show both a wavelength range and device-specific dependence of the wavelength meter response, as was confirmed in the next measurements.

2.2 WSX-frequency comb comparison

A third series of wavelength meter tests was performed at the COllinear Apparatus for Laser spectroscopy and Applied physics (COALA) at TU Darmstadt, Germany. This laboratory was originally designed for accurate high-voltage evaluations based on Collinear Laser Spectroscopy (CLS) operation. Nowadays, precise measurements of absolute transition frequencies and isotope shifts in ions are also performed to benchmark atomic theory and to support on-line investigations of short-lived isotopes. For this purpose, a cw laser system based on Ti:sapphire lasers combined with Wavetrain frequency doublers is available alongside a GPS-referenced frequency comb to determine and stabilize its frequency [1, 26, 27].

2.2.1 Measurement protocol

At the COALA laboratory, the output of both the IGLIS WS7-60 wavelength meter and the in-house WS7-60-IR (630–1750 nm, acquired in 2007) device was compared to the frequency comb (FC1500-250-WG, Menlo Systems)

and the accuracy of the wavelength meter's absolute readout could be tested. The setup is shown in Fig. 1b. A Ti:sapphire laser (Matisse 2 TS, Sirah) is stabilized to its reference cavity to avoid short-term frequency fluctuations. Additionally, a slower stabilization feedback loop for long-term stabilization is realized using the frequency comb. To achieve this, the beat frequency between the nearest comb mode and the Ti:sapphire beam is measured in a fiber-coupled beat detection unit (BDU) and digitally communicated to the Matisse commander software, which adapts the length of the reference cavity to keep the beat frequency constant. In this way, an accurate and stable absolute reference is available with a precision of better than 100 kHz, limited by the linewidth of the Matisse. For the measurements performed here, the laser is scanned across a similar frequency range as in the IGLIS/RISIKO measurements, locked to the frequency comb at every wavelength step. The customized data acquisition system records the readout from both the frequency comb and the two WS7-60 wavelength meters. With this setup, both relative and absolute performance of the WS7-60 can be mapped across a large wavelength range.

As the combination of the frequency comb and the Matisse laser at the COALA laboratory offers a reference with a well-known frequency, one can go a step further than Eq. (1) and compare directly the frequency output of both devices:

$$\Delta_{\mathrm{Comb-WSX}}(\nu) = \nu_{\mathrm{Comb}} - \nu_{\mathrm{WSX}}. \tag{3}$$

In this case, the wavelength meters are not only tested in their ability to determine $\nu_{\alpha\beta}$ but also in measuring ν_{α} itself.

2.2.2 Results

The results for the comparison between the WS7-60 and WS7-60-IR wavelength meters and the FC-1500 frequency comb, performed at the COALA laboratory, are shown in Fig. 4. They are obtained from a scan of the Matisse laser across ≈ 16 GHz around 805.56 nm and 795.56 nm, and across ≈ 8 GHz around 856.45 nm, respectively. The wavelength meters are calibrated at 812.77 nm using the frequency-comb stabilized Matisse, for the measurements at 805 nm and 856 nm and at 632.99 nm with a frequency-stabilized HeNe laser (SIOS SL 03, Meßtechnik GmbH) for the measurement at 795.56 nm. To identify device-dependent effects, a WS7-60-IR was included in the measurements. From Fig. 4, it follows that similar periodic patterns arise at different wavelength ranges, with similar peak-to-peak discrepancies for both wavelength meters. The structure is found to be highly reproducible over months in the previous measurements performed at COALA [1]. Inspecting both Figs. 2 and 4 indicates a wavelength dependence of the discrepancy between the reference and the WS7-60. Additionally, both devices do not react in the same way, indicating

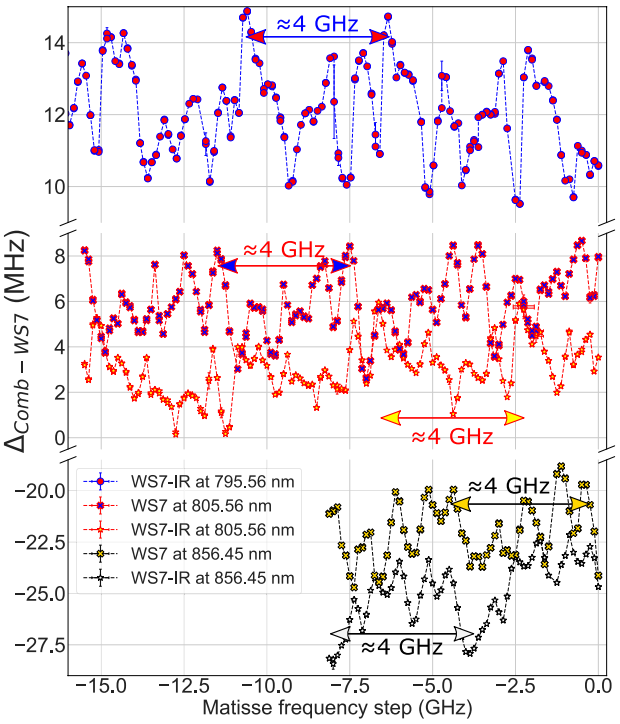

Fig. 4 Benchmarking the performance of two different WS7-60 devices, in the vicinity of 805.56 nm, 856.45 nm, and 795.56 nm against a frequency-comb measurement of the laser frequency resulting in $\Delta_{\mathrm{Comb-WS7}}(\nu)$

an additional device-dependent effect on the results of $\Delta_{\mathrm{Comb-WS7}}(\nu)$. Finally, it should be mentioned that the structure in the results of Fig. 4 also does not depend on the specific calibration point of the laser. Only the absolute offset to the real wavelength determined with the frequency comb might change, which is strongly wavelength-dependent itself. This, as well as, a full description of the frequency-comb-based specification of various high-precision wavelength meters is presented in [1].

2.3 WSX-ionic resonance comparison

A final series of measurements was done at the IGISOL facility of the Accelerator Laboratory in the University of Jyväskylä, Finland. This facility uses the ion guide technique for the production and study of low-energy beams of exotic radioactive nuclei [28]. Fundamental nuclear ground and isomeric state properties and mass are probed using a variety of ion (and atom) manipulation devices including ion traps, radiofrequency (rf) cooler-bunchers, as well as methods of optical spectroscopy. Over the years, an expanding program of optical spectroscopy at the facility has resulted in a variety of improvements to methods including collinear laser spectroscopy as well as resonance ionization spectroscopy. The former technique is applied for high-resolution

spectroscopy on fast ionic and atomic beams, routinely providing measurements of optical frequency splittings to 1–10 MHz precision. For these applications, a high-resolution laser spectroscopy setup based on a Matisse 2 TS laser and a Wavetrain frequency doubler is available. Additional infrastructure includes an injection-locked Ti:sapphire laser, seeded by the Matisse cw light, and several wavelength reference options.

2.3.1 Measurement protocol

At the IGISOL facility beam line for collinear laser spectroscopy, a wavelength meter (WSU-10, acquired in 2017), with a specified 10 MHz accuracy, was investigated. A schematic of the laser system and light collection region of the collinear beam line can be seen in Fig. 1c. More details on the beamline and data acquisition system can be found in [29]. Stable ^{89}Y, produced by a spark discharge source, was measured on the 363.4157 nm transition from the ionic ground state using the Matisse TS laser, pumped by a cw frequency-doubled YAG-laser (Millenia eV, Spectra Physics) and stabilized to a fixed setpoint in the wavelength meter. Resonant interaction between the anti-collinear laser beam and ions is measured by monitoring the optical deexcitation of the excited state with a segmented Photo Multiplier Tube (PMT). The hyperfine structure can be mapped by tuning the acceleration voltage of the ion beam. To probe systematic discrepancies between the WSU-10 and the centroid of the 363.4157 nm transition used as a reference, the stabilization setpoint was changed in steps of 600 MHz, and for each setpoint, a spectrum with sufficient statistics (> 1000 counts on the resonance peak) was collected.

For the IGISOL wavelength meter tests, the centroid of ^{89}Y presents an absolute reference while it is assumed that the voltage scan is identical for every measurement. This results in:

$$\Delta_{\text{Centroid}}(\nu) = \left(V_{\text{Centroid},\nu} - V_{\text{Centroid},\nu_0}\right)\frac{\partial \nu}{\partial V}. \tag{4}$$

Here, $V_{\text{Centroid},\nu}$ is the voltage at which the centroid of the transition is obtained for a random measurement at fixed setpoint ν and $V_{\text{Centroid},\nu_0}$ is the same for a reference measurement. $\partial\nu/\partial V$ converts the acceleration voltage difference to a frequency difference via the Doppler shift. In this way, similar results are obtained as for Eqs. (1) and (3).

2.3.2 Results

The resulting ^{89}Y hyperfine spectrum consists of an unresolved doublet, which was fitted by fixing the hyperfine parameter of the upper state to the literature value of 32.6(1) MHz [30]. The fitted centroid frequencies of the 363.4157 nm transition, obtained from the collinear beam line at IGISOL, are depicted in Fig. 5. A triangular-wave pattern applied to the data, following Eq. (2), resulted in a peak-to-peak amplitude of $A_{727}^{\text{WSU10}} = 1.3(3)$ MHz, which is almost an order of magnitude smaller than for the WS7-60. The period $T_{727}^{\text{WSU10}} = 1.99(12)$ GHz, is consistent with the ≈ 2 GHz FSR of the most precise interferometer in the wavelength meter.

2.4 Summary

In summary, the results indicate that each wavelength meter has its characteristic $\Delta\nu_{\alpha\beta}$ that is unique for every instrument separately. It can be extracted from $\Delta_{\text{SFPI-WSX}}(\nu)$, $\Delta_{\text{Comb-WSX}}(\nu)$ and $\Delta_{\text{Centroid}}(\nu)$, depends on the wavelength range of interest and is characterized by a periodic structure which follows the FSR of the most precise interferometer in the device. To obtain a value for $\Delta\nu_{\alpha\beta}$, one should perform a characterization procedure as presented here and further elaborated in Sect. 4, or otherwise remain with the conservative absolute accuracy mentioned by the manufacturer. To assess the potential systematic uncertainty to be expected, our data are summarized in Table 1, which contains the A_{λ}^{WSX} alongside the outer boundaries of the $\Delta_{\text{SFPI-WSX}}(\nu)$, $\Delta_{\text{Comb-WSX}}(\nu)$ and $\Delta_{\text{Centroid}}(\nu)$ distributions covering 95% or 99.7% of all measurements.

3 Temporal stability of ν_{α}(WSX)

Following a comparison of the performance of different wavelength meters in determining $\nu_{\alpha\beta}$ in a range of ~ 10 GHz with that of an SFPI and a frequency comb, its stability over time is mapped. A well-known feature of these wavelength

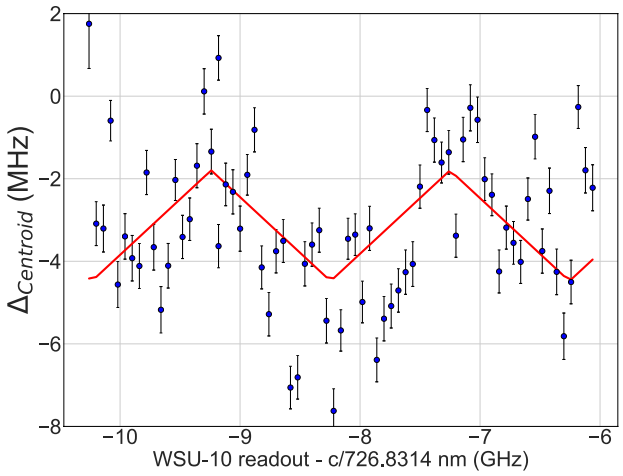

Fig. 5 Fitted centroid of the ^{89}Y hyperfine structure at changing laser stabilization setpoints using the WSU-10 wavelength meter (blue). The resulting data have been fitted using a triangular-wave function according to Eq. (2) (red solid line)

Table 1 Peak-to-peak amplitude A_λ^{WSX} and outer boundaries of the $\Delta_{\mathrm{SFPI-WSX}}(\nu)$, $\Delta_{\mathrm{Comb-WSX}}(\nu)$ and $\Delta_{\mathrm{Centroid}}(\nu)$ distributions, covering 95% or 99.7% of all measurements performed, Q_{95} and $Q_{99.7}$

Wavelength meter	Wavelength probe (nm) [±5 − 20 GHz]	A_λ^{WSX} (MHz)	Q_{95} (MHz)	$Q_{99.7}$ (MHz)
WS7-60	655.0	8.2(2)	11.7	18.0
WS7-60	856.5	≈ 3.5	5.0	5.9
WS7-60	805.6	≈ 5	5.1	6.1
WS7-60-IR	856.5	≈ 4	5.7	6.2
WS7-60-IR	805.6	≈ 3.5	4.7	5.8
WS7-60-IR	795.6	≈ 5	4.5	5.4
WSU-30	655.0	≈ 5	6.4	7.3
WSU-30	905.8	5.1(3)	8.8	13.7
WSU-30	938.9	5.3(2)	7.2	11.6
WSU-10	726.8	1.3(3)	7.2	9.2

When no explicit correction to the wavelength meter output is applied, see Sect. 4, Q_{95} and $Q_{99.7}$ should be taken into account to determine the systematic uncertainty on a determination of $\Delta\nu_{\alpha\beta}$ in a specific wavelength range. The Q values are not only influenced by the wavelength meter but also by the uncertainty of the analysis procedure. The values of A_λ^{WSX} are approximated, in case the discrepancy of the wavelength meter shows a significant deviation from Eq. (2)

meters is their tendency to drift over longer periods of time, strongly correlated to external temperature and/or pressure instabilities. The magnitude of these drifts is most often in the range of a few MHz/hour dependent on the magnitude of the time derivative of the external conditions. During longer measurement times, these drifts will have a profound impact on the results obtained. Two options exist to compensate for the time-dependent readout of the wavelength. First of all, one can correct for the drift of the scanning laser by monitoring the wavelength of an externally locked reference laser at the same time, which will be discussed in Sect. 3.1. Second, a periodical calibration of the wavelength meter can be included in the control software of the laser, see Sect. 3.2.

To exemplify the importance of a well-controlled external environment on the wavelength meter's long-term performance, the Matisse 2 TS laser at IGISOL was stabilized to a Rb hyperfine peak using a side-of-fringe stabilization method implemented in LabVIEW while being monitored by the WSU-10. Any wavelength meter drifts are then transferred to the device's readout. The largest variation seen is approximately 4 MHz over 24 h. This stability is in part due to the stable laboratory environment, with laboratory temperature control and minimal disturbance. To account for larger drifts in less stable conditions, they can be corrected for by (auto-)calibrating the device to a frequency-stabilized HeNe laser at certain times suitable to the ongoing measurements, see Sect. 3.2. Because the high-resolution work at the collinear beam line of IGISOL is performed with a fixed laser frequency setpoint, the Matisse transfer cavity can be used to bypass the wavelength meter in general. In this case, a digital plugin of the Matisse control software uses the intensity of the HeNe (HRS015B, Thorlabs Inc.) measured behind the reference cell with a photodiode (PDA36A-EC, Thorlabs Inc.) to stabilize the reference cell length with the side-of-fringe locking method. In this manner, the absolute frequency stability is now directly related to the frequency stability of the HeNe laser, eliminating the need for the wavelength meter. Collinear laser spectroscopy on stable even–even ytterbium isotopes was performed using either the wavelength meter or the transfer cavity for frequency stabilization to verify proper functioning of the transfer cavity. The scatter on the fitted centroids for each isotope, measured in the course of a few hours, was reduced when stabilized to the transfer cavity compared to the wavelength meter, confirming the wavelength meter as a possible source of systematic uncertainty, see Fig. 6.

3.1 Drift correction

The most general correction to drifts in the wavelength meter output, in the presence of a reference laser, can be written as follows:

$$\nu'_{\mathrm{corr,WSX}} = \nu_{\mathrm{set}} + \beta(\nu_{\mathrm{set}}, \nu_{\mathrm{ref}}, t)(\nu_{\mathrm{ref}} - \nu_{\mathrm{ref,WSX}}). \tag{5}$$

ν_{set} is the originally defined setpoint at which the laser should be stabilized, ν_{ref} represents the absolute frequency of the reference laser, and $\nu_{\mathrm{ref,WSX}}$ is the reference's wavelength meter readout. The parameter $\beta(\nu_{\mathrm{set}}, \nu_{\mathrm{ref}}, t)$ takes into account any kind of frequency and/or time-dependent differences between the drift of the reference laser and the probe laser. As outlined in [15], the IGLIS control software stabilizes the scanning TA:pro's frequency at a wavelength $\nu'_{\mathrm{set,WS7}}$ in the WS7-60, with $\beta(\nu_{\mathrm{set}}, \nu_{\mathrm{ref}}, t) = 1$. Doing so, wavelength meter-dependent drifts in time, which can be as large as 5 MHz/h for the WS7-60 of interest, are corrected. To identify higher order (wavelength and/or time-dependent) corrections to $\nu'_{\mathrm{set,WS7}}$ in the form of $\beta(\nu_{\mathrm{set}}, \nu_{\mathrm{ref}}, t) = \frac{\nu'_{\mathrm{set,WS7}} - \nu_{\mathrm{set}}}{\nu_{\mathrm{ref}} - \nu_{\mathrm{ref,WS7}}}$, three inde-

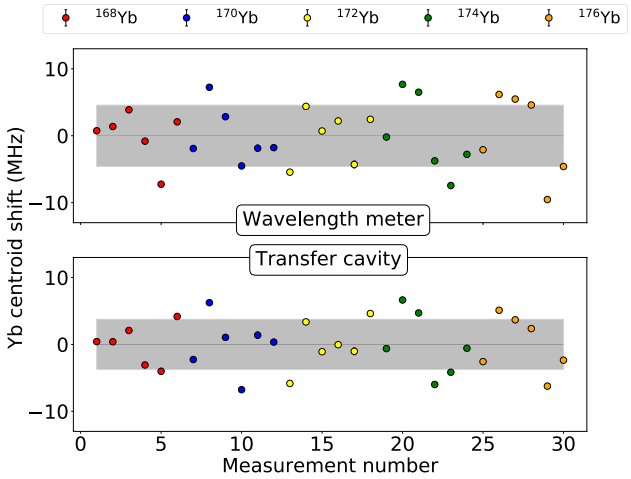

Fig. 6 Scatter of the ^{168}Yb, ^{170}Yb, ^{172}Yb, ^{174}Yb and ^{176}Yb centroids, obtained through collinear laser spectroscopy for different measurements stabilizing the probe laser to either the WSU-10 wavelength meter or the Matisse 2 TS transfer cavity. All centroids of a specific isotope, which were measured with a total of six different laser setpoints, are compared to their average. The 1σ confidence level was reduced from 4.6 to 3.8 MHz when stabilization to the transfer cavity was done

pendent measurements were done both at the IGLIS laboratory, a temperature-controlled (±0.5 °C) ISO8 clean room, and the COALA laboratory (see Fig. 7a–c). In all three cases, a HeNe laser was used both to calibrate the wavelength meter and as reference for the correction applied as it is the most common reference source. In addition to the HeNe, another externally stabilized laser, a proxy for the laser to be monitored during the experiment, was read out by the WS7-60 to search for any frequency dependence in $\beta(\nu_{\mathrm{set}}, \nu_{\mathrm{ref}}, t)$. First, the IGLIS TA:pro, stabilized to the wavelength meter readout at 654.97538 nm was included. Second, a potassium-locked diode was used at 770.10878 nm, also at the IGLIS laboratory. Finally, a Matisse 2 TS Ti:sapphire laser, locked to the FC1500 frequency comb at the COALA laboratory, was monitored at a wavelength of 787.82884 nm. The drift of the TA:pro was measured by supplying the laser, stabilized to ν_{set} in the WS7-60, also to the SFPI. The data analysis of these results remains the same as described in Sect. 2.2. For all three measurements, the full drift of the WS7-60's response in ≈ 6 h is mapped together with the results of available corrections. These corrections include $\beta(\nu_{\mathrm{set}}, \nu_{\mathrm{ref}}, t) = 0$, $\beta(\nu_{\mathrm{set}}, \nu_{\mathrm{ref}}, t) = 1$ and $\beta(\nu_{\mathrm{set}}, \nu_{\mathrm{ref}}, t) = \beta(\nu_{\mathrm{set}}, \nu_{\mathrm{ref}})$. The factor $\beta(\nu_{\mathrm{set}}, \nu_{\mathrm{ref}})$ is a reproducible, wavelength-dependent constant, which is obtained after longer periods of drift as can be seen in Fig. 7a–c. This number is reproducible for different measurements, independent of the drift rate, showing only a dependence on the device, ν_{set} and ν_{ref}. From the data, one can see that the WS7-60 does not provide a stable read out of the wavelength over time (this would be the case $\beta(\nu_{\mathrm{set}}, \nu_{\mathrm{ref}}, t) = 0$). For the TA:pro at 654.98 nm, $\beta(\nu_{\mathrm{set}}, \nu_{\mathrm{ref}}, t) = 1$ is sufficiently accurate to keep the laser stable to within 1 MHz. This 1 MHz limit was chosen arbitrarily as it is similar to other uncertainties contributing to the laser stability, as will be discussed in Sect. 4. For both infrared lasers, the inclusion of the $\beta(\nu_{\mathrm{set}}, \nu_{\mathrm{ref}})$ factor is required to ensure a similar stability over this time domain. Through these measurements, it can be concluded that a correction to the WS7-60 output with $\beta(\nu_{\mathrm{set}}, \nu_{\mathrm{ref}}, t) = 1$ is sufficient up to scan times of ≈ 30 min. For longer scans, either the $\beta(\nu_{\mathrm{set}}, \nu_{\mathrm{ref}})$ factor has to be determined and applied, or a recalibration is required with a repetition rate higher than once every ≈ 30 min, as will be discussed next.

3.2 Periodical calibration

The stability of the WSU-30 wavelength meter readout at the RISIKO laboratory was tested over a period of ≈ 1 day by monitoring the measured frequencies of the Rb-locked ECDL and the HeNe after one initial calibration to the Rb D2 line. In a second measurement, 1 day later, the wavelength meter was auto-calibrated to the Rb-locked ECDL with a cycle of 10 min. The results are presented in Fig. 8.

It can be clearly seen that without auto-calibration (AC), the wavelength meter readout drifts over a few tens of MHz, strongly correlated to the temperature. Moreover, at large deviations from the nominal frequency, the HeNe readout seems to drift further than the Rb-locked ECDL, indicating also here $\beta(\nu_{\mathrm{set}}, \nu_{\mathrm{ref}}, t) \neq 1$.

Auto-calibration resolves the long-term stability issues of the wavelength meter readout almost completely. The deviation $\nu - \nu_{\mathrm{cal}}$ to the calibration frequency is < 2 MHz over the measurement duration and can be further reduced by a shorter calibration interval. As a consequence, an AC routine was added to the data acquisition cycle, so that the wavelength meter can be calibrated (taking less than 1 s) before moving to the next frequency setpoint. Alternatively, a stable temperature environment for the wavelength meter should provide superior frequency stability than in our test without AC. In this case, one should also consider the air pressure in the room, which could not be measured with our device. Newer devices usually have an integrated pressure sensor.

4 Validation

The reliability of the laser system in general and the WS7-60 wavelength meter in particular was tested by performing hyperfine spectroscopy on the $4s\,^2S_{1/2}$ ground-state (g.s.) to the $4p\,^2P_{1/2}$ excited-state (e.s.) transition in ^{63,65}Cu, in an Atomic-Beam Unit (ABU) and in a gas jet, and comparing the results with the literature. The resulting data as

well as the excitation and ionization scheme are presented in Fig. 10. To achieve the excitation at 327.49 nm, light from the scanning TA:pro laser is amplified in a Pulsed Dye Amplifier (PDA, Sirah Lasertechnik GmbH) and frequency doubled in a BBO nonlinear crystal. The ionization step of 287.98 nm is provided by a broadband tunable dye laser (CREDO, Sirah Lasertechnik GmbH) with also an integrated frequency conversion unit. Both PDA and broadband dye lasers are pumped by Nd:YAG lasers (INNOSLAB, Edgewave GmbH) at 1 kHz with a pulse length of ≈ 7 ns. The ABU provides a copper atom plume by resistively heating a graphite tube filled with copper. After ionization, these atoms experience a two-stage acceleration region before a field-free drift towards a Multi Channel Plate (MCP) detector. At the MCP, the time-of-flight of copper ions is recorded to provide a mass-resolving power of $R \approx 150$ for ^{63}Cu.

For the gas jet, copper atoms are produced by resistively heating a copper filament inside a buffer gas cell filled with argon. After laser ionization in the jet formed by a de Laval nozzle, placed at the gas-cell exit, these ions are transported through a set of Radio-Frequency Quadrupoles (RFQ's) and ion optical elements to a dipole magnet mass separator ($R \approx 300$) on high voltage. The mass-separated ions are finally detected by an MCP. More details on the setup system are available in [15, 31]. A schematic overview of the laser setup for an ABU measurement is shown in Fig. 9. The scheme for in-gas-jet measurements is similar with the exception that the laser beams are sent to the adjacent separator laboratory for overlap in the gas jet. An example of the resulting hyperfine structure, obtained from an ABU measurement, is visualized in the bottom part of Fig. 10.

The measuring protocol, automatized in the IGLIS Control Software and outlined in [15], provides, together with additional systematic checks, all data required to specify the expected uncertainties on both the ion rate and wavelength determination. The uncertainty on the ion arrival rate, I, is deduced from the standard deviation of a number of measurements, $I \pm \Delta I = \langle I \rangle \pm \sqrt{\langle I^2 \rangle - \langle I \rangle^2}$, at a specific wavelength,. The uncertainty on the wavelength ν comprises several components $\Delta\nu_{\mathrm{stat}}, \Delta\nu_{\mathrm{stab}}, \Delta\nu_{\mathrm{drift}}, \Delta\nu_{\mathrm{corr}}$, combining to $\nu_\alpha \pm \Delta\nu_\alpha = \langle \nu \rangle \pm \sqrt{(\Delta\nu_{\mathrm{stat}})^2 + (\Delta\nu_{\mathrm{stab}})^2 + (\Delta\nu_{\mathrm{drift}})^2 + (\Delta\nu_{\mathrm{corr}})^2}$ Here, $\Delta\nu_{\mathrm{stat}}$ represents the standard deviation of all wavelength values read out by the WS7-60 in a specific wavelength step, typically $\Delta\nu_{\mathrm{stat}} \approx 1$ MHz, see [15]. $\Delta\nu_{\mathrm{stab}}$ covers the stability of the frequency reference, ≈ 1 MHz in 1 h for the HeNe and < 1 MHz for the potassium-locked diode laser. Third, $\Delta\nu_{\mathrm{drift}}$ describes the uncertainty on the WS7-60's drift correction. For the IGLIS control software, $\beta(\nu_{\mathrm{set}}, \nu_{\mathrm{ref}}, t) = 1$. In this case, $\Delta\nu_{\mathrm{drift}}$ remains < 1 MHz for a scan at 654.98 nm, see Fig. 7a. Finally, $\Delta\nu_{\mathrm{corr}}$ can be added to account for any applied corrections to the WS7-60 output. Within these specifications, a multitude of scans are performed in high-resolution mode in the ABU. For each scan, a delay of around 6 ns between excitation and ionization laser pulses was implemented to find the optimal compromise between linewidth reduction and scan time [32]. The obtained FWHM of the resonances was between 110 and 130 MHz, including the natural linewidth, the Fourier-limited amplified TA:pro laser linewidth (≈ 70 MHz), and some residual power broadening from the ionization laser. In addition, for the in-gas-jet data, a resolution of ≈ 400 MHz was achieved, consisting of the components already mentioned added to a $T \approx 22$ K Doppler ensemble in a Mach 7.5 jet. The final results for the hyperfine parameters of ^{63,65}Cu are summarized in Table 2. These values are obtained after evaluation with the Statistical Analysis Toolbox for Laser Spectroscopy (SATLAS) module in python [33]. This software is designed specifically to analyze the data of laser spectroscopy experiments and allows for both χ^2 and maximum-likelihood fitting procedures. A model for the hyperfine structure of the element of interest is fitted directly to the experimental spectrum, providing both hyperfine parameters and resonance characteristics. From Table 2, a consistent and reproducible disagreement $> 10\sigma$ with the literature on the value $a(^{63}\mathrm{Cu,g.s.})$ is found. The WS7-60-to-SFPI comparison in Fig. 10 shows, however, an overestimation of the relative distances, defining, for example, the ^{63}Cu ground-state splitting, as indicated by the relative difference in position on the $\Delta_{\mathrm{SFPI-WS7}}(\nu)$ function of the particular resonances in the figure. Therefore, to improve the WS7-60's precision, the wavelength array in the hyperfine spectra is corrected by a fit of the waveform in Fig. 10. Because the fine structure of $\Delta_{\mathrm{SFPI-WS7}}(\nu)$ as a function of wavelength is much more complex than a triangular waveform, a spline generated by the *splrep* function of the *scipy* python library, weighted by the errors on each measurement point, was used to describe its behavior by finding the B-spline representation of the curve. The distribution of residuals from this spline was used to define $\Delta\nu_{\mathrm{corr}} \approx 1$ MHz. The resulting hyperfine parameters, obtained after correcting the wavelength array of each scan by the spline function, are shown in Table 2. This correction procedure alters the readout of the WS7-60, such that it would match that of the SFPI reference. Agreement with the literature is obtained for ^{63,65}Cu within $1\sigma = 0.5(^{63}\mathrm{Cu}), 0.8(^{65}\mathrm{Cu})$ MHz for the ABU, and $1.5\sigma = 3$ MHz for the gas jet, respectively, taking into account only statistical errors. This correspondence means that with the correction applied to the WS7-60 output, an uncertainty $\Delta\nu^{654.98}_{\alpha\beta,\mathrm{total}} = 3$ MHz is achieved in this specific wavelength region. Combining the results for both hyperfine a parameters of ^{63,65}Cu reveals $a(^{63}\mathrm{Cu,g.s.})/a(^{63}\mathrm{Cu,e.s.}) = 1.600(11)$ and

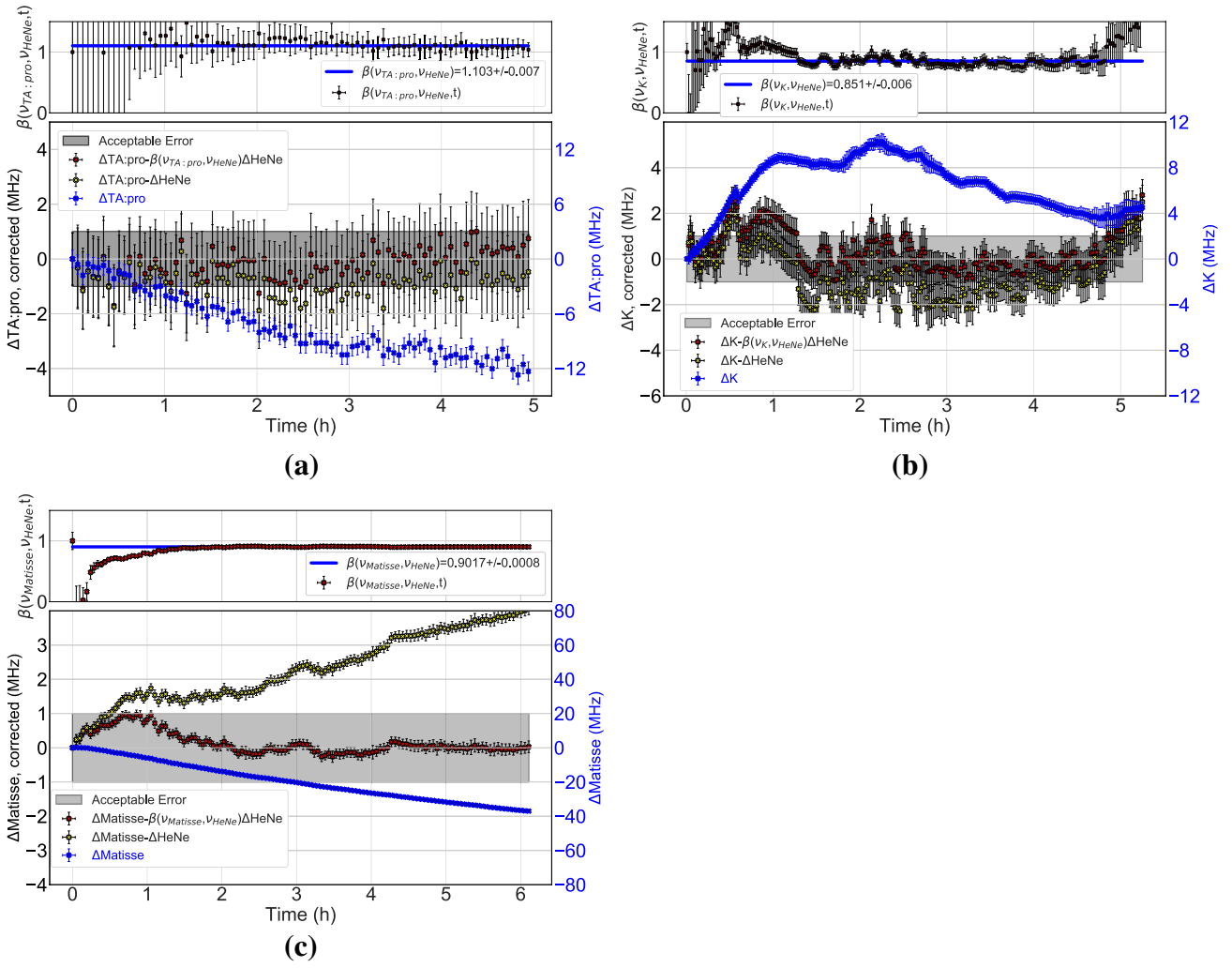

Fig. 7 Time dependence of the WS7-60's response to an externally locked laser at 654.97538 nm (**a**), 770.10878 nm (**b**), and 787.82884 nm (**c**), respectively. The drift is defined as $\Delta X = \nu_{\mathrm{WS7}}(t) - \nu_{\mathrm{WS7}}(t_0)$, with t_0 being the time of calibration and X the specific laser used. The uncorrected readout (right axis, blue) is plotted alongside possible corrections (left axis, yellow for $\beta(\nu_{\mathrm{set}}, \nu_{\mathrm{ref}}, t) = 1$ and red for $\beta(\nu_{\mathrm{set}}, \nu_{\mathrm{ref}}, t) = \beta(\nu_{\mathrm{set}}, \nu_{\mathrm{ref}})$), see text for details. The measured correction factor $\beta(\nu_{\mathrm{set}}, \nu_{\mathrm{ref}}, t)$, with its stable value, $\beta(\nu_{\mathrm{set}}, \nu_{\mathrm{ref}})$, fitted to the data, is added to the top panel of each figure. The different drift amplitudes originate from differences in the external conditions during the measurement

$a(^{65}\mathrm{Cu,g.s.})/a(^{65}\mathrm{Cu,e.s.}) = 11.620(17)$, respectively, excluding any hyperfine anomaly within this precision. An isotope shift $\delta\nu^{63-65}$ of 573.7(18) MHz can also be extracted from the data, also in agreement with the literature [34, 35].

In case no spline correction were applied, an additional non-stochastic systematic error would have to be introduced to the resulting observables, $a_{\mathrm{Cu,g.s.}}$, $a_{\mathrm{Cu,e.s.}}$ and $\delta\nu^{63-65}$, such that $\Delta\nu^{654.98}_{\alpha\beta,\mathrm{total}}$ is bound by a specific condition from Table1. When no information is available on the wavelength meter response in the required range, the conservative absolute uncertainty of the device (60 MHz for WS7-60) should be taken into account.

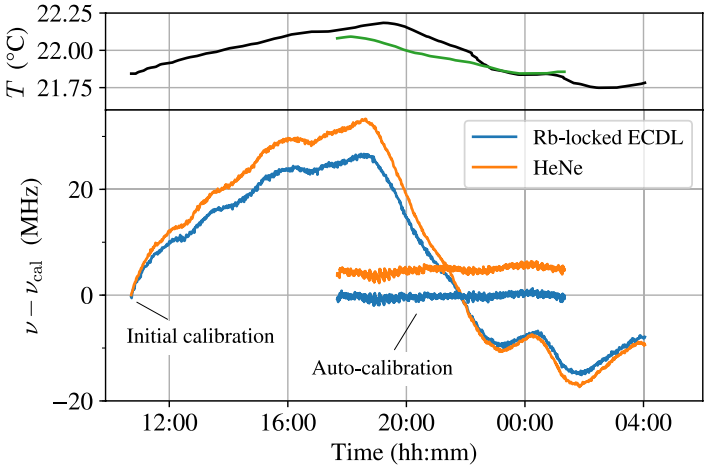

Fig. 8 Long-term frequency drifts in the readout of the WSU-30 for the HeNe laser (orange) and the Rb-locked ECDL (blue). Lower panel: deviation of the frequency readout ν to the frequency readout at the time of calibration ν_{cal}. The measurement was performed two times: first with one initial calibration and second with auto-calibration (AC) in a 10 min interval to the Rb-locked ECDL. For a better readability, the HeNe frequency has an offset of +5 MHz in the measurement with AC. Upper panel: temperature readout of the WSU-30 for the measurement without AC (black) and with AC (green)

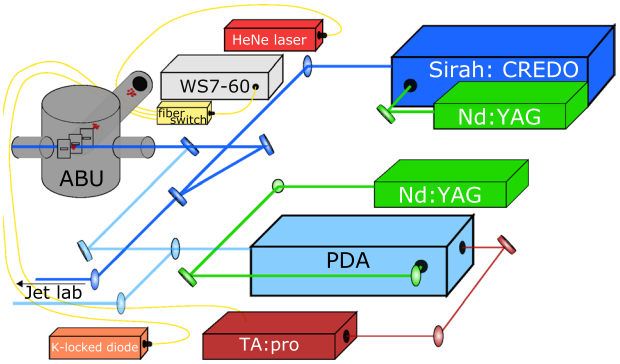

Fig. 9 Schematic overview of the setup used to determine the hyperfine parameters of the $4s\,^2S_{1/2}$ to $4p\,^2P_{1/2}$ transition. For the in-gas-jet measurements, the UV laser beams were guided to the adjacent offline beam separator laboratory, see [15, 31]

5 Conclusion

In this paper, two performance aspects of several commercial wavelength meters (HighFinesse GmbH), which are commonly used to monitor, stabilize and scan a laser's wavelength in medium/high-resolution laser hyperfine spectroscopy experiments, are investigated in a number of laboratories. First, the measurement uncertainty of frequency differences in the order of 10 GHz, $\Delta\nu_{\alpha\beta}$, which is directly related to the final physical observables of interest, is determined by a comparison to both an SFPI and a GPS-referenced frequency comb. For these frequency differences, induced by the hyperfine interaction, it was observed that the wavelength meters, which were all performing within specifications of the manufacturer, exhibit reproducible, quasi-periodic wavelength and device-dependent discrepancies with other reference sources, with the period lying close to the free spectral range of the device's most precise interferometer. This rather inexpensive, practical, and simple characterization allows for a firm determination of the $\Delta\nu_{\alpha\beta}$ in the wavelength range of interest. Either $\Delta\nu_{\alpha\beta}$ can be reduced to the measurement uncertainty of the comparison, by correcting the observed periodic behavior or, the peak-to-peak discrepancy of the observed pattern is used to define an additional systematic uncertainty $\Delta\nu_{\alpha\beta}$. In case no comparison is performed, the absolute uncertainty, quoted by the manufacturer, remains the only trustworthy source for $\Delta\nu_{\alpha\beta}$. This procedure was validated by laser spectroscopy on $^{63-65}$Cu isotopes in an Atomic Beam Unit (ABU) and in a gas jet. Finally, to ensure stable performance when probing rare exotic isotopes over longer times, two different solutions are validated, both taking advantage of an external reference source's wavelength stability. In conclusion, the quoted absolute measurement uncertainty of the specific wavelength meter should coincide with the expected attainable precision on the physical observables of the experimental laser-spectroscopy technique. In case the former significantly exceeds the latter, an extra characterization of the wavelength meter, as described here, should be performed in the specific wavelength range of interest to provide a trustworthy estimate of the measurement uncertainty. This statement, alongside

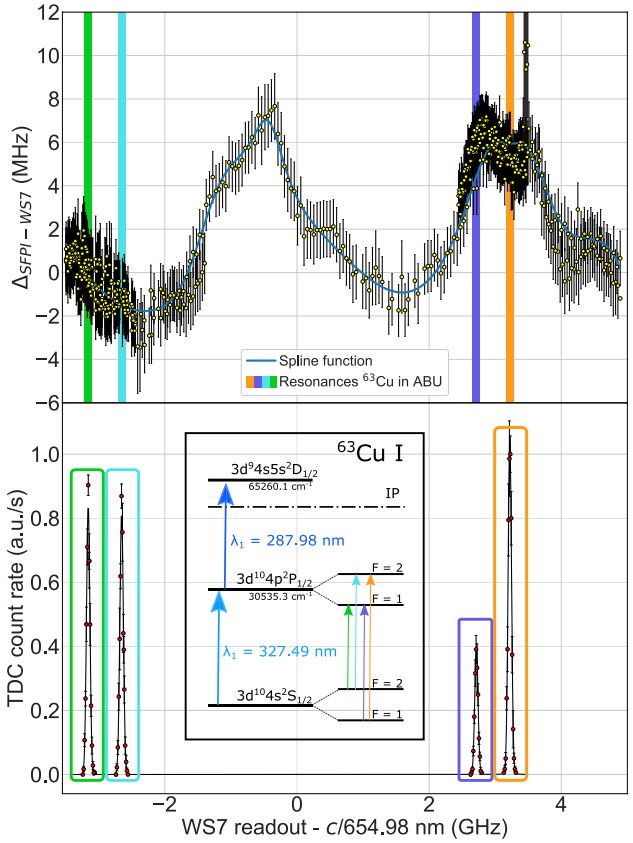

Fig. 10 Visualization of the correction to the WS7-60 output. The upper panel shows a zoom of $\Delta_{\mathrm{SFPI-WSX}}(\nu)$ in the wavelength range of the $4s\,^2S_{1/2}$ to $4p\,^2P_{1/2}$ hyperfine structure in copper. The spline function corrects each individual wavelength number given by the WS7-60 during the frequency scan, such that $\Delta_{\mathrm{SFPI-WSX}}(\nu) = 0$ and no apparent disagreement with the SFPI reference exists. The bottom panel shows a typical copper hyperfine spectrum with the fitted lineshape. All frequency values have been reported with respect to the fundamental wavelength, which is read by the wavelength meter. The results of the $\Delta_{\mathrm{SFPI-WSX}}(\nu) = 0$ correction on the hyperfine parameters are shown in Table 2

complementary investigations discussed here and in [1], should provide guidelines for users of these devices, both in their operation and in potential new acquisitions.

Acknowledgements This work has received funding from Research Foundation Flanders (FWO, Belgium), from the Excellence of Science program (EOS, FWO-FNRS, Belgium), by GOA/2015/010 and STG/15/031 (BOF KU Leuven), by the Interuniversity Attraction Poles Program initiated by the Belgian Science Policy Office (BriX network P7/12), from the European Union's Horizon 2020 research and innovation program under Grants Agreement no. 654002 (ENSAR2), from the European Research Council under the European Union's Seventh Framework Program (ERC-2011-AdG-291561-HELIOS), from the German Federal Ministry of Educations and Research (BMBF) under contracts 05P19RDFN1 and 05P18RFCIA, and from the German Research Foundation (DFG) under contract DU 1134/1-2. M.V. is supported by an FWO grant (Aspirant-1121820N). A significant share of the research work described herein originates from R&D carried out in the frame of the FAIR Phase-0 program of LASPEC/NUSTAR.

Table 2 Literature values for the hyperfine parameters of the $4s\,^2S_{1/2}$ to $4p\,^2P_{1/2}$ transition in ^{63}Cu and ^{65}Cu compared to results obtained for the measurements in the ABU and in a gas jet

Literature	$a(^{63}$Cu,g.s.) (MHz)	$a(^{63}$Cu,e.s.) (MHz)
	5866.90871(2)	505.2 (8)
Experiment	$a(^{63}$Cu,g.s.) (MHz)	$a(^{63}$Cu,e.s.) (MHz)
ABU	5874.4(5)	505.0(5)
$\overline{\text{ABU}}$	5866.9(5)	505.8(5)
Gas jet	5873(2)	506(2)
$\overline{\text{Gas jet}}$	5870(2)	506(2)
Literature	$a(^{65}$Cu,g.s.) (MHz)	$a(^{65}$Cu,e.s.) (MHz)
	6284.38997(6)	542.9(16)
Experiment	$a(^{65}$Cu,g.s.) (MHz)	$a(^{65}$Cu,e.s.) (MHz)
ABU	6290.9(8)	539.9(8)
$\overline{\text{ABU}}$	6284.0(8)	541.0(8)

The correction to the WS7-60 wavelength meter output, discussed in the text, was applied to the data with the $\overline{X}$ mark [34–37]

The authors would like to thank both F. Karlewski (HighFinesse) for his efforts and the fruitful discussions and P. Imgram (TU Darmstadt) for his support with the transfer cavity setup at JYFL.

References

1. K. König, P. Imgram, J. Krämer, B. Maaβ, K. Mohr, T. Ratajczyk, F. Sommer, W. Nörtershäuser, On the performance of wavelength meters −− Part 2: frequency-comb based characterization revealing their relative limitations and offering opportunities for more accurate absolute wavelength determinations. Appl. Phys. B (2020). https://doi.org/10.1007/s00340-020-07433-4
2. B. Sanguinetti, H.O. Majeed, M.L. Jones, B.T. Varcoe, J. Phys. B At. Mol. Opt. Phys. **42**, 165004 (2009). https://doi.org/10.1088/0953-4075/42/16/165004
3. K. Saleh, J. Millo, A. Didier, Y. Kersalé, C. Lacroûte, Appl. Opt. **54**, 9446 (2015). https://doi.org/10.1364/ao.54.009446
4. L. Couturier, I. Nosske, F. Hu, C. Tan, C. Qiao, Y.H. Jiang, P. Chen, M. Weidemüller, Rev. Sci. Instrum. **89**, 043103 (2018). https://doi.org/10.1063/1.5025537
5. L.A. Johnson, H.O. Majeed, B. Sanguinetti, T. Becker, B.T. Varcoe, New J. Phys. **12**, 063028 (2010). https://doi.org/10.1088/1367-2630/12/6/063028
6. A. Koszorus, Precision measurements of the charge radii of potassium isotopes. Phys. Rev. C **100**, 034304 (2019)
7. K. Blaum, J. Dilling, W. Nörtershäuser, Phys. Scr. T **152**, 014017 (2013)
8. P. Campbell, I.D. Moore, M. Pearson, Prog. Part. Nucl. Phys. **86**, 127–180 (2016)
9. V.N. Fedosseev, Y. Kudryavtsev, V.I. Mishin, Phys. Scr. **85**, 058104 (2012). https://doi.org/10.1088/0031-8949/85/05/058104
10. B.A. Marsh, T.D. Goodacre, S. Sels, Y. Tsunoda, B. Andel, A.N. Andreyev, N.A. Althubiti, D. Atanasov, A.E. Barzakh, J. Billowes, K. Blaum, T.E. Cocolios, J.G. Cubiss, J. Dobaczewski, G.J. Farooq-Smith, D.V. Fedorov, V.N. Fedosseev, K.T. Flanagan, L.P. Gaffney, L. Ghys, M. Huyse, S. Kreim, D. Lunney, K.M. Lynch, V. Manea, Y.M. Palenzuela, P.L. Molkanov, T. Otsuka, A. Pastore, M. Rosenbusch, R.E. Rossel, S. Rothe, L. Schweikhard,

M.D. Seliverstov, P. Spagnoletti, C. Van Beveren, P. Van Duppen, M. Veinhard, E. Verstraelen, A. Welker, K. Wendt, F. Wienholtz, R.N. Wolf, A. Zadvornaya, K. Zuber, Nat. Phys. **14**, 1163 (2018). https://doi.org/10.1038/s41567-018-0292-8
11. R. Ferrer, A. Barzakh, B. Bastin, R. Beerwerth, M. Block, P. Creemers, H. Grawe, R. de Groote, P. Delahaye, X. Fléchard, S. Franchoo, S. Fritzsche, L.P. Gaffney, L. Ghys, W. Gins, C. Granados, R. Heinke, L. Hijazi, M. Huyse, T. Kron, Y. Kudryavtsev, M. Laatiaoui, N. Lecesne, M. Loiselet, F. Lutton, I.D. Moore, Y. Martínez, E. Mogilevskiy, P. Naubereit, J. Piot, S. Raeder, S. Rothe, H. Savajols, S. Sels, V. Sonnenschein, J.C. Thomas, E. Traykov, C. Van Beveren, P. Van den Bergh, P. Van Duppen, K. Wendt, A. Zadvornaya, Nat. Commun. **8**, 14520 (2017). https://doi.org/10.1038/ncomms14520
12. S. Raeder, T. Kron, R. Heinke, J.L. Henares, N. Lecesne, P. Schönberg, M. Trümper, K. Wendt, Hyperfine Interact. **238**, 15 (2017). https://doi.org/10.1007/s10751-016-1389-z
13. R. Neugart, J. Billowes, M. Bissell, K. Blaum, B. Cheal, K. Flanagan, G. Neyens, W. Nörtershäuser, D.T. Yordanov, J. Phys. G **44**, 064002 (2017)
14. Y. Kudryavtsev, R. Ferrer, M. Huyse, P. Van den Bergh, P. Van Duppen, Nucl. Instrum. Methods B **297**, 7 (2013). https://doi.org/10.1016/j.nimb.2012.12.008
15. K. Dockx, T.E. Cocolios, R. Ferrer, C. Granados, S. Kraemer, Y. Kudryavtsev, S. Sels, P. Van den Bergh, P. Van Duppen, M. Verlinde, E. Verstraelen, A. Zadvornaya, Nucl. Instrum. Methods B **463**, 297 (2020). https://doi.org/10.1016/j.nimb.2019.04.082
16. S. Rothe, B.A. Marsh, C. Mattolat, V.N. Fedosseev, K. Wendt, J. Phys. Conf. Ser. **312**, 052020 (2011)
17. S. Raeder, S. Fies, H. Tomita, K.D.A. Wendt, T. Iguchi, K. Watanabe, in *booktitle AIP Conference Proceedings* (publisher AIP, 6–10 October 2008). p. 96–101
18. H. Tomita, C. Mattolat, T. Kessler, S. Raeder, F. Schwellnus, K.D.A. Wendt, K. Watanabe, T. Iguichi, J. Nucl. Sci. Technol. **45**, 37 (2008)
19. V. Sonnenschein, S. Raeder, A. Hakimi, I.D. Moore, K. Wendt, J. Phys. B **45**, 165005 (2012)
20. A. Hakimi, T. Fischbach, S. Raeder, N. Trautmann, K. Wendt, Hyperfine Interact. **216**, 59 (2013)
21. R. Heinke, T. Kron, S. Raeder, T. Reich, P. Schönberg, M. Trümper, C. Weichhold, K. Wendt, Hyperfine Interact. **238**, 127 (2017)
22. T. Kessler, H. Tomita, C. Mattolat, S. Raeder, K. Wendt, Laser Phys. **18**, 842 (2008)
23. V. Sonnenschein, I.D. Moore, S. Raeder, M. Reponen, H. Tomita, K. Wendt, Laser Phys. **27**, 085701 (2017)
24. W. Zhao, J. Simsarian, L. Orozco, G. Sprouse, Rev. Sci. Instrum. **69**, 3737 (1998)
25. D. Studer, J. Ulrich, S. Braccini, T.S. Carzaniga, R. Dressler, K. Eberhardt, R. Heinke, U. Köster, S. Raeder, K. Wendt, Eur. Phys. J. A **56**, 69 (2020). https://doi.org/10.1140/epja/s10050-020-00061-8
26. J. Krämer, K. König, C. Geppert, P. Imgram, B. Maaß, J. Meisner, E. Otten, S. Passon, T. Ratajczyk, J. Ullmann, W. Nörtershäuser, Metrologia **55**, 268 (2018)
27. P. Imgram, K. König, J. Krämer, T. Ratajczyk, R. Müller, A. Surzhykov, W. Nörtershäuser, Phys. Rev. A **99**, 012511 (2019)
28. I. Moore, T. Eronen, D. Gorelov, J. Hakala, A. Jokinen, A. Kankainen, V. Kolhinen, J. Koponen, H. Penttilß, I. Pohjalainen, M. Reponen, J. Rissanen, A. Saastamoinen, S. Rinta-Antila, V. Sonnenschein, and J. Äystö, Nucl. Instrum. Methods B **317**, 208 (2013). xVIth International Conference on ElectroMagnetic Isotope Separators and Techniques Related to their Applications, December 2–7, 2012 at Matsue, Japan. https://doi.org/10.1016/j.nimb.2013.06.036
29. R. de Groote, A. de Roubin, P. Campbell, B. Cheal, C. Devlin, T. Eronen, S. Geldhof, I. Moore, M. Reponen, S. Rinta-Antila, M. Schuh, Nucl. Instrum. Methods B **463**, 437 (2019)
30. B. Cheal, M. Gardner, M. Avgoulea, J. Billowes, M. Bissell, P. Campbell, T. Eronen, K. Flanagan, D. Forest, J. Huikari, A. Jokinen, B. Marsh, I. Moore, A. Nieminen, H. Penttilä, S. Rinta-Antila, B. Tordoff, G. Tungate, J. Äystö, Phys. Lett. B **645**, 133 (2007). https://doi.org/10.1016/j.physletb.2006.12.053
31. A. Zadvornaya, P. Creemers, K. Dockx, R. Ferrer, L.P. Gaffney, W. Gins, C. Granados, M. Huyse, Y. Kudryavtsev, M. Laatiaoui, E. Mogilevskiy, S. Raeder, S. Sels, P. Van Den Bergh, P. Van Duppen, M. Verlinde, E. Verstraelen, M. Nabuurs, D. Reynaerts, P. Papadakis, Phys. Rev. X **8**, 41008 (2018). https://doi.org/10.1103/PhysRevX.8.041008
32. R.P. De Groote, M. Verlinde, V. Sonnenschein, K.T. Flanagan, I. Moore, G. Neyens, Phys. Rev. A **95**, 1 (2017). https://doi.org/10.1103/PhysRevA.95.032502
33. W. Gins, R.P. de Groote, M.L. Bissell, C.G. Buitrago, R. Ferrer, K.M. Lynch, G. Neyens, S. Sels, Comput. Phys. Commun. **222**, 286 (2018). https://doi.org/10.1016/j.cpc.2017.09.012
34. P. Vingerhoets, Nuclear structure of Cu isotopes studied with collinear laser spectroscopy, Ph.D. thesis, school KU Leuven (2011)
35. G. Hermann, G. Lasnitschka, C. Schwabe, D. Spengler, Spectrochim. Acta Part B **48B**, 1259 (1993). https://doi.org/10.1016/0584-8547(93)80110-G
36. H. Figger, D. Schmitt, S. Penselin, Colloq. Int. C.N.R.S **164**, 355 (1967)
37. H. Bucka, J. Ney, P. Wirtnik, Zeitschrift für Physik **202**, 22 (1967)

4.6 Publication V: High-resolution laser resonance ionization spectroscopy of $^{143-147}$Pm

The following manuscript was published as a regular article in the European Physical Journal A: Hadrons and Nuclei **56**, 69 (2020) DOI 10.1140/epja/s10050-020-00061-8. Based on the laser ionization schemes developed in the scope of Publication III, more challenging high-resolution spectroscopic experiments on Pm were prepared at the RISIKO mass separator, using the novel PI-LIST ion source module [41]. First, the feasibility was demonstrated using the remains of the ^{147}Pm sample from the previous broadband spectroscopic measurements. Afterwards, a number of long-lived Pm isotopes were produced by proton irradiation of natural Nd at the Bern medical cyclotron, followed by chemical purification at PSI Villigen. The sample solution delivered to Mainz contained about 10^{12} atoms per isotope of $^{143-147}$Pm, which is a factor of ≈ 100 lower than the previously used ^{147}Pm sample, and included an isobaric contamination of Pm : Nd $\approx 1 : 100$ after chemical separation. Under these challenging conditions, i.e. low sample amounts and high isobaric contamination, the experiment was a perfect test case for the PI-LIST performance. Additionally, it marks the first precision laser spectroscopy of neutral Pm. The measured hyperfine spectra and isotope shifts could be used to determine electromagnetic moments and changes in mean square charge radii for the investigated isotopes. Some of these properties were measured for the first time, while others improved existing literature values. Altogether the experiment set an important stepping stone towards on-line laser spectroscopy on Pm isotopes, most probably using the PI-LIST, which is currently tested and adapted for on-line application after the long shutdown at CERN in 2021.

Author contribution

The author performed the major part of the experimental set-up and spectroscopic measurements, which are the central topic of this publication, with support of R.H. and S.R. during the ion source and laser setup, respectively. The ^{147}Pm sample production was performed by U.K. at ILL. J.U. coordinated the production of the cyclotron samples in collaboration with S.B. and T.S.C. (AEC-LHEP Bern), and afterwards performed the chemical separation at PSI. The author evaluated the spectroscopic data and prepared the manuscript draft. This project was supervised by R.D. and K.W. Note that this article features an authors contributions section, where individual tasks are summarized.

Eur. Phys. J. A (2020) 56:69
https://doi.org/10.1140/epja/s10050-020-00061-8

THE EUROPEAN PHYSICAL JOURNAL A

Regular Article - Experimental Physics

High-resolution laser resonance ionization spectroscopy of $^{143-147}$Pm

Dominik Studer[1,a], **Jiri Ulrich**[2], **Saverio Braccini**[3], **Tommaso Stefano Carzaniga**[3], **Rugard Dressler**[2], **Klaus Eberhardt**[4], **Reinhard Heinke**[1], **Ulli Köster**[5], **Sebastian Raeder**[6,7], **Klaus Wendt**[1]

[1] Institut für Physik, Johannes Gutenberg-Universität Mainz, 55099 Mainz, Germany
[2] Paul-Scherrer Institut, 5232 Villigen, Switzerland
[3] Albert Einstein Center for Fundamental Physics, Laboratory for High Energy Physics, University of Bern, 3012 Bern, Switzerland
[4] Institut für Kernchemie, Johannes Gutenberg-Universität Mainz, 55099 Mainz, Germany
[5] Institut Laue-Langevin, 38042 Grenoble, France
[6] Helmholtz-Institut Mainz, 55099 Mainz, Germany
[7] GSI Helmholtzzentrum für Schwerionenforschung, 64291 Darmstadt, Germany

Received: 9 October 2019 / Accepted: 7 January 2020

Communicated by Ari Jokinen

Abstract We present the results of high-resolution laser spectroscopy of the long-lived radioactive isotopes $^{143-147}$Pm. The hyperfine structures and isotope shifts in two different atomic ground-state transitions at 452 nm and 468 nm were probed by in-source laser spectroscopy at the RISIKO mass separator in Mainz, using the PI-LIST ion source. From the hyperfine coupling constants the nuclear magnetic dipole and electric quadrupole moments for $^{143-147}$Pm were derived, and the measured isotope shifts allowed the extraction of changes in nuclear mean square charge radii.

1 Introduction

High-resolution laser spectroscopy of atomic transitions can be used as a high precision, model-independent probe for a number of fundamental properties of nuclear ground states or long-lived isomers. The analysis of hyperfine splittings allows the extraction of nuclear spin, magnetic dipole moment and electric quadrupole moment, while isotope shifts are linked to changes in mean square charge radii along a series of isotopes [1–3]. During the last decades, with the use of radioactive ion beam facilities based on the Isotope Separation On-Line (ISOL) technique in combination with sensitive laser spectroscopy methods, such studies continued to push further away from the valley of beta-stability, towards very exotic short-lived radioisotopes. In this regard the region of lanthanide elements is one of the most thoroughly studied along the entire chart of nuclei. Promethium (Pm, $Z = 61$), however, marks a gap in the map of investigated nuclei [1], which can be attributed to its exclusively radioactive nature and its complex atomic spectrum, rendering preparatory experiments difficult.

Precision spectroscopy in the Pm isotopic chain is of high relevance to gain information on nuclear moments and for the study of nuclear shape transition phenomena. Leander et al. expect a transition from spherical nuclei to a regime of strong deformation towards neutron deficient isotopes in the light lanthanide region, which is predicted to be best accessible (at $N < 75$) and particularly sharp in the case of Pm [4]. On the neutron-rich side, the shape transition to deformed nuclei for $N > 88$ can be studied. The influence of ^{146}Gd, which shows certain features typical for a doubly magic nucleus [5], has been related to the abrupt change in charge radii in this region. Budick et al. observe a remarkable degree of deformation in ^{151}Pm compared to ^{147}Pm, measured via atomic beam magnetic resonance (ABMR) [6], similar to what has been observed for the corresponding isotones of Eu [7]. Although we cannot access these neutron numbers in our off-line experiment, a valuable basis for on-line studies can be established.[1]

Modern cyclotrons are capable of producing a number of long-lived Pm isotopes in relevant quantities and with suitable specific activity, rendering laser spectroscopic experiments feasible. In the historical context Pm spectroscopy is not entirely new, however, experiments were most often limited to the easiest accessible isotope, ^{147}Pm. First hyper-

[a] e-mail: dstuder@uni-mainz.de (corresponding author)

[1] In this context, on-line means the experiment is coupled to the isotope production site, enabling experiments on short-lived nuclei.

Published online: 24 February 2020

fine patterns were measured in the 1960s by Klinkenberg et al. [8] and Reader et al. [9]. In these experiments, milligram amounts of ^{147}Pm were used in both, electrodeless discharge or hollow cathode light sources and studied using grating-based and Fabry–Pérot spectrographs. Although several hundred lines were measured, the assignment of the associated energy levels was not possible in most cases, and sometimes even the information was lacking whether a specific line belongs to the spectrum of neutral (Pm I) or singly ionized (Pm II) promethium. Nonetheless, a nuclear spin of $I = +7/2$ and nuclear moments of $\mu_I = 2.58(7)\,\mu_N$ and $Q_s = 0.74(20)\,e$b for ^{147}Pm could be extracted, which are the most precise values until today (together with values obtained from complementary measurement methods). First direct excitation spectroscopy was performed in the 1990s by Alkhazov et al. [10] and Otto et al. [11] by means of collinear fast beam laser spectroscopy using dye lasers. In both experiments transitions in the spectrum of Pm II were studied. Alkhazov et al. also had ^{145}Pm at their disposal, which was produced in the reaction ^{144}Sm$(n,\gamma)^{145}$Sm(EC)^{145}Pm, and accordingly also extracted nuclear moments for this nuclide, with the precision limited by the reference nuclear moments in ^{147}Pm [12].

Other than these laser spectroscopic studies on Pm II transitions, our work is dedicated to the study of Pm I. In the scope of our recent work on the atomic structure of neutral Pm, we identified several laser ionization schemes and determined the first ionization potential of Pm [13]. Utilizing these schemes, two atomic ground state transitions at 452 nm and 468 nm are investigated here. In contrast to many state-of-the-art spectroscopy experiments based on collinear laser spectroscopy of fast atom- or ion beams, we performed in-source spectroscopy directly in the atomic beam effusing from a hot atom source. This concept is implemented in the PI-LIST (perpendicularly illuminated laser ion source and trap), which presents a complementary technique to collinear laser spectroscopy and has undergone various performance tests on stable and radioactive species lately [14].

2 Experimental setup

2.1 Sample production and purification

The samples for our experiment originate from two different production routes. One sample, containing some 10^{14} atoms of ^{147}Pm, was produced by neutron activation of enriched ^{146}Nd at the high-flux reactor at ILL Grenoble and purified at PSI Villigen. For details on the production we refer to [15]. Part of this sample was already used for our studies of the atomic structure of Pm [13]. Other suitable isotopes for offline experiments are ^{143,144,145,146,148m}Pm, with half-lives of at least some 10 of days, which is required for chemical purification and shipping. To complement the isotopes accessible by neutron irradiation we opted for proton irradiation of a natural neodymium target, which was performed at the 18 MeV proton cyclotron at Bern University Hospital [16]. A target pellet with 1 cm diameter and thickness of 0.65 mm was pressed from a mixture of natural Nd_2O_3 and graphite powder with a total weight of 113 mg. The addition of approx. 25 wt% graphite as binding agent was necessary to increase the mechanical stability of the pressed pellet, which was then encapsulated in an aluminum sample holder and irradiated with an integrated current of approximately 12 µAh. After irradiation, the pellet was removed from the aluminum holder, the Nd_2O_3 was dissolved in 7M HNO_3 and the graphite was removed by filtration. The radiochemical separation of the produced Pm isotopes from the Nd bulk material was performed by ion exchange chromatography on the SYKAM cation exchange resin, following the procedure described in [15]. As a tracer of the Nd-fraction during the chemical separation, 1 MBq of ^{147}Nd was produced by neutron activation of a natural Nd_2O_3 solution in the TRIGA research reactor at the Department of Nuclear Chemistry at Mainz University, and afterwards shipped to PSI Villigen, where the radiochemical separation took place. An ICP-MS analysis of the Pm fraction was performed after separation. A Nd:Pm ratio of approx. 100:1 indicates a decontamination factor of Pm from Nd of around $6\cdot10^5$. A separate publication with detailed information on the production and separation is in preparation, in which also half-life measurements of ^{143,144}Pm will be presented [17].

Table 1 comprises all Pm nuclides which were produced in relevant quantities. Half-lives are taken from the Evaluated Nuclear Structure Data File (ENSDF, [18]). The activity was measured via γ-spectroscopy at PSI Villigen, and the atom number of each nuclide n was derived from the γ-activity. No γ-lines for ^{145}Pm and ^{147}Pm could be observed in the

Table 1 Composition of the Pm sample produced by irradiation of a Nd_2O_3 target with 12 µAh of 18 MeV protons. Half-lives were taken from [18]. The activity and atom number n were determined by γ-spectroscopy. The mass ratio was measured via RIMS (see Fig. 1) 19 days after production

Nuclide	$T_{1/2}$	Activity (kBq)	$n/10^{12}$	Mass ratio (%)
^{143}Pm	265(7) d	60.7(7)	2.00(6)	17.2(15)
^{144}Pm	363(14) d	84.9(8)	3.8(2)	35.2(24)
^{145}Pm	17.7(4) y			17.6(15)
^{146}Pm	5.53(5) y	6.9(2)	1.74(6)	18.7(16)
^{147}Pm	2.6234(2) y			9.9(11)
^{148}Pm	5.368(7) d	116(2)	0.077(1)	1.1(3)∗
^{148m}Pm	41.29(11) d	18.1(2)	0.093(1)	

The value of 1.1(3)% marked with an asterisk gives the combined mass ratio for ^{148}Pm and ^{148m}Pm

γ-spectra and thus no activity and atom numbers could be determined by means of γ-spectroscopy for these isotopes. This is expected as both isotopes have significantly longer half-lives, resulting in lower emission rates of their decay radiation in the sample. Furthermore, the γ-ray emission probabilities during the decay of both isotopes are low in general (especially for ^{147}Pm they are well below 10^{-4}). The possibly detectable line of ^{145}Pm at 72.5 keV is obscured in the measured spectrum with the much more prominent $K\alpha_2$ line of lead at 72.8 keV, originating from X-ray fluorescence of the detector shielding. For an additional analysis of the sample composition, mass spectra were recorded via resonance ionization mass spectrometry (RIMS). The RIMS measurements were performed 19 days after the γ-spectroscopy (details on this measurement are discussed in Sect. 2.3). While RIMS itself does not give information about absolute atom numbers, the isotope ratios can be compared with the ones from γ-spectroscopy. The ratios match within the uncertainties (with consideration of the decay time), so we can conclude that atom numbers of ^{145}Pm and ^{147}Pm are also in the order of 10^{12} atoms, similar to the other long-lived isotopes ^{143,144,146}Pm.

2.2 Laser setup

Our Pm laser ion source relies on two different laser ionization schemes, which we developed in our previous work [13]. Both schemes use three laser steps $\lambda_1, \lambda_2, \lambda_3$ to consecutively excite sample atoms to higher lying atomic states, with the final state having an excitation energy above the first ionization potential and thus undergoing auto-ionization.

$$0 \xrightarrow[\lambda_1]{452\,\text{nm}} 22\,080.06 \xrightarrow[\lambda_2]{887\,\text{nm}} 33\,352.2 \xrightarrow[\lambda_3]{849\,\text{nm}} 45\,135.8 \quad \text{(A)}$$

$$0 \xrightarrow[\lambda_1]{468\,\text{nm}} 21\,348.21 \xrightarrow[\lambda_2]{882\,\text{nm}} 32\,683.7 \xrightarrow[\lambda_3]{804\,\text{nm}} 45\,128.4 \quad \text{(B)}$$

All level energies are given in units of cm^{-1}.

By measuring the number of produced ions as a function of the laser wavelength, spectroscopy can be performed. The ionization schemes will be abbreviated in the following by (A) and (B), respectively, where λ_1 is the spectroscopy transition in both schemes. Each step was driven by a 10 kHz repetition rate pulsed Ti:sapphire laser, with pulse lengths of 40–60 ns, an average output power of 3–4 W, and a spectral linewidth of 5–10 GHz. For a detailed description of these home-built "Z-cavity" lasers, which are in use at on-line radioactive ion beam facilities worldwide, see e.g. [19,20]. Since λ_1 is in the blue wavelength regime, we generated the second harmonic intra-cavity, using a beta barium borate (BBO) crystal. For measuring hyperfine spectra we can alternatively produce λ_1 by an injection-locked Ti:sapphire laser with a Fourier-limited linewidth of $\approx$ 20 MHz for the spectroscopy transition [21,22], seeded by an external cavity diode laser (master ECDL). In this case the second harmonic was generated outside the cavity by focusing the laser into a BBO crystal in simple single-pass transmission. For the master ECDL we used two different laser diodes: Eagleyard RWE-920 and RWE-980 for scheme (A) and (B), respectively. It was stabilized with an iScan unit (TEM Messtechnik GmbH). For a relative laser frequency measurement we simultaneously recorded the output of the master ECDL and a stabilized HeNe laser (SIOS SL-03) in a home-built scanning Fabry–Pérot-interferometer (S-FPI) with a free spectral range of 299.721 MHz and a finesse of $\mathcal{F} \approx 400$. The frequency offset to an arbitrary anchor point can be deduced from the distance of the transmission fringes of the master ECDL laser when using the transmission fringes of the HeNe as a ruler. For a complementary, absolute frequency measurement we used a wavelength meter (High Finesse WSU-30). An additional ECDL (Toptica DL pro 780), locked to a Rb saturation absorption spectroscopy unit (TEM CoSy 4.0) served as a calibration source for the wavelength meter. Note that in a comparative study of the wavelength meter and the S-FPI readout, performed at different laboratories, we observed periodic deviation patterns which necessitate a correction to recorded spectra [23]. The data presented here was corrected for this periodic behavior by subtracting a frequency deviation term, according to Eq. 1 in [23], from the wavelength meter data. A drift correction was not applied to the data, but rather a frequent calibration of the wavelength meter to the reference laser (see section IIIB in [23]). The reference also provides a more detailed description of the cw-laser setup.

2.3 Ion source setup

The laser spectroscopy was performed at the RISIKO mass separator at JGU Mainz, using the resonance ionization spectroscopy technique. The used setup, i.e. its standard configuration, is described in [24]. The sample solution was dried on a titanium carrier foil, folded and put into a tubular tantalum atomizer, which can be resistively heated up to 2000 °C. For the experiment we used a refined version of the well-proven Laser Ion Source and Trap (LIST) [25–27]. It features a dual repeller electrode on the side facing the atomizer oven, a rf quadrupole for radial confinement of ions, and an exit electrode to prevent field leakage of the strong extraction potential in the LIST volume. It has two modes of operation. When operated in ion-guide (IG) mode both repellers are set on a negative voltage, so that positive ions are extracted from the source. The ions are guided towards the exit electrode by the rf field. Upon passing the exit electrode, they are accelerated to 30 keV (from the source potential at + 30 kV towards the grounded extraction electrode). The IG mode

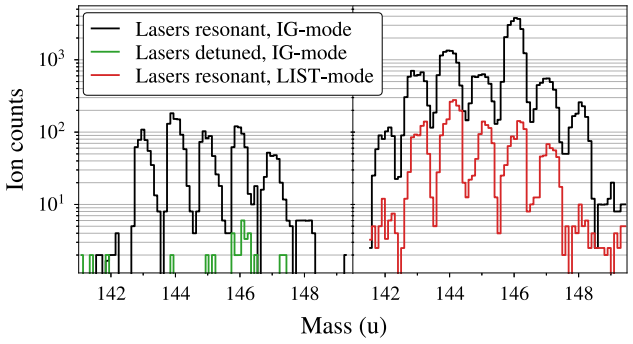

Fig. 1 Mass spectra of the cyclotron-produced Pm samples. Left panel: Cold ion source. Right panel: Hot ion source at ≈ 1500 °C. For details see text

resembles the standard laser ion source operation without a LIST unit, with an efficiency loss factor of < 2 [25]. In the second mode of operation (LIST mode) one repeller is set on a positive voltage, so that ionized species from the source region (e.g. via surface ionization) are suppressed. The negative repeller electrode deflects electrons emitted from the hot oven, preventing electron impact ionization within the LIST volume. The LIST mode thus offers a suppression of ions which are produced independently of the laser, in particular isobaric contaminants which cannot be mass-separated. Since laser-ionized species from the source region are lost, this gain in ion beam purity comes at the cost of ionization efficiency. Despite this trade-off this technique offers unique opportunities whenever the ion beam composition is dominated by isobars of the nuclides of interest, which cause strong background. In the present experiment this was the case for e.g. Nd isotopes from the cyclotron target. Figure. 1 shows mass scans in the Pm region for different ion source conditions. For these scans we used the broadband laser system tuned to scheme (A), so that full hyperfine splittings and isotope shifts were covered by the laser linewidth and all Pm isotopes were equally ionized. In the left panel, no heating current is applied to the atomizer and the LIST is operated in IG-mode. The release of sample atoms was caused by heating of the atomizer by the incident laser beams. In this situation the influence of the laser ionization scheme could be well tested, as the contribution of surface ionization was negligible. We observe the isotope ratio as expected from the γ-spectroscopy measurements given in Table 1, with a slight interference of about 3 % intensity at mass 146, occurring when the lasers were detuned from the Pm ionization scheme. In the right panel, at a temperature of approximately 1500 °C, the measured isotope ratios in IG-mode are significantly different. The dominant components of the surface ionized pattern are expected to be atomic neodymium from the cyclotron target and a so-far unidentified species on mass 146. The latter was weakly influenced by the 452 nm laser radiation and shows a pattern of equidistant resonances with a ≈ 4.2 GHz spacing. We therefore presume a molecular species (possibly in a higher charge state) where a vibrational band was excited by the laser light, and which was subsequently ionized non-resonantly by a second photon.

When switching to LIST-mode, these contaminants were suppressed and the ion beam composition was similar to the one of the cold ion source. Isotope ratios were measured with both, a cold source in IG-mode and with the hot source in LIST-mode in good agreement, mean values are given in Table 1. In the following, for the high-resolution spectroscopy application, the ion source was exclusively operated in LIST-mode, introducing the injection seeded probe laser for the spectroscopy transition in perpendicular geometry [14]. The probe laser beam was horizontally widened with a profile of approximately 40 mm × 2 mm for a large overlap area with the ionizing lasers. A sketch of the experimental arrangement is given in Fig. 2.

3 Hyperfine spectroscopy

The hyperfine splittings of both spectroscopy transitions, at 452 nm and 468 nm, are schematically illustrated in Fig. 3. The positions and spacings of the arrows indicating individual hyperfine transitions are chosen in such a way that they depict the position of the respective line in the spectrum, as plotted exemplarily for the case of ^{147}Pm. In order to achieve a sufficiently narrow experimental linewidth to resolve the hyperfine patterns, several parameters which are specific to the ionization scheme were characterized. Firstly, the power of the spectroscopy laser has to be properly chosen to prevent saturation broadening of the spectral lines. The laser power influence on the two spectroscopy transitions of interest was measured, and is shown in the left panels of Fig. 4. In scheme (A) we chose the $F = 6 \rightarrow F' = 5$ transition and in scheme (B) the $F = 5 \rightarrow F' = 6$ transition between the ground state and the respective first excited state. A fit according to the procedure described in [28] yields saturation powers (defined as the power at which half of the maximum ion signal is reached) of $P_s^{452} = 8(2)$ mW and $P_s^{468} = 0.6(2)$ mW for the transitions at 452 nm and 468 nm, respectively. As not all components of the hyperfine spectrum were investigated and the values are specific to the individual hyperfine transitions, these values are used as guide figures to estimate the power threshold upon which saturation broadening occurs. In the earlier broadband spectroscopy experiment [13] we measured a comparable saturation power of $P_{s,\mathrm{ref}}^{452} = 7(4)$ mW in the first step of scheme (A). In scheme (B), however, the earlier measured value of $P_{s,\mathrm{ref}}^{468} = 10(5)$ mW deviates by an order of magnitude from the value in this work, which is ascribed to different operation conditions, i.e. a change of the laser power density by a variation in the laser beam profile, as well as the relatively high intensity of the $F = 5 \rightarrow F' = 6$

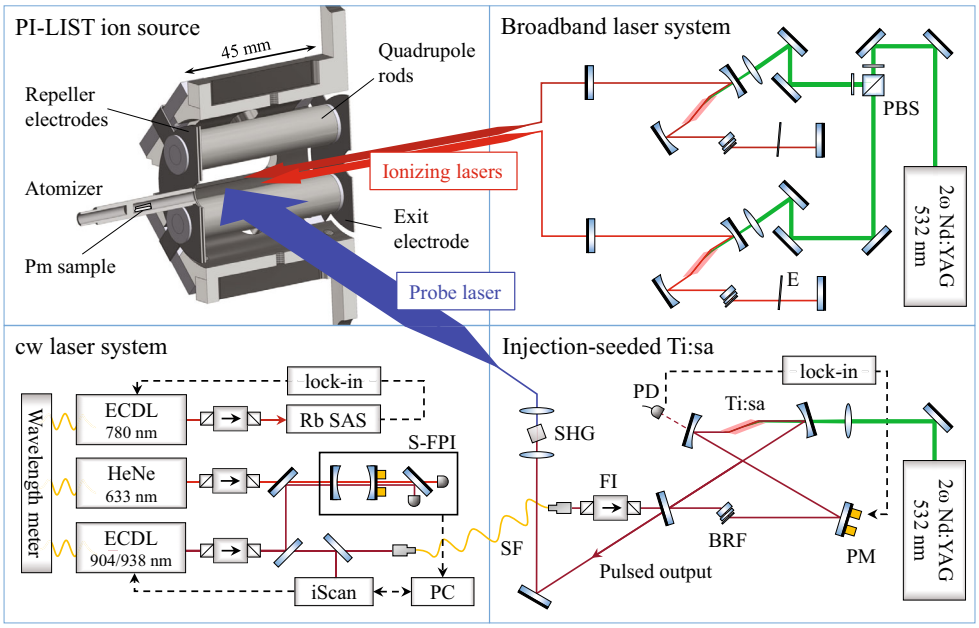

Fig. 2 Sketch of the experimental setup. Top left: vertical cross section of the PI-LIST ion source unit with indicated incident laser beams. For the sake of clarity the mounting and heat shielding of the resistively heated atomizer is not shown. Top right: broadband pulsed Ti:sapphire lasers for ionizing transitions. Bottom left: cw laser system with seeding diode laser and frequency measurement references. Bottom right: pulsed, injection-seeded Ti:sapphire ring cavity for spectroscopy transition. A legend for the used abbreviations is given on the right

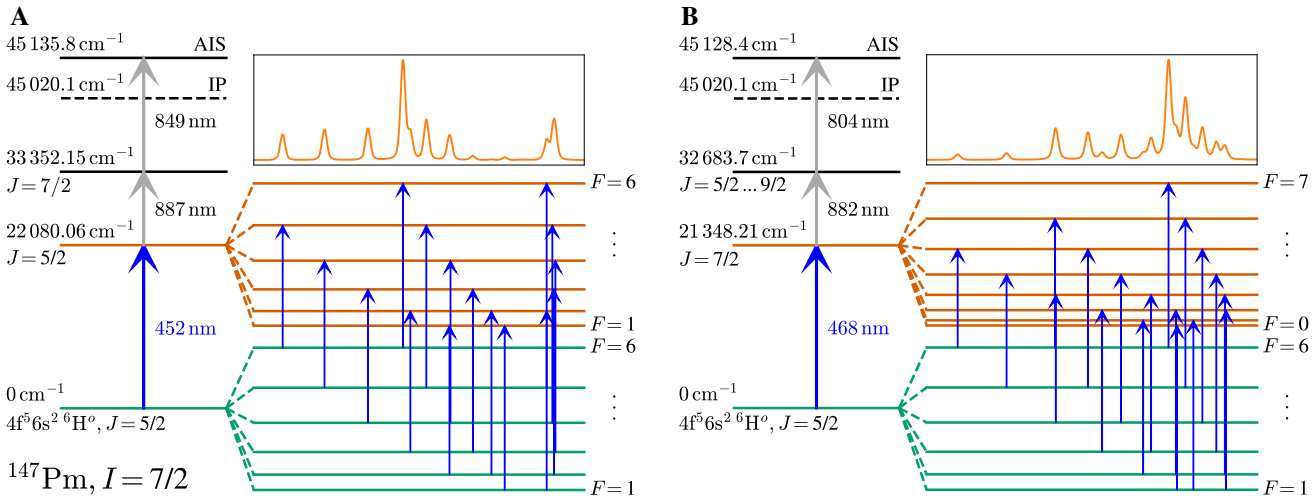

Fig. 3 Excitation schemes (**A**) (left) and (**B**) (right) illustrating the hyperfine splitting of the atomic ground state and respective first excited state. The blue arrows indicate allowed hyperfine transitions, with the positions chosen in relation to the example spectrum presented above. For the spectrum we chose the fit function to our ^{147}Pm data. IP: Ionization potential; AIS: Auto-ionizing state

transition in the pattern of the 468 nm transition. For hyperfine spectroscopy in the 452 nm and 468 nm transitions, the first excitation laser were correspondingly operated at 5 mW and 0.5 mW, respectively.

Another spectral line broadening effect is caused by the high-power ionization lasers, which couple the excited state to the ionization continuum. When the probe and the ionization lasers are synchronized, the lifetime of the excited state is effectively shortened, causing a line broadening [29]. In order to avoid this effect, the ionization laser has to be decoupled from the excitation step by temporal delay. However, depending on the excited state lifetime, the population decay causes a certain loss in efficiency. The loss factor was measured for the transitions of interest by simultaneous and stepwise shifting the second- and third laser (λ_2, λ_3) pulse delays relative to the spectroscopy excitation. Since the probe laser is pumped by a separate pump laser, the second- and third laser pulses can be delayed simultaneously by adjust-

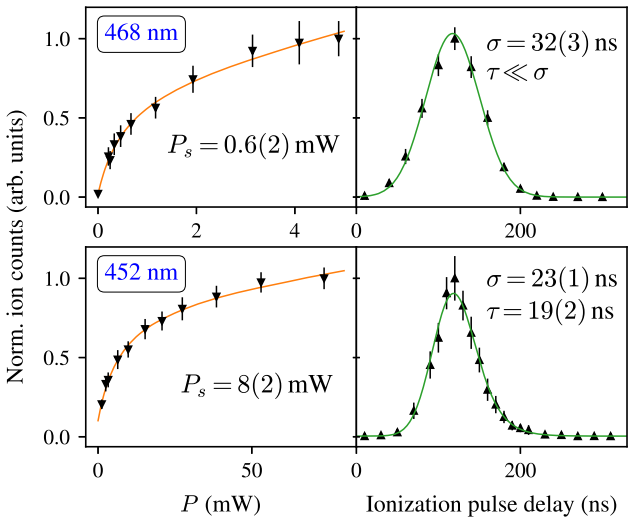

Fig. 4 Laser power (left) and ionization pulse delay (right) influence on the ion signal for the transitions at 468 nm and 452 nm. Saturation curves (orange) are fitted according to [28]. The lifetime is fitted with a convolution of a Gaussian distribution with an exponential decay law (green). The zero-point of the ionization pulse delay is arbitrary

ing the pump laser triggers relative to each other. The probe laser was tuned to the same hyperfine transitions as used in the measurement of saturation powers, with a power of 70 mW in the 452 nm transition and 5 mW in the 468 nm transition. The response of the ion signal is shown in the right panels of Fig. 4. It can be fitted with a convolution of the approximately Gaussian laser pulse shape with an exponential decay contribution for the lifetime of the excited state [30]. In the case of the 452 nm transition, a lifetime of $\tau_{452} = 19(2)$ ns is extracted for the upper state. For the 468 nm transition, however, the signal shape is completely dominated by the Gaussian contribution. The larger Gaussian standard deviation compared to the measurement in the 452 nm transition is caused by the laser operation near the edge of the Ti:sapphire gain profile, leading to an extended laser pulse length. As a consequence the lifetime of the excited state of the 468 nm transition can only be constrained to be significantly shorter than the laser pulse length. This finding is consistent with the much lower saturation power compared to the 452 nm transition. For the spectroscopy experiment a delay between 30 and 50 ns was chosen for both transitions, as a reasonable compromise between linewidth and efficiency. In the 452 nm transition, we measured an efficiency loss factor of ≈ 6 for a delay of 30 ns and a laser power of 5 mW, while the linewidth improved to a value of ≈ 150 MHz full width at half maximum (FWHM), down from ≈ 250 MHz FWHM as determined without delay and with ≈ 70 mW laser power.

Scans of the hyperfine spectra were performed by tuning the ECDL master laser in steps of 10 MHz while recording the ion signal. Depending on the counting statistics for the measured isotope, data was taken for 3–5 s per step, so that one spectrum took approximately 1–2 h to record. The wavelength meter was calibrated to the Rb-locked ECDL every 10 steps in order to keep drifts of the wavelength readout at minimum. This is particularly important since one isotope at a time is measured, and the accuracy of extracted isotope shifts relies on the reproducibility of the data. The recorded spectra are shown in Fig. 5. For all isotopes, with the exception of ^{143}Pm, at least two datasets could be recorded per isotope and transition. In the 452 nm transition the spectral resolution varies between 100 and 170 MHz FWHM, whereas the 468 nm spectra are somewhat inferior with regard to counting statistics and linewidths lying between 150 and 250 MHz FWHM. The spectra were fitted with a sum of Voigt profiles, using the SATLAS python package [31], which is tailored to the evaluation of hyperfine spectra. The nuclear spins of each isotope could be fixed to literature values (^{143}Pm: [32], ^{144}Pm: [33], ^{145}Pm: [10], ^{146}Pm: [34], ^{147}Pm: [10,35], with the values comprised in Table 3). In order to estimate the statistical uncertainties, all datasets were fitted with both, the wavelength meter and the S-FPI laser frequency data, and for three different binning sizes. The resulting fit parameters were averaged and the standard deviation taken as uncertainty. Afterwards, for different datasets of one isotope, a weighted average was determined. For the isotope shifts we added a systematic error of 4 MHz, based on the stability of the ^{87}Rb saturated absorption spectroscopy, which serves as reference for the wavelength meter. In both transitions, the data for the ^{147}Pm isotope has the highest quality in terms of linewidth and counting statistics, since the scan was performed with a dedicated sample with larger atom numbers ($\approx 3\times10^{12}$ atoms), whereas the cyclotron-produced samples were comparatively small (few 10^{11} atoms) and suffered a larger Nd contamination. Additionally, ^{147}Pm has the highest nuclear quadruple moment Q_s among the studied isotopes. For these reasons it was used as a reference for the ratio of the electric quadrupole hyperfine coupling constant of lower and upper level, i.e. $\mathcal{B}^l/\mathcal{B}^u$, which is expected to be constant over the series of isotopes [1]. Correspondingly, in the fits of both transitions, this ratio was fixed to the result of ^{147}Pm in the SATLAS fit of the other isotopes. Also, for reasons of superior data quality in the 452 nm transition, $\mathcal{B}^l_{468}$ was fixed to $\mathcal{B}^l_{452}$, since both transitions couple to the atomic ground state. The magnetic dipole hyperfine coupling constants $\mathcal{A}_l$ and $\mathcal{A}_u$, on the other hand, remained a free parameter in all fits.

The final values for isotope shifts $\delta\nu$, as well as $\mathcal{A}$- and $\mathcal{B}$-parameters are given in Table 2. The resulting $\mathcal{A}^l/\mathcal{A}^u$ ratios for both transitions remained within the statistical uncertainty ($\mathcal{A}^l_{452}/\mathcal{A}^u_{452} = 1.2401(2)$, $\mathcal{A}^l_{468}/\mathcal{A}^u_{468} = 1.455(10)$). From the two independent parameters $\mathcal{A}^l_{452}$ and $\mathcal{A}^l_{468}$, which are also expected to be identical as both transitions couple to the atomic ground state, we estimate an additional error of 1 MHz for all $\mathcal{A}$ hyperfine coupling constants (which is included in

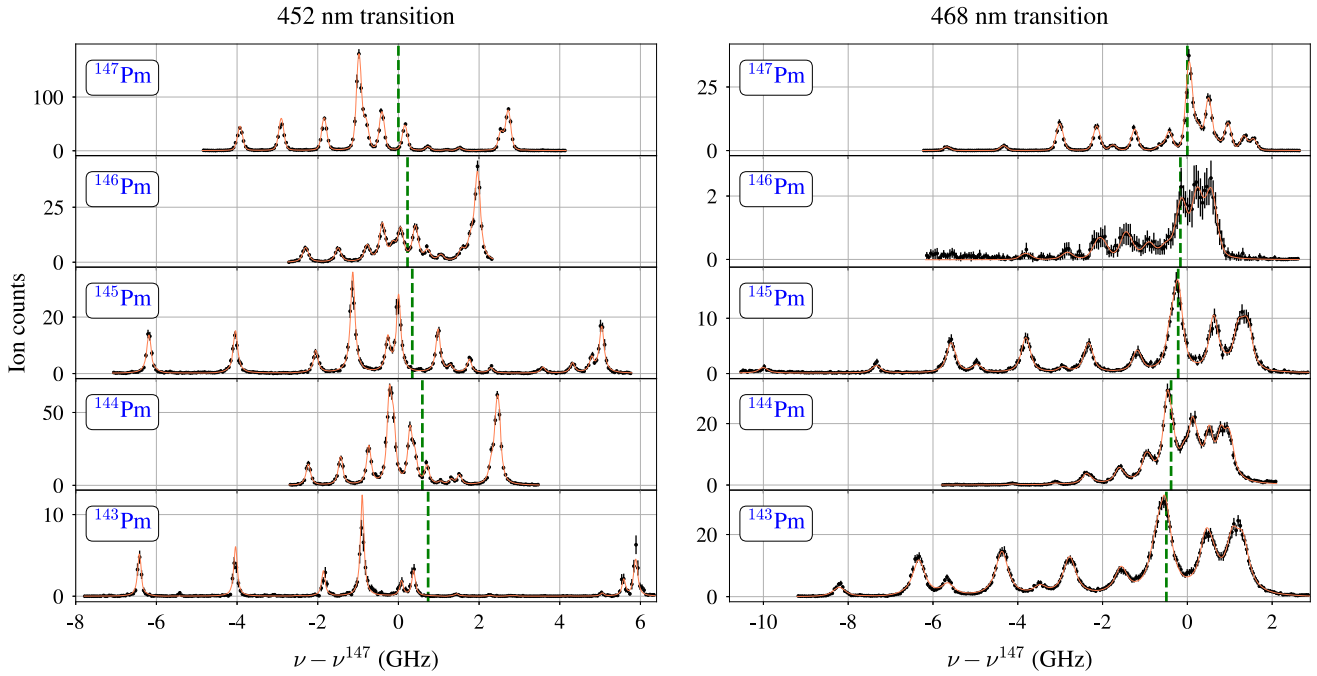

Fig. 5 Measured hyperfine spectra in the ground state transitions of scheme (**A**) at 452 nm (left) and of scheme (**B**) at 468 nm (right). The centroid frequency of the ^{147}Pm hyperfine structure is taken as reference for the frequency offset $\nu - \nu^{147}$, which is indicated by the green dashed line. Fit parameters are given in Table 2

Table 2 Extracted parameters from the hyperfine spectra of the 452 nm and the 468 nm transitions. The superscripts l and u denote the associated lower and upper level of the respective transition. Isotope shifts $\delta\nu$ are given with respect to the reference isotope ^{147}Pm. For details on fixed and dependent parameters see text. All values are given in units of MHz

Isotope	$\delta\nu_{452}^{147,A'}$	$\mathcal{A}^l_{452}$	$\mathcal{B}^l_{452}$	$\mathcal{A}^u_{452}$	$\mathcal{B}^u_{452}$	$\delta\nu_{468}^{147,A'}$	$\mathcal{A}^l_{468}$	$\mathcal{B}^l_{468}$	$\mathcal{A}^u_{468}$	$\mathcal{B}^u_{468}$
^{147}Pm	0	620.3(14)	−407(18)	500.0(14)	−119(15)	0	619.4(17)	−407*	438.2(15)	−48(13)
^{146}Pm	226(12)	429.8(22)	8(19)	347.1(22)	2†	−164(16)	429.7(40)	8*	302.6(24)	1†
^{145}Pm	344(10)	1255.7(11)	−135(17)	1011.7(15)	−40†	−216(11)	1254.8(15)	−135*	886.8(13)	−16†
^{144}Pm	594(10)	329.0(12)	131(13)	265.2(11)	39†	−384(13)	322.0(56)	131*	227.6(46)	15†
^{143}Pm	737(11)	1368.9(25)	−47(18)	1104.0(28)	−14†	−495(14)	1363.9(29)	−47*	964.8(23)	−6†

∗Fixed parameter; $\mathcal{B}^l_{468}$ set to the value of $\mathcal{B}^l_{452}$
†Dependent parameter; $\mathcal{B}^l/\mathcal{B}^u$ set to the result for ^{147}Pm

Table 2). Similarly, for the $\mathcal{B}$ hyperfine coupling constants, an additional error of 10 MHz was added, based upon fit deviations in the 468 nm transition with free $\mathcal{B}^l_{468}$-parameters. Note that in these fits the $\mathcal{A}^l_{468}$ changed by much less than 1 MHz compared to the fits with $\mathcal{B}^l_{468}$ fixed to $\mathcal{B}^l_{452}$. We did not include the results for $\mathcal{B}^l_{468}$ in Table 2, since we deem $\mathcal{B}^l_{452}$ parameters to be much more accurate. Looking at the values in Table 2, we observe a perfect agreement of $\mathcal{A}^l_{452}$ with $\mathcal{A}^l_{468}$ for the isotopes ^{145,146,147}Pm. In ^{143,144}Pm, on the other hand, there is a deviation of few MHz. Considering the rather large uncertainty in $\mathcal{A}^l_{468}(^{144}\text{Pm})$, this deviation is covered within $1.3\,\sigma$. In ^{143}Pm, the error margins of $\mathcal{A}^l_{452}$ and $\mathcal{A}^l_{468}$ barely overlap. The significance of these deviations is therefore rather low, but should be noted.

4 Results and discussion

4.1 Nuclear moments

Magnetic dipole moments and electric quadrupole moments for Pm isotopes are given in Table 3. Earlier values reported in literature are included. The most precise values are available for ^{147}Pm, which were measured with different complementary methods, i.e. paramagnetic resonance of Pm IV [41], ABMR of Pm I [6] and optical spectroscopy of Pm II [12], all with similar precision. The result of $\mu_I^{\text{lit}}(^{147}\text{Pm}) = 2.58(7)\mu_N$ given in the work of Reader et al. is based on the evaluation of the Gouldsmit–Fermi–Segré formula [42]. The authors used a magnetic splitting factor of $\mathcal{A} =$

Table 3 Nuclear spins I^π, magnetic dipole moments μ_I and electric quadrupole moments Q_s for several Pm nuclei. Values with no leading sign indicate that only an absolute value is known. The results for μ_I and Q_s are calculated according to Eq. 1, with the reference isotope ^{147}Pm. References for literature values of μ_I^{lit} are given in the last column for the individual isotopes. The values from the reference for ^{144}Pm and ^{147}Pm were re-evaluated in this work, for details see text. The values for ^{145}Pm and ^{149m}Pm are based on the new reference value of ^{147}Pm. The Schmidt limits for a $g_{7/2}$ and a $d_{5/2}$ proton are $\mu_I^S(g_{7/2}) = 1.72\,\mu_N$ and $\mu_I^S(d_{5/2}) = 4.79\,\mu_N$, respectively. All literature values of Q_s^{lit} are taken from [36]

Isotope	N	I^π	μ_I (μ_N)	Q_s (eb)	μ_I^{lit} (μ_N)	Q_s^{lit} (eb)	References
			This work	This work	Literature	Literature	
^{151}Pm	90	$5/2^+$			1.8(2)	2.2(9)	[6]
^{149m}Pm	88	$5/2^+$			2.0(2)		[37]
^{149}Pm	88	$7/2^+$			3.3(5)		[38]
^{148}Pm	87	1^-			+2.1(2)	+0.2(2)	[38]
^{147m}Pm	86	$5/2^+$			3.53(6)*		[39]
^{147}Pm	86	$7/2^+$			+2.57(4)*	+0.74(20)	[12]
^{146}Pm	85	3^-	+1.53(3)	−0.01(4)			
^{145}Pm	84	$5/2^+$	+3.72(5)	+0.25(7)	+3.71(5)*	+0.23(8)	[10]
^{144}Pm	83	5^-	+1.95(4)	−0.24(7)	1.71(14)*		[40]
^{143}Pm	82	$5/2^+$	+4.05(6)	+0.08(4)	3.8(5)		[38]

*Re-evaluated results. For details see text

647(13) MHz for the $4f^5 6s^2\,{}^6H_{5/2}$ atomic ground state, which is not a direct experimental result, but was estimated on the basis of experimental data for the $4f^5 6s^2\,{}^6H_{7/2}$ state from the ABMR measurements in [6]. When we re-evaluate the Gouldsmit–Fermi–Segré formula in Reader's work, but with our experimental value of $\mathcal{A} = 619.9(7)$ MHz (the weighted average of $\mathcal{A}_l^{452}$ and $\mathcal{A}_l^{468}$) for the atomic ground state splitting, the result for the magnetic moment changes to $\mu_I^{\text{lit}}(^{147}\text{Pm}) = 2.51(5)\mu_N$. The other values for μ_I from [41] and [6] were re-evaluated in the scope of [12], based on more recent theoretical results of $\langle r^{-3}\rangle$. Since there is no reason to prefer one of these experimental values over the other, we calculate the weighted average $\mu_I^{\text{lit}}(^{147}\text{Pm}) = 2.57(4)\mu_N$. For the electric quadrupole moment, we take the value of $Q_s^{\text{lit}}(^{147}\text{Pm}) = 0.74(20)\,e$b from [36] as reference. It is based on the laser spectroscopy measurements of Alkhazov et al. [43], but takes into account more recent results for the electric field gradient at the location of the nucleus of Pyykkö [44], which no longer rely on Sternheimer corrections. In order to determine nuclear moments μ_I and Q_s for $^{143-146}$Pm, we use the relations

$$\mu_I = \frac{\mathcal{A}}{\mathcal{A}_{\text{ref}}}\frac{I}{I_{\text{ref}}}\mu_{I,\text{ref}} \tag{1}$$

$$Q_s = \frac{\mathcal{B}}{\mathcal{B}_{\text{ref}}}Q_{s,\text{ref}} \tag{2}$$

with ^{147}Pm as reference isotope. The results are given in Table 3. With the exception of $\mu_I(^{144}\text{Pm})$, the obtained values agree with the ones previously reported in literature. In the case of ^{144}Pm, the magnetic dipole moment was determined from the temperature dependence of low temperature nuclear orientation measured via anisotropy of the γ-radiation of oriented ^{144}Pm nuclei [40]. If we re-evaluate their experimental result using the same value for $\langle r^{-3}\rangle$ as was used in [12], we obtain $|\mu_I^{\text{lit}}|(^{144}\text{Pm}) = 1.71(14)\,\mu_N$ (assuming an unchanged uncertainty), which approaches the result from our work, but still lies outside its uncertainty. One might consider a hyperfine anomaly ${}^i\Delta^j$ in this case, which specifies a relative deviation from Eq. 1, i.e. $\mathcal{A}^i/\mathcal{A}^j = g_I^i/g_I^j(1 - {}^i\Delta^j)$, with $g_I = -\mu_I/I$ the gyromagnetic ratio for the respective isotopes i, j. However, the hyperfine anomaly is usually in the order of $< 1\%$ [45], and should thus be covered within the given uncertainty of μ_I (in order to explain this deviation a hyperfine anomaly of ${}^{147}\Delta^{144} = 0.12(7)$ would be required). Also note that the difference of the $\mathcal{A}_{452}^l$ and $\mathcal{A}_{468}^l$ hyperfine coupling constants in ^{144}Pm, as mentioned in Sect. 3, is covered by the uncertainty of μ_I and therefore not sufficient to explain this large discrepancy with literature. Since our results for $\mu_I(^{145}\text{Pm})$ are in perfect agreement with laser spectroscopy measurements of Alkhazov et al. [10] (both for μ_I and Q_s), who studied a different transition in singly ionized Pm, we are confident with our results and expect an inconsistency between the literature values of $\mu_I^{\text{lit}}(^{147}\text{Pm})$ and $\mu_I^{\text{lit}}(^{144}\text{Pm})$, with the former being used as reference for the values in our work. Looking at the even-neutron-number isotopes, one clearly observes the expected trend of increasing deformation from a rather spherical nucleus at the magic neutron number $N = 82$ towards more neutron rich isotopes. The trend in g_I factors is plotted in Fig. 6. Due to their small deformation, ^{143}Pm and ^{145}Pm can be represented by the $d_{5/2}$ shell model state. They lie close to the Schmidt limit

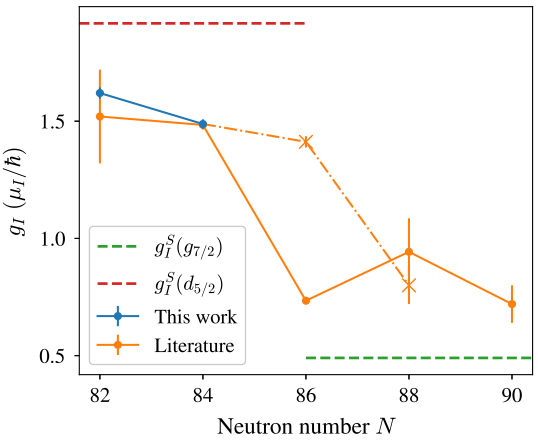

Fig. 6 g_I factors for the even-neutron-number Pm isotopes. The dashed lines mark the Schmidt limits of the $d_{5/2}$ and $g_{7/2}$ shell model configurations. The cross markers indicate the isomers ^{147m}Pm and ^{149m}Pm at excitation energies of 91 keV and 114 keV, respectively. They are connected to the ^{145}Pm ground state by the dash-dotted line to guide the eye

of $g_I^S(d_{5/2}) = 1.92\,\mu_N/\hbar$. Adding more neutrons changes this situation. After a small decrease of g_I from ^{143}Pm to ^{145}Pm, a sudden drop is observed towards ^{147}Pm. As can be seen in Fig. 6, ^{147,149,151}Pm lie closer to the Schmidt limit of $g_I^S(g_{7/2}) = 0.49\mu_N/\hbar$. This can be explained by a positive (prolate) quadrupole deformation, leading to the population of the 7/2[404] Nilsson orbital in ^{147,149}Pm and the 5/2[413] orbital in ^{151}Pm [46], both belonging to the $g_{7/2}$ shell model state. The same transition can be observed in the isomeric states ^{147m}Pm at 91 keV and ^{149m}Pm at 114 keV excitation energy, but shifted by two N, indicating that the $d_{5/2}$ states are located at increasingly high excitation energy. In the quadrupole moments, the increasing deformation is even more clearly visible. The unpaired proton induces a prolate ($Q_s > 0$) deformation as neutrons are added, with the trend becoming very steep towards ^{151}Pm [6]. For the odd-neutron-number isotopes, on the other hand, the unpaired neutron induces an oblate ($Q_s < 0$) deformation, which to some degree compensates the one from the unpaired proton, but is much less pronounced. Consequently, ^{144}Pm exhibits a negative quadrupole moment of $Q_s = -0.24(7)\,e$b, increasing to $Q_s = -0.01(4)\,e$b for ^{146}Pm, where the deformation induced by the single proton and neutron states compensate, and continues to larger positive quadrupole moments for ^{147,151}Pm, where the influence of the valence proton becomes dominant.

4.2 Isotope shifts

The isotope shift defines the frequency difference $\delta\nu$ in an atomic transition i for two isotopes with mass numbers A and A',

$$\delta\nu_i^{A,A'} = \nu_i^A - \nu_i^{A'}. \tag{3}$$

Our measured results for $^{143-147}$Pm are included in Table 2, extracted from the center of gravity of the individual hyperfine structures relative to the center frequency of ^{147}Pm. The data shows a different sign for isotope shifts in the 452 nm and the 468 nm transition, i.e. $\delta\nu_{452}^{A,A'} > 0$ and $\delta\nu_{468}^{A,A'} < 0$ for $A > A'$. The sign of the isotope shift gives hints on the configuration of the upper levels in the respective transition. For the 468 nm transition, we expect a $4f^5 6s^2 \rightarrow 4f^5 6s 6p$, since the involved s electron requires a higher transition frequency for lighter (i.e. smaller) nuclei. From the positive isotope shifts in the 452 nm transition we conclude that no s electron is involved and expect a $4f^5 6s^2 \rightarrow 4f^4 5d 6s$ transition. However these assignments are based on the expected change in electron density at the nucleus and should be used with care.

In order to analyze the data with regard to changes in mean square charge radii, one can express the isotope shift as

$$\delta\nu_i^{A,A'} = \delta\nu_{i,M}^{A,A'} + \delta\nu_{i,F}^{A,A'} = K_i \frac{1}{\mu^{A,A'}} + F_i \delta\langle r^2\rangle^{A,A'} \tag{4}$$

where $\delta\nu_{i,M}^{A,A'}$ denotes the mass shift and $\delta\nu_{i,F}^{A,A'}$ the field shift, accounting for the change of mass and volume of the nucleus, respectively. They depend on the mass shift constant K_i, the reduced mass $\mu^{A,A'} = m_A m_{A'}/(m_A - m_{A'})$, the field shift constant F_i and the change in the mean square charge radius $\delta\langle r^2\rangle^{A,A'}$ between two isotopes with mass numbers A and A'. Both, K_i and F_i depend on the atomic transition and have to be carefully analyzed in order to quantitatively extract $\delta\langle r^2\rangle^{A,A'}$. In our case this analysis is hampered by an uncertain assignment of the excited atomic levels and the lack of theory input. Still, from the data of well-studied neighboring elements and the fact that we have measured isotope shifts in two atomic transitions, an evaluation may be attempted.

The mass shift can be further separated to the so-called normal mass shift (NMS) and the specific mass shift (SMS), accounting for the change in the center of motion and electron-electron correlations, respectively. While the former can be exactly calculated via $\mathrm{NMS}_i = \nu_i/1836.1$ [42], estimations about the SMS require theory input. However, the SMS is often in the order of the NMS, and we thus assume $\mathrm{SMS}_i = 0 \pm \mathrm{NMS}_i$, as often done in cases where SMS_i is not known [1]. With Eq. 4 we can then calculate the field shift $\delta\nu_{i,F}^{A,A'}$, which usually dominates the isotope shift in heavy atoms. In order to extract values for F_i and $\delta\langle r^2\rangle^{A,A'}$, we rely on data of neighboring elements, as compiled in [47]. In the reference, data from K X-ray shifts, elastic electron scattering, muonic atoms and optical isotope shifts is evaluated for the extraction of root mean square charge radii. However, the listed changes in rms charge radii $\delta\langle r^2\rangle^{A,A'}$

Table 4 Change in mean square charge radius per two neutrons for different light lanthanide elements, evaluated for neutron numbers $N = 82, 84, 86$. Nuclear charge radii data is taken from [47]

Z	Element	$\delta\langle r^2\rangle^{N,N+2}$ (fm^2)
64	Gd	0.282(8)
63	Eu	0.272(12)
62	Sm	0.274(22)
60	Nd	0.296(20)
59	Ce	0.256(14)

only take optical isotope shifts into account. The following analysis is based on the latter. Starting from the neutron shell closures at $N = 28, 50, 82$ and 126, the increase in nuclear charge radii is approximately linear towards neutron-rich isotopes and neighboring elements exhibit similar slopes, with few exceptions. Assuming this trend holds valid for Pm, we can use this regularity to extract the field shift constant F_i. The mean square charge radii of the Pm neighbors Ce, Nd, Sm, Eu and Gd over the even neutron number isotopes, i.e. $N = 82, 84, 86$ is given in Table 4. As a weighted average we obtain $\overline{\delta\langle r^2\rangle^{N,N+2}} = 0.276(13)$ fm^2. The field shift constant F_i of the two investigated transitions is varied until the change in mean square charge radii, related to F_i with Eq. 4, matches this value. We obtain

$$F_{452} = -1210(60)\,\text{MHz/fm}^2$$
$$F_{468} = +1015(55)\,\text{MHz/fm}^2$$

in the 452 nm and 468 nm transition, respectively, where the uncertainty is derived from the standard deviation of $\delta\langle r^2\rangle^{N,N+2}$ in Table 4. The results, together with the data of the neighboring elements from [47], are displayed in Fig. 7.

The trend in charge radii exhibits several interesting features. Most noticeable is the kink in the curve of all elements at the magic neutron number $N = 82$, followed by a similar slope in $\delta\langle r^2\rangle^{A,A'}$ for all displayed elements with increasing neutron number. Below $N = 82$, a Z-dependence in the slope can be observed. While Ce and Nd charge radii are rather constant, Sm and Gd show increasing charge radii towards neutron deficient isotopes. Pm lies exactly in between these two trends, which highly motivates further measurements in this region. Note that an even more distinct Z-dependence is observed around the $N = 28$ shell closure, which is discussed e.g. in [48]. Lastly, one should note the sudden increase in the charge radius of Eu from $N = 88$ to $N = 89$, which has been related to the influence of the almost-doubly magic ^{146}Gd [5].

In order to verify the results of the neighboring elements analysis and to obtain a reasonable error estimate on F_i, and accordingly on $\delta\langle r^2\rangle^{A,A'}$, a complementary King-plot analysis was performed. A King–Plot can be used to determine

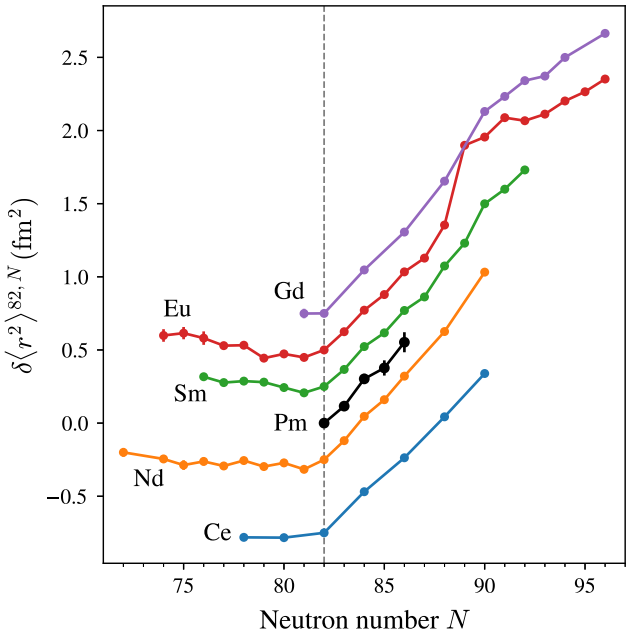

Fig. 7 Changes in mean square charge radii in the promethium region. Data for the neighboring elements is taken from [47]. Arbitrary offsets of multiples of 0.2 fm^2 are added to the different isotopic chains for visual separation. For details see text

F_{468}/F_{452} with just the isotope shifts as underlying data, i.e. independent of the assumptions made above. The relation between the modified isotope shifts $\mu\delta\nu^{A,A'}$ in different atomic transitions i, j is expected to be linear up to high precision, and can be expressed as

$$\mu\delta\nu_i^{A,A'} = \frac{F_i}{F_j}\mu\delta\nu_j^{A,A'} + \left(K_i - \frac{F_i}{F_j}K_j\right). \tag{5}$$

The ratio of the respective field shift constants is given by the line slope. The King–Plot of the modified 452 nm and 468 nm isotope shifts is presented in Fig. 8. The best fit to the data yields a slope of $F_{468}/F_{452} = -0.82(24)$, in excellent agreement with the value of $F_{468}/F_{452} = -0.84(6)$ from the neighboring element analysis. Note that using this ratio from the King–Plot, the F_i values would be shifted apart from each other by ≈ 30 MHz, well within the stated uncertainty from the neighboring element analysis. For the mass shift constants K_i, on the other hand, the King–Plot analysis is less conclusive, since the uncertainty of the offset is in the order of 150 % of the value itself and consistent with zero. From the best fit we can extract

$$K_{468} + 0.82(24) \cdot K_{452} = 620(940)\,\text{GHz/u}$$

which agrees with our assumption of

$$\text{NMS}_{468} + 0.84(6) \cdot \text{NMS}_{452} = 640(14)\,\text{GHz/u} \tag{6}$$

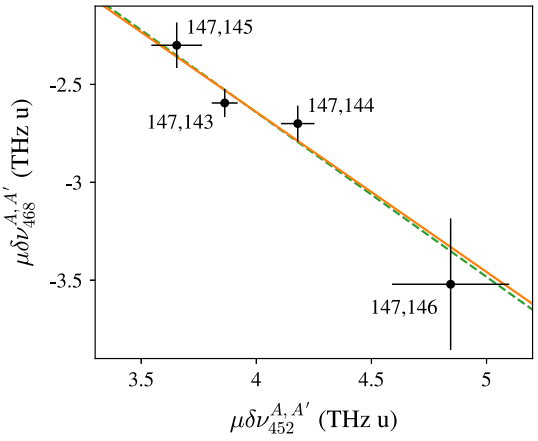

Fig. 8 King–Plot analysis of the investigated optical ground-state transitions at 452 nm and 468 nm. The modified isotope shifts are plotted with respect to the reference isotope ^{147}Pm. The solid orange line displays the best fit to the data and the green dashed line has a fixed slope of $F_{468}/F_{452} = 0.84$, as obtained from the analysis of neighboring elements

Table 5 Changes in mean square charge radii with respect to ^{147}Pm. The values derived from isotope shifts in the 452 nm and the 468 nm transitions are averaged, with uncertainties in brackets. The last column contains the staggering parameter γ_A for the odd-neutron-number isotopes

A	$\delta\langle r^2\rangle_{\text{avg}}^{147,A}$ (fm^2)	γ_A
146	−0.17(2)	0.60(17)
145	−0.24(3)	
144	−0.42(5)	0.77(15)
143	−0.53(6)	

but prevents any reasonable conclusions about the individual components. Note that the uncertainty in (6) would increase to 460 GHz/u when the assumption $\text{SMS}_i = 0 \pm \text{NMS}_i$ would have been considered.

Finally, we extract values for the changes in nuclear mean square charge radii, as given in Table 5. From the values of $\delta\langle r^2\rangle_{452}^{147,A}$ and $\delta\langle r^2\rangle_{468}^{147,A}$, individually derived from the isotope shifts in the transitions under investigation, we calculated an average $\delta\langle r^2\rangle_{\text{avg}}^{147,A}$. The results indicate an odd-even staggering in mean square charge radii, which is defined via

$$\gamma_A = \frac{2\delta\langle r^2\rangle^{A-1,A}}{\delta\langle r^2\rangle^{A-1,A+1}} \tag{7}$$

for odd-neutron-number isotopes, with the staggering parameter γ_A [49]. For $\gamma_A < 1$, this is referred to as normal odd-even staggering. It is qualitatively related to the quadrupole deformation, as given in Table 3. In ^{144}Pm, γ_A is closer to 1 (little staggering), since the deformation in ^{144,145}Pm is similar, despite the different sign in Q_s. ^{146}Pm, however, is almost spherical due to the compensating deformation induced by the single proton and the single neutron orbitals, whereas in particular the neighboring ^{147}Pm has a rather high quadrupole moment, resulting in a staggering parameter significantly different from 1.

5 Summary

We measured hyperfine spectra of the five long-lived promethium isotopes $^{143-147}$Pm in two different atomic ground state transitions, allowing the precise extraction of hyperfine coupling constants and isotope shifts. From this data, refined values for the magnetic moments of ^{143,144,145}Pm were extracted. The magnetic moment of ^{146}Pm and quadrupole moments of ^{143,144,146}Pm were determined for the first time. Since the excited state configuration in the transitions under investigation is unknown, a precise analysis of the isotope shifts was hampered. However, a comparison with neighboring elements allowed good estimate on the transitions' field shift constants and changes in mean square charge radii. The results indicate that the specific mass shift in both transitions is small compared to the field shift. A King–Plot analysis confirmed the consistency of our results and allowed an estimate of systematic uncertainties.

For a better understanding of the evolution of deformation, visible in nuclear moments and changes in mean square charge radii, it is of high relevance to continue laser spectroscopy studies of Pm, both towards ^{151}Pm, but also of light Pm nuclei below $N = 82$. With this work we established a basis for future experiments aiming for more exotic nuclei at radioactive ion beam facilities, possibly by using the PI-LIST ion source, which has recently been adapted for on-line application.

Acknowledgements Open Access funding provided by Projekt DEAL. The authors thank Stephan Fritzsche, Randolf Beerwerth and Dorothea Schumann for their ideas and stimulating discussions. We would also like to thank Nick van der Meulen for support with the target pellet preparation. D. Studer acknowledges financial support from the EU through ENSAR2-RESIST (Grant No. 654002) and from the Bundesministerium für Bildung und Forschung (BMBF, Germany) under grant No. 02NUK044B. R. Heinke acknowledges financial support from the BMBF Germany under Grant No. 05P15UMCIA. S. Braccini and T.S. Carzaniga acknowledge the support of the Swiss National Science Foundation (SNSF) (Grants: 200021-175749, CRSII5-180352, CR23I2-156852).

Author contributions Irradiation of the Nd-target at the Bern medical cyclotron by T.S. Carzaniga and S. Braccini. Target production, post-irradiation radiochemical separation and γ-spectroscopic measurements by J. Ulrich. ^{147}Nd tracer production by K. Eberhardt. ^{147}Pm sample production by U. Köster. Laser spectroscopic measurements by D. Studer, R. Heinke and S. Raeder. Data analysis, figures and manuscript draft by D. Studer. All authors contributed to the final manuscript. The supervisors of this project were R. Dressler (PSI) and K. Wendt (U. Mainz).

Data Availability Statement This manuscript has no associated data or the data will not be deposited. [Author's comment: comment: The spectroscopic data of all laser scans which were performed within the scope of this work are available upon request to the corresponding author. All other relevant data is included in the presented manuscript.]

References

1. P. Campbell, I.D. Moore, M.R. Pearson, Prog. Part. Nucl. Phys. **86**, 127 (2016). https://doi.org/10.1016/j.ppnp.2015.09.003
2. D.A. Bromley (ed.), *Treatise on heavy ion science: volume 8: nuclei far from stability* (Springer US, Boston, MA, 1989). https://doi.org/10.1007/978-1-4613-0713-6
3. K. Heilig, A. Steudel, At. Data Nucl. Data Tables **14**(5–6), 613 (1974). https://doi.org/10.1016/S0092-640X(74)80006-9
4. G.A. Leander, P. Möller, Phys. Lett. B **110**(1), 17 (1982). https://doi.org/10.1016/0370-2693(82)90942-X
5. R.F. Casten, Dd Warner, D.S. Brenner, R.L. Gill, Phys. Rev. Lett. **47**(20), 1433 (1981). https://doi.org/10.1103/PhysRevLett.47.1433
6. B. Budick, R. Marrus, Phys. Rev. **132**(2), 723 (1963). https://doi.org/10.1103/PhysRev.132.723
7. S.A. Ahmad, W. Klempt, C. Ekström, R. Neugart, K. Wendt, Z. Physik A **321**(1), 35 (1985). https://doi.org/10.1007/BF01411941
8. P. Klinkenberg, F.S. Tomkins, Physica **26**(2), 103 (1960). https://doi.org/10.1016/0031-8914(60)90067-7
9. J. Reader, S.P. Davis, J. Opt. Soc. Am. **53**(4), 431 (1963). https://doi.org/10.1364/JOSA.53.000431
10. G.D. Alkhazov, A.E. Barzakh, H. Huhnermann, K. Kesper, A. Mazumdar, W. Moller, R. Otto, V.N. Pantelejev, A.G. Poljakov, C. Reese, H. Wagner, J. Phys. B: At. Mol. Opt. Phys. **25**, 571 (1992). https://doi.org/10.1088/0953-4075/25/2/023
11. R. Otto, H. Hühnermann, J. Reader, J.F. Wyart, J. Phys. B. At. Mol. Opt. Phys. **28**, 3615 (1995). https://doi.org/10.1088/0953-4075/28/16/014
12. J. Reader, Phys. Rev. **141**(3), 1123 (1966). https://doi.org/10.1103/PhysRev.141.1123
13. D. Studer, S. Heinitz, R. Heinke, P. Naubereit, R. Dressler, C. Guerrero, U. Köster, D. Schumann, K. Wendt, Phys. Rev. A **99**, 062513 (2019). https://doi.org/10.1103/PhysRevA.99.062513
14. R. Heinke, T. Kron, S. Raeder, T. Reich, P. Schönberg, M. Trümper, C. Weichhold, K. Wendt, Hyper. Interact. **238**, 15 (2017). https://doi.org/10.1007/s10751-016-1386-2
15. S. Heinitz, E.A. Maugeri, D. Schumann, R. Dressler, N. Kivel, C. Guerrero, U. Köster, M. Tessler, M. Paul, S. Halfon, Radiochim. Acta **105**(10), 801 (2017). https://doi.org/10.1515/ract-2016-2728
16. S. Braccini, A.I.P. Conf, Proc. **1525**, 144 (2013). https://doi.org/10.1063/1.4802308
17. J. Ulrich, in preparation
18. ENSDF database as of December 2019. http://www.nndc.bnl.gov/ensarchivals/
19. C. Mattolat, S. Rothe, F. Schwellnus, T. Gottwald, S. Raeder, K. Wendt, T. Iguchi, K. Watanabe, A.I.P. Conf, Proc. **1104**, 114 (2009). https://doi.org/10.1063/1.3115586
20. S. Rothe, B.A. Marsh, C. Mattolat, V.N. Fedosseev, K. Wendt, J. Phys. Conf. Ser. **312**, 052020 (2011). https://doi.org/10.1088/1742-6596/312/5/052020
21. T. Kessler, H. Tomita, C. Mattolat, S. Raeder, K. Wendt, Laser Phys. **18**(7), 842 (2008). https://doi.org/10.1134/S1054660X08070074
22. V. Sonnenschein, I.D. Moore, S. Raeder, M. Reponen, H. Tomita, K. Wendt, Laser Phys. **27**, 085701 (2017). https://doi.org/10.1088/1555-6611/aa7834
23. M. Verlinde, K. Dockx, S. Geldhof, K. König, D. Studer, T.E. Cocolios, R. de Groote, R. Ferrer, T. Kieck, I.D. Moore, W. Nörtershäuser, S. Raeder, P. van den Bergh, P. van Duppen, K. Wendt, submitted to Appl. Phys. B (2019)
24. T. Kieck, S. Biebricher, C.E. Düllmann, K. Wendt, Rev. Sci. Instrum. **90**, 053304 (2019). https://doi.org/10.1063/1.5081094
25. D.A. Fink, S.D. Richter, K. Blaum, R. Catherall, B. Crepieux, V.N. Fedosseev, A. Gottberg, T. Kron, B.A. Marsh, C. Mattolat, S. Raeder, R.E. Rossel, S. Rothe, F. Schwellnus, M.D. Seliverstov, M. Sjödin, T. Stora, P. Suominen, K. Wendt, Nucl. Instrum. Methods Phys. Res. B **344**, 83 (2015). https://doi.org/10.1016/j.nimb.2014.12.007
26. D.A. Fink, T.E. Cocolios, A.N. Andreyev, S. Antalic, A.E. Barzakh, B. Bastin, D.V. Fedorov, V.N. Fedosseev, K.T. Flanagan, L. Ghys, A. Gottberg, M. Huyse, N. Imai, T. Kron, N. Lecesne, K.M. Lynch, B.A. Marsh, D. Pauwels, E. Rapisarda, S.D. Richter, R.E. Rossel, S. Rothe, M.D. Seliverstov, A.M. Sjödin, C. van Beveren, P. van Duppen, K.D.A. Wendt, Phys. Rev. X **5**, 011018 (2015). https://doi.org/10.1103/PhysRevX.5.011018
27. S. Raeder, H. Heggen, J. Lassen, F. Ames, D. Bishop, P. Bricault, P. Kunz, A. Mjøs, A. Teigelhöfer, Rev. Sci. Instrum. **85**, 033309 (2014). https://doi.org/10.1063/1.4868496
28. F. Schneider, K. Chrysalidis, H. Dorrer, C. Düllmann, K. Eberhardt, R. Haas, T. Kieck, C. Mokry, P. Naubereit, S. Schmidt, K. Wendt, Nucl. Instrum. Methods Phys. Res. B **376**, 388 (2016). https://doi.org/10.1016/j.nimb.2015.12.012
29. R.P. de Groote, M. Verlinde, V. Sonnenschein, K.T. Flanagan, I. Moore, G. Neyens, Phys. Rev. A **95**, 031693 (2017). https://doi.org/10.1103/PhysRevA.95.032502
30. G.C. King, F.H. Read, R.E. Imhof, J. Phys. B. At. Mol. Phys. **8**(4), 665 (1975). https://doi.org/10.1088/0022-3700/8/4/027
31. W. Gins, R.P. de Groote, M.L. Bissell, C. Granados Buitrago, R. Ferrer, K.M. Lynch, G. Neyens, S. Sels, Comput. Phys. Commun. **222**, 286 (2018). https://doi.org/10.1016/j.cpc.2017.09.012
32. T. Ishimatsu, H. Ohmura, T. Awaya, T. Nakagawa, H. Orihara, K. Yagi, J. Phys. Soc. Jpn. **28**(2), 291 (1970). https://doi.org/10.1143/JPSJ.28.291
33. M.R. Macphail, R.G. Summers-Gill, Nucl. Phys. A **263**(1), 12 (1976). https://doi.org/10.1016/0375-9474(76)90180-9
34. P. Drehmann, Z. Physik **271**(4), 349 (1974). https://doi.org/10.1007/BF02126189
35. A. Cabezas, I. Lindgren, E. Lipworth, R. Marrus, M. Rubinstein, Nucl. Phys. **20**, 509 (1960). https://doi.org/10.1016/0029-5582(60)90192-9
36. N.J. Stone, At. Data Nucl. Data Tables **111–112**, 1 (2016). https://doi.org/10.1016/j.adt.2015.12.002
37. T. Seo, T. Hayashi, A. Aoki, Nucl. Phys. A **159**(2), 494 (1970). https://doi.org/10.1016/0375-9474(70)90722-0
38. R.W. Grant, D.A. Shirley, Phys. Rev. **130**(3), 1100 (1963). https://doi.org/10.1103/PhysRev.130.1100
39. E.R. Bauminger, D. Froindlich, A. Mustachi, S. Ofer, M. Perkal, Phys. Lett. B **32**(8), 678 (1970). https://doi.org/10.1016/0370-2693(70)90442-9

40. D.A. Shirley, J.F. Schooley, J.O. Rasmussen, Phys. Rev. **121**(2), 558 (1961). https://doi.org/10.1103/PhysRev.121.558
41. H.J. Stapleton, C.D. Jeffries, D.A. Shirley, Phys. Rev. **124**(5), 1455 (1961). https://doi.org/10.1103/PhysRev.124.1455
42. H. Kopferman, E.E. Schneider, H.S.W. Massey, *Nuclear moments*, 2nd edn. (Elsevier Science, Burlington, 1958)
43. G.D. Alkhazov, A.E. Barzakh, V.A. Bolshakov, V.P. Denisov, V.S. Ivanov, Y.Y. Sergeyev, I.Y. Chubukov, V.I. Tikhonov, V.S. Letokhov, V.I. Mishin, S.K. Sekatsky, V.N. Fedoseyev, Z. Physik A **337**(3), 257 (1990). https://doi.org/10.1007/BF01289691
44. P. Pyykkö, Mol. Phys. **106**(16–18), 1965 (2008). https://doi.org/10.1080/00268970802018367
45. J.R. Persson, At. Data Nucl. Data Tables **99**(1), 62 (2013). https://doi.org/10.1016/j.adt.2012.04.002
46. D. Nosek, R.K. Sheline, P.C. Sood, J. Kvasil, Z. Physik A **344**(3), 277 (1992). https://doi.org/10.1007/BF01303021
47. I. Angeli, K.P. Marinova, At. Data Nucl. Data Tables **99**(1), 69 (2013). https://doi.org/10.1016/j.adt.2011.12.006
48. M. Avgoulea, Y.P. Gangrsky, K.P. Marinova, S.G. Zemlyanoi, S. Fritzsche, D. Iablonskyi, C. Barbieri, E.C. Simpson, P.D. Stevenson, J. Billowes, P. Campbell, B. Cheal, B. Tordoff, M.L. Bissell, D.H. Forest, M.D. Gardner, G. Tungate, J. Huikari, A. Nieminen, H. Penttilä, J. Äystö, J. Phys. G. Nucl. Part. Phys. **38**(2), 025104 (2011). https://doi.org/10.1088/0954-3899/38/2/025104
49. W.J. Tomlinson, H.H. Stroke, Nucl. Phys. **60**(4), 614 (1964). https://doi.org/10.1016/0029-5582(64)90098-7

Chapter 5

Summary and outlook

The scope of this dissertation spans over various applications of laser resonance ionization, specifically covering sensitive spectroscopy for atomic and nuclear structure research. Several publications emerged from this work, five of which were presented within this thesis. Development efforts concerned technical aspects of narrowband lasers, accurate wavelength measurements and performance tests of the novel PI-LIST ion source. On top of that specific spectroscopic techniques, i.e. resonant de-excitation, a refined approach in saddle-point ionization and new laser excitation schemes for Dy and Pm were addressed. Nonetheless, the included publications primarily focus on measurements of fundamental atomic and nuclear properties, significantly refining and extending existing literature data. In this context, the outstanding capabilities of RIS, covering both atomic and structure research, were demonstrated.

Publication I focused on the search for a specific atomic ground-state transition in Dy. Its characteristics, being both extremely weak and with its wavelength of $\lambda \approx 1001\,\text{nm}$ close to the infrared edge of the Ti:sapphire gain profile, rendered this experiment extremely challenging and called for an unconventional spectroscopic approach. Rather than direct excitation spectroscopy, a full three-step ionization scheme was established based on a stronger ground-state transition with a similar configuration in the upper energy level. The searched upper level of the 1001 nm transition could then be localized by resonant de-excitation of the second excited state, competing with the resonant ionization process, thus causing a dip in the ion signal. Direct excitation spectroscopy became feasible through this previously established ionization scheme. Isotope shifts in both investigated ground-state transitions, at 741 nm and 1001 nm, were measured for all stable isotopes, including the least abundant ones, ^{156}Dy (0.0056 %) and ^{158}Dy (0.095 %). The obtained data served as an important stepping stone towards precision spectroscopy of the 1001 nm transition on cold atoms trapped in a MOT, which was afterwards successfully performed [115].

Publication II, also dealing with Dy atomic structure, represents an exemplary case for the measurement of the IP in a rare-earth atomic system through Rydberg-spectroscopy. Spectroscopic data obtained in different excitation schemes was evaluated and Rydberg-convergences could be identified. Although they were partly subject to strong perturbations, a precise value of $\mathrm{IP}_{\mathrm{Dy}}^{\mathrm{Ryd}} = 47\,901.76(5)\,\mathrm{cm}^{-1}$ could be determined. Note that this is in perfect agreement with the result of $\mathrm{IP}_{\mathrm{Dy}}^{\mathrm{SP}} = 47\,901.8(3)\,\mathrm{cm}^{-1}$, obtained from saddle-point ionization [128, 138], i.e. the technique which was used in Publication III for the determination of $\mathrm{IP}_{\mathrm{Pm}}$. Additionally, the efficiency of the investigated ionization schemes was assessed. For a three-step scheme, where all transitions could be saturated, an efficiency of 25(4) % was demonstrated in a series of dedicated measurements on calibrated samples. It serves as an alternative to previously used schemes relying on dye lasers or non-resonant ionization (cf. [37]), and was later used for measurements on Dy isotope ratios in a ^{163}Ho sample used for the ECHo project [137].

Moving on to the scarcely studied atomic system of Pm, Publication III represents one of the most comprehensive spectroscopic investigations of this element so far. Over 1000 atomic transitions were measured in different RIS schemes, and are tabulated in appendix A.3. This extraordinarily rich atomic spectrum prevented an unambiguous identification of Rydberg states, as carried out successfully in Dy. Consequently, the approach of saddle-point ionization was applied for the determination of the IP. In order to overcome limitations through the efficiency of this method, the measurement process was turned around: rather than scanning the laser frequency across ionization thresholds for a number of given field strengths, the electric field strength was varied to effectively scan the threshold itself across several weakly bound atomic levels, while keeping the laser on resonance. While this introduced some operational complications, the sensitivity was increased by at least two orders of magnitude, rendering the experiment feasible in the first place. The precision of the extracted value of $\mathrm{IP}_{\mathrm{Pm}} = 45\,020.8(3)\,\mathrm{cm}^{-1}$ is comparable to that of most stable elements and closes the last gap for an experimental value of this fundamental property in the Periodic Table below $Z = 100$ (cf. Fig. 1 in Publication III). Although the efficiency of the newly developed ionization schemes could not be quantified due to the limited sample amounts, two promising schemes were added to the RILIS database [37]. They form the basis of the high-resolution spectroscopy studies of Publication V.

Publication IV presents a characterization of laser frequency measurement in high-resolution spectroscopy. Several commercial wavelength meters were tested with respect to their long-term stability and relative accuracy by a collaboration of European RIS teams. Long-term drifts could be effectively suppressed by frequent calibration or data post-processing, using an absolute frequency reference. In Mainz, a Rb saturated absorption spectroscopy setup was installed for this purpose. More importantly, device-specific systematic deviations in relative frequency measure-

ment were discovered using complementary measurement methods, i.e. frequency combs and scanning Fabry-Pérot interferometers. The latter is a cost-efficient addition to any narrow-linewidth laser setup and may be used to eliminate systematic effects introduced by wavelength meters. As a result, a long-term relative accuracy in the range of 2 MHz can be achieved.
Finally, Publication V deals with high-resolution spectroscopy on a chain of long-lived Pm isotopes, which were produced in a cyclotron. This work marks the first high-precision laser spectroscopic study on neutral Pm. Additionally, the experiment is an important performance test for the PI-LIST ion source, demonstrating its capabilities with regard to isobaric background suppression, efficiency and spectroscopic linewidth. Even with high isobaric contamination of Pm/Nd $\approx$ 1/100 and low sample amounts in the order of 10^{11} atoms, experimental linewidths between 100 and 200 MHz were achieved. The two investigated atomic ground-state transitions were characterized and the obtained spectra delivered valuable data for the extraction of nuclear moments and mean square charge radii. For the majority of investigated nuclides these quantities were previously unknown. Furthermore, the results serve as starting point for high-resolution in-source spectroscopy studies at on-line RIB facilities and pave the way for the extraction of nuclear properties of short-lived Pm isotopes. An on-line experiment at CERN-ISOLDE will be assessed after the long shutdown in 2021 the RILIS team using the PI-LIST ion source, which is currently prepared for on-line application.
In conclusion, goals of the EU RTN project RESIST could be well addressed, at the same time providing fundamental atomic and nuclear structure data. The PI-LIST was proven to be a valuable tool for high-resolution spectroscopic studies under challenging conditions, which served as further step towards routine operation of this novel instrument. Under the aspect of laser development, the accuracy of precision frequency measurement was characterized, ensuring the reliability of future spectroscopy results. Additionally, two laser prototypes were developed as part of this thesis (see appendix A.1). The compact-footprint injection-seeded laser was used successfully for Doppler-free two-photon spectroscopy at ISOLDE [59] and has now become a permanent part of the RILIS laser setup. The concept of the unseeded bowtie-resonator laser, on the other hand, was abandoned due to spectral stability problems, which could not be overcome. As a future prospect, this laser concept is now being adapted for cw operation, offering superior stability [60, 61]. With recently upcoming high-power laser diodes, which are suitable as Ti:sapphire laser pump source, it is a cost-efficient alternative to expensive commercial laser systems. It will be used as seed for a pulsed amplifier, i.e. an injection-seeded Ti:sapphire laser. Compared to ECDL master lasers, the spectral coverage naturally matches the Ti:sapphire amplifier emission range and eliminates the need for frequent modification of the laser setup. Lastly, the applied spectroscopic techniques will be highly beneficial in the upcoming LISA (Laser Ionization and Spectroscopy of Actinides) project, which acts as a follow-up to RESIST. Specifically, resonant

de-excitation is now considered in search of the lowest-lying odd-parity states in Ac, which were not observed so far. Recent atomic structure calculations [162] serve as a starting point for this experiment, and the experimental results can later be used to benchmark the theoretical predictions. Another objective of LISA is the determination of precision values for electron affinities and ionization potentials of actinide elements. In context of the latter, saddle-point ionization may play an important role. As demonstrated in Pm, it is perfectly suited for application in the actinide series, where similarly low sample amounts and complex spectra are expected.

Chapter A

Appendix

A.1 Laser prototypes

The following section briefly introduces two laser prototypes, that were developed in the framework of this dissertation. The development was based on a Wolfram Mathematica script implementing Gaussian ray transfer matrix calculations, more specifically the so-called ABCD formalism. In simple terms, an incident Gaussian beam with position vector $\boldsymbol{r}_i = (r_i, \phi_i)$, where r_i and ϕ_i are the distance and angle to the z-axis, respectively, is transformed to $\boldsymbol{r}_f = (r_f, \phi_f)$ through a 4×4 matrix $\mathcal{M}$ representing an optical element. The beam transport along a laser resonator can thus be calculated through composition of all optical elements and free beam paths. In order to obtain a stable resonator, the beam should be transferred to its original position vector after one round trip. Moreover, the difference in tangential and sagittal beam waist, i.e. parallel and perpendicular to the resonator plane, should be minimized for an optimal beam profile. For details on the ABCD formalism, which shall not be further discussed here, the reader is referred to [58] or to [62], where the latter gives a compact summary of the most important concepts and equations.
The script that was used here directly generates beam waist plots for the chosen resonator geometry, as well as a printable 2D layout, which can be fixed to an optical breadboard and allows for fast setup and testing. All calculations were performed for a wavelength of 800 nm, near the gain maximum of the Ti:sapphire laser medium. Calculated Brewster angles should thus be close to optimum over the whole Ti:sapphire output range.
Printable layouts of both laser types are attached at the end of this section. Note that the radius of curvature for curved mirrors is $r_{\mathrm{curv}} = 75\,\mathrm{mm}$. Unlabeled optical mounts serve as alignment help. All length units are given in mm.

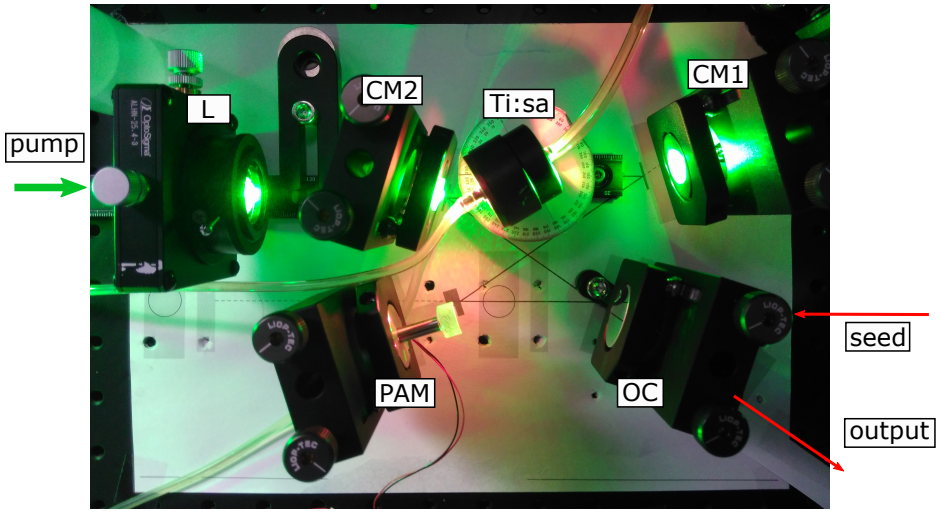

Figure A.1.: Photograph of the compact-footprint injection-seeded Ti:sapphire laser prototype at the ISOLDE-RILIS. **L:** plano-convex lens; **CM:** curved mirror; **Ti:sa:** Ti:sapphire crystal; **PAM:** piezo-actuated mirror; **OC:** output-coupler.

A.1.1 Compact-footprint injection-seeded laser

As the name suggests, the compact-footprint injection-seeded laser is based on the injection-seeded laser presented in Sec. 2.1.3. It was designed and successfully used for Doppler-free two-photon in-source spectroscopy at the ISOLDE-RILIS [59]. Considering the operation purpose, the resonator was designed as small as possible. A photograph and the calculated $1/e$ beam waist of the resonator are shown in Figs. A.1 and A.2, respectively. Apart from the practical advantage of taking up less valuable space on the laser table (which is particularly important at ISOLDE-RILIS), the shorter resonator exhibits a larger FSR and shorter pulse length compared to the "standard" injection-seeded laser. The large FSR close to 900 MHz greatly suppresses side-modes and thus allows for higher dither amplitudes in the resonator lock, if needed. The short pulse length increases the power density of the output radiation, which is particularly important in the non-linear process of two-photon excitation. Moreover, it facilitates temporal de-coupling of subsequent excitation steps, which is sometimes necessary to avoid power broadening (see Sec. 3.3.4). On the other hand, shorter pulses lead to an increase in the Fourier-limited linewidth, which was measured as 21 MHz in [59]. With a Gaussian time-to-bandwidth product of TDP $= 0.44$, this corresponds to a pulse length of 21 ns.
This laser was installed at ISOLDE-RILIS by the author in March 2017, where lasing could be achieved within several days. Further optimization and locking was then performed by the local PhD student Katerina Chrysalidis.
The printable layout attached to the end of this section uses top-adjustable LIOPTEC 1" *Star* mounts, with round 1" diameter posts.

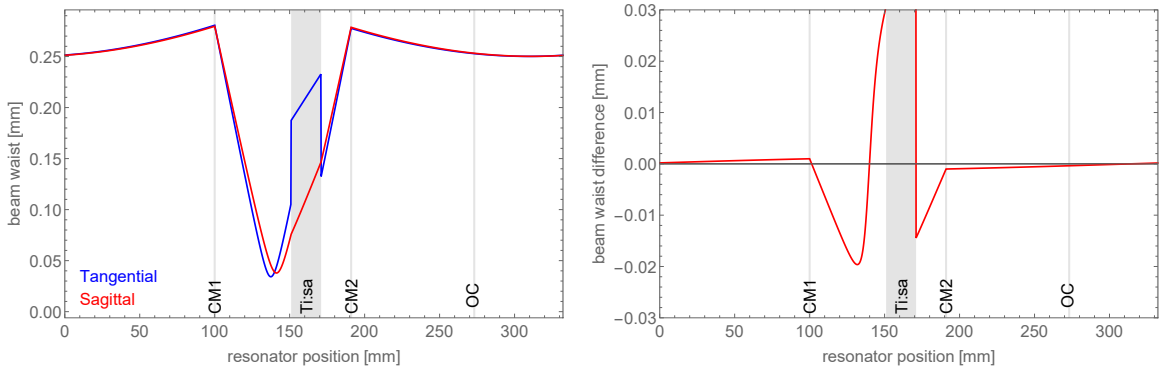

Figure A.2.: Left: Calculated $1/e$ beam waist for the compact-footprint injection-seeded laser in the sagittal and tangential resonator planes. The piezo-actuated mirror marks the zero position of the resonator. Right: $1/e$ beam waist difference (tangential−sagittal).

A.1.2 Unseeded bowtie-resonator laser

The unseeded bowtie-resonator laser is based on a previous design by T. Kron, which is described in [74] and was already used for high-resolution spectroscopy on stable copper isotopes [91] and long-lived Tc isotopes [163]. It is designed to achieve single-mode operation without the use of a cw master laser, hence the name *unseeded* laser. The bowtie-shaped geometry, which is necessary to avoid spatial hole burning, is adapted from the injection-seeded laser. Single-mode operation is achieved by combination of several frequency-selective elements, i.e. a LF and a 0.3 mm FPE, similar to the standard Ti:sapphire laser (see Sec. 2.1.1), with an additional air-spaced etalon (ASE). The latter is composed of two wedged mirrors with a partially reflective coating on one side and an anti-reflection coating on the other side. Frequency scanning can be performed by piezo-actuators on one cavity mirror and one of the mirrors of the ASE.
The novel design presented here was developed to improve the stability of single-mode operation by minimizing the resonator length, thus increasing the FSR, as well as by improving the mechanical damping of the cavity base plate through sorbothane isolators. Additionally, the $R = 0.3$ mirrors used in the ASE were replaced by $R = 0.4$ mirrors for increased finesse. The resulting geometry is shown in Fig. A.3, with the corresponding beam waist calculations in Fig. A.4. This laser type was used for spectroscopy in the 741 nm transition of Dy, presented in Publication I. Although single-mode operation could be achieved, it was difficult to maintain while scanning the laser frequency, which resulted in visible side-modes in the recorded spectrum, similar to what has been observed in Cu [91]. Consequently, it was concluded that this design did not offer major advantages over its predecessor. However, one should note that as an alternative mode of operation, it is possible to set a fast voltage ramp on the piezo-actuated cavity mirror, resulting in a "scrambled" frequency output with an average linewidth of ≈ 600 MHz, which

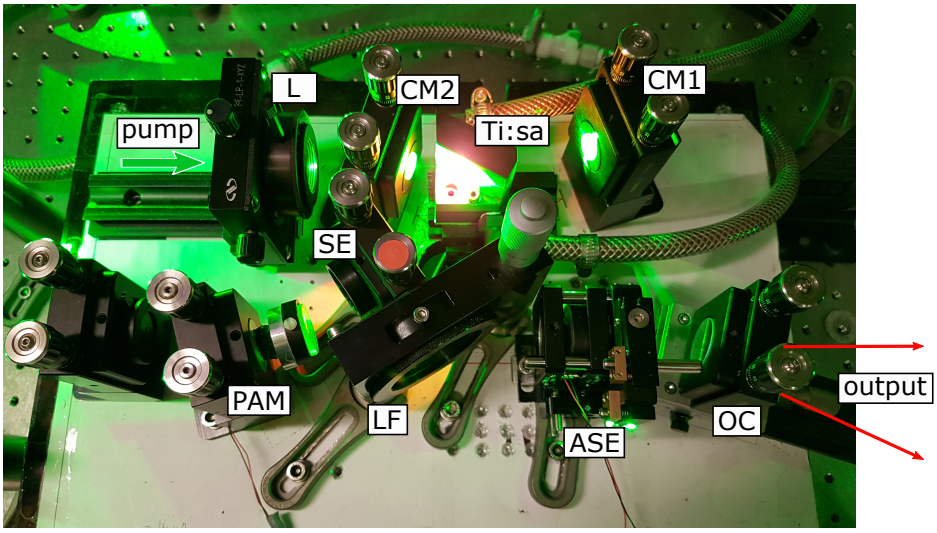

Figure A.3.: Photograph of the unseeded bowtie-resonator Ti:sapphire laser prototype. **L:** plano-convex lens; **CM:** curved mirror; **Ti:sa:** Ti:sapphire crystal; **SE:** solid thin etalon; **PAM:** piezo-actuated mirror; **LF:** Lyot filter; **ASE:** air-spaced etalon; **OC:** output-coupler.

is superior to the standard dual-etalon laser [50]. A comparison between normal and "scrambled" scanning operation is shown in Fig. A.5. The left panel corresponds to Fig. 4 in Publication I, whereas the right panel shows the same spectra in "scramble" mode. While this does not offer superior data quality in the present case, laser operation is strongly simplified and may be considered for in-source spectroscopy of actinide elements, where the expected Doppler-broadening is in the order of $\approx 1\,\mathrm{GHz}$ due to their high mass (cf. Fig. 3.2).
The printable layout as given at the end of this section uses Thorlabs VM1-M mounts with custom-build rectangular posts for easy alignment. Etalons are not included in the layout, since their position does not notably influence the resonator geometry. Note that this layout is designed to fit on A3 paper size and was scaled down by $\sqrt{2}$ to fit on an A4 paper. For printing it needs to be re-scaled accordingly.

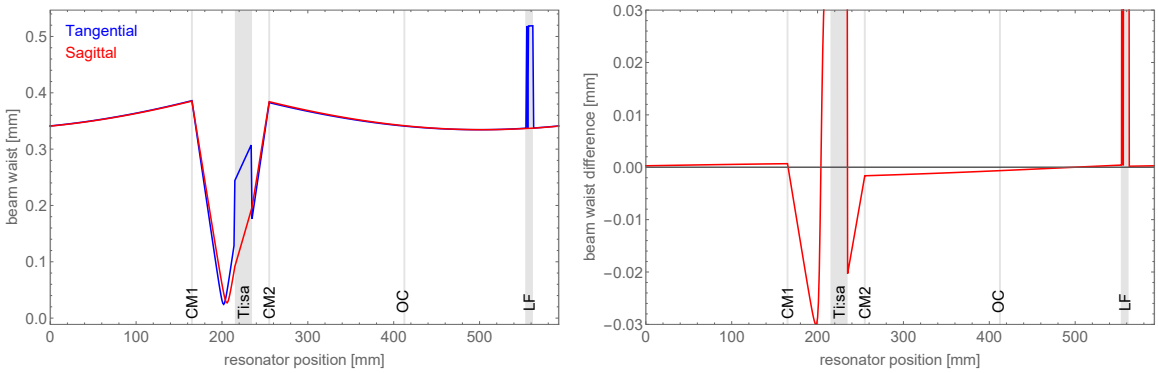

Figure A.4.: Left: Calculated $1/e$ beam waist for the unseeded bowtie-resonator laser in the sagittal and tangential resonator planes. The piezo-actuated mirror marks the zero position of the resonator. Right: $1/e$ beam waist difference (tangential−sagittal).

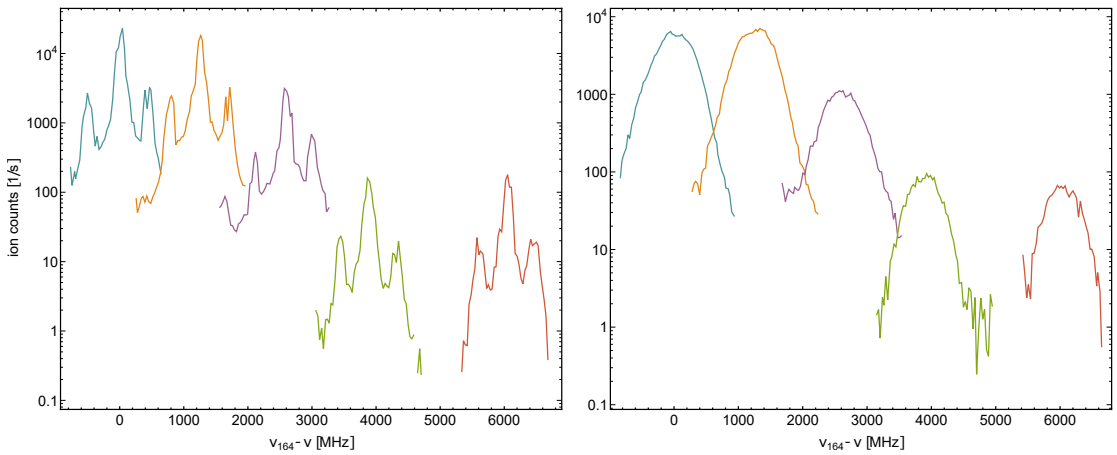

Figure A.5.: Spectrum of the 741 nm line in Dy for all stable even-even isotopes (no HFS) using the unseeded bowtie-resonator laser. Left: normal operation, corresponding to Fig. 4 in Publication I. Right: "scramble" mode, with a fast piezo ramp on the piezo-actuated cavity mirror, resulting in an average linewidth of ≈ 600 MHz.

Compact-footprint injection-seeded laser

Print on A4 paper.
Make sure to select "actual size"
in printer settings.

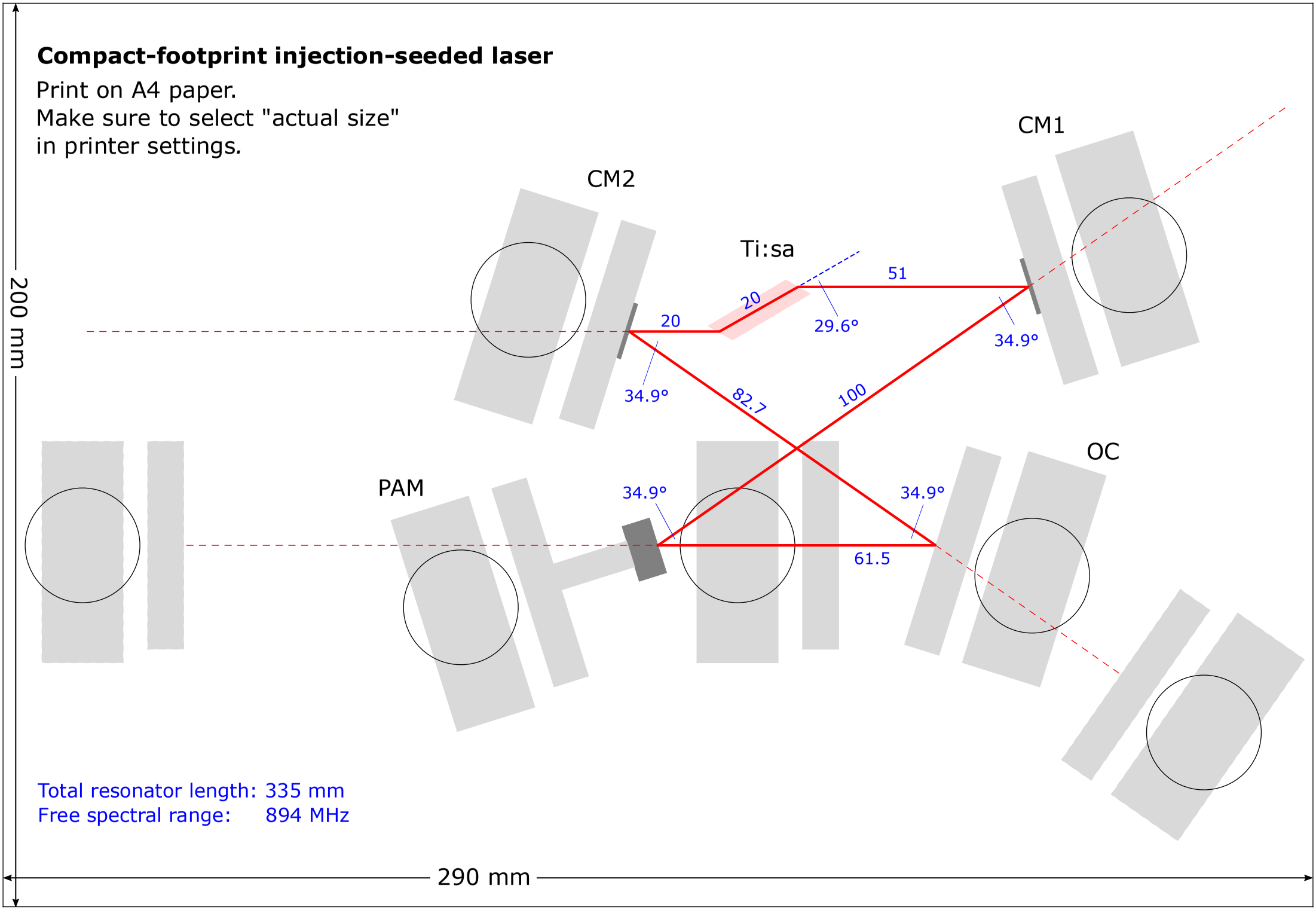

Total resonator length: 335 mm
Free spectral range: 894 MHz

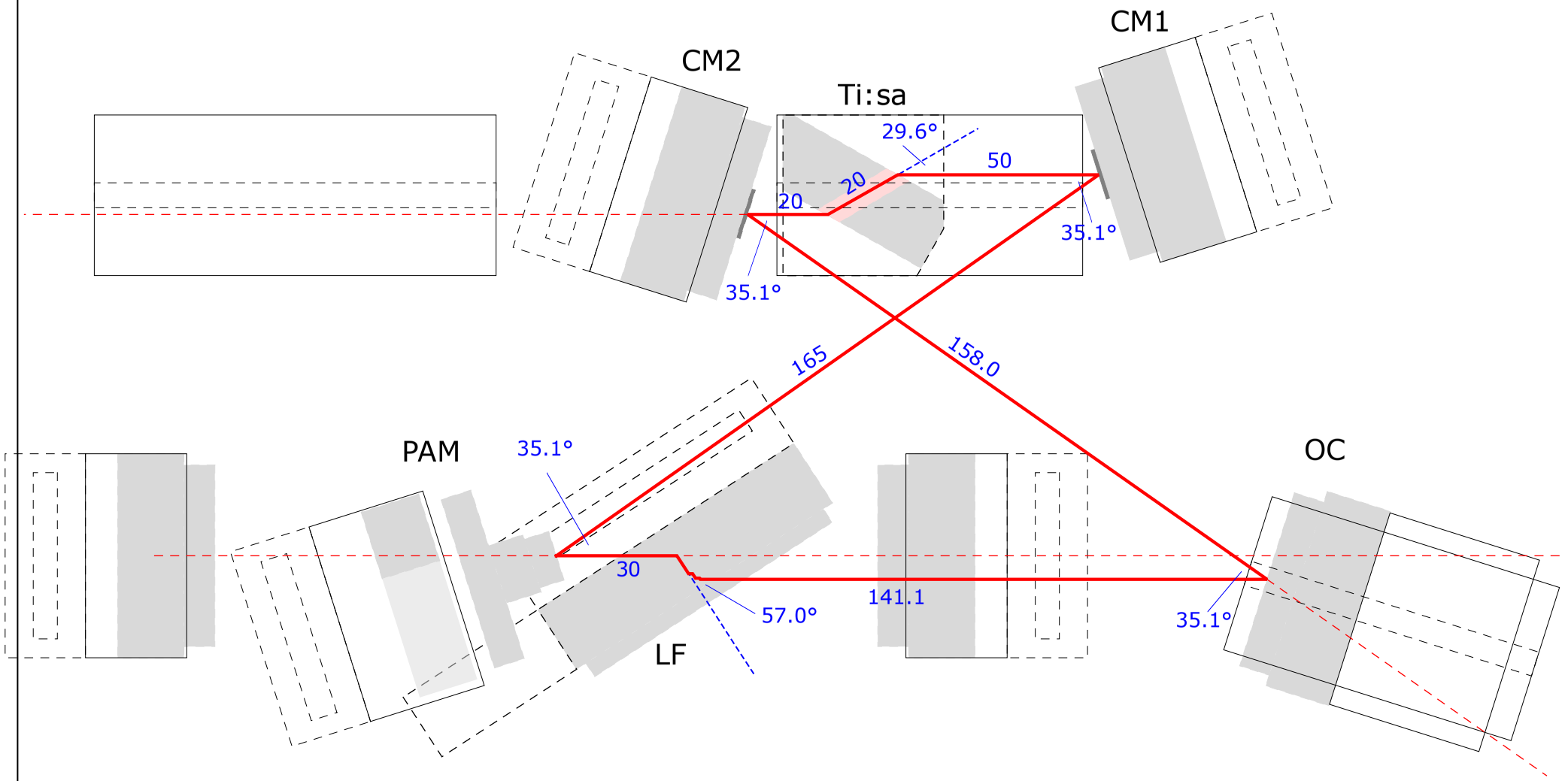

Unseeded bowtie-resonator laser

Print on A3 paper.
Make sure to use 141.4 % (=√2) scaling
in the printer settings.

Total resonator length: 593 mm
Free spectral range: 506 MHz

285 mm

395 mm

A.2 Supplemental Material for "Laser spectroscopy of the 1001-nm ground-state transition in dysprosium"

The following table contains atomic transition data in dysprosium, that was published as supplemental material to Publication I: Phys. Rev. A **98**, 042504 (2018) DOI 10.1103/PhysRevA.98.042504. The data was obtained by scanning a laser from 401 nm to 437 nm, with a fixed first excitation step at 740.962 nm and a non-resonant ionization laser near 780 nm. The corresponding spectrum is given in Fig. A.6.

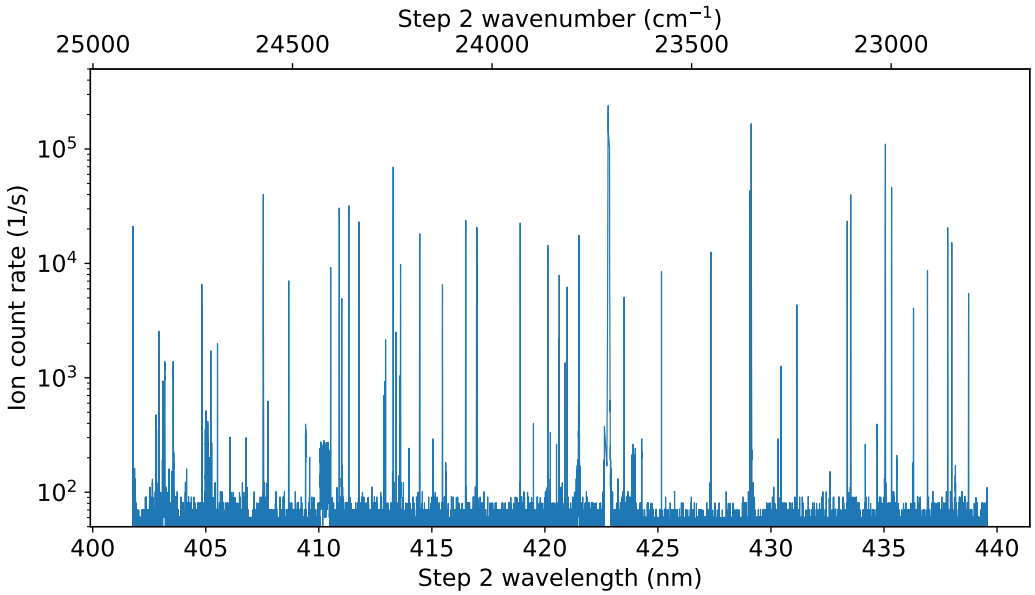

Figure A.6.: Spectrum of the second excitation step in Dy, starting from the 13 495.96 cm^{-1} excited state. For details see text.

Supplemental material for "Laser spectroscopy of the 1000 nm ground state transition in dysprosium"

D. Studer, L. Maske, P. Windpassinger, and K. Wendt
Institut für Physik, Johannes Gutenberg-Universität Mainz, 55128 Mainz, Germany
(Dated: July 20, 2018)

TABLE I. Complete list of second excitation steps starting from the level at $13495.96\,\mathrm{cm}^{-1}(J=9)$. The transition wavelength error is 0.0015 nm. If within the error range, corresponding upper energy levels and J-values, as listed in the NIST database [1], are included.

λ [nm]	E_{up} [cm^{-1}]	J
439.9536		
439.1222		
436.7539	36392.11	8
434.9479	36487.20	9
434.8932	36490.07	10
433.6905	36553.84	8
433.5572		
432.8343	36599.44	8
431.3647		
430.6329	36717.57	9
430.4753		
429.8364	36760.64	8
429.3162		
428.9732	36807.39	8
428.6989	36822.27	9
428.4753		
427.7745		
427.1762	36905.44	10
426.2856	36954.32	9
426.1049	36964.32	9
425.3207	37007.58	10
423.8807	37087.47	8
424.0865		
423.6245		
423.5194		
422.3842		
422.3642		
422.2508		
422.2356		
422.2243		
422.2075		
422.1893		
422.0029		
421.9295		
421.7075		
421.6332		

λ [nm]	E_{up} [cm^{-1}]	J
continued		
421.2404		
421.2120		
420.1685	37295.97	7†
420.0148		
419.9625		
419.8388		
419.7614		
419.6717		
419.6589		
419.5268		
419.4721		
419.4336		
419.3938	37339.89	8
419.3034		
419.2812		
419.2463		
419.1803		
418.9332	37366.09	7†
418.8958		
418.8343		
418.8091		
418.7886		
418.7574		
418.7415		
418.7256		
418.6708		
418.6350		
418.3647	37398.46	8
417.7956		
416.1240	37527.15	8
415.9216		
415.0086	37591.83	9
414.0714	37646.28	8°
413.5472	37676.89	8
413.5864		

λ [nm]	E_{up} [cm^{-1}]	J
continued		
413.1506 *	24204.19	8
413.0479	37706.12	10
412.7220 *	24229.22	9
412.2835	37751.03	9
411.1571		
411.1114	37820.22	8
411.0837		
410.7457	37841.84	8
410.6156 *	24353.58	7
410.1022		
410.0151		
409.6383		
409.2031	37933.63	9
408.6275		
408.2147	37992.78	8
407.2033		
406.7968	38078.12	8
408.0718		
406.2176		
405.6035	38150.52	8
405.4961		
405.2414		
405.0809		
405.0487		
404.7105		
404.5512		
404.3931		
404.3583		
403.9844		
403.8934	38254.97	8
403.3975	38285.36	9
402.6736	38329.91	10
402.2465	38356.27	8

* ground state transition
† $\Delta J > \pm 1$
$^{\circ}$ odd parity

[1] A. Kramida, Y. Ralchenko, J. Reader, and the NIST ASD Team, "NIST Atomic Spectra Database," (2018).

A.3 Supplemental Material for "Atomic transitions and the first ionization potential of promethium determined by laser spectroscopy"

The following tables contain atomic transition and energy level data for neutral promethium, that was published as supplemental material in Publication III: Phys. Rev. A **99**, 062513 (2019) DOI 10.1103/PhysRevA.99.062513.
Table I to Table VII list observed atomic lines. For an overview of the used excitation schemes and the respective abbreviations see Fig. 3 in the article. Since the tables also include relative intensities for most observed lines, plots of the spectra are not included here.
Table VIII and Table IX list odd and even energy levels, respectively. The assignments are inferred according to the rules presented in [164].
Table X comprises values of the first ionization potential for all elements up to $Z = 103$ and the respective uncertainties, which were used for Fig. 1 in the article.

Supplemental material for "Atomic transitions and the first ionization potential of promethium determined by laser spectroscopy"

Dominik Studer,[1,*] Stephan Heinitz,[2] Reinhard Heinke,[1] Pascal Naubereit,[1] Rugard Dressler,[2] Carlos Guerrero,[3] Ulli Köster,[4] Dorothea Schumann,[2] and Klaus Wendt[1]

[1] *Institut für Physik, Johannes Gutenberg-Universität Mainz, 55128 Mainz, Germany*
[2] *Paul-Scherrer Institut, 5232 Villigen, Switzerland*
[3] *Dpto. de Física Atómica, Molecular y Nuclear, Universidad de Sevilla, 41012 Sevilla, Spain*
[4] *Institut Laue-Langevin, 38042 Grenoble, France*

(Dated: May 29, 2019)

I. ATOMIC TRANSITIONS IN PM I BY WAVELENGTH

TABLE I. Wavelengths and transition wavenumbers of new Pm I transitions, as observed in the excitation scheme FES, starting from the $4f^5 6s^2\,{}^5\mathrm{H}^o_J$ ground state fine structure multiplet ($J = {}^5/_2, \ldots, {}^{13}/_2$) in the range from 415 nm to 472 nm. Lines that can be found in [1] are not given. A transition wavenumber error of $0.09\,\mathrm{cm}^{-1}$ is estimated from deviations of observed lines to corresponding literature values in [1].

λ (nm)	$\widetilde{\nu}$ (cm^{-1})	λ (nm)	$\widetilde{\nu}$ (cm^{-1})
467.1271	21 407.45	432.9483	23 097.44
464.5078	21 528.16	431.7275	23 162.76
461.2212	21 681.57	430.3682	23 235.92
459.2919	21 772.65	429.6406	23 275.27
456.8613	21 888.48	427.2667	23 404.58
454.9335	21 981.24	427.1864	23 408.98
452.8707	22 081.36	426.1191	23 467.62
452.3198	22 108.25	425.7047	23 490.46
451.9271	22 127.46	423.1948	23 629.78
450.2230	22 211.22	422.4935	23 669.00
445.6781	22 437.72	421.9184	23 701.26
435.4264	22 965.99	420.7243	23 768.53
435.3269	22 971.24	417.9427	23 926.73
433.8384	23 050.06	417.1122	23 974.37
433.7817	23 053.07	416.5837	24 004.78
433.6554	23 059.79	416.4680	24 011.45

TABLE II. Second excitation steps, as observed in the excitation schemes SES_A, SES_B and SES_C. The transition wavenumber uncertainty is $0.06\,cm^{-1}$. Corresponding to the excitation scheme, lower level energies E_l and total angular momenta J_l are given. The upper energy levels have *odd* parity for all schemes. Relative intensities are given, but should be treated carefully as the third excitation step has an arbitrary wavelength and may be resonant to an auto-ionizing transition.

λ (nm)	E_l(cm^{-1})	J_l	E_u(cm^{-1})	I_{rel}	λ (nm)	E_l(cm^{-1})	J_l	E_u(cm^{-1})	I_{rel}
909.1162	22 080.08	5/2	33 079.8	57	878.5937	22 080.08	5/2	33 461.9	644
907.8514	21 348.22	7/2	32 363.2	25	878.5307	21 348.22	7/2	32 730.9	119
907.6267	21 348.22	7/2	32 366.0	161	877.7962	21 348.22	7/2	32 740.4	304
907.2064	22 080.08	5/2	33 102.9	44	877.6647	21 348.22	7/2	32 742.1	76
905.6460	21 348.22	7/2	32 390.1	33	877.2443	22 080.08	5/2	33 479.4	85
904.3576	22 080.08	5/2	33 137.7	85	877.0358	22 080.08	5/2	33 482.1	616
903.9762	22 080.08	5/2	33 142.3	96	876.9105	21 143.06	7/2	32 546.7	8
901.8636	22 080.08	5/2	33 168.2	24	876.0522	21 348.22	7/2	32 763.1	131
900.8337	21 348.22	7/2	32 449.0	259	875.9097	21 143.06	7/2	32 559.7	8
900.0311	22 080.08	5/2	33 190.8	341	875.8704	22 080.08	5/2	33 497.3	441
898.7373	21 348.22	7/2	32 474.9	105	875.7395	21 348.22	7/2	32 767.1	90
898.4834	22 080.08	5/2	33 209.9	98	874.8512	22 080.08	5/2	33 510.6	870
897.2069	21 348.22	7/2	32 493.9	65	874.4846	21 143.06	7/2	32 578.4	67
897.1827	22 080.08	5/2	33 226.1	93	874.1081	22 080.08	5/2	33 520.3	2285
897.0471	22 080.08	5/2	33 227.8	321	873.7907	21 143.06	7/2	32 587.5	4
895.8691	21 348.22	7/2	32 510.6	38	873.2634	22 080.08	5/2	33 531.4	457
895.1104	21 348.22	7/2	32 520.0	20	871.8625	21 348.22	7/2	32 817.9	526
891.9396	21 348.22	7/2	32 559.7	374	871.5657	21 143.06	7/2	32 616.6	23
891.0338	21 143.06	7/2	32 366.0	46	870.9198	22 080.08	5/2	33 562.2	429
890.9575	22 080.08	5/2	33 304.0	89	870.5816	22 080.08	5/2	33 566.7	454
890.4639	21 348.22	7/2	32 578.4	56	868.6450	21 348.22	7/2	32 860.4	63
889.7613	22 080.08	5/2	33 319.0	152	868.1676	21 348.22	7/2	32 866.8	77
889.7364	21 348.22	7/2	32 587.5	115	867.2384	22 080.08	5/2	33 610.9	53
888.3754	21 348.22	7/2	32 604.7	107	866.9691	21 348.22	7/2	32 882.7	29
888.2549	22 080.08	5/2	33 338.1	271	866.5053	21 143.06	7/2	32 683.7	6
887.4418	21 348.22	7/2	32 616.6	148	865.6487	22 080.08	5/2	33 632.2	124
887.1423	22 080.08	5/2	33 352.3	218	865.2606	21 348.22	7/2	32 905.4	34
886.8169	21 348.22	7/2	32 624.5	22	864.8667	22 080.08	5/2	33 642.6	468
886.3874	22 080.08	5/2	33 361.9	426	864.4839	22 080.08	5/2	33 647.7	81
885.3811	22 080.08	5/2	33 374.7	628	864.0721	22 080.08	5/2	33 653.2	232
884.5260	21 348.22	7/2	32 653.7	6	863.4338	21 143.06	7/2	32 724.7	13
883.3989	21 348.22	7/2	32 668.1	292	862.4271	21 348.22	7/2	32 943.4	77
882.6909	22 080.08	5/2	33 409.1	280	861.7821	21 348.22	7/2	32 952.1	142
882.4663	21 143.06	7/2	32 474.9	259	861.6819	22 080.08	5/2	33 685.3	222
882.1863	21 348.22	7/2	32 683.7	451	861.6411	22 080.08	5/2	33 685.8	22
881.9959	21 348.22	7/2	32 686.1	172	860.5925	21 143.06	7/2	32 763.1	10
881.3313	21 143.06	7/2	32 489.5	5	860.3704	22 080.08	5/2	33 703.0	10
879.6942	21 143.06	7/2	32 510.6	12	860.2220	21 348.22	7/2	32 973.1	30
879.2967	22 080.08	5/2	33 452.8	21	859.7980	22 080.08	5/2	33 710.7	9
879.0109	21 348.22	7/2	32 724.7	293	859.7276	22 080.08	5/2	33 711.7	63
878.9688	21 143.06	7/2	32 520.0	11	859.6579	21 348.22	7/2	32 980.8	18

(Continued on next page.)

TABLE II: *(Continued.)*

λ (nm)	E_l(cm^{-1})	J_l	E_u(cm^{-1})	$I_{\rm rel}$	λ (nm)	E_l(cm^{-1})	J_l	E_u(cm^{-1})	$I_{\rm rel}$
858.5175	22 080.08	5/2	33 728.1	50	834.0306	21 348.22	7/2	33 338.1	27
857.9137	22 080.08	5/2	33 736.3	68	833.0502	21 348.22	7/2	33 352.3	40
856.6005	21 348.22	7/2	33 022.3	293	832.5344	21 348.22	7/2	33 359.7	252
856.5406	21 143.06	7/2	32 817.9	31	832.3808	21 348.22	7/2	33 361.9	29
856.3304	22 080.08	5/2	33 757.8	351	831.4941	21 348.22	7/2	33 374.7	65
856.1504	22 080.08	5/2	33 760.3	82	830.6553	21 348.22	7/2	33 386.9	257
855.1672	22 080.08	5/2	33 773.7	107	829.1234	21 348.22	7/2	33 409.1	208
854.5395	22 080.08	5/2	33 782.3	595	827.1163	21 348.22	7/2	33 438.4	142
853.4363	21 143.06	7/2	32 860.4	11	826.1281	21 348.22	7/2	33 452.8	6
852.9640	21 143.06	7/2	32 866.8	22	825.4299	21 348.22	7/2	33 463.1	247
851.8174	21 143.06	7/2	32 882.7	38	824.1364	21 348.22	7/2	33 482.1	178
850.9522	22 080.08	5/2	33 831.6	237	822.2062	21 348.22	7/2	33 510.6	95
850.7232	21 348.22	7/2	33 102.9	56	821.5500	21 348.22	7/2	33 520.3	82
850.1717	21 143.06	7/2	32 905.4	15	820.7988	21 348.22	7/2	33 531.4	84
848.8406	22 080.08	5/2	33 860.9	465	820.5950	21 348.22	7/2	33 534.5	122
848.7463	22 080.08	5/2	33 862.2	213	818.7294	21 348.22	7/2	33 562.2	39
848.2634	21 348.22	7/2	33 137.0	310	818.4347	21 348.22	7/2	33 566.7	52
848.2169	21 348.22	7/2	33 137.7	42	814.0621	21 348.22	7/2	33 632.2	176
847.8814	21 348.22	7/2	33 142.3	69	813.0423	21 348.22	7/2	33 647.7	167
846.0866	22 080.08	5/2	33 899.2	827	812.6791	21 348.22	7/2	33 653.2	186
844.5634	22 080.08	5/2	33 920.5	807	811.5166	21 348.22	7/2	33 670.8	136
844.4525	22 080.08	5/2	33 922.1	1031	810.5625	21 348.22	7/2	33 685.3	431
843.9424	22 080.08	5/2	33 929.2	205	810.1528	21 348.22	7/2	33 691.6	496
842.9201	22 080.08	5/2	33 943.6	199	808.8326	21 348.22	7/2	33 711.7	49
841.7066	22 080.08	5/2	33 960.7	33	808.2331	21 348.22	7/2	33 720.9	201
840.4995	22 080.08	5/2	33 977.8	87	807.7634	21 348.22	7/2	33 728.1	65
839.5658	22 080.08	5/2	33 991.0	29	805.8254	21 348.22	7/2	33 757.8	84
838.9859	21 348.22	7/2	33 267.4	160	804.7952	21 348.22	7/2	33 773.7	53
838.8404	22 080.08	5/2	34 001.3	258	804.2384	21348.22	7/2	33 782.3	945
837.9388	22 080.08	5/2	34 014.1	24	803.5399	21 348.22	7/2	33 793.2	215
837.4111	22 080.08	5/2	34 021.6	28	801.0632	21 348.22	7/2	33 831.6	866
836.4164	21 348.22	7/2	33 304.0	22	800.9863	21 348.22	7/2	33 832.8	681
835.3611	21 348.22	7/2	33 319.1	97	800.4523	21 348.22	7/2	33 841.2	449
835.3536	22 080.08	5/2	34 051.1	38	799.1909	21 348.22	7/2	33 860.9	140
834.9238	22 080.08	5/2	34 057.2	50					

TABLE III. Ionizing transitions obtained in the two-step excitation scheme B0. Upper energy levels have *odd* parity and possible total angular momenta of $J = {}^{5}/_{2},{}^{7}/_{2},{}^{9}/_{2}$. The transition wavenumber uncertainty is $0.06\,\mathrm{cm}^{-1}$. Resonances with a gaussian width of $> 0.5\,\mathrm{cm}^{-1}$ are marked with w. Relative line intensities are given.

λ (nm)	E_u (cm^{-1})	I_{rel}	λ (nm)	E_u (cm^{-1})	I_{rel}	λ (nm)	E_u (cm^{-1})	I_{rel}
432.4560	44 472.0	1	426.7000	44 783.9	25	424.1209^{w}	44 926.4	83
431.7280	44 510.9	47	426.6425	44 787.0	18	424.0939	44 927.9	33
431.4429	44 526.3	17	426.6085	44 787.6	15	424.0836	44 928.5	41
431.4288	44 527.0	14	426.6323	44 788.9	28	424.0719	44 929.1	21
431.2497	44 536.6	93	426.5533	44 791.9	70	424.0427^{w}	44 930.8	64
430.8989	44 555.5	29	426.5326	44 793.1	36	424.0223	44 931.9	42
430.4517	44 565.6	22	426.2568	44 808.3	30	424.0129	44 932.4	136
430.7114	44 567.0	11	426.2085	44 810.9	31	423.9839	44 934.0	37
430.6857	44 579.6	15	426.1398	44 814.7	21	423.9534^{w}	44 935.7	29
430.3098	44 587.3	9	426.0186	44 821.4	47	423.8910	44 939.2	91
430.0654	44 600.5	48	425.9810	44 823.4	17	423.8611	44 940.9	32
430.0378	44 602.0	18	425.8371	44 831.4	32	423.8329	44 942.4	101
429.9929	44 604.4	13	425.7625	44 835.5	20	423.8172	44 943.3	49
429.9521	44 606.6	15	425.7053	44 838.7	46	423.7780	44 945.5	78
429.9103	44 608.9	36	425.6616	44 841.1	81	423.7170^{w}	44 948.9	80
429.8640	44 611.4	23	425.6313	44 842.7	17	423.6585^{w}	44 952.1	93
429.8503	44 612.1	22	425.5579	44 846.8	50	423.6291	44 953.8	88
429.7917	44 615.3	136	425.5409	44 847.7	115	423.6136	44 954.6	57
429.7423	44 618.0	50	425.5053	44 849.7	27	423.5807	44 956.5	20
429.5372	44 629.1	19	425.4869	44 850.7	18	423.5659	44 957.3	22
429.5161	44 630.2	45	425.3641	44 857.5	11	423.5497	44 958.2	39
429.4196	44 635.5	27	425.3456	44 858.5	18	423.5148	44 960.1	17
429.0687	44 654.5	11	425.3067	44 860.7	15	423.4687	44 962.7	107
428.9895	44 658.8	19	425.1762	44 867.9	25	423.4586	44 963.3	299
428.7328	44 672.8	30	425.1185	44 871.1	31	423.4466	44 963.9	84
428.5846	44 680.8	13	425.0373	44 875.6	12	423.4059	44 966.2	216
428.5600	44 682.2	33	424.9829	44 878.6	12	423.3767^{w}	44 967.9	171
428.4969	44 685.6	84	424.9479	44 880.5	16	423.3540	44 969.1	81
428.2358	44 699.8	7	424.9036^{w}	44 883.0	16	423.3187	44 971.1	30
428.1675	44 703.6	57	424.8233	44 887.4	83	423.2207	44 976.6	19
428.0749	44 705.7	17	424.7822	44 889.7	123	423.1885	44 978.3	9
428.1292	44 708.6	10	424.7242	44 892.9	57	423.1635	44 979.7	51
427.8505	44 720.9	22	424.7119	44 893.6	46	423.1512	44 980.4	83
427.5124	44 739.4	30	424.6452	44 897.3	10	423.1300	44 981.6	37
427.4327	44 743.7	58	424.5665	44 901.7	21	423.1074	44 982.9	38
427.3429	44 748.6	41	424.4490	44 908.2	20	423.0971	44 983.5	149
427.2668	44 752.8	35	424.3063	44 916.1	43	423.0861	44 984.1	79
427.1720	44 758.0	27	424.2277	44 920.5	18	423.0707	44 984.9	46
427.0975	44 762.1	12	424.2089	44 921.5	182	423.0385^{w}	44 986.7	256
427.0885	44 762.6	16	424.1758	44 923.4	175	423.0176	44 987.9	19
427.0697	44 763.6	26	424.1681	44 923.8	65	422.9589^{w}	44 991.2	58
426.7537	44 780.9	72	424.1563	44 924.4	162	422.9336	44 992.6	308

(Continued on next page.)

TABLE III: *(Continued.)*

λ (nm)	E_u(cm^{-1})	$I_{\rm rel}$	λ (nm)	E_u(cm^{-1})	$I_{\rm rel}$	λ (nm)	E_u(cm^{-1})	$I_{\rm rel}$
422.9178	44 993.5	324	422.5234	45 015.5	142	421.9484	45 047.8	215
422.8407^w	44 997.8	97	422.5135	45 016.1	864	421.9195^w	45 049.4	322
422.7662	45 002.0	53	422.4464^w	45 019.9	263	421.9038	45 050.3	102
422.7396	45 003.4	28	422.3694^w	45 024.2	244	421.8789	45 051.7	53
422.7091	45 005.2	454	422.2592^w	45 030.4	314	421.8370^w	45 054.1	130
422.6934^w	45 006.0	372	422.1570	45 036.1	98	421.7745^w	45 057.6	191
422.6407^w	45 009.0	522	422.0817	45 040.3	167	421.7142	45 061.0	742
422.5985	45 011.3	136	422.0537	45 041.9	72			
422.5439^w	45 014.4	151	421.9727	45 046.4	754			

TABLE IV. Ionizing transitions obtained in the three-step excitation scheme B1. Upper energy levels have *even* parity and possible total angular momenta of $J = {}^3/_2, \ldots, {}^{11}/_2$. The transition wavenumber uncertainty is 0.06 cm^{-1}. Resonances with a gaussian width of > 0.5 cm^{-1} are marked with w. Relative line intensities are given.

λ (nm)	E_u(cm^{-1})	$I_{\rm rel}$	λ (nm)	E_u(cm^{-1})	$I_{\rm rel}$	λ (nm)	E_u(cm^{-1})	$I_{\rm rel}$
819.0206	44 893.4	72	810.7189^w	45 018.4	774	787.3963	45 383.8	57
817.9992	44 908.6	47	810.6722	45 019.1	519	787.2544	45 386.1	25
816.8487	44 925.9	31	810.0609	45 028.4	382	787.1913	45 387.1	218
816.3039	44 934.0	56	809.9504	45 030.1	396	787.1447	45 387.8	321
815.2687	44 949.6	56	809.7886	45 032.6	535	786.9946	45 390.3	16
814.5609	44 960.2	29	809.7315^w	45 033.5	135	786.5994	45 396.6	55
814.5238	44 960.8	40	809.6608	45 034.5	249	786.5150^w	45 398.0	13
813.9676	44 969.2	20	809.5841^w	45 035.7	53	786.3612	45 400.5	46
813.8146	44 971.5	39	809.4568^w	45 037.7	114	786.2654	45 402.0	23
813.4912	44 976.4	88	809.3407	45 039.4	148	785.9697	45 406.8	12
813.4302	44 977.3	30	809.0619^w	45 043.7	513	785.8403	45 408.9	69
813.3676^w	44 978.3	10	808.9287^w	45 045.7	172	785.7813^w	45 409.9	99
813.2538	44 980.0	111	808.8858^w	45 046.4	159	785.6933	45 411.3	162
812.8847	44 985.6	50	808.6691	45 049.7	102	785.4083	45 415.9	144
812.8334	44 986.3	28	808.5382^w	45 051.7	62	785.2617	45 418.3	70
812.7397^w	44 987.8	59	808.4302^w	45 053.3	97	785.1844	45 419.6	46
812.6135	44 989.7	40	808.1689^w	45 057.3	276	785.0768	45 421.3	19
812.5482	44 990.7	11	807.8098	45 062.8	329	784.3010^w	45 433.9	19
811.9349	45 000.0	58	787.7888	45 377.5	58	783.7188^w	45 443.4	25
811.6228	45 004.7	210	787.7083	45 378.7	132	783.2479^w	45 451.0	35
811.4806^w	45 006.8	339	787.6982	45 378.9	71	782.7559^w	45 459.1	80
811.3164	45 009.3	609	787.5557	45 381.2	114	782.4369^w	45 464.3	33
810.7948^w	45 017.3	196	787.5276	45 381.7	52	782.1880^w	45 468.3	94

TABLE V. Ionizing transitions obtained in the three-step excitation scheme B2. Upper energy levels have *even* parity and possible total angular momenta of $J = {}^3/_2, \ldots, {}^{11}/_2$. The transition wavenumber uncertainty is $0.06\,\mathrm{cm}^{-1}$. Resonances with a gaussian width of $> 0.5\,\mathrm{cm}^{-1}$ are marked with w. Relative line intensities are given.

λ (nm)	E_u(cm^{-1})	I_{rel}	λ (nm)	E_u(cm^{-1})	I_{rel}	λ (nm)	E_u(cm^{-1})	I_{rel}
822.4679	44 883.3	72	815.9752	44 978.0	421	807.0533^w	45 115.5	370
821.9221	44 891.3	173	815.6037	44 985.6	242	806.7470^w	45 120.2	921
821.9136	44 891.5	291	814.9075^w	44 996.1	86	806.5472	45 123.3	181
821.7348	44 894.1	196	814.6500	44 999.9	74	806.5184	45 123.7	144
821.3921	44 899.2	111	814.3345	45 004.7	1206	806.3652	45 126.1	488
821.2155	44 901.8	39	814.1922	45 006.8	333	806.2119	45 128.4	195
821.1784	44 902.3	104	814.1767^w	45 007.1	218	805.8802	45 133.5	193
821.1707	44 902.5	105	814.0297	45 009.3	197	805.7290	45 135.8	830
821.0480	44 904.3	46	813.4216	45 018.5	153	805.7057^w	45 136.2	277
820.7501	44 908.7	614	813.3781	45 019.1	805	804.6297^w	45 152.8	200
820.7361	44 908.9	74	812.7615	45 028.5	846	804.3002	45 157.9	747
820.5869	44 911.1	251	812.6715	45 029.8	299	803.8078^w	45 165.5	101
820.2094	44 916.7	1402	812.4990	45 032.4	163	803.7406	45 166.6	170
819.9344^w	44 920.8	94	812.2912^w	45 035.6	66	803.5020^w	45 170.2	114
819.8858	44 921.5	293	812.1569	45 037.6	580	803.3928^w	45 171.9	134
819.7749	44 923.2	127	812.0366	45 039.4	92	802.6290	45 183.8	82
819.7096	44 924.2	602	811.7521^w	45 043.8	857	802.2769	45 189.2	36
819.6391	44 925.2	261	811.3681	45 049.6	95	802.1959	45 190.5	64
819.5963	44 925.9	1875	811.1357^w	45 053.1	445	801.7143^w	45 198.0	194
819.5077	44 927.2	486	810.4948	45 062.9	260	800.7735^w	45 212.7	592
819.0454	44 934.1	141	809.2524	45 081.8	65	800.4824^w	45 217.2	136
818.7411	44 938.6	40	809.2072	45 082.5	90	800.3686	45 219.0	248
817.8426	44 952.0	86	809.1607	45 083.2	204	800.1738	45 222.0	72
817.7225	44 953.8	134	808.6827^w	45 090.5	63	800.1267	45 222.7	148
817.2788^w	44 960.5	366	808.4868^w	45 093.5	154	799.8503^w	45 227.1	245
817.1536	44 962.3	88	808.3572^w	45 095.5	332	799.6636	45 230.0	518
816.5408	44 971.5	220	807.3360^w	45 111.1	580	799.6239	45 230.6	1117
816.2223	44 976.3	796	807.1967	45 113.3	519			

TABLE VI. Ionizing transitions obtained in the three-step excitation scheme C1. Upper energy levels have *even* parity and possible total angular momenta of $J = 7/2,\ 9/2$. The transition wavenumber uncertainty is $0.06\,\mathrm{cm}^{-1}$. Resonances with a gaussian width of $> 0.5\,\mathrm{cm}^{-1}$ are marked with w. Relative line intensities are given.

λ (nm)	E_u(cm^{-1})	I_{rel}	λ (nm)	E_u(cm^{-1})	I_{rel}	λ (nm)	E_u(cm^{-1})	I_{rel}
889.0614	44 551.8	43	876.4427	44 713.7	43	867.2276	44 835.0	246
888.8840	44 554.0	25	876.1254	44 717.9	18	867.0568	44 837.2	141
888.8003	44 555.1	36	876.0725	44 718.5	66	866.9393	44 838.8	109
887.8069	44 567.7	20	875.7511	44 722.7	17	866.7106	44 841.8	53
887.6414	44 569.8	18	875.4612	44 726.5	86	866.6362	44 842.8	31
887.5464	44 571.0	18	875.4122	44 727.2	62	866.4588	44 845.2	206
886.6061	44 582.9	58	875.3753	44 727.6	54	866.3693	44 846.4	58
886.4557	44 584.8	16	874.9650	44 733.0	14	866.2562	44 847.9	73
886.2651	44 587.3	10	874.4142	44 740.2	20	866.2098	44 848.5	24
885.9486	44 591.3	15	873.5054	44 752.1	13	865.7387	44 854.8	58
885.7865	44 593.4	23	873.4162	44 753.3	103	865.6799	44 855.6	243
885.5437	44 596.5	43	872.7596	44 761.9	14	865.5950	44 856.7	44
885.4058	44 598.2	8	872.3611	44 767.1	79	865.5561	44 857.2	12
885.2142	44 600.7	64	872.2642	44 768.4	106	865.4970	44 858.0	92
884.3971	44 611.1	22	872.1402	44 770.0	86	865.4187	44 859.1	21
884.1963	44 613.7	27	871.9050	44 773.1	211	865.3507	44 860.0	52
883.9162	44 617.3	7	871.5944	44 777.2	140	864.9712	44 865.0	151
883.7663	44 619.2	31	871.4806	44 778.7	14	864.9283	44 865.6	173
883.1731	44 626.8	35	871.3134	44 780.9	127	864.7110	44 868.5	38
883.0409	44 628.5	53	870.7984	44 787.7	124	864.5320	44 870.9	493
882.9753	44 629.3	51	870.6353	44 789.8	50	864.4389	44 872.2	29
882.6307	44 633.7	34	870.5361	44 791.1	24	864.2247	44 875.0	241
882.5431	44 634.9	39	870.4903	44 791.7	50	863.6797^{w}	44 882.3	59
882.4323	44 636.3	12	870.4558	44 792.2	85	863.0059	44 891.4	60
882.1649	44 639.7	46	870.1038	44 796.8	57	862.6270	44 896.5	276
881.2510	44 651.5	23	869.8353	44 800.4	19	862.5894	44 897.0	144
881.2075	44 652.0	15	869.6539	44 802.8	133	862.5353	44 897.7	174
881.0871	44 653.6	14	869.5512	44 804.2	226	862.2423	44 901.6	283
880.5088	44 661.0	65	869.3946	44 806.2	26	862.1958	44 902.3	432
879.9638	44 668.1	16	869.3207	44 807.2	53	862.1348	44 903.1	26
879.9064	44 668.8	74	869.1559	44 809.4	299	861.9918	44 905.0	121
879.2710	44 677.0	9	869.0529	44 810.7	60	861.8088	44 907.5	108
878.4523	44 687.6	27	869.0115	44 811.3	26	861.4830	44 911.9	49
878.2950	44 689.7	55	868.8640	44 813.2	33	861.1429	44 916.4	53
878.0095	44 693.4	34	868.7286	44 815.0	11	861.0998	44 917.0	76
877.6725	44 697.7	14	868.5676	44 817.2	33	860.6458	44 923.1	83
877.1437	44 704.6	10	868.3480	44 820.1	220	860.4508	44 925.8	95
877.0735	44 705.5	94	868.1403	44 822.8	36	860.3987	44 926.5	29
876.9313	44 707.4	34	868.0815	44 823.6	157	860.3544	44 927.1	97
876.6993	44 710.4	59	867.7877	44 827.5	14	860.1982	44 929.2	25
876.6713	44 710.7	60	867.6025	44 830.0	25	860.0046^{w}	44 931.8	14
876.4732	44 713.3	22	867.3289	44 833.6	211	859.9031	44 933.2	71

(Continued on next page.)

TABLE VI: *(Continued.)*

λ (nm)	E_u (cm^{-1})	$I_{\rm rel}$	λ (nm)	E_u (cm^{-1})	$I_{\rm rel}$	λ (nm)	E_u (cm^{-1})	$I_{\rm rel}$
859.8467	44 933.9	56	848.9594	45 083.1	448	839.0356	45 222.4	1459
859.6537^w	44 936.6	14	848.7971^w	45 085.3	1100	838.7191^w	45 226.9	1012
858.8990	44 946.8	13	848.5859^w	45 088.3	363	838.5380	45 229.5	901
858.6784	44 949.8	50	847.4400^w	45 104.2	1822	838.3684^w	45 231.9	498
858.5892	44 951.0	57	847.2255^w	45 107.2	257	838.0849^w	45 235.9	528
858.4668	44 952.6	365	847.1284^w	45 108.6	1690	837.9972	45 237.2	890
858.3100^w	44 954.8	52	846.7275^w	45 114.1	1199	837.8715	45 239.0	1525
858.0745^w	44 958.0	20	846.6365^w	45 115.4	547	837.8214^w	45 239.7	1374
857.7520	44 962.3	232	846.2712^w	45 120.5	234	837.7163	45 241.2	1317
857.7004^w	44 963.0	59	845.4882	45 131.5	53	837.6036	45 242.8	328
856.9210^w	44 973.7	73	845.3353	45 133.6	162	837.5629	45 243.4	854
856.6102	44 977.9	458	845.1430^w	45 136.3	536	837.4225	45 245.4	204
856.0995	44 984.9	476	844.9208	45 139.4	181	837.2035	45 248.5	512
855.8272	44 988.6	45	844.6538^w	45 143.1	751	837.0550	45 250.6	649
855.6656^w	44 990.8	93	844.1612^w	45 150.0	98	836.9868^w	45 251.6	2151
855.3240^w	44 995.4	20	843.5784	45 158.2	270	836.8740^w	45 253.2	1648
853.6503^w	45 018.4	2041	843.4756	45 159.7	1091	836.5837	45 257.3	1612
853.0070^w	45 027.2	227	843.3950^w	45 160.8	160	836.4971^w	45 258.6	1084
852.8354	45 029.6	215	843.0637^w	45 165.5	285	836.2994	45 261.4	1594
852.5481^w	45 033.5	344	842.9915	45 166.5	258	836.2309	45 262.4	3881
852.4778	45 034.5	362	842.6284^w	45 171.6	141	835.9462^w	45 266.5	1149
852.2309^w	45 037.9	129	842.5934^w	45 172.1	395	835.5868^w	45 271.6	1418
852.1223	45 039.4	405	842.2045	45 177.6	1664	835.4529^w	45 273.5	1049
851.7982^w	45 043.8	389	841.7833	45 183.5	121	835.3047	45 275.6	851
851.6871^w	45 045.4	215	841.3731	45 189.3	226	835.1602	45 277.7	2111
851.5150^w	45 047.7	444	841.1478	45 192.5	102	835.0929^w	45 278.7	2625
851.3746	45 049.7	915	840.9101^w	45 195.8	121	835.0005^w	45 280.0	741
851.1256^w	45 053.1	906	839.7309^w	45 212.5	286	834.8671^w	45 281.9	731
850.8642^w	45 056.7	1007	839.6713	45 213.4	762	834.5098^w	45 287.0	201
849.5410^w	45 075.0	436	839.5690	45 214.8	313	834.2975^w	45 290.1	315
849.0814	45 081.4	828	839.4982	45 215.8	99	834.1156	45 292.7	940
849.0247	45 082.2	142	839.1205	45 221.2	358			

TABLE VII. Ionizing transitions obtained in the three-step excitation scheme C2. Upper energy levels have *even* parity and possible total angular momenta of $J = 5/2,\ 7/2,\ 9/2$. The transition wavenumber uncertainty is $0.06\,\mathrm{cm}^{-1}$. Resonances with a gaussian width of $> 0.5\,\mathrm{cm}^{-1}$ are marked with w. Relative line intensities are given.

λ (nm)	E_u(cm^{-1})	I_{rel}	λ (nm)	E_u(cm^{-1})	I_{rel}	λ (nm)	E_u(cm^{-1})	I_{rel}
908.4307	44 360.1	20	893.7441	44 541.0	21	882.4787	44 683.9	200
908.3437	44 361.2	38	893.4710	44 544.5	12	882.2898	44 686.3	31
908.1052	44 364.1	52	893.4004	44 545.3	89	882.1919	44 687.6	15
906.7472	44 380.6	23	893.0931	44 549.2	41	882.0245	44 689.7	379
906.2476	44 386.7	18	892.7131	44 554.0	22	881.9699	44 690.4	155
905.6792	44 393.6	20	892.2981	44 559.2	259	881.9374	44 690.8	140
905.2883	44 398.4	22	891.8086	44 565.3	130	881.8875	44 691.5	64
904.8632	44 403.5	60	891.6292	44 567.6	40	881.7666	44 693.0	58
904.3479	44 409.8	24	891.2803	44 572.0	32	881.7434	44 693.3	160
903.8462	44 416.0	15	890.9916	44 575.6	70	881.7235	44 693.6	196
903.2961	44 422.7	14	890.4141	44 582.9	52	881.7021	44 693.9	79
903.1850	44 424.1	93	890.3165	44 584.1	126	881.4423	44 697.2	91
902.9641	44 426.8	45	890.2627	44 584.8	14	881.4014	44 697.7	26
902.3636	44 434.2	30	890.1781	44 585.9	25	881.2664	44 699.5	143
902.2528	44 435.5	75	889.9630	44 588.6	49	880.8024	44 705.4	126
902.1248	44 437.1	20	889.8799	44 589.6	31	880.6932	44 706.8	141
901.6221	44 443.3	67	889.8066	44 590.6	64	880.6584	44 707.3	137
901.2265	44 448.1	65	889.5909	44 593.3	44	880.4239	44 710.3	238
900.8133	44 453.2	46	889.4645	44 594.9	80	880.4042	44 710.6	152
899.8408	44 465.2	150	888.9105	44 601.9	23	880.2403	44 712.7	13
899.2636	44 472.4	13	888.4093	44 608.2	37	880.1998	44 713.2	33
898.9682	44 476.0	38	888.2963	44 609.7	186	879.8470	44 717.8	356
898.7558	44 478.6	106	888.1863	44 611.1	124	879.7907	44 718.5	88
898.4926	44 481.9	77	887.9857	44 613.6	77	879.7030	44 719.6	367
898.3547	44 483.6	70	887.7029	44 617.2	190	879.4721	44 722.6	52
898.0485	44 487.4	53	886.9932	44 626.2	314	879.3358	44 724.4	180
897.9627	44 488.5	66	886.8211	44 628.4	208	879.1412	44 726.9	126
897.7772	44 490.8	43	886.4033	44 633.7	39	879.0935	44 727.5	110
897.4490	44 494.8	11	886.3543	44 634.3	145	878.8141	44 731.1	85
896.9372	44 501.2	95	886.0495	44 638.2	42	878.6848	44 732.8	92
896.4072	44 507.8	83	885.9035	44 640.1	172	878.1224	44 740.1	96
896.2298	44 510.0	49	885.0968	44 650.4	292	877.9766	44 742.0	297
895.8598	44 514.6	51	885.0147	44 651.4	23	877.9150	44 742.8	23
895.7932	44 515.4	68	884.6771	44 655.7	246	877.6299	44 746.5	104
895.5056	44 519.0	30	884.5169	44 657.8	60	877.5133	44 748.0	1259
895.3596	44 520.9	94	884.2680	44 660.9	370	877.4145^{w}	44 749.3	22
895.1220	44 523.8	83	883.7809	44 667.2	253	877.2190	44 751.8	101
894.9999	44 525.3	16	883.6585	44 668.7	214	877.1988	44 752.1	149
894.7310	44 528.7	27	883.4237	44 671.8	218	877.1120	44 753.2	150
894.4545	44 532.2	228	883.0137	44 677.0	112	876.7926	44 757.4	295
893.9296	44 538.7	123	882.9819	44 677.4	71	876.5812	44 760.1	541
893.7733	44 540.7	158	882.9349	44 678.0	28	876.4492	44 761.8	116

(Continued on next page.)

TABLE VII: *(Continued.)*

λ (nm)	E_u(cm^{-1})	$I_{\rm rel}$	λ (nm)	E_u(cm^{-1})	$I_{\rm rel}$	λ (nm)	E_u(cm^{-1})	$I_{\rm rel}$
876.3138	44 763.6	90	871.2505	44 829.9	427	867.2969	44 882.2	78
876.2793	44 764.0	613	871.1810	44 830.8	777	867.2778	44 882.5	126
876.0490	44 767.0	50	871.1541	44 831.2	342	867.2402	44 883.0	53
875.9719	44 768.0	63	871.0609	44 832.4	70	867.1895	44 883.7	76
875.9557	44 768.3	140	870.9931	44 833.3	649	867.0621	44 885.4	819
875.9419	44 768.4	139	870.9741	44 833.6	171	866.8238	44 888.5	108
875.6609	44 772.1	938	870.8716	44 834.9	907	866.7776	44 889.1	201
875.5881	44 773.0	34	870.7937	44 835.9	73	866.6763	44 890.5	28
875.2784	44 777.1	397	870.3478	44 841.8	1851	866.6140	44 891.3	133
875.1640	44 778.6	539	870.2859	44 842.6	537	866.5620	44 892.0	35
875.0448	44 780.1	595	870.2652	44 842.9	588	866.4707	44 893.2	73
874.9944	44 780.8	929	870.1765	44 844.1	204	866.2325	44 896.4	3314
874.6627	44 785.1	540	870.1396	44 844.6	3741	866.2024	44 896.8	600
874.3114	44 789.7	534	870.1161	44 844.9	794	866.1528	44 897.5	2191
874.2480	44 790.6	609	870.0432	44 845.8	789	866.0391	44 899.0	2525
874.2091	44 791.1	126	870.0098	44 846.3	945	866.0116	44 899.3	1088
874.1670	44 791.6	143	869.9787	44 846.7	798	865.9925	44 899.6	1794
874.1293	44 792.1	718	869.9010	44 847.7	89	865.9012	44 900.8	4945
873.9802	44 794.1	879	869.7253	44 850.0	302	865.8397	44 901.6	1131
873.8733	44 795.5	94	869.6004	44 851.7	560	865.7969	44 902.2	1725
873.7799	44 796.7	1151	869.3720	44 854.7	2400	865.7343	44 903.0	141
873.6756	44 798.1	213	869.3124	44 855.5	1567	865.6428	44 904.3	182
873.5031	44 800.3	109	869.2787	44 855.9	920	865.6079	44 904.7	209
873.4552	44 800.9	194	869.2593	44 856.2	1325	865.5735^{w}	44 905.2	403
873.3209	44 802.7	580	869.2340	44 856.5	803	865.4210	44 907.2	260
873.2176	44 804.1	209	869.1874	44 857.2	1663	865.0560^{w}	44 912.1	967
873.1679	44 804.7	471	869.0738	44 858.7	3445	864.9523	44 913.5	5188
872.9857	44 807.1	120	869.0422	44 859.1	495	864.8595	44 914.7	1633
872.8202	44 809.3	249	868.9788	44 859.9	1138	864.7354	44 916.4	1674
872.7286	44 810.5	414	868.7460	44 863.0	572	864.7220	44 916.6	2214
872.5254	44 813.1	175	868.6018	44 864.9	1943	864.6936	44 916.9	4467
872.3705	44 815.2	45	868.5551	44 865.5	3189	864.6634	44 917.3	267
872.3219	44 815.8	552	868.5185	44 866.0	158	864.6108	44 918.1	1110
872.3029	44 816.1	569	868.3592	44 868.1	132	864.5976	44 918.2	1697
872.2243	44 817.1	104	868.3198^{w}	44 868.6	70	864.5630	44 918.7	430
872.1655	44 817.9	150	868.1776	44 870.5	124	864.5327	44 919.1	767
872.0049	44 820.0	1306	868.1553	44 870.8	1468	864.4839	44 919.8	81
871.8537	44 822.0	293	868.0735	44 871.9	422	864.4199^{w}	44 920.6	1166
871.7352	44 823.5	285	868.0550	44 872.2	495	864.3675	44 921.3	1018
871.7042	44 823.9	1006	867.8507	44 874.9	424	864.2378	44 923.0	5697
871.6081	44 825.2	378	867.7536	44 876.2	2178	864.2009	44 923.5	3782
871.5590	44 825.8	176	867.5357	44 879.1	330	864.1723	44 923.9	660
871.4681	44 827.0	435	867.3899	44 881.0	68	864.1253	44 924.6	3043
871.4201	44 827.7	43	867.3165	44 882.0	33	864.0707	44 925.3	1197

(Continued on next page.)

TABLE VII: *(Continued.)*

λ (nm)	E_u(cm^{-1})	$I_{\rm rel}$	λ (nm)	E_u(cm^{-1})	$I_{\rm rel}$	λ (nm)	E_u(cm^{-1})	$I_{\rm rel}$
864.0401	44 925.7	1729	860.4861	44 973.5	195	854.6439^{w}	45 052.9	4609
864.0149	44 926.0	4159	860.2910	44 976.1	864	854.5395	45 054.4	595
863.9874	44 926.4	1055	860.1686	44 977.8	347	854.3786^{w}	45 056.6	2839
863.9410	44 927.0	2905	860.0060	44 980.0	4640	853.9320	45 062.7	499
863.7354	44 929.8	341	859.7277	44 983.7	162	853.0394^{w}	45 074.9	174
863.6477^{w}	44 930.9	385	859.6515	44 984.8	283	852.9241	45 076.5	2842
863.5913	44 931.7	292	859.4535	44 987.5	1378	852.5821	45 081.2	1104
863.4364	44 933.8	8744	859.3781	44 988.5	1631	852.5519	45 081.6	1333
863.3654^{w}	44 934.7	4743	859.3097	44 989.4	2251	852.5213	45 082.1	2281
863.3196	44 935.4	994	859.2219^{w}	44 990.6	416	852.4745	45 082.7	747
863.2604^{w}	44 936.1	903	858.8613^{w}	44 995.5	267	851.9071^{w}	45 090.5	3618
863.0481	44 939.0	955	858.7671^{w}	44 996.8	128	851.6947^{w}	45 093.5	2713
862.7394	44 943.1	506	858.5465	44 999.7	2128	851.6200	45 094.5	524
862.4749	44 946.7	836	858.1964	45 004.5	5737	851.5465^{w}	45 095.5	3603
862.2731	44 949.4	3560	857.8533	45 009.2	381	850.9228^{w}	45 104.1	1522
862.2503	44 949.7	1117	857.2765	45 017.0	6712	850.6113	45 108.4	1138
862.1641	44 950.9	157	857.1811^{w}	45 018.3	7584	850.4314^{w}	45 110.9	2047
862.0918	44 951.8	4365	856.5425^{w}	45 027.0	606	850.2721	45 113.1	3358
862.0373	44 952.6	1378	856.3281	45 029.9	2993	850.2017^{w}	45 114.1	2840
861.8853^{w}	44 954.6	121	856.1590	45 032.2	1169	850.1147^{w}	45 115.3	2203
861.4825	44 960.1	1809	856.0752^{w}	45 033.4	2323	849.7752^{w}	45 120.0	7561
861.4608^{w}	44 960.3	2500	855.7362^{w}	45 038.0	1058	849.3482^{w}	45 125.9	6235
861.3194	44 962.2	2903	855.6347^{w}	45 039.4	2016	848.8412	45 132.9	1767
861.2873^{w}	44 962.7	809	855.3382	45 043.4	547	848.7998	45 133.5	2887
860.9722	44 966.9	144	855.1990^{w}	45 045.3	603	848.6396	45 135.7	11882
860.6996	44 970.6	2564	855.1470^{w}	45 046.1	1823	848.6010	45 136.3	1114
860.6044	44 971.9	183	854.9058^{w}	45 049.4	1772	844.4525	45 194.1	1031
860.5446	44 972.7	140	854.7518^{w}	45 051.5	1818	833.3896	45 351.3	106

II. EXCITED LEVELS IN PM I BY ENERGY

TABLE VIII. Odd parity energy levels in neutral Pm, derived from lines in the excitation schemes SES_A, SES_B and SES_C (see TABLE II - III). According to the selection rules for dipole transitions $\Delta J = 0, \pm 1$, possible values for the total angular momentum J are given. Values of $^3/_2$ and $^9/_2$, which are marked with an asterisk are deemed more likely, as a transition could not be observed starting from a state at $^7/_2$ and $^5/_2$, respectively. The value of $J = ^7/_2$ for the state at 33352.3 cm^{-1} was verified by a measurement of the hyperfine structure of the 22020.08 $cm^{-1} \rightarrow$ 33352.3 cm^{-1} transition.

E (cm^{-1})	J	E (cm^{-1})	J	E (cm^{-1})	J	E (cm^{-1})	J
32 363.2	$\frac{5}{2}, \frac{7}{2}, \frac{9}{2}$	33 137.0	$\frac{5}{2}, \frac{7}{2}, \frac{9}{2}^*$	33 685.8	$\frac{3}{2}^*, \frac{5}{2}, \frac{7}{2}$	44 567.0	$\frac{5}{2}, \frac{7}{2}, \frac{9}{2}$
32 366.0	$\frac{5}{2}, \frac{7}{2}, \frac{9}{2}$	33 137.7	$\frac{7}{2}, \frac{9}{2}$	33 691.6	$\frac{5}{2}, \frac{7}{2}, \frac{9}{2}^*$	44 579.6	$\frac{5}{2}, \frac{7}{2}, \frac{9}{2}$
32 390.1	$\frac{5}{2}, \frac{7}{2}, \frac{9}{2}$	33 142.3	$\frac{7}{2}, \frac{9}{2}$	33 703.0	$\frac{3}{2}*, \frac{5}{2}, \frac{7}{2}$	44 587.3	$\frac{5}{2}, \frac{7}{2}, \frac{9}{2}$
32 449.0	$\frac{5}{2}, \frac{7}{2}, \frac{9}{2}$	33 168.2	$\frac{3}{2}^*, \frac{5}{2}, \frac{7}{2}$	33 710.7	$\frac{3}{2}^*, \frac{5}{2}, \frac{7}{2}$	44 600.5	$\frac{5}{2}, \frac{7}{2}, \frac{9}{2}$
32 474.9	$\frac{5}{2}, \frac{7}{2}, \frac{9}{2}$	33 190.8	$\frac{3}{2}^*, \frac{5}{2}, \frac{7}{2}$	33 711.7	$\frac{7}{2}, \frac{9}{2}$	44 602.0	$\frac{5}{2}, \frac{7}{2}, \frac{9}{2}$
32 489.5	$\frac{5}{2}, \frac{7}{2}, \frac{9}{2}$	33 209.9	$\frac{3}{2}^*, \frac{5}{2}, \frac{7}{2}$	33 720.9	$\frac{5}{2}, \frac{7}{2}, \frac{9}{2}^*$	44 604.4	$\frac{5}{2}, \frac{7}{2}, \frac{9}{2}$
32 493.9	$\frac{5}{2}, \frac{7}{2}, \frac{9}{2}$	33 226.1	$\frac{3}{2}^*, \frac{5}{2}, \frac{7}{2}$	33 728.1	$\frac{7}{2}, \frac{9}{2}$	44 606.6	$\frac{5}{2}, \frac{7}{2}, \frac{9}{2}$
32 510.6	$\frac{5}{2}, \frac{7}{2}, \frac{9}{2}$	33 227.8	$\frac{3}{2}^*, \frac{5}{2}, \frac{7}{2}$	33 736.3	$\frac{3}{2}^*, \frac{5}{2}, \frac{7}{2}$	44 608.9	$\frac{5}{2}, \frac{7}{2}, \frac{9}{2}$
32 520.0	$\frac{5}{2}, \frac{7}{2}, \frac{9}{2}$	33 267.4	$\frac{5}{2}, \frac{7}{2}, \frac{9}{2}^*$	33 757.8	$\frac{7}{2}, \frac{9}{2}$	44 611.4	$\frac{5}{2}, \frac{7}{2}, \frac{9}{2}$
32 546.7	$\frac{5}{2}, \frac{7}{2}, \frac{9}{2}$	33 304.0	$\frac{7}{2}, \frac{9}{2}$	33 760.3	$\frac{3}{2}^*, \frac{5}{2}, \frac{7}{2}$	44 612.1	$\frac{5}{2}, \frac{7}{2}, \frac{9}{2}$
32 559.7	$\frac{5}{2}, \frac{7}{2}, \frac{9}{2}$	33 319.1	$\frac{7}{2}, \frac{9}{2}$	33 773.7	$\frac{7}{2}, \frac{9}{2}$	44 615.3	$\frac{5}{2}, \frac{7}{2}, \frac{9}{2}$
32 578.4	$\frac{5}{2}, \frac{7}{2}, \frac{9}{2}$	33 338.1	$\frac{7}{2}, \frac{9}{2}$	33 782.3	$\frac{7}{2}, \frac{9}{2}$	44 618.0	$\frac{5}{2}, \frac{7}{2}, \frac{9}{2}$
32 587.5	$\frac{5}{2}, \frac{7}{2}, \frac{9}{2}$	33 352.3	$\frac{7}{2}$	33 793.2	$\frac{5}{2}, \frac{7}{2}, \frac{9}{2}^*$	44 629.1	$\frac{5}{2}, \frac{7}{2}, \frac{9}{2}$
32 604.7	$\frac{5}{2}, \frac{7}{2}, \frac{9}{2}$	33 359.7	$\frac{5}{2}, \frac{7}{2}, \frac{9}{2}^*$	33 831.6	$\frac{7}{2}, \frac{9}{2}$	44 630.2	$\frac{5}{2}, \frac{7}{2}, \frac{9}{2}$
32 616.6	$\frac{5}{2}, \frac{7}{2}, \frac{9}{2}$	33 361.9	$\frac{7}{2}, \frac{9}{2}$	33 832.8	$\frac{5}{2}, \frac{7}{2}, \frac{9}{2}^*$	44 635.5	$\frac{5}{2}, \frac{7}{2}, \frac{9}{2}$
32 624.5	$\frac{5}{2}, \frac{7}{2}, \frac{9}{2}$	33 374.7	$\frac{7}{2}, \frac{9}{2}$	33 841.2	$\frac{5}{2}, \frac{7}{2}, \frac{9}{2}^*$	44 654.5	$\frac{5}{2}, \frac{7}{2}, \frac{9}{2}$
32 653.7	$\frac{5}{2}, \frac{7}{2}, \frac{9}{2}$	33 386.9	$\frac{5}{2}, \frac{7}{2}, \frac{9}{2}^*$	33 860.9	$\frac{7}{2}, \frac{9}{2}$	44 658.8	$\frac{5}{2}, \frac{7}{2}, \frac{9}{2}$
32 668.1	$\frac{5}{2}, \frac{7}{2}, \frac{9}{2}$	33 409.1	$\frac{7}{2}, \frac{9}{2}$	33 862.2	$\frac{3}{2}, \frac{5}{2}, \frac{7}{2}$	44 672.8	$\frac{5}{2}, \frac{7}{2}, \frac{9}{2}$
32 683.7	$\frac{5}{2}, \frac{7}{2}, \frac{9}{2}$	33 438.4	$\frac{5}{2}, \frac{7}{2}, \frac{9}{2}^*$	33 899.2	$\frac{3}{2}, \frac{5}{2}, \frac{7}{2}$	44 680.8	$\frac{5}{2}, \frac{7}{2}, \frac{9}{2}$
32 686.1	$\frac{5}{2}, \frac{7}{2}, \frac{9}{2}$	33 452.8	$\frac{7}{2}, \frac{9}{2}$	33 920.5	$\frac{3}{2}, \frac{5}{2}, \frac{7}{2}$	44 682.2	$\frac{5}{2}, \frac{7}{2}, \frac{9}{2}$
32 724.7	$\frac{5}{2}, \frac{7}{2}, \frac{9}{2}$	33 461.9	$\frac{3}{2}^*, \frac{5}{2}, \frac{7}{2}$	33 922.1	$\frac{3}{2}, \frac{5}{2}, \frac{7}{2}$	44 685.6	$\frac{5}{2}, \frac{7}{2}, \frac{9}{2}$
32 730.9	$\frac{5}{2}, \frac{7}{2}, \frac{9}{2}$	33 463.1	$\frac{5}{2}, \frac{7}{2}, \frac{9}{2}^*$	33 929.2	$\frac{3}{2}, \frac{5}{2}, \frac{7}{2}$	44 699.8	$\frac{5}{2}, \frac{7}{2}, \frac{9}{2}$
32 740.4	$\frac{5}{2}, \frac{7}{2}, \frac{9}{2}$	33 479.4	$\frac{3}{2}^*, \frac{5}{2}, \frac{7}{2}$	33 943.6	$\frac{3}{2}, \frac{5}{2}, \frac{7}{2}$	44 703.6	$\frac{5}{2}, \frac{7}{2}, \frac{9}{2}$
32 742.1	$\frac{5}{2}, \frac{7}{2}, \frac{9}{2}$	33 482.1	$\frac{7}{2}, \frac{9}{2}$	33 960.7	$\frac{3}{2}, \frac{5}{2}, \frac{7}{2}$	44 705.7	$\frac{5}{2}, \frac{7}{2}, \frac{9}{2}$
32 763.1	$\frac{5}{2}, \frac{7}{2}, \frac{9}{2}$	33 497.3	$\frac{3}{2}^*, \frac{5}{2}, \frac{7}{2}$	33 977.8	$\frac{3}{2}, \frac{5}{2}, \frac{7}{2}$	44 708.6	$\frac{5}{2}, \frac{7}{2}, \frac{9}{2}$
32 767.1	$\frac{5}{2}, \frac{7}{2}, \frac{9}{2}$	33 510.6	$\frac{7}{2}, \frac{9}{2}$	33 991.0	$\frac{3}{2}, \frac{5}{2}, \frac{7}{2}$	44 720.9	$\frac{5}{2}, \frac{7}{2}, \frac{9}{2}$
32 817.9	$\frac{5}{2}, \frac{7}{2}, \frac{9}{2}$	33 520.3	$\frac{7}{2}, \frac{9}{2}$	34 001.3	$\frac{3}{2}, \frac{5}{2}, \frac{7}{2}$	44 739.4	$\frac{5}{2}, \frac{7}{2}, \frac{9}{2}$
32 860.4	$\frac{5}{2}, \frac{7}{2}, \frac{9}{2}$	33 531.4	$\frac{7}{2}, \frac{9}{2}$	34 014.1	$\frac{3}{2}, \frac{5}{2}, \frac{7}{2}$	44 743.7	$\frac{5}{2}, \frac{7}{2}, \frac{9}{2}$
32 866.8	$\frac{5}{2}, \frac{7}{2}, \frac{9}{2}$	33 534.5	$\frac{5}{2}, \frac{7}{2}, \frac{9}{2}^*$	34 021.6	$\frac{3}{2}, \frac{5}{2}, \frac{7}{2}$	44 748.6	$\frac{5}{2}, \frac{7}{2}, \frac{9}{2}$
32 882.7	$\frac{5}{2}, \frac{7}{2}, \frac{9}{2}$	33 562.2	$\frac{7}{2}, \frac{9}{2}$	34 051.1	$\frac{3}{2}, \frac{5}{2}, \frac{7}{2}$	44 752.8	$\frac{5}{2}, \frac{7}{2}, \frac{9}{2}$
32 905.4	$\frac{5}{2}, \frac{7}{2}, \frac{9}{2}$	33 566.7	$\frac{7}{2}, \frac{9}{2}$	34 057.2	$\frac{3}{2}, \frac{5}{2}, \frac{7}{2}$	44 758.0	$\frac{5}{2}, \frac{7}{2}, \frac{9}{2}$
32 943.4	$\frac{5}{2}, \frac{7}{2}, \frac{9}{2}$	33 610.9	$\frac{3}{2}^*, \frac{5}{2}, \frac{7}{2}$	44 472.0	$\frac{5}{2}, \frac{7}{2}, \frac{9}{2}$	44 762.1	$\frac{5}{2}, \frac{7}{2}, \frac{9}{2}$
32 952.1	$\frac{5}{2}, \frac{7}{2}, \frac{9}{2}$	33 632.2	$\frac{7}{2}, \frac{9}{2}$	44 510.9	$\frac{5}{2}, \frac{7}{2}, \frac{9}{2}$	44 762.6	$\frac{5}{2}, \frac{7}{2}, \frac{9}{2}$
32 973.1	$\frac{5}{2}, \frac{7}{2}, \frac{9}{2}$	33 642.6	$\frac{3}{2}^*, \frac{5}{2}, \frac{7}{2}$	44 526.3	$\frac{5}{2}, \frac{7}{2}, \frac{9}{2}$	44 763.6	$\frac{5}{2}, \frac{7}{2}, \frac{9}{2}$
32 980.8	$\frac{5}{2}, \frac{7}{2}, \frac{9}{2}$	33 647.7	$\frac{7}{2}, \frac{9}{2}$	44 527.0	$\frac{5}{2}, \frac{7}{2}, \frac{9}{2}$	44 780.9	$\frac{5}{2}, \frac{7}{2}, \frac{9}{2}$
33 022.3	$\frac{5}{2}, \frac{7}{2}, \frac{9}{2}$	33 653.2	$\frac{7}{2}, \frac{9}{2}$	44 536.6	$\frac{5}{2}, \frac{7}{2}, \frac{9}{2}$	44 783.9	$\frac{5}{2}, \frac{7}{2}, \frac{9}{2}$
33 079.8	$\frac{3}{2}^*, \frac{5}{2}, \frac{7}{2}$	33 670.8	$\frac{5}{2}, \frac{7}{2}, \frac{9}{2}^*$	44 555.5	$\frac{5}{2}, \frac{7}{2}, \frac{9}{2}$	44 787.0	$\frac{5}{2}, \frac{7}{2}, \frac{9}{2}$
33 102.9	$\frac{7}{2}, \frac{9}{2}$	33 685.3	$\frac{7}{2}, \frac{9}{2}$	44 565.6	$\frac{5}{2}, \frac{7}{2}, \frac{9}{2}$	44 787.6	$\frac{5}{2}, \frac{7}{2}, \frac{9}{2}$

(Continued on next page.)

TABLE VIII: *(Continued.)*

E (cm^{-1})	J	E (cm^{-1})	J	E (cm^{-1})	J	E (cm^{-1})	J
44 788.9	$\frac{5}{2}, \frac{7}{2}, \frac{9}{2}$	44 889.7	$\frac{5}{2}, \frac{7}{2}, \frac{9}{2}$	44 952.1	$\frac{5}{2}, \frac{7}{2}, \frac{9}{2}$	44 993.5	$\frac{5}{2}, \frac{7}{2}, \frac{9}{2}$
44 791.9	$\frac{5}{2}, \frac{7}{2}, \frac{9}{2}$	44 892.9	$\frac{5}{2}, \frac{7}{2}, \frac{9}{2}$	44 953.8	$\frac{5}{2}, \frac{7}{2}, \frac{9}{2}$	44 997.8	$\frac{5}{2}, \frac{7}{2}, \frac{9}{2}$
44 793.1	$\frac{5}{2}, \frac{7}{2}, \frac{9}{2}$	44 893.6	$\frac{5}{2}, \frac{7}{2}, \frac{9}{2}$	44 954.6	$\frac{5}{2}, \frac{7}{2}, \frac{9}{2}$	45 002.0	$\frac{5}{2}, \frac{7}{2}, \frac{9}{2}$
44 808.3	$\frac{5}{2}, \frac{7}{2}, \frac{9}{2}$	44 897.3	$\frac{5}{2}, \frac{7}{2}, \frac{9}{2}$	44 956.5	$\frac{5}{2}, \frac{7}{2}, \frac{9}{2}$	45 003.4	$\frac{5}{2}, \frac{7}{2}, \frac{9}{2}$
44 810.9	$\frac{5}{2}, \frac{7}{2}, \frac{9}{2}$	44 901.7	$\frac{5}{2}, \frac{7}{2}, \frac{9}{2}$	44 957.3	$\frac{5}{2}, \frac{7}{2}, \frac{9}{2}$	45 005.2	$\frac{5}{2}, \frac{7}{2}, \frac{9}{2}$
44 814.7	$\frac{5}{2}, \frac{7}{2}, \frac{9}{2}$	44 908.2	$\frac{5}{2}, \frac{7}{2}, \frac{9}{2}$	44 958.2	$\frac{5}{2}, \frac{7}{2}, \frac{9}{2}$	45 006.0	$\frac{5}{2}, \frac{7}{2}, \frac{9}{2}$
44 821.4	$\frac{5}{2}, \frac{7}{2}, \frac{9}{2}$	44 916.1	$\frac{5}{2}, \frac{7}{2}, \frac{9}{2}$	44 960.1	$\frac{5}{2}, \frac{7}{2}, \frac{9}{2}$	45 009.0	$\frac{5}{2}, \frac{7}{2}, \frac{9}{2}$
44 823.4	$\frac{5}{2}, \frac{7}{2}, \frac{9}{2}$	44 920.5	$\frac{5}{2}, \frac{7}{2}, \frac{9}{2}$	44 962.7	$\frac{5}{2}, \frac{7}{2}, \frac{9}{2}$	45 011.3	$\frac{5}{2}, \frac{7}{2}, \frac{9}{2}$
44 831.4	$\frac{5}{2}, \frac{7}{2}, \frac{9}{2}$	44 921.5	$\frac{5}{2}, \frac{7}{2}, \frac{9}{2}$	44 963.3	$\frac{5}{2}, \frac{7}{2}, \frac{9}{2}$	45 014.4	$\frac{5}{2}, \frac{7}{2}, \frac{9}{2}$
44 835.5	$\frac{5}{2}, \frac{7}{2}, \frac{9}{2}$	44 923.4	$\frac{5}{2}, \frac{7}{2}, \frac{9}{2}$	44 963.9	$\frac{5}{2}, \frac{7}{2}, \frac{9}{2}$	45 015.5	$\frac{5}{2}, \frac{7}{2}, \frac{9}{2}$
44 838.6	$\frac{5}{2}, \frac{7}{2}, \frac{9}{2}$	44 923.8	$\frac{5}{2}, \frac{7}{2}, \frac{9}{2}$	44 966.2	$\frac{5}{2}, \frac{7}{2}, \frac{9}{2}$	45 016.1	$\frac{5}{2}, \frac{7}{2}, \frac{9}{2}$
44 841.1	$\frac{5}{2}, \frac{7}{2}, \frac{9}{2}$	44 924.4	$\frac{5}{2}, \frac{7}{2}, \frac{9}{2}$	44 967.8	$\frac{5}{2}, \frac{7}{2}, \frac{9}{2}$	45 019.9	$\frac{5}{2}, \frac{7}{2}, \frac{9}{2}$
44 842.7	$\frac{5}{2}, \frac{7}{2}, \frac{9}{2}$	44 926.4	$\frac{5}{2}, \frac{7}{2}, \frac{9}{2}$	44 969.1	$\frac{5}{2}, \frac{7}{2}, \frac{9}{2}$	45 024.2	$\frac{5}{2}, \frac{7}{2}, \frac{9}{2}$
44 846.8	$\frac{5}{2}, \frac{7}{2}, \frac{9}{2}$	44 927.9	$\frac{5}{2}, \frac{7}{2}, \frac{9}{2}$	44 971.1	$\frac{5}{2}, \frac{7}{2}, \frac{9}{2}$	45 030.4	$\frac{5}{2}, \frac{7}{2}, \frac{9}{2}$
44 847.7	$\frac{5}{2}, \frac{7}{2}, \frac{9}{2}$	44 928.5	$\frac{5}{2}, \frac{7}{2}, \frac{9}{2}$	44 976.6	$\frac{5}{2}, \frac{7}{2}, \frac{9}{2}$	45 036.1	$\frac{5}{2}, \frac{7}{2}, \frac{9}{2}$
44 849.7	$\frac{5}{2}, \frac{7}{2}, \frac{9}{2}$	44 929.1	$\frac{5}{2}, \frac{7}{2}, \frac{9}{2}$	44 978.3	$\frac{5}{2}, \frac{7}{2}, \frac{9}{2}$	45 040.3	$\frac{5}{2}, \frac{7}{2}, \frac{9}{2}$
44 850.7	$\frac{5}{2}, \frac{7}{2}, \frac{9}{2}$	44 930.8	$\frac{5}{2}, \frac{7}{2}, \frac{9}{2}$	44 979.7	$\frac{5}{2}, \frac{7}{2}, \frac{9}{2}$	45 041.9	$\frac{5}{2}, \frac{7}{2}, \frac{9}{2}$
44 857.5	$\frac{5}{2}, \frac{7}{2}, \frac{9}{2}$	44 931.9	$\frac{5}{2}, \frac{7}{2}, \frac{9}{2}$	44 980.4	$\frac{5}{2}, \frac{7}{2}, \frac{9}{2}$	45 046.4	$\frac{5}{2}, \frac{7}{2}, \frac{9}{2}$
44 858.5	$\frac{5}{2}, \frac{7}{2}, \frac{9}{2}$	44 932.4	$\frac{5}{2}, \frac{7}{2}, \frac{9}{2}$	44 981.6	$\frac{5}{2}, \frac{7}{2}, \frac{9}{2}$	45 047.8	$\frac{5}{2}, \frac{7}{2}, \frac{9}{2}$
44 860.7	$\frac{5}{2}, \frac{7}{2}, \frac{9}{2}$	44 934.0	$\frac{5}{2}, \frac{7}{2}, \frac{9}{2}$	44 982.9	$\frac{5}{2}, \frac{7}{2}, \frac{9}{2}$	45 049.4	$\frac{5}{2}, \frac{7}{2}, \frac{9}{2}$
44 867.9	$\frac{5}{2}, \frac{7}{2}, \frac{9}{2}$	44 935.7	$\frac{5}{2}, \frac{7}{2}, \frac{9}{2}$	44 983.5	$\frac{5}{2}, \frac{7}{2}, \frac{9}{2}$	45 050.3	$\frac{5}{2}, \frac{7}{2}, \frac{9}{2}$
44 871.1	$\frac{5}{2}, \frac{7}{2}, \frac{9}{2}$	44 939.2	$\frac{5}{2}, \frac{7}{2}, \frac{9}{2}$	44 984.1	$\frac{5}{2}, \frac{7}{2}, \frac{9}{2}$	45 051.7	$\frac{5}{2}, \frac{7}{2}, \frac{9}{2}$
44 875.6	$\frac{5}{2}, \frac{7}{2}, \frac{9}{2}$	44 940.9	$\frac{5}{2}, \frac{7}{2}, \frac{9}{2}$	44 984.9	$\frac{5}{2}, \frac{7}{2}, \frac{9}{2}$	45 054.1	$\frac{5}{2}, \frac{7}{2}, \frac{9}{2}$
44 878.6	$\frac{5}{2}, \frac{7}{2}, \frac{9}{2}$	44 942.4	$\frac{5}{2}, \frac{7}{2}, \frac{9}{2}$	44 986.7	$\frac{5}{2}, \frac{7}{2}, \frac{9}{2}$	45 057.6	$\frac{5}{2}, \frac{7}{2}, \frac{9}{2}$
44 880.5	$\frac{5}{2}, \frac{7}{2}, \frac{9}{2}$	44 943.3	$\frac{5}{2}, \frac{7}{2}, \frac{9}{2}$	44 987.9	$\frac{5}{2}, \frac{7}{2}, \frac{9}{2}$	45 061.0	$\frac{5}{2}, \frac{7}{2}, \frac{9}{2}$
44 883.0	$\frac{5}{2}, \frac{7}{2}, \frac{9}{2}$	44 945.5	$\frac{5}{2}, \frac{7}{2}, \frac{9}{2}$	44 991.2	$\frac{5}{2}, \frac{7}{2}, \frac{9}{2}$		
44 887.4	$\frac{5}{2}, \frac{7}{2}, \frac{9}{2}$	44 948.9	$\frac{5}{2}, \frac{7}{2}, \frac{9}{2}$	44 992.6	$\frac{5}{2}, \frac{7}{2}, \frac{9}{2}$		

TABLE IX. Even parity energy levels in neutral Pm, derived from lines in the excitation schemes B1, B2, C1 and C2 (see TABLE IV - VII). According to the selection rules for dipole transitions $\Delta J = 0, \pm 1$, possible values for the total angular momentum J are given.

E (cm^{-1})	J	E (cm^{-1})	J	E (cm^{-1})	J	E (cm^{-1})	J
44 360.1	$\frac{5}{2}, \frac{7}{2}, \frac{9}{2}$	44 541.0	$\frac{5}{2}, \frac{7}{2}, \frac{9}{2}$	44 634.9	$\frac{5}{2}, ..., \frac{11}{2}$	44 713.7	$\frac{5}{2}, ..., \frac{11}{2}$
44 361.2	$\frac{5}{2}, \frac{7}{2}, \frac{9}{2}$	44 544.5	$\frac{5}{2}, \frac{7}{2}, \frac{9}{2}$	44 636.3	$\frac{5}{2}, ..., \frac{11}{2}$	44 717.8	$\frac{5}{2}, \frac{7}{2}, \frac{9}{2}$
44 364.1	$\frac{5}{2}, \frac{7}{2}, \frac{9}{2}$	44 545.3	$\frac{5}{2}, \frac{7}{2}, \frac{9}{2}$	44 638.2	$\frac{5}{2}, \frac{7}{2}, \frac{9}{2}$	44 718.5	$\frac{5}{2}, \frac{7}{2}, \frac{9}{2}$
44 380.6	$\frac{5}{2}, \frac{7}{2}, \frac{9}{2}$	44 549.2	$\frac{5}{2}, \frac{7}{2}, \frac{9}{2}$	44 639.7	$\frac{5}{2}, ..., \frac{11}{2}$	44 719.6	$\frac{5}{2}, \frac{7}{2}, \frac{9}{2}$
44 386.7	$\frac{5}{2}, \frac{7}{2}, \frac{9}{2}$	44 551.8	$\frac{5}{2}, ..., \frac{11}{2}$	44 640.1	$\frac{5}{2}, \frac{7}{2}, \frac{9}{2}$	44 722.7	$\frac{5}{2}, \frac{7}{2}, \frac{9}{2}$
44 393.6	$\frac{5}{2}, \frac{7}{2}, \frac{9}{2}$	44 554.0	$\frac{5}{2}, \frac{7}{2}, \frac{9}{2}$	44 650.4	$\frac{5}{2}, \frac{7}{2}, \frac{9}{2}$	44 724.4	$\frac{5}{2}, \frac{7}{2}, \frac{9}{2}$
44 398.4	$\frac{5}{2}, \frac{7}{2}, \frac{9}{2}$	44 554.0	$\frac{5}{2}, ..., \frac{11}{2}$	44 651.4	$\frac{5}{2}, \frac{7}{2}, \frac{9}{2}$	44 726.5	$\frac{5}{2}, ..., \frac{11}{2}$
44 403.5	$\frac{5}{2}, \frac{7}{2}, \frac{9}{2}$	44 555.1	$\frac{5}{2}, ..., \frac{11}{2}$	44 652.0	$\frac{5}{2}, ..., \frac{11}{2}$	44 726.9	$\frac{5}{2}, \frac{7}{2}, \frac{9}{2}$
44 409.8	$\frac{5}{2}, \frac{7}{2}, \frac{9}{2}$	44 559.2	$\frac{5}{2}, \frac{7}{2}, \frac{9}{2}$	44 653.6	$\frac{5}{2}, ..., \frac{11}{2}$	44 727.2	$\frac{5}{2}, ..., \frac{11}{2}$
44 416.0	$\frac{5}{2}, \frac{7}{2}, \frac{9}{2}$	44 565.3	$\frac{5}{2}, \frac{7}{2}, \frac{9}{2}$	44 655.7	$\frac{5}{2}, \frac{7}{2}, \frac{9}{2}$	44 727.6	$\frac{5}{2}, \frac{7}{2}, \frac{9}{2}$
44 422.7	$\frac{5}{2}, \frac{7}{2}, \frac{9}{2}$	44 567.6	$\frac{5}{2}, \frac{7}{2}, \frac{9}{2}$	44 657.8	$\frac{5}{2}, \frac{7}{2}, \frac{9}{2}$	44 731.1	$\frac{5}{2}, \frac{7}{2}, \frac{9}{2}$
44 424.1	$\frac{5}{2}, \frac{7}{2}, \frac{9}{2}$	44 569.8	$\frac{5}{2}, ..., \frac{11}{2}$	44 660.9	$\frac{5}{2}, \frac{7}{2}, \frac{9}{2}$	44 732.9	$\frac{5}{2}, \frac{7}{2}, \frac{9}{2}$
44 426.8	$\frac{5}{2}, \frac{7}{2}, \frac{9}{2}$	44 571.0	$\frac{5}{2}, ..., \frac{11}{2}$	44 661.0	$\frac{5}{2}, ..., \frac{11}{2}$	44 740.1	$\frac{5}{2}, \frac{7}{2}, \frac{9}{2}$
44 434.2	$\frac{5}{2}, \frac{7}{2}, \frac{9}{2}$	44 572.0	$\frac{5}{2}, \frac{7}{2}, \frac{9}{2}$	44 667.2	$\frac{5}{2}, \frac{7}{2}, \frac{9}{2}$	44 742.0	$\frac{5}{2}, \frac{7}{2}, \frac{9}{2}$
44 435.5	$\frac{5}{2}, \frac{7}{2}, \frac{9}{2}$	44 575.6	$\frac{5}{2}, \frac{7}{2}, \frac{9}{2}$	44 668.1	$\frac{5}{2}, ..., \frac{11}{2}$	44 742.8	$\frac{5}{2}, \frac{7}{2}, \frac{9}{2}$
44 437.1	$\frac{5}{2}, \frac{7}{2}, \frac{9}{2}$	44 582.9	$\frac{5}{2}, \frac{7}{2}, \frac{9}{2}$	44 668.8	$\frac{5}{2}, \frac{7}{2}, \frac{9}{2}$	44 746.5	$\frac{5}{2}, \frac{7}{2}, \frac{9}{2}$
44 443.3	$\frac{5}{2}, \frac{7}{2}, \frac{9}{2}$	44 584.1	$\frac{5}{2}, \frac{7}{2}, \frac{9}{2}$	44 671.8	$\frac{5}{2}, \frac{7}{2}, \frac{9}{2}$	44 748.0	$\frac{5}{2}, \frac{7}{2}, \frac{9}{2}$
44 448.1	$\frac{5}{2}, \frac{7}{2}, \frac{9}{2}$	44 584.8	$\frac{5}{2}, \frac{7}{2}, \frac{9}{2}$	44 677.0	$\frac{5}{2}, \frac{7}{2}, \frac{9}{2}$	44 749.3	$\frac{5}{2}, \frac{7}{2}, \frac{9}{2}$
44 453.2	$\frac{5}{2}, \frac{7}{2}, \frac{9}{2}$	44 585.9	$\frac{5}{2}, \frac{7}{2}, \frac{9}{2}$	44 677.4	$\frac{5}{2}, \frac{7}{2}, \frac{9}{2}$	44 751.8	$\frac{5}{2}, \frac{7}{2}, \frac{9}{2}$
44 465.2	$\frac{5}{2}, \frac{7}{2}, \frac{9}{2}$	44 587.3	$\frac{5}{2}, ..., \frac{11}{2}$	44 678.0	$\frac{5}{2}, \frac{7}{2}, \frac{9}{2}$	44 752.1	$\frac{5}{2}, \frac{7}{2}, \frac{9}{2}$
44 472.4	$\frac{5}{2}, \frac{7}{2}, \frac{9}{2}$	44 588.6	$\frac{5}{2}, \frac{7}{2}, \frac{9}{2}$	44 683.9	$\frac{5}{2}, \frac{7}{2}, \frac{9}{2}$	44 753.2	$\frac{5}{2}, \frac{7}{2}, \frac{9}{2}$
44 476.0	$\frac{5}{2}, \frac{7}{2}, \frac{9}{2}$	44 589.6	$\frac{5}{2}, \frac{7}{2}, \frac{9}{2}$	44 686.3	$\frac{5}{2}, \frac{7}{2}, \frac{9}{2}$	44 757.4	$\frac{5}{2}, \frac{7}{2}, \frac{9}{2}$
44 478.6	$\frac{5}{2}, \frac{7}{2}, \frac{9}{2}$	44 590.6	$\frac{5}{2}, \frac{7}{2}, \frac{9}{2}$	44 687.6	$\frac{5}{2}, \frac{7}{2}, \frac{9}{2}$	44 760.1	$\frac{5}{2}, \frac{7}{2}, \frac{9}{2}$
44 481.9	$\frac{5}{2}, \frac{7}{2}, \frac{9}{2}$	44 591.3	$\frac{5}{2}, ..., \frac{11}{2}$	44 689.7	$\frac{5}{2}, \frac{7}{2}, \frac{9}{2}$	44 761.8	$\frac{5}{2}, \frac{7}{2}, \frac{9}{2}$
44 483.6	$\frac{5}{2}, \frac{7}{2}, \frac{9}{2}$	44 593.3	$\frac{5}{2}, \frac{7}{2}, \frac{9}{2}$	44 690.4	$\frac{5}{2}, \frac{7}{2}, \frac{9}{2}$	44 763.6	$\frac{5}{2}, \frac{7}{2}, \frac{9}{2}$
44 487.4	$\frac{5}{2}, \frac{7}{2}, \frac{9}{2}$	44 594.9	$\frac{5}{2}, \frac{7}{2}, \frac{9}{2}$	44 690.8	$\frac{5}{2}, \frac{7}{2}, \frac{9}{2}$	44 764.0	$\frac{5}{2}, \frac{7}{2}, \frac{9}{2}$
44 488.5	$\frac{5}{2}, \frac{7}{2}, \frac{9}{2}$	44 596.5	$\frac{5}{2}, ..., \frac{11}{2}$	44 691.5	$\frac{5}{2}, \frac{7}{2}, \frac{9}{2}$	44 767.0	$\frac{5}{2}, \frac{7}{2}, \frac{9}{2}$
44 490.8	$\frac{5}{2}, \frac{7}{2}, \frac{9}{2}$	44 598.2	$\frac{5}{2}, ..., \frac{11}{2}$	44 693.0	$\frac{5}{2}, \frac{7}{2}, \frac{9}{2}$	44 768.0	$\frac{5}{2}, \frac{7}{2}, \frac{9}{2}$
44 494.8	$\frac{5}{2}, \frac{7}{2}, \frac{9}{2}$	44 600.7	$\frac{5}{2}, ..., \frac{11}{2}$	44 693.3	$\frac{5}{2}, \frac{7}{2}, \frac{9}{2}$	44 768.3	$\frac{5}{2}, \frac{7}{2}, \frac{9}{2}$
44 501.2	$\frac{5}{2}, \frac{7}{2}, \frac{9}{2}$	44 601.9	$\frac{5}{2}, \frac{7}{2}, \frac{9}{2}$	44 693.6	$\frac{5}{2}, \frac{7}{2}, \frac{9}{2}$	44 768.4	$\frac{5}{2}, \frac{7}{2}, \frac{9}{2}$
44 507.8	$\frac{5}{2}, \frac{7}{2}, \frac{9}{2}$	44 608.2	$\frac{5}{2}, \frac{7}{2}, \frac{9}{2}$	44 693.9	$\frac{5}{2}, \frac{7}{2}, \frac{9}{2}$	44 770.0	$\frac{5}{2}, ..., \frac{11}{2}$
44 510.0	$\frac{5}{2}, \frac{7}{2}, \frac{9}{2}$	44 609.7	$\frac{5}{2}, \frac{7}{2}, \frac{9}{2}$	44 697.2	$\frac{5}{2}, \frac{7}{2}, \frac{9}{2}$	44 772.1	$\frac{5}{2}, \frac{7}{2}, \frac{9}{2}$
44 514.6	$\frac{5}{2}, \frac{7}{2}, \frac{9}{2}$	44 611.1	$\frac{5}{2}, \frac{7}{2}, \frac{9}{2}$	44 697.7	$\frac{5}{2}, \frac{7}{2}, \frac{9}{2}$	44 773.1	$\frac{5}{2}, \frac{7}{2}, \frac{9}{2}$
44 515.4	$\frac{5}{2}, \frac{7}{2}, \frac{9}{2}$	44 613.6	$\frac{5}{2}, \frac{7}{2}, \frac{9}{2}$	44 699.5	$\frac{5}{2}, \frac{7}{2}, \frac{9}{2}$	44 777.1	$\frac{5}{2}, \frac{7}{2}, \frac{9}{2}$
44 519.0	$\frac{5}{2}, \frac{7}{2}, \frac{9}{2}$	44 617.2	$\frac{5}{2}, \frac{7}{2}, \frac{9}{2}$	44 704.6	$\frac{5}{2}, ..., \frac{11}{2}$	44 778.6	$\frac{5}{2}, \frac{7}{2}, \frac{9}{2}$
44 520.9	$\frac{5}{2}, \frac{7}{2}, \frac{9}{2}$	44 619.2	$\frac{5}{2}, ..., \frac{11}{2}$	44 705.5	$\frac{5}{2}, \frac{7}{2}, \frac{9}{2}$	44 780.1	$\frac{5}{2}, \frac{7}{2}, \frac{9}{2}$
44 523.8	$\frac{5}{2}, \frac{7}{2}, \frac{9}{2}$	44 626.2	$\frac{5}{2}, \frac{7}{2}, \frac{9}{2}$	44 706.8	$\frac{5}{2}, \frac{7}{2}, \frac{9}{2}$	44 780.8	$\frac{5}{2}, \frac{7}{2}, \frac{9}{2}$
44 525.3	$\frac{5}{2}, \frac{7}{2}, \frac{9}{2}$	44 626.8	$\frac{5}{2}, ..., \frac{11}{2}$	44 707.3	$\frac{5}{2}, \frac{7}{2}, \frac{9}{2}$	44 785.1	$\frac{5}{2}, \frac{7}{2}, \frac{9}{2}$
44 528.7	$\frac{5}{2}, \frac{7}{2}, \frac{9}{2}$	44 628.4	$\frac{5}{2}, \frac{7}{2}, \frac{9}{2}$	44 710.3	$\frac{5}{2}, \frac{7}{2}, \frac{9}{2}$	44 787.7	$\frac{5}{2}, ..., \frac{11}{2}$
44 532.2	$\frac{5}{2}, \frac{7}{2}, \frac{9}{2}$	44 629.3	$\frac{5}{2}, ..., \frac{11}{2}$	44 710.6	$\frac{5}{2}, \frac{7}{2}, \frac{9}{2}$	44 789.7	$\frac{5}{2}, \frac{7}{2}, \frac{9}{2}$
44 538.7	$\frac{5}{2}, \frac{7}{2}, \frac{9}{2}$	44 633.7	$\frac{5}{2}, \frac{7}{2}, \frac{9}{2}$	44 712.7	$\frac{5}{2}, \frac{7}{2}, \frac{9}{2}$	44 790.6	$\frac{5}{2}, \frac{7}{2}, \frac{9}{2}$
44 540.7	$\frac{5}{2}, \frac{7}{2}, \frac{9}{2}$	44 634.3	$\frac{5}{2}, \frac{7}{2}, \frac{9}{2}$	44 713.3	$\frac{5}{2}, \frac{7}{2}, \frac{9}{2}$	44 791.1	$\frac{5}{2}, \frac{7}{2}, \frac{9}{2}$

(Continued on next page.)

TABLE IX: *(Continued.)*

E (cm^{-1})	J	E (cm^{-1})	J	E (cm^{-1})	J	E (cm^{-1})	J
44 791.7	$\frac{5}{2}, \frac{7}{2}, \frac{9}{2}$	44 842.8	$\frac{5}{2}, \frac{7}{2}, \frac{9}{2}$	44 888.5	$\frac{5}{2}, \frac{7}{2}, \frac{9}{2}$	44 921.3	$\frac{5}{2}, \frac{7}{2}, \frac{9}{2}$
44 792.1	$\frac{5}{2}, \frac{7}{2}, \frac{9}{2}$	44 844.1	$\frac{5}{2}, \frac{7}{2}, \frac{9}{2}$	44 889.1	$\frac{5}{2}, \frac{7}{2}, \frac{9}{2}$	44 921.5	$\frac{3}{2}, ..., \frac{11}{2}$
44 794.1	$\frac{5}{2}, \frac{7}{2}, \frac{9}{2}$	44 844.6	$\frac{5}{2}, \frac{7}{2}, \frac{9}{2}$	44 890.5	$\frac{5}{2}, \frac{7}{2}, \frac{9}{2}$	44 923.1	$\frac{5}{2}, \frac{7}{2}, \frac{9}{2}$
44 795.5	$\frac{5}{2}, \frac{7}{2}, \frac{9}{2}$	44 844.9	$\frac{5}{2}, \frac{7}{2}, \frac{9}{2}$	44 891.4	$\frac{5}{2}, \frac{7}{2}, \frac{9}{2}$	44 923.2	$\frac{3}{2}, ..., \frac{11}{2}$
44 796.7	$\frac{5}{2}, \frac{7}{2}, \frac{9}{2}$	44 845.2	$\frac{5}{2}, ..., \frac{11}{2}$	44 892.0	$\frac{5}{2}, \frac{7}{2}, \frac{9}{2}$	44 923.5	$\frac{5}{2}, \frac{7}{2}, \frac{9}{2}$
44 798.1	$\frac{5}{2}, \frac{7}{2}, \frac{9}{2}$	44 845.8	$\frac{5}{2}, \frac{7}{2}, \frac{9}{2}$	44 893.2	$\frac{5}{2}, \frac{7}{2}, \frac{9}{2}$	44 923.9	$\frac{5}{2}, \frac{7}{2}, \frac{9}{2}$
44 800.3	$\frac{5}{2}, \frac{7}{2}, \frac{9}{2}$	44 846.3	$\frac{5}{2}, \frac{7}{2}, \frac{9}{2}$	44 894.1	$\frac{3}{2}, ..., \frac{11}{2}$	44 924.2	$\frac{3}{2}, ..., \frac{11}{2}$
44 800.9	$\frac{5}{2}, \frac{7}{2}, \frac{9}{2}$	44 846.7	$\frac{5}{2}, \frac{7}{2}, \frac{9}{2}$	44 896.4	$\frac{5}{2}, \frac{7}{2}, \frac{9}{2}$	44 924.6	$\frac{5}{2}, \frac{7}{2}, \frac{9}{2}$
44 802.7	$\frac{5}{2}, \frac{7}{2}, \frac{9}{2}$	44 847.8	$\frac{5}{2}, \frac{7}{2}, \frac{9}{2}$	44 896.9	$\frac{5}{2}, \frac{7}{2}, \frac{9}{2}$	44 925.2	$\frac{5}{2}, \frac{7}{2}, \frac{9}{2}$
44 804.1	$\frac{5}{2}, \frac{7}{2}, \frac{9}{2}$	44 848.5	$\frac{5}{2}, ..., \frac{11}{2}$	44 897.5	$\frac{5}{2}, \frac{7}{2}, \frac{9}{2}$	44 925.7	$\frac{5}{2}, \frac{7}{2}, \frac{9}{2}$
44 804.7	$\frac{5}{2}, \frac{7}{2}, \frac{9}{2}$	44 850.0	$\frac{5}{2}, \frac{7}{2}, \frac{9}{2}$	44 897.7	$\frac{5}{2}, ..., \frac{11}{2}$	44 925.9	$\frac{3}{2}, ..., \frac{11}{2}$
44 806.2	$\frac{5}{2}, ..., \frac{11}{2}$	44 851.7	$\frac{5}{2}, \frac{7}{2}, \frac{9}{2}$	44 899.0	$\frac{5}{2}, \frac{7}{2}, \frac{9}{2}$	44 926.0	$\frac{5}{2}, \frac{7}{2}, \frac{9}{2}$
44 807.1	$\frac{5}{2}, \frac{7}{2}, \frac{9}{2}$	44 854.7	$\frac{5}{2}, \frac{7}{2}, \frac{9}{2}$	44 899.2	$\frac{3}{2}, ..., \frac{11}{2}$	44 926.4	$\frac{5}{2}, \frac{7}{2}, \frac{9}{2}$
44 809.3	$\frac{5}{2}, \frac{7}{2}, \frac{9}{2}$	44 855.5	$\frac{5}{2}, \frac{7}{2}, \frac{9}{2}$	44 899.3	$\frac{5}{2}, \frac{7}{2}, \frac{9}{2}$	44 927.0	$\frac{5}{2}, \frac{7}{2}, \frac{9}{2}$
44 810.5	$\frac{5}{2}, \frac{7}{2}, \frac{9}{2}$	44 855.9	$\frac{5}{2}, \frac{7}{2}, \frac{9}{2}$	44 899.6	$\frac{5}{2}, \frac{7}{2}, \frac{9}{2}$	44 927.2	$\frac{3}{2}, ..., \frac{11}{2}$
44 810.7	$\frac{5}{2}, ..., \frac{11}{2}$	44 856.2	$\frac{5}{2}, \frac{7}{2}, \frac{9}{2}$	44 900.8	$\frac{5}{2}, \frac{7}{2}, \frac{9}{2}$	44 929.2	$\frac{5}{2}, ..., \frac{11}{2}$
44 811.3	$\frac{5}{2}, ..., \frac{11}{2}$	44 856.6	$\frac{5}{2}, \frac{7}{2}, \frac{9}{2}$	44 901.6	$\frac{5}{2}, \frac{7}{2}, \frac{9}{2}$	44 929.8	$\frac{5}{2}, \frac{7}{2}, \frac{9}{2}$
44 813.2	$\frac{5}{2}, \frac{7}{2}, \frac{9}{2}$	44 857.2	$\frac{5}{2}, \frac{7}{2}, \frac{9}{2}$	44 901.8	$\frac{3}{2}, ..., \frac{11}{2}$	44 930.9	$\frac{5}{2}, \frac{7}{2}, \frac{9}{2}$
44 815.1	$\frac{5}{2}, \frac{7}{2}, \frac{9}{2}$	44 858.0	$\frac{5}{2}, ..., \frac{11}{2}$	44 902.2	$\frac{5}{2}, \frac{7}{2}, \frac{9}{2}$	44 931.7	$\frac{5}{2}, \frac{7}{2}, \frac{9}{2}$
44 815.8	$\frac{5}{2}, \frac{7}{2}, \frac{9}{2}$	44 858.7	$\frac{5}{2}, \frac{7}{2}, \frac{9}{2}$	44 902.3	$\frac{3}{2}, ..., \frac{11}{2}$	44 933.2	$\frac{5}{2}, ..., \frac{11}{2}$
44 816.1	$\frac{5}{2}, \frac{7}{2}, \frac{9}{2}$	44 859.1	$\frac{5}{2}, \frac{7}{2}, \frac{9}{2}$	44 902.5	$\frac{3}{2}, ..., \frac{11}{2}$	44 933.8	$\frac{5}{2}, \frac{7}{2}, \frac{9}{2}$
44 817.1	$\frac{5}{2}, \frac{7}{2}, \frac{9}{2}$	44 859.9	$\frac{5}{2}, \frac{7}{2}, \frac{9}{2}$	44 903.0	$\frac{5}{2}, \frac{7}{2}, \frac{9}{2}$	44 934.0	$\frac{5}{2}, ..., \frac{11}{2}$
44 817.9	$\frac{5}{2}, \frac{7}{2}, \frac{9}{2}$	44 863.0	$\frac{5}{2}, \frac{7}{2}, \frac{9}{2}$	44 904.3	$\frac{5}{2}, \frac{7}{2}, \frac{9}{2}$	44 934.7	$\frac{5}{2}, \frac{7}{2}, \frac{9}{2}$
44 820.0	$\frac{5}{2}, \frac{7}{2}, \frac{9}{2}$	44 864.9	$\frac{5}{2}, \frac{7}{2}, \frac{9}{2}$	44 904.7	$\frac{5}{2}, \frac{7}{2}, \frac{9}{2}$	44 935.4	$\frac{5}{2}, \frac{7}{2}, \frac{9}{2}$
44 820.1	$\frac{5}{2}, ..., \frac{11}{2}$	44 865.0	$\frac{5}{2}, ..., \frac{11}{2}$	44 905.1	$\frac{5}{2}, \frac{7}{2}, \frac{9}{2}$	44 936.1	$\frac{5}{2}, \frac{7}{2}, \frac{9}{2}$
44 822.0	$\frac{5}{2}, \frac{7}{2}, \frac{9}{2}$	44 865.5	$\frac{5}{2}, \frac{7}{2}, \frac{9}{2}$	44 907.2	$\frac{5}{2}, \frac{7}{2}, \frac{9}{2}$	44 936.6	$\frac{5}{2}, ..., \frac{11}{2}$
44 822.8	$\frac{5}{2}, ..., \frac{11}{2}$	44 866.0	$\frac{5}{2}, \frac{7}{2}, \frac{9}{2}$	44 907.5	$\frac{5}{2}, ..., \frac{11}{2}$	44 938.6	$\frac{3}{2}, ..., \frac{11}{2}$
44 823.6	$\frac{5}{2}, \frac{7}{2}, \frac{9}{2}$	44 868.1	$\frac{5}{2}, \frac{7}{2}, \frac{9}{2}$	44 908.7	$\frac{3}{2}, ..., \frac{11}{2}$	44 939.0	$\frac{5}{2}, \frac{7}{2}, \frac{9}{2}$
44 823.9	$\frac{5}{2}, \frac{7}{2}, \frac{9}{2}$	44 868.6	$\frac{5}{2}, \frac{7}{2}, \frac{9}{2}$	44 908.9	$\frac{3}{2}, ..., \frac{11}{2}$	44 943.1	$\frac{5}{2}, \frac{7}{2}, \frac{9}{2}$
44 825.2	$\frac{5}{2}, \frac{7}{2}, \frac{9}{2}$	44 870.5	$\frac{5}{2}, \frac{7}{2}, \frac{9}{2}$	44 911.1	$\frac{3}{2}, ..., \frac{11}{2}$	44 946.7	$\frac{5}{2}, \frac{7}{2}, \frac{9}{2}$
44 825.8	$\frac{5}{2}, \frac{7}{2}, \frac{9}{2}$	44 870.9	$\frac{5}{2}, \frac{7}{2}, \frac{9}{2}$	44 911.9	$\frac{5}{2}, ..., \frac{11}{2}$	44 949.4	$\frac{5}{2}, \frac{7}{2}, \frac{9}{2}$
44 827.0	$\frac{5}{2}, \frac{7}{2}, \frac{9}{2}$	44 871.9	$\frac{5}{2}, \frac{7}{2}, \frac{9}{2}$	44 912.1	$\frac{5}{2}, \frac{7}{2}, \frac{9}{2}$	44 949.6	$\frac{3}{2}, ..., \frac{11}{2}$
44 827.6	$\frac{5}{2}, \frac{7}{2}, \frac{9}{2}$	44 872.2	$\frac{5}{2}, \frac{7}{2}, \frac{9}{2}$	44 913.5	$\frac{5}{2}, \frac{7}{2}, \frac{9}{2}$	44 949.7	$\frac{5}{2}, \frac{7}{2}, \frac{9}{2}$
44 829.9	$\frac{5}{2}, \frac{7}{2}, \frac{9}{2}$	44 874.9	$\frac{5}{2}, \frac{7}{2}, \frac{9}{2}$	44 914.7	$\frac{5}{2}, \frac{7}{2}, \frac{9}{2}$	44 949.8	$\frac{5}{2}, ..., \frac{11}{2}$
44 830.8	$\frac{5}{2}, \frac{7}{2}, \frac{9}{2}$	44 876.2	$\frac{5}{2}, \frac{7}{2}, \frac{9}{2}$	44 916.4	$\frac{5}{2}, \frac{7}{2}, \frac{9}{2}$	44 950.9	$\frac{5}{2}, \frac{7}{2}, \frac{9}{2}$
44 831.2	$\frac{5}{2}, \frac{7}{2}, \frac{9}{2}$	44 879.1	$\frac{5}{2}, \frac{7}{2}, \frac{9}{2}$	44 916.6	$\frac{5}{2}, \frac{7}{2}, \frac{9}{2}$	44 951.8	$\frac{5}{2}, \frac{7}{2}, \frac{9}{2}$
44 832.4	$\frac{5}{2}, \frac{7}{2}, \frac{9}{2}$	44 881.0	$\frac{5}{2}, \frac{7}{2}, \frac{9}{2}$	44 916.9	$\frac{5}{2}, \frac{7}{2}, \frac{9}{2}$	44 952.0	$\frac{3}{2}, ..., \frac{11}{2}$
44 833.3	$\frac{5}{2}, \frac{7}{2}, \frac{9}{2}$	44 882.0	$\frac{5}{2}, \frac{7}{2}, \frac{9}{2}$	44 917.3	$\frac{5}{2}, \frac{7}{2}, \frac{9}{2}$	44 952.6	$\frac{5}{2}, \frac{7}{2}, \frac{9}{2}$
44 833.6	$\frac{5}{2}, \frac{7}{2}, \frac{9}{2}$	44 882.3	$\frac{5}{2}, \frac{7}{2}, \frac{9}{2}$	44 918.1	$\frac{5}{2}, \frac{7}{2}, \frac{9}{2}$	44 953.8	$\frac{3}{2}, ..., \frac{11}{2}$
44 834.9	$\frac{5}{2}, \frac{7}{2}, \frac{9}{2}$	44 882.5	$\frac{5}{2}, \frac{7}{2}, \frac{9}{2}$	44 918.2	$\frac{5}{2}, \frac{7}{2}, \frac{9}{2}$	44 954.7	$\frac{5}{2}, \frac{7}{2}, \frac{9}{2}$
44 835.9	$\frac{5}{2}, \frac{7}{2}, \frac{9}{2}$	44 883.0	$\frac{5}{2}, \frac{7}{2}, \frac{9}{2}$	44 918.7	$\frac{5}{2}, \frac{7}{2}, \frac{9}{2}$	44 958.0	$\frac{5}{2}, ..., \frac{11}{2}$
44 837.2	$\frac{5}{2}, ..., \frac{11}{2}$	44 883.3	$\frac{3}{2}, ..., \frac{11}{2}$	44 919.1	$\frac{5}{2}, \frac{7}{2}, \frac{9}{2}$	44 960.1	$\frac{5}{2}, \frac{7}{2}, \frac{9}{2}$
44 838.8	$\frac{5}{2}, ..., \frac{11}{2}$	44 883.7	$\frac{5}{2}, \frac{7}{2}, \frac{9}{2}$	44 919.8	$\frac{5}{2}, \frac{7}{2}, \frac{9}{2}$	44 960.3	$\frac{5}{2}, \frac{7}{2}, \frac{9}{2}$
44 841.8	$\frac{5}{2}, \frac{7}{2}, \frac{9}{2}$	44 885.4	$\frac{5}{2}, \frac{7}{2}, \frac{9}{2}$	44 920.7	$\frac{5}{2}, \frac{7}{2}, \frac{9}{2}$	44 960.5	$\frac{3}{2}, ..., \frac{11}{2}$

(Continued on next page.)

TABLE IX: *(Continued.)*

E (cm^{-1})	J	E (cm^{-1})	J	E (cm^{-1})	J	E (cm^{-1})	J
44 960.8	$\frac{3}{2}, ..., \frac{11}{2}$	45 029.9	$\frac{5}{2}, \frac{7}{2}, \frac{9}{2}$	45 107.2	$\frac{5}{2}, ..., \frac{11}{2}$	45 213.4	$\frac{5}{2}, ..., \frac{11}{2}$
44 962.3	$\frac{5}{2}, \frac{7}{2}, \frac{9}{2}$	45 030.1	$\frac{3}{2}, ..., \frac{11}{2}$	45 108.5	$\frac{5}{2}, \frac{7}{2}, \frac{9}{2}$	45 214.8	$\frac{5}{2}, ..., \frac{11}{2}$
44 962.7	$\frac{5}{2}, \frac{7}{2}, \frac{9}{2}$	45 032.2	$\frac{5}{2}, \frac{7}{2}, \frac{9}{2}$	45 110.9	$\frac{5}{2}, \frac{7}{2}, \frac{9}{2}$	45 215.8	$\frac{5}{2}, ..., \frac{11}{2}$
44 963.0	$\frac{5}{2}, ..., \frac{11}{2}$	45 032.5	$\frac{3}{2}, ..., \frac{11}{2}$	45 111.1	$\frac{3}{2}, ..., \frac{11}{2}$	45 217.2	$\frac{3}{2}, ..., \frac{11}{2}$
44 966.9	$\frac{5}{2}, \frac{7}{2}, \frac{9}{2}$	45 033.4	$\frac{5}{2}, \frac{7}{2}, \frac{9}{2}$	45 113.2	$\frac{5}{2}, \frac{7}{2}, \frac{9}{2}$	45 219.0	$\frac{3}{2}, ..., \frac{11}{2}$
44 969.2	$\frac{3}{2}, ..., \frac{11}{2}$	45 034.5	$\frac{5}{2}, ..., \frac{11}{2}$	45 114.1	$\frac{5}{2}, \frac{7}{2}, \frac{9}{2}$	45 221.2	$\frac{5}{2}, ..., \frac{11}{2}$
44 970.6	$\frac{5}{2}, \frac{7}{2}, \frac{9}{2}$	45 035.6	$\frac{3}{2}, ..., \frac{11}{2}$	45 115.3	$\frac{5}{2}, \frac{7}{2}, \frac{9}{2}$	45 222.0	$\frac{3}{2}, ..., \frac{11}{2}$
44 971.5	$\frac{3}{2}, ..., \frac{11}{2}$	45 037.6	$\frac{3}{2}, ..., \frac{11}{2}$	45 115.5	$\frac{3}{2}, ..., \frac{11}{2}$	45 222.4	$\frac{5}{2}, ..., \frac{11}{2}$
44 971.9	$\frac{5}{2}, \frac{7}{2}, \frac{9}{2}$	45 037.9	$\frac{5}{2}, \frac{7}{2}, \frac{9}{2}$	45 120.0	$\frac{5}{2}, \frac{7}{2}, \frac{9}{2}$	45 222.7	$\frac{3}{2}, ..., \frac{11}{2}$
44 972.7	$\frac{5}{2}, \frac{7}{2}, \frac{9}{2}$	45 039.4	$\frac{5}{2}, \frac{7}{2}, \frac{9}{2}$	45 120.2	$\frac{3}{2}, ..., \frac{11}{2}$	45 227.0	$\frac{5}{2}, ..., \frac{11}{2}$
44 973.5	$\frac{5}{2}, \frac{7}{2}, \frac{9}{2}$	45 043.4	$\frac{5}{2}, \frac{7}{2}, \frac{9}{2}$	45 120.5	$\frac{5}{2}, ..., \frac{11}{2}$	45 229.5	$\frac{5}{2}, ..., \frac{11}{2}$
44 976.3	$\frac{3}{2}, ..., \frac{11}{2}$	45 043.7	$\frac{3}{2}, ..., \frac{11}{2}$	45 123.3	$\frac{3}{2}, ..., \frac{11}{2}$	45 230.0	$\frac{3}{2}, ..., \frac{11}{2}$
44 977.3	$\frac{3}{2}, ..., \frac{11}{2}$	45 045.3	$\frac{5}{2}, \frac{7}{2}, \frac{9}{2}$	45 123.7	$\frac{3}{2}, ..., \frac{11}{2}$	45 230.6	$\frac{3}{2}, ..., \frac{11}{2}$
44 977.8	$\frac{5}{2}, \frac{7}{2}, \frac{9}{2}$	45 045.7	$\frac{3}{2}, ..., \frac{11}{2}$	45 125.9	$\frac{5}{2}, \frac{7}{2}, \frac{9}{2}$	45 231.9	$\frac{5}{2}, ..., \frac{11}{2}$
44 978.3	$\frac{3}{2}, ..., \frac{11}{2}$	45 046.1	$\frac{5}{2}, \frac{7}{2}, \frac{9}{2}$	45 126.1	$\frac{3}{2}, ..., \frac{11}{2}$	45 235.9	$\frac{5}{2}, ..., \frac{11}{2}$
44 980.0	$\frac{3}{2}, ..., \frac{11}{2}$	45 046.4	$\frac{3}{2}, ..., \frac{11}{2}$	45 128.4	$\frac{3}{2}, ..., \frac{11}{2}$	45 237.2	$\frac{5}{2}, ..., \frac{11}{2}$
44 983.7	$\frac{5}{2}, \frac{7}{2}, \frac{9}{2}$	45 047.7	$\frac{5}{2}, ..., \frac{11}{2}$	45 131.5	$\frac{5}{2}, ..., \frac{11}{2}$	45 239.0	$\frac{5}{2}, ..., \frac{11}{2}$
44 984.8	$\frac{5}{2}, \frac{7}{2}, \frac{9}{2}$	45 049.4	$\frac{5}{2}, \frac{7}{2}, \frac{9}{2}$	45 132.9	$\frac{5}{2}, \frac{7}{2}, \frac{9}{2}$	45 239.7	$\frac{5}{2}, ..., \frac{11}{2}$
44 985.6	$\frac{3}{2}, ..., \frac{11}{2}$	45 049.7	$\frac{5}{2}, ..., \frac{11}{2}$	45 133.5	$\frac{5}{2}, \frac{7}{2}, \frac{9}{2}$	45 241.2	$\frac{5}{2}, ..., \frac{11}{2}$
44 986.3	$\frac{3}{2}, ..., \frac{11}{2}$	45 051.5	$\frac{5}{2}, \frac{7}{2}, \frac{9}{2}$	45 135.8	$\frac{5}{2}, \frac{7}{2}, \frac{9}{2}$	45 242.8	$\frac{5}{2}, ..., \frac{11}{2}$
44 987.5	$\frac{5}{2}, \frac{7}{2}, \frac{9}{2}$	45 051.7	$\frac{3}{2}, ..., \frac{11}{2}$	45 136.3	$\frac{5}{2}, \frac{7}{2}, \frac{9}{2}$	45 243.4	$\frac{5}{2}, ..., \frac{11}{2}$
44 987.8	$\frac{3}{2}, ..., \frac{11}{2}$	45 053.0	$\frac{5}{2}, \frac{7}{2}, \frac{9}{2}$	45 139.4	$\frac{5}{2}, ..., \frac{11}{2}$	45 245.4	$\frac{5}{2}, ..., \frac{11}{2}$
44 988.5	$\frac{5}{2}, \frac{7}{2}, \frac{9}{2}$	45 053.1	$\frac{3}{2}, ..., \frac{11}{2}$	45 143.1	$\frac{5}{2}, ..., \frac{11}{2}$	45 248.5	$\frac{5}{2}, ..., \frac{11}{2}$
44 989.4	$\frac{5}{2}, \frac{7}{2}, \frac{9}{2}$	45 053.3	$\frac{3}{2}, ..., \frac{11}{2}$	45 150.0	$\frac{5}{2}, ..., \frac{11}{2}$	45 250.6	$\frac{5}{2}, ..., \frac{11}{2}$
44 989.7	$\frac{3}{2}, ..., \frac{11}{2}$	45 054.4	$\frac{5}{2}, \frac{7}{2}, \frac{9}{2}$	45 152.8	$\frac{3}{2}, ..., \frac{11}{2}$	45 251.6	$\frac{5}{2}, ..., \frac{11}{2}$
44 990.6	$\frac{5}{2}, \frac{7}{2}, \frac{9}{2}$	45 056.6	$\frac{5}{2}, \frac{7}{2}, \frac{9}{2}$	45 157.9	$\frac{3}{2}, ..., \frac{11}{2}$	45 253.2	$\frac{5}{2}, ..., \frac{11}{2}$
44 995.5	$\frac{5}{2}, \frac{7}{2}, \frac{9}{2}$	45 057.3	$\frac{3}{2}, ..., \frac{11}{2}$	45 158.2	$\frac{5}{2}, ..., \frac{11}{2}$	45 257.3	$\frac{5}{2}, ..., \frac{11}{2}$
44 996.1	$\frac{3}{2}, ..., \frac{11}{2}$	45 062.8	$\frac{3}{2}, ..., \frac{11}{2}$	45 159.7	$\frac{5}{2}, ..., \frac{11}{2}$	45 258.6	$\frac{5}{2}, ..., \frac{11}{2}$
44 996.8	$\frac{5}{2}, \frac{7}{2}, \frac{9}{2}$	45 075.0	$\frac{5}{2}, \frac{7}{2}, \frac{9}{2}$	45 160.8	$\frac{5}{2}, ..., \frac{11}{2}$	45 261.4	$\frac{5}{2}, ..., \frac{11}{2}$
44 999.7	$\frac{5}{2}, \frac{7}{2}, \frac{9}{2}$	45 076.5	$\frac{5}{2}, \frac{7}{2}, \frac{9}{2}$	45 165.5	$\frac{5}{2}, ..., \frac{11}{2}$	45 262.4	$\frac{5}{2}, ..., \frac{11}{2}$
44 999.9	$\frac{3}{2}, ..., \frac{11}{2}$	45 081.3	$\frac{5}{2}, \frac{7}{2}, \frac{9}{2}$	45 166.5	$\frac{5}{2}, ..., \frac{11}{2}$	45 266.5	$\frac{5}{2}, ..., \frac{11}{2}$
45 004.5	$\frac{5}{2}, \frac{7}{2}, \frac{9}{2}$	45 081.7	$\frac{5}{2}, \frac{7}{2}, \frac{9}{2}$	45 170.2	$\frac{3}{2}, ..., \frac{11}{2}$	45 271.6	$\frac{5}{2}, ..., \frac{11}{2}$
45 004.7	$\frac{3}{2}, ..., \frac{11}{2}$	45 082.1	$\frac{5}{2}, \frac{7}{2}, \frac{9}{2}$	45 171.6	$\frac{5}{2}, ..., \frac{11}{2}$	45 273.5	$\frac{5}{2}, ..., \frac{11}{2}$
45 006.8	$\frac{3}{2}, ..., \frac{11}{2}$	45 082.2	$\frac{5}{2}, ..., \frac{11}{2}$	45 172.0	$\frac{5}{2}, ..., \frac{11}{2}$	45 275.6	$\frac{5}{2}, ..., \frac{11}{2}$
45 007.1	$\frac{3}{2}, ..., \frac{11}{2}$	45 082.5	$\frac{3}{2}, ..., \frac{11}{2}$	45 177.6	$\frac{5}{2}, ..., \frac{11}{2}$	45 277.7	$\frac{5}{2}, ..., \frac{11}{2}$
45 009.2	$\frac{5}{2}, \frac{7}{2}, \frac{9}{2}$	45 082.7	$\frac{5}{2}, \frac{7}{2}, \frac{9}{2}$	45 183.5	$\frac{5}{2}, ..., \frac{11}{2}$	45 278.7	$\frac{5}{2}, ..., \frac{11}{2}$
45 009.3	$\frac{3}{2}, ..., \frac{11}{2}$	45 083.1	$\frac{5}{2}, ..., \frac{11}{2}$	45 183.8	$\frac{3}{2}, ..., \frac{11}{2}$	45 280.0	$\frac{5}{2}, ..., \frac{11}{2}$
45 017.0	$\frac{5}{2}, \frac{7}{2}, \frac{9}{2}$	45 085.3	$\frac{5}{2}, ..., \frac{11}{2}$	45 189.3	$\frac{5}{2}, ..., \frac{11}{2}$	45 281.9	$\frac{5}{2}, ..., \frac{11}{2}$
45 017.3	$\frac{3}{2}, ..., \frac{11}{2}$	45 088.3	$\frac{5}{2}, ..., \frac{11}{2}$	45 190.5	$\frac{3}{2}, ..., \frac{11}{2}$	45 287.0	$\frac{5}{2}, ..., \frac{11}{2}$
45 018.4	$\frac{5}{2}, \frac{7}{2}, \frac{9}{2}$	45 090.5	$\frac{5}{2}, \frac{7}{2}, \frac{9}{2}$	45 192.5	$\frac{5}{2}, ..., \frac{11}{2}$	45 290.1	$\frac{5}{2}, ..., \frac{11}{2}$
45 019.1	$\frac{3}{2}, ..., \frac{11}{2}$	45 093.5	$\frac{5}{2}, \frac{7}{2}, \frac{9}{2}$	45 194.1	$\frac{5}{2}, \frac{7}{2}, \frac{9}{2}$	45 292.7	$\frac{5}{2}, ..., \frac{11}{2}$
45 027.1	$\frac{5}{2}, \frac{7}{2}, \frac{9}{2}$	45 094.5	$\frac{5}{2}, \frac{7}{2}, \frac{9}{2}$	45 195.8	$\frac{5}{2}, ..., \frac{11}{2}$	45 351.3	$\frac{5}{2}, \frac{7}{2}, \frac{9}{2}$
45 028.4	$\frac{3}{2}, ..., \frac{11}{2}$	45 095.5	$\frac{5}{2}, \frac{7}{2}, \frac{9}{2}$	45 198.0	$\frac{3}{2}, ..., \frac{11}{2}$	45 377.5	$\frac{3}{2}, ..., \frac{11}{2}$
45 029.6	$\frac{5}{2}, ..., \frac{11}{2}$	45 104.2	$\frac{5}{2}, \frac{7}{2}, \frac{9}{2}$	45 212.6	$\frac{5}{2}, ..., \frac{11}{2}$	45 378.7	$\frac{3}{2}, ..., \frac{11}{2}$

(Continued on next page.)

TABLE IX: *(Continued.)*

E (cm^{-1})	J	E (cm^{-1})	J	E (cm^{-1})	J	E (cm^{-1})	J
45 378.9	$\frac{3}{2}, ..., \frac{11}{2}$	45 390.3	$\frac{3}{2}, ..., \frac{11}{2}$	45 409.9	$\frac{3}{2}, ..., \frac{11}{2}$	45 443.4	$\frac{3}{2}, ..., \frac{11}{2}$
45 381.2	$\frac{3}{2}, ..., \frac{11}{2}$	45 396.6	$\frac{3}{2}, ..., \frac{11}{2}$	45 411.3	$\frac{3}{2}, ..., \frac{11}{2}$	45 451.0	$\frac{3}{2}, ..., \frac{11}{2}$
45 381.7	$\frac{3}{2}, ..., \frac{11}{2}$	45 398.0	$\frac{3}{2}, ..., \frac{11}{2}$	45 415.9	$\frac{3}{2}, ..., \frac{11}{2}$	45 459.1	$\frac{3}{2}, ..., \frac{11}{2}$
45 383.8	$\frac{3}{2}, ..., \frac{11}{2}$	45 400.5	$\frac{3}{2}, ..., \frac{11}{2}$	45 418.3	$\frac{3}{2}, ..., \frac{11}{2}$	45 464.3	$\frac{3}{2}, ..., \frac{11}{2}$
45 386.1	$\frac{3}{2}, ..., \frac{11}{2}$	45 402.0	$\frac{3}{2}, ..., \frac{11}{2}$	45 419.6	$\frac{3}{2}, ..., \frac{11}{2}$	45 468.3	$\frac{3}{2}, ..., \frac{11}{2}$
45 387.1	$\frac{3}{2}, ..., \frac{11}{2}$	45 406.8	$\frac{3}{2}, ..., \frac{11}{2}$	45 421.3	$\frac{3}{2}, ..., \frac{11}{2}$		
45 387.8	$\frac{3}{2}, ..., \frac{11}{2}$	45 408.9	$\frac{3}{2}, ..., \frac{11}{2}$	45 433.9	$\frac{3}{2}, ..., \frac{11}{2}$		

TABLE X. List of values for the first ionization potential (IP) and uncertainties (ΔIP) up to proton number $Z = 103$. For elements where no reference is given see [2] and references therein. In the case of Rn no uncertainty is given in the reference.

Z	Symb.	IP (eV)	ΔIP (eV)	Ref.	Z	Symb.	IP (eV)	ΔIP (eV)	Ref.
1	H	13.59843449	8.0E-08		53	I	10.451260	2.5E-05	
2	He	24.58738880	1.5E-07		54	Xe	12.1298436	1.5E-06	
3	Li	5.39171495	4.0E-08		55	Cs	3.893905695	2.4E-08	
4	Be	9.322699	7.0E-06		56	Ba	5.2116646	1.2E-06	
5	B	8.298019	3.0E-06		57	La	5.5769	6.0E-04	
6	C	11.2602880	1.1E-06		58	Ce	5.5386	4.0E-04	
7	N	14.53413	4.0E-05		59	Pr	5.47018	3.7E-04	[3]
8	O	13.618055	7.0E-06		60	Nd	5.5250	6.0E-04	
9	F	17.42282	5.0E-05		61	Pm	5.58188	3.7E-05	this work
10	Ne	21.564540	7.0E-06		62	Sm	5.64371	1.7E-04	
11	Na	5.1390769	3.0E-07		63	Eu	5.670385	5.0E-06	
12	Mg	7.646236	4.0E-06		64	Gd	6.14980	4.0E-05	
13	Al	5.985769	3.0E-06		65	Tb	5.8638	6.0E-04	
14	Si	8.15168	3.0E-05		66	Dy	5.939061	6.2E-06	[4]
15	P	10.486686	1.5E-05		67	Ho	6.0214048	3.7E-07	[5]
16	S	10.36001	1.2E-04		68	Er	6.1077	1.1E-05	
17	Cl	12.967632	1.6E-05		69	Tm	6.18431	6.0E-05	
18	Ar	15.7596117	5.0E-07		70	Yb	6.254160	1.2E-05	
19	K	4.34066369	9.0E-08		71	Lu	5.425871	1.2E-05	
20	Ca	6.1131554	3.0E-07		72	Hf	6.825070	1.2E-05	
21	Sc	6.56149	6.0E-05		73	Ta	7.549571	2.5E-05	
22	Ti	6.828120	1.2E-05		74	W	7.86403	1.0E-04	
23	V	6.746187	2.1E-05		75	Re	7.83352	1.1E-04	
24	Cr	6.76651	4.0E-05		76	Os	8.43823	2.0E-04	
25	Mn	7.4340379	1.2E-06		77	Ir	8.96702	2.2E-04	
26	Fe	7.9024681	1.2E-06		78	Pt	8.95883	1.0E-04	
27	Co	7.88101	1.2E-04		79	Au	9.225554	4.0E-06	
28	Ni	7.639878	1.7E-05		80	Hg	10.437504	6.0E-06	
29	Cu	7.726380	4.0E-06		81	Tl	6.1082873	1.2E-06	
30	Zn	9.394197	6.0E-06		82	Pb	7.4166799	6.0E-07	
31	Ga	5.9993020	1.2E-06		83	Bi	7.285516	6.0E-06	
32	Ge	7.899435	1.2E-05		84	Po	8.418069	5.1E-06	[6, 7]
33	As	9.78855	2.5E-04		85	At	9.31751	8.0E-05	
34	Se	9.752392	1.5E-05		86	Rn	10.74850	*	
35	Br	11.81381	6.0E-05		87	Fr	4.0727410	1.1E-06	
36	Kr	13.9996053	2.0E-06		88	Ra	5.2784239	2.5E-06	
37	Rb	4.1771280	1.2E-06		89	Ac	5.380226	2.4E-05	
38	Sr	5.69486740	1.3E-07		90	Th	6.30670	2.5E-04	
39	Y	6.21726	1.0E-04		91	Pa	6.08	1.4E-02	[3]
40	Zr	6.63412	6.0E-05		92	U	6.19405	6.0E-05	
41	Nb	6.75885	4.0E-05		93	Np	6.26554	2.5E-04	
42	Mo	7.09243	4.0E-05		94	Pu	6.02576	2.5E-04	
43	Tc	7.11938	3.0E-05		95	Am	5.97381	2.5E-04	
44	Ru	7.36050	5.0E-05		96	Cm	5.99141	2.5E-04	
45	Rh	7.45890	5.0E-05		97	Bk	6.19785	2.5E-04	
46	Pd	8.336839	1.0E-05		98	Cf	6.28166	2.5E-04	
47	Ag	7.576234	2.5E-05		99	Es	6.36758	2.5E-04	
48	Cd	8.993820	1.6E-05		100	Fm	6.52	1.3E-01	[8]
49	In	5.7863556	7.0E-07		101	Md	6.59	1.3E-01	[8]
50	Sn	7.343918	1.2E-05		102	No	6.62621	5.0E-05	[9]
51	Sb	8.608389	1.2E-05		103	Lr	4.96	8.0E-02	
52	Te	9.009803	5.5E-06	[10]					

[1] J. Reader and S. P. Davis, Journal of Research of the National Bureau of Standards - A. Physica and Chemistry **71A**, 587 (1967).
[2] A. Kramida and Y. Ralchenko, "NIST Atomic Spectra Database, NIST Standard Reference Database 78,".
[3] K. Wendt, T. Gottwald, C. Mattolat, and S. Raeder, Hyperfine Interactions **227**, 55 (2014).
[4] D. Studer, P. Dyrauf, P. Naubereit, R. Heinke, and K. Wendt, Hyperfine Interactions **238**, 02A916 (2017).
[5] J. Hostetter, J. D. Pritchard, J. E. Lawler, and M. Saffman, Physical Review A **91**, 71 (2015).
[6] S. Raeder, H. Heggen, A. Teigelhöfer, and J. Lassen, Spectrochimica Acta Part B: Atomic Spectroscopy **151**, 65 (2019).
[7] D. A. Fink, K. Blaum, V. N. Fedosseev, B. A. Marsh, R. E. Rossel, and S. Rothe, Spectrochimica Acta Part B: Atomic Spectroscopy **151**, 72 (2019).
[8] T. K. Sato, M. Asai, A. Borschevsky, R. Beerwerth, Y. Kaneya, H. Makii, A. Mitsukai, Y. Nagame, A. Osa, A. Toyoshima, K. Tsukada, M. Sakama, S. Takeda, K. Ooe, D. Sato, Y. Shigekawa, S.-I. Ichikawa, C. E. Düllmann, J. Grund, D. Renisch, J. V. Kratz, M. Schädel, E. Eliav, U. Kaldor, S. Fritzsche, and T. Stora, Journal of the American chemical society **140**, 14609 (2018).
[9] P. Chhetri, D. Ackermann, H. Backe, M. Block, B. Cheal, C. Droese, C. E. Düllmann, J. Even, R. Ferrer, F. Giacoppo, S. Götz, F. P. Heßberger, M. Huyse, O. Kaleja, J. Khuyagbaatar, P. Kunz, M. Laatiaoui, F. Lautenschläger, W. Lauth, N. Lecesne, L. Lens, E. Minaya Ramirez, A. K. Mistry, S. Raeder, P. van Duppen, T. Walther, A. Yakushev, and Z. Zhang, Physical Review Letters **120**, 263003 (2018).
[10] T. Kieck, Y. Liu, R. Li, J. Lassen, and K. D. A. Wendt, submitted to Phys. Rev. A (2019).

List of Figures

List of Tables

List of Abbreviations

AEC-LHEP Albert Einstein Center for Fundamental Physics - Laboratory for High Energy Physics, Bern. 107

AIS Auto-ionizing state. 47, 48

ASE Air-spaced etalon. 127

BBO Beta barium borate. 17, 18

CEM Channel electron multiplier. 30, 31

CERN European Organization for Nuclear Research, Geneva; acronym from french: *Conseil européen pour la recherche nucléaire*. 5, 10, 24, 31, 92, 107, 123, 181

CRIS Collinear Resonance Ionization Spectroscopy; experiment at ISOLDE. 32

cw Continuous wave. 9, 14–16, 50, 123, 127

DC Direct current; opposite: AC for alternating current. 2, 51

ECDL External cavity diode laser. 15, 16, 21–24, 123

ECHo Electron Capture in ^{163}Ho. 5, 24, 59, 122

FC Faraday cup. 30

FI Fizeau interferometer. 19, 20

FPE Fabry-Pérot etalon. 11, 13, 127

FPI Fabry-Pérot inteferometer. 19, 20, 23

FS Fine structure. 36, 37, 87

FSR Free spectral range. 11, 13, 19, 20, 23, 126, 127

FWHM Full width at half maximum. 11, 41, 43, 44, 48

GANDALPH Gothenburg Anion Detector for Affinity Measurements by Laser Photodetachment. 31

GSI Helmholtzzentrum für Schwerionenforschung, Darmstadt; formerly: *Gesellschaft für Schwerionenforschung*. v, 92

HFS Hyperfine structure. 87, 89, 90, 129

IGISOL Ion Guide Isotope Separation On-Line. 5, 32

ILL Institut Laue-Langevin, Grenoble. 71, 107

IP Ionization potential. v, 2, 4, 27, 36, 39, 48–52, 59, 71, 122

IS Isotope shift. 87, 90

ISAC Isotope separator and Accelerator, TRIUMF. 5, 10, 32

ISOL Isotope separation on-line. 31

ISOLDE Isotope Separation On-Line Device, CERN. 5, 9, 10, 16, 24, 31, 32, 123, 126

JYFL Jyväskylä accelerator laboratory. 5, 32

LARISSA Laser Resonance Ionization Spectroscopy for Selective Applications. 5, 19, 20, 22, 24, 31, 50, 53

LF Lyot-Filter. 11, 13, 15, 127

LIST Laser Ion Source and Trap. 27, 28, 32

MABU Mainz Atomic Beam Unit. 30, 31, 71

MCU Micro controller unit. 30

MOT Magneto-optical trap. 53, 121

Nd:YAG Neodymium-doped yttrium aluminium garnet. 10, 47

NIST U.S. National Institute of Standards and Technology. 38, 87

OES Odd-even staggering. 87

PBE Prism beam expander. 14

PI-LIST Perpendicularly Illuminated Laser Ion Source and Trap. 27, 28, 32, 43, 107, 121, 123

PSB Proton synchrotron booster. 31

PSI Paul Scherrer Institut, Villigen. 71, 107, 181

QMF Quadrupole mass filter. 31

QUANTUM Quanten-, Atom- und Neutronenphysik (research group at Mainz University). v, 181

RESIST Resonance Ionization Techniques for Separators. 6, 24, 123

RF Radio frequency. 27

RI Resonance ionization. 5–7, 14, 38, 46, 47

RIB Radioactive ion beam. 5, 24, 123

RILIS Resonance Ionization Laser Ion Source. 5, 10, 16, 24, 27, 28, 31, 32, 46, 122, 123, 126

RIMS Resonance ionization mass spectrometry. 5, 6, 24

RIS Resonance ionization spectroscopy. 2, 5–7, 10, 18, 19, 40, 42, 45, 46, 49, 50, 53, 71, 89, 121, 122

RISIKO Resonance Ionization Spectroscopy in Collinear geometry; from german: *Resonanzionisations-Spektroskopie in kollinearer Geometrie*. 10, 24–26, 28–32, 43, 107

SAS Saturated absorption spectroscopy. 20, 22, 92

SATLAS Statistical Analysis Toolbox for Laser Spectroscopy; python package. 45, 89

SFPI Scanning Fabry-Pérot inteferometer. 22, 23, 92

SHG Second harmonic generation. 17, 18

SIRIUS Secondary Ionisation of Radioactive Isotopes for Ultra trace analysis. 5

TRIUMF TRI University Meson Facility, Vancouver. 5, 14, 32

UV Ultraviolet. 10, 16

YAG Yttrium aluminium garnet. 13

Bibliography

[1] E. Rutherford, *LXXIX. The scattering of α and β particles by matter and the structure of the atom*, Lond. Edinb. Dubl. Phil. Mag. **21**, 669–688 (1911). doi:10.1080/14786440508637080.

[2] C. F. v. Weizsäcker, *Zur Theorie der Kernmassen*, Z. Physik **96**, 431–458 (1935). doi:10.1007/BF01337700.

[3] M. G. Mayer, *On Closed Shells in Nuclei. II*, Phys. Rev. **75**, 1969–1970 (1949). doi:10.1103/PhysRev.75.1969.

[4] J. H. D. Jensen, J. M. Luttinger, *Angular Momentum Distributions in the Thomas-Fermi Model*, Phys. Rev. **86**, 907–910 (1952). doi:10.1103/PhysRev.86.907.

[5] S. G. Nilsson, *Binding States of Individual Nucleons in Strongly Deformed Nuclei*, Dan. Mat. Fys. Medd. **29**, 1–69 (1955).
URL http://cds.cern.ch/record/212345/files/p1.pdf

[6] S. A. Moszkowski, *Particle States in Spheroidal Nuclei*, Phys. Rev. **99**, 803–809 (1955). doi:10.1103/PhysRev.99.803.

[7] P. Campbell, I. D. Moore, M. R. Pearson, *Laser spectroscopy for nuclear structure physics*, Prog. Part. Nucl. Phys. **86**, 127–180 (2016). doi:10.1016/j.ppnp.2015.09.003.

[8] L. Rolla, L. Fernandes, *Florentium or Illinium?*, Nature **119**, 637–638 (1927). doi:10.1038/119637a0.

[9] W. A. Noyes, *Florentium or Illinium?*, Nature **120**, 14 (1927). doi:10.1038/120014c0.

[10] J. A. Marinsky, L. E. Glendenin, C. D. Coryell, *The chemical identification of radioisotopes of neodymium and of element 61*, J. Am. Chem. Soc. **69**, 2781–2785 (1947). doi:10.1021/ja01203a059.

[11] J. Mattauch, *Zur Systematik der Isotopen*, Z. Physik **91**, 361–371 (1934). doi:10.1007/BF01342557.

[12] IAEA Nuclear Data Section, *Live Chart of Nuclides: Nuclear Structure and Decay Data* (2019).
URL https://www-nds.iaea.org/relnsd/vcharthtml/VChartHTML.html

[13] H. Flicker, J. J. Loferski, T. S. Elleman, *Construction of a promethium-147 atomic battery*, IEEE Trans. Electron Devices **11**, 2–8 (1964). doi:10.1109/T-ED.1964.15271.

[14] M. Kumar, J. Udhayakumar, J. Nuwad, R. Shukla, C. G. S. Pillai, A. Dash, M. Venkatesh, *Development of a ^{147}Pm source for beta-backscatter thickness gauge applications*, Appl. Radiat. Isot. **69**, 580–587 (2011). doi:10.1016/j.apradiso.2010.11.026.

[15] G. J. Beyer, T. J. Ruth, *The role of electromagnetic separators in the production of radiotracers for bio-medical research and nuclear medical application*, Nucl. Instrum. Methods Phys. Res., Sect. B **204**, 694–700 (2003). doi:10.1016/S0168-583X(03)00489-0.

[16] H. Mohsin, F. Jia, J. N. Bryan, G. Sivaguru, C. S. Cutler, A. R. Ketring, W. H. Miller, J. Simón, R. K. Frank, L. J. Theodore, D. B. Axworthy, S. S. Jurisson, M. R. Lewis, *Comparison of pretargeted and conventional CC49 radioimmunotherapy using ^{149}Pm, ^{166}Ho, and ^{177}Lu*, Bioconjugate Chem. **22**, 2444–2452 (2011). doi:10.1021/bc200258x.

[17] G. E. Boyd, *Technetium and Promethium*, J. Chem. Educ. **36**, 3–14 (1959). doi:10.1021/ed036p3.

[18] G. A. Leander, P. Möller, *Possibly abrupt transition to a new structure regime in very light Pm and Sm nuclei*, Phys. Lett. B **110**, 17–20 (1982). doi:10.1016/0370-2693(82)90942-X.

[19] V. S. Letokhov, V. I. Mishin, S. K. Sekatsky, V. N. Fedoseyev, G. D. Alkhazov, A. E. Barzakh, V. P. Denisov, V. E. Starodubsky, *Laser spectroscopic studies of nuclei with neutron number $N < 82$ (Eu, Sm and Nd isotopes)*, J. Phys. G: Nucl. Part. Phys. **18**, 1177–1193 (1992). doi:10.1088/0954-3899/18/7/008.

[20] B. Cheal, M. Avgoulea, J. Billowes, P. Campbell, K. T. Flanagan, D. H. Forest, M. D. Gardner, J. Huikari, B. A. Marsh, A. Nieminen, H. L. Thayer, G. Tungate, J. Äystö, *Collinear laser spectroscopy of neutron-rich cerium isotopes near the $N = 88$ shape transition*, Nucl. Instrum. Methods Phys. Res., Sect. A **29**, 2479–2484 (2003). doi:10.1088/0954-3899/29/11/003.

[21] K. A. H. Leeuwen, E. R. Eliel, B. H. Post, W. Hogervorst, *High resolution measurements of hyperfine structure and isotope shifts in 9 spectral lines of Nd I*, Z. Physik A **301**, 95–99 (1981). doi:10.1007/BF01419237.

[22] M. Hongliang, S. Wei, Y. Bin, L. Yong, F. Dufei, L. Fuquan, T. Jiayong, Y. Fujia, *Optical isotope shifts of Nd II by collinear fast-ion-beam laser spectroscopy*, J. Phys. B: At. Mol. Opt. Phys. **30**, 3355–3360 (1997). doi:10.1088/0953-4075/30/15/008.

[23] J. G. England, I. S. Grant, J. A. R. Griffith, D. E. Evans, D. A. Eastham, G. W. A. Newton, P. M. Walker, *Isotope shifts and hyperfine splitting in $^{144-154}$Sm I*, J. Phys. G: Nucl. Part. Phys. **16**, 105–123 (1990). doi:10.1088/0954-3899/16/1/014.

[24] S. A. Ahmad, W. Klempt, C. Ekström, R. Neugart, K. Wendt, *Nuclear spins, moments, and changes of the mean square charge radii of $^{140-153}$Eu*, Z. Physik A **321**, 35–45 (1985). doi:10.1007/BF01411941.

[25] R. F. Casten, D. d. Warner, D. S. Brenner, R. L. Gill, *Relation between the $Z = 64$ Shell Closure and the Onset of Deformation at $N = 88 - 90$*, Phys. Rev. Lett. **47**, 1433–1436 (1981). doi:10.1103/PhysRevLett.47.1433.

[26] R. V. Ambartzumian, V. S. Letokhov, *Selective Two-Step (STS) Photoionization of Atoms and Photodissociation of Molecules by Laser Radiation*, Appl. Opt. **11**, 354–358 (1972). doi:10.1364/AO.11.000354.

[27] V. S. Letokhov, V. I. Mishin, *Highly selective multistep ionization of atoms by laser radiation*, Opt. Commun. **29**, 168–171 (1979). doi:10.1016/0030-4018(79)90009-9.

[28] M. Franzmann, H. Bosco, C. Walther, K. Wendt, *A new resonant Laser-SNMS system for environmental ultra-trace analysis: Installation and optimization*, Int. J. Mass Spectrom. **423**, 27–32 (2017). doi:10.1016/j.ijms.2017.10.003.

[29] T. Stephan, R. Trappitsch, A. M. Davis, M. J. Pellin, D. Rost, M. R. Savina, R. Yokochi, N. Liu, *CHILI – the Chicago Instrument for Laser Ionization: a new tool for isotope measurements in cosmochemistry*, Int. J. Mass Spectrom. **407**, 1–15 (2016). doi:10.1016/j.ijms.2016.06.001.

[30] M. R. Savina, M. J. Pellin, C. Tripa, I. V. Veryovkin, W. F. Calaway, A. M. Davis, *Analyzing individual presolar grains with CHARISMA*, Geochim. Cosmochim. Acta **67**, 3215–3225 (2003). doi:10.1016/S0016-7037(03)00082-6.

[31] H. Tomita, C. Mattolat, S. Raeder, S. Sasada, Y. Higuchi, K. Takezawa, T. Muramatsu, T. Iguchi, K. Wendt, *Development of laser ablation assisted resonant ionization mass spectrometry for isotope analysis*, Hyperfine Interact. **196**, 169–176 (2010). doi:10.1007/s10751-009-0143-1.

[32] F. Schneider, K. Chrysalidis, H. Dorrer, C. Düllmann, K. Eberhardt, R. Haas, T. Kieck, C. Mokry, P. Naubereit, S. Schmidt, K. Wendt, *Resonance ionization of holmium for ion implantation in microcalorimeters*, Nucl. Instrum. Methods Phys. Res. B **376**, 388–392 (2016). doi:10.1016/j.nimb.2015.12.012.

[33] T. Kieck, S. Biebricher, C. E. Düllmann, K. Wendt, *Optimization of a laser ion source for ^{163}Ho isotope separation*, Rev. Sci. Instrum. **90**, 053304 (2019). doi:10.1063/1.5081094.

[34] T. Kieck, H. Dorrer, C. E. Düllmann, V. Gadelshin, F. Schneider, K. Wendt, *Highly efficient isotope separation and ion implantation of ^{163}Ho for the ECHo project*, Nucl. Instrum. Methods Phys. Res., Sect. A **945**, 162602 (2019). doi:10.1016/j.nima.2019.162602.

[35] M. Franzmann, H. Bosco, L. Hamann, C. Walther, K. Wendt, *Resonant laser–SNMS for spatially resolved and element selective ultra-trace analysis of radionuclides*, J. Anal. At. Spectrom. **33**, 730–737 (2018). doi:10.1039/C7JA00423K.

[36] S. Raeder, N. Kneip, T. Reich, D. Studer, N. Trautmann, K. Wendt, *Recent developments in resonance ionization mass spectrometry for ultra-trace analysis of actinide elements*, Radiochim. Acta **107**, 645–652 (2019). doi:10.1515/ract-2019-0001.

[37] *RILIS Elements Database v0.06* (2013).
URL http://riliselements.web.cern.ch/riliselements/

[38] D. A. Fink, S. D. Richter, B. Bastin, K. Blaum, R. Catherall, T. E. Cocolios, D. V. Fedorov, V. N. Fedosseev, K. T. Flanagan, L. Ghys, A. Gottberg, N. Imai, T. Kron, N. Lecesne, K. M. Lynch, B. A. Marsh, T. M. Mendonca, D. Pauwels, E. Rapisarda, J. P. Ramos, R. E. Rossel, S. Rothe, M. D. Seliverstov, M. Sjödin, T. Stora, C. van Beveren, K. Wendt, *First application of the Laser Ion Source and Trap (LIST) for on-line experiments at ISOLDE*, Nucl. Instrum. Methods Phys. Res. B **317**, 417–421 (2013). doi:10.1016/j.nimb.2013.06.039.

[39] S. Raeder, H. Heggen, J. Lassen, F. Ames, D. Bishop, P. Bricault, P. Kunz, A. Mjøs, A. Teigelhöfer, *An ion guide laser ion source for isobar-suppressed rare isotope beams*, Rev. Sci. Instrum. **85**, 033309 (2014). doi:10.1063/1.4868496.

[40] D. A. Fink, S. D. Richter, K. Blaum, R. Catherall, B. Crepieux, V. N. Fedosseev, A. Gottberg, T. Kron, B. A. Marsh, C. Mattolat, S. Raeder, R. E. Rossel, S. Rothe, F. Schwellnus, M. D. Seliverstov, M. Sjödin, T. Stora, P. Suominen, K. Wendt, *On-line implementation and first operation of the Laser Ion Source and Trap at ISOLDE/CERN*, Nucl. Instrum. Methods Phys. Res. B **344**, 83–95 (2015). doi:10.1016/j.nimb.2014.12.007.

[41] R. Heinke, T. Kron, S. Raeder, T. Reich, P. Schönberg, M. Trümper, C. Weichhold, K. Wendt, *High-resolution in-source laser spectroscopy in perpendicular geometry*, Hyperfine Interact. **238**, 6 (2017). doi:10.1007/s10751-016-1386-2.

[42] R. Horn, *Aufbau eines Systems gepulster, abstimmbarer Festkörperlaser zum Einsatz in der Resonanzsionisations-Massenspektrometrie*, Dissertation, Johannes Gutenberg-Universität, Mainz (2003).

[43] C. Rauth, C. Geppert, R. Horn, J. Lassen, P. Bricault, K. Wendt, *First laser ions at an off-line mass separator of the ISAC facility at TRIUMF*, Nucl. Instrum. Methods Phys. Res. B **215**, 268–277 (2004). doi:10.1016/j.nimb.2003.08.029.

[44] S. Rothe, B. A. Marsh, C. Mattolat, V. N. Fedosseev, K. Wendt, *A complementary laser system for ISOLDE RILIS*, J. Phys.: Conf. Ser. **312**, 052020 (2011). doi:10.1088/1742-6596/312/5/052020.

[45] G. S. Hurst, M. G. Payne, S. D. Kramer, J. P. Young, *Resonance ionization spectroscopy and one-atom detection*, Rev. Mod. Phys. **51**, 767–819 (1979). doi:10.1103/RevModPhys.51.767.

[46] W. Happer, *Optical Pumping*, Rev. Mod. Phys. **44**, 169–249 (1972). doi:10.1103/RevModPhys.44.169.

[47] R. Neugart, *Laser spectroscopy on mass-separated radioactive beams*, Nucl. Instrum. Methods Phys. Res. **186**, 165–175 (1981). doi:10.1016/0029-554X(81)90902-2.

[48] T. J. Procter, H. Aghaei-Khozani, J. Billowes, M. L. Bissell, F. Le Blanc, B. Cheal, T. E. Cocolios, K. T. Flanagan, H. Hori, T. Kobayashi, D. Lunney, K. M. Lynch, B. A. Marsh, G. Neyens, J. Papuga, M. M. Rajabali, S. Rothe, G. Simpson, A. J. Smith, H. H. Stroke, W. Vanderheijden, K. Wendt, *Development of the CRIS (Collinear Resonant Ionisation Spectroscopy) beam line*, J. Phys.: Conf. Ser. **381**, 012070 (2012). doi:10.1088/1742-6596/381/1/012070.

[49] W. Demtröder, *Laserspektroskopie*, 6th Edition, Springer, Berlin, 2011. doi:10.1007/978-3-642-21306-9.

[50] V. Sonnenschein, I. D. Moore, H. Khan, I. Pohjalainen, M. Reponen, *Characterization of a dual-etalon Ti:sapphire laser via resonance ionization spectroscopy of stable copper isotopes*, Hyperfine Interact. **227**, 113–123 (2014). doi:10.1007/s10751-013-1000-9.

[51] C. Mattolat, *Spektroskopische Untersuchungen an Technetium und Silizium: Ein Festkörperlasersystem für die Resonanzionisationsspektroskopie*, Dissertation, Johannes Gutenberg-Universität, Mainz (2010).
URL https://publications.ub.uni-mainz.de/theses/volltexte/2010/2451/pdf/2451.pdf

[52] A. Teigelhöfer, P. Bricault, O. Chachkova, M. Gillner, J. Lassen, J. P. Lavoie, R. Li, J. Meißner, W. Neu, K. D. A. Wendt, *Grating tuned Ti:Sa laser for in-source spectroscopy of Rydberg and autoionizing states*, Hyperfine Interact. **196**, 161–168 (2010). doi:10.1007/s10751-010-0171-x.

[53] V. Sonnenschein, *Laser developments and high resolution resonance ionization spectroscopy of actinide elements*, Dissertation, University of Jyväskylä, Jyväskylä (2014).
URL http://urn.fi/URN:ISBN:978-951-39-6050-6

[54] V. Sonnenschein, I. D. Moore, S. Raeder, M. Reponen, H. Tomita, K. Wendt, *Characterization of a pulsed injection-locked Ti:sapphire laser and its application to high resolution resonance ionization spectroscopy of copper*, Laser Phys. **27**, 085701 (2017). doi:10.1088/1555-6611/aa7834.

[55] J. J. Zayhowski, *Limits imposed by spatial hole burning on the single-mode operation of standing-wave laser cavities*, Opt. Lett. **15**, 431–433 (1990). doi:10.1364/OL.15.000431.

[56] T. Fischbach, *Aufbau und Charakterisierung einer interferometrischen Frequenzstabilisierung für Diodenlaser*, Diploma thesis, Johannes Gutenberg-Universität, Mainz (2012).

[57] A. Hakimi, *Diodenlaserbasierte Resonanzionisations-Massenspektrometrie zur Spektroskopie und Ultraspurenanalyse an Uranisotopen*, Dissertation, Johannes Gutenberg-Universität, Mainz (2013).
URL https://inis.iaea.org/collection/NCLCollectionStore/_Public/45/102/45102198.pdf

[58] A. E. Siegman, *Lasers*, University Science Books, Mill Valley, California, 1986.

[59] K. Chrysalidis, S. G. Wilkins, R. Heinke, Á. Koszorús, R. de Groote, V. N. Fedosseev, B. Marsh, S. Rothe, R. Garcia Ruiz, D. Studer, A. Vernon, K. Wendt, *First demonstration of Doppler-free 2-photon in-source laser spectroscopy at the ISOLDE-RILIS*, Nucl. Instrum. Methods Phys. Res. B **463**, 476–481 (2020). doi:10.1016/j.nimb.2019.04.020.

[60] V. Sonnenschein, M. Ohashi, H. Tomita, T. Iguchi, *A direct diode pumped continuous-wave Ti:sapphire laser as seed of a pulsed amplifier for high-resolution resonance ionization spectroscopy*, Nucl. Instrum. Methods Phys. Res. B **463**, 512–514 (2020). doi:10.1016/j.nimb.2019.03.017.

[61] V. Sonnenschein, H. Tomita, K. Kotaro, H. Koya, D. Studer, R. Terabayashi, F. Weber, K. Wendt, N. Nishizawa, T. Iguchi, *A direct diode pumped Ti:sapphire laser with singe-frequency operation for high-resolution spectroscopy*, Hyperfine Interact. **241**, 32 (2020). doi:10.1007/s10751-020-1706-4.

[62] P. Naubereit, *Weiterentwicklung eines weitabstimmbaren Titan:Saphir-Lasers und sein Einsatz zur Spektroskopie hochliegender Resonanzen in Holmium*, Master thesis, Johannes Gutenberg-Universität, Mainz (2014).

[63] R. Menzel, *Photonics: Linear and Nonlinear Interactions of Laser Light and Matter*, Springer, Berlin, Heidelberg, 2007. doi:10.1007/978-3-540-45158-7.

[64] R. W. Boyd, *Nonlinear optics*, 3rd Edition, Elsevier Academic Press, Amsterdam, 2008.

[65] S. Wolf, D. Studer, K. Wendt, F. Schmidt-Kaler, *Efficient and robust photoionization loading of beryllium ions*, Appl. Phys. B **124**, 30 (2018). doi:10.1007/s00340-018-6903-3.

[66] P. Naubereit, J. Marín-Sáez, F. Schneider, A. Hakimi, M. Franzmann, T. Kron, S. Richter, K. Wendt, *Resonance ionization spectroscopy of sodium Rydberg levels using difference frequency generation of high-repetition-rate pulsed Ti:sapphire lasers*, Phys. Rev. A **93**, 052518 (2016). doi:10.1103/PhysRevA.93.052518.

[67] A. Fast, *Modernisierung eines Lambdameters*, Bachelor thesis, Technische Universität Darmstadt, Darmstadt (2010).
URL http://www.iap.tu-darmstadt.de/fileadmin/nlq/theses/BSc_Thesis/BSc_Thesis_Fast.pdf

[68] O. Novák, I. S. Falconer, R. Sanginés, M. Lattemann, R. N. Tarrant, D. R. McKenzie, M. M. M. Bilek, *Fizeau interferometer system for fast high resolution studies of spectral line shapes*, Rev. Sci. Instrum. **82**, 023105 (2011). doi:10.1063/1.3525102.

[69] T. A. Hall, *Fizeau interferometer profiles at finite acceptance angles*, J. Phys. E: Sci. Instrum. **2**, 837–840 (1969). doi:10.1088/0022-3735/2/10/301.

[70] D. W. Preston, *Doppler–free saturated absorption: Laser spectroscopy*, Am. J. Phys. **64**, 1432–1436 (1996). doi:10.1119/1.18457.

[71] D. A. Steck, *Rubidium 87 D Line Data, revision 2.2.1* (11/2019).
URL https://steck.us/alkalidata

[72] S. Raeder, *Spurenanalyse von Aktiniden in der Umwelt mittels Resonanzionisations-Massenspektrometrie*, Dissertation, Johannes Gutenberg-Universität, Mainz (2010).
URL https://publications.ub.uni-mainz.de/theses/volltexte/2011/2775/pdf/2775.pdf

[73] K. Zimmer, *Konzeption, Aufbau und Test der Ionenoptik des RISIKO-Massenseparators*, Diploma thesis, Johannes Gutenberg-Universität, Mainz (1990).

[74] T. Kron, *Pushing the Limits of Resonance Ionization Mass Spectrometry: Ionization Efficiency in Palladium an Spectral Resolution in Technetium*, Dissertation,

Johannes Gutenberg-Universität, Mainz (2016).
URL https://publications.ub.uni-mainz.de/theses/volltexte/2017/100001505/pdf/100001505.pdf

[75] V. Gadelshin, T. Cocolios, V. Fedoseev, R. Heinke, T. Kieck, B. Marsh, P. Naubereit, S. Rothe, T. Stora, D. Studer, P. van Duppen, K. Wendt, *Laser resonance ionization spectroscopy on lutetium for the MEDICIS project*, Hyperfine Interact. **238**, 28 (2017). doi:10.1007/s10751-017-1406-x.

[76] R. Heinke, *In-source high-resolution spectroscopy of holmium radioisotopes: On-line tailored perpendicular laser interaction at ISOLDE's Laser Ion Source and Trap LIST*, Dissertation, Johannes Gutenberg-Universität, Mainz (2019).
URL https://publications.ub.uni-mainz.de/theses/volltexte/2019/100003129/pdf/100003129.pdf

[77] M. J. Dresser, *The Saha–Langmuir Equation and its Application*, J. Appl. Phys. **39**, 338–339 (1968). doi:10.1063/1.1655755.

[78] F. Schwellnus, R. Catherall, B. Crepieux, V. N. Fedosseev, B. A. Marsh, C. Mattolat, M. Menna, F. K. Österdahl, S. Raeder, T. Stora, K. Wendt, *Study of low work function materials for hot cavity resonance ionization laser ion sources*, Nucl. Instrum. Methods Phys. Res. B **267**, 1856–1861 (2009). doi:10.1016/j.nimb.2009.02.068.

[79] K. Blaum, C. Geppert, H.-J. Kluge, M. Mukherjee, S. Schwarz, K. Wendt, *A novel scheme for a highly selective laser ion source*, Nucl. Instrum. Methods Phys. Res. B **204**, 331–335 (2003). doi:10.1016/S0168-583X(02)01942-0.

[80] F. Schwellnus, K. Blaum, C. Geppert, T. Gottwald, H.-J. Kluge, C. Mattolat, W. Nörtershäuser, K. Wies, K. Wendt, *The laser ion source and trap (LIST): A highly selective ion source*, Nucl. Instrum. Methods Phys. Res. B **266**, 4383–4386 (2008). doi:10.1016/j.nimb.2008.05.065.

[81] S. Richter, *Implementierung der Laserionenquellenfalle LIST bei ISOLDE und Validierung der Spezifikationen Effizienz und Selektivität*, Dissertation, Johannes Gutenberg-Universität, Mainz (2015).
URL http://inspirehep.net/record/1653560/?ln=de

[82] J. Lettry, R. Catherall, U. Köster, U. Georg, O. Jonsson, S. Marzari, V. Fedosseev, *Alkali suppression within laser ion-source cavities and time structure of the laser ionized ion-bunches*, Nucl. Instrum. Methods Phys. Res. B **204**, 363–367 (2003). doi:10.1016/S0168-583X(02)01967-5.

[83] M. Franzmann, *Resonanzionisations-Massenspektrometrie an Aktiniden mit der Mainzer Atomstrahlquelle MABU*, Diploma thesis, Johannes Gutenberg-Universität, Mainz (2013).

[84] J. Roßnagel, *Aufbau einer Atomstrahl-Massenspektrometer-Apparatur zur resonanten Laserionisation*, Diploma thesis, Johannes Gutenberg-Universität, Mainz (2011).

[85] K. Blaum, *Resonante Laserionisations-Massenspektrometrie an Gadolinium zur Isotopenhäufigkeitsanalyse mit geringsten Mengen*, Dissertation, Johannes Gutenberg-Universität, Mainz (2000).

[86] S. Raeder, V. Sonnenschein, T. Gottwald, I. D. Moore, M. Reponen, S. Rothe, N. Trautmann, K. Wendt, *Resonance ionization spectroscopy of thorium isotopes–towards a laser spectroscopic identification of the low-lying 7.6 eV isomer of ^{229}Th*, J. Phys. B: At. Mol. Opt. Phys. **44**, 165005 (2011). doi:10.1088/0953-4075/44/16/165005.

[87] C. Mattolat, T. Gottwald, S. Raeder, S. Rothe, F. Schwellnus, K. Wendt, P. Thörle-Pospiech, N. Trautmann, *Determination of the first ionization potential of technetium*, Phys. Rev. A **81**, 052513 (2010). doi:10.1103/PhysRevA.81.052513.

[88] J. Roßnagel, S. Raeder, A. Hakimi, R. Ferrer, N. Trautmann, K. Wendt, *Determination of the first ionization potential of actinium*, Phys. Rev. A **85**, 012525 (2012). doi:10.1103/PhysRevA.85.012525.

[89] V. Sonnenschein, S. Raeder, A. Hakimi, I. D. Moore, K. Wendt, *Determination of the ground-state hyperfine structure in neutral ^{229}Th*, J. Phys. B: At. Mol. Opt. Phys. **45**, 165005 (2012). doi:10.1088/0953-4075/45/16/165005.

[90] K. Wendt, C. Mattolat, T. Gottwald, T. Kron, S. Raeder, S. Rothe, F. Schwellnus, H. Tomita, *Hyperfine structure and isotope shift in the $3s^2\,3p^2\,3P_{0,1,2} \rightarrow 3s^2\,3p\,4p^3\,P_{0,1,2}$ transitions in silicon by Doppler-free in-source two-photon resonance-ionization spectroscopy*, Phys. Rev. A **88**, 052510 (2013). doi:10.1103/PhysRevA.88.052510.

[91] R. P. de Groote, T. Kron, A. Hakimi, G. Neyens, K. Wendt, *Double-resonance-ionization mapping of the hyperfine structure of the stable Cu isotopes using pulsed narrowband Ti:sapphire lasers*, Phys. Rev. A **92**, 022506 (2015). doi:10.1103/PhysRevA.92.022506.

[92] E. Kugler, D. Fiander, B. Johnson, H. Haas, A. Przewloka, H. L. Ravn, D. J. Simon, K. Zimmer, *The new CERN-ISOLDE on-line mass-separator facility at the PS-Booster*, Nucl. Instrum. Methods Phys. Res. B **70**, 41–49 (1992). doi:10.1016/0168-583X(92)95907-9.

[93] R. Catherall, W. Andreazza, M. Breitenfeldt, A. Dorsival, G. J. Focker, T. P. Gharsa, G. T J, J.-L. Grenard, F. Locci, P. Martins, S. Marzari, J. Schipper, A. Shornikov, T. Stora, *The ISOLDE facility*, J. Phys. G: Nucl. Part. Phys. **44**, 094002 (2017). doi:10.1088/1361-6471/aa7eba.

[94] S. Rothe, J. Sundberg, J. Welander, K. Chrysalidis, T. D. Goodacre, V. Fedosseev, S. Fiotakis, O. Forstner, R. Heinke, K. Johnston, T. Kron, U. Köster, Y. Liu, B. Marsh, A. Ringvall-Moberg, R. E. Rossel, C. Seiffert, D. Studer, K. Wendt, D. Hanstorp, *Laser photodetachment of radioactive* $^{128}I^{-}$, J. Phys. G: Nucl. Part. Phys. **44**, 104003 (2017). doi:10.1088/1361-6471/aa80aa.

[95] D. Leimbach, J. Sundberg, Y. Guo, R. Ahmed, J. Ballof, L. Bengtsson, F. Boix Pamies, A. Borschevsky, K. Chrysalidis, E. Eliav, D. V. Fedorov, V. N. Fedosseev, O. Forstner, N. Galland, R. F. Garcia Ruiz, C. Granados, R. Heinke, K. Johnston, Á. Koszorús, U. Köster, M. K. Kristiansson, Y. Liu, B. A. Marsh, P. L. Molkanov, L. F. Pašteka, J. P. Ramos, E. Renault, M. Reponen, A. Ringvall-Moberg, R. E. Rossel, D. Studer, A. Vernon, J. Warbinek, J. Welander, K. D. A. Wendt, S. G. Wilkins, D. Hanstorp, S. Rothe, *The electron affinity of astatine*, submitted to Nat. Commun. (2020).

[96] A. Gottberg, *Target materials for exotic ISOL beams*, Nucl. Instrum. Methods Phys. Res. B **376**, 8–15 (2016). doi:10.1016/j.nimb.2016.01.020.

[97] T. Kron, Y. Liu, S. Richter, F. Schneider, K. Wendt, *High efficiency resonance ionization of palladium with Ti:sapphire lasers*, J. Phys. B: At. Mol. Opt. Phys. **49**, 185003 (2016). doi:10.1088/0953-4075/49/18/185003.

[98] V. M. Gadelshin, R. Heinke, T. Kieck, T. Kron, P. Naubereit, F. Rösch, T. Stora, D. Studer, K. Wendt, *Measurement of the laser resonance ionization efficiency for lutetium*, Radiochim. Acta **107**, 653–661 (2019). doi:10.1515/ract-2019-3118.

[99] K. Chrysalidis, A. E. Barzakh, R. Ahmed, A. N. Andreyev, J. Ballof, J. G. Cubiss, D. V. Fedorov, V. N. Fedosseev, L. M. Fraile, R. D. Harding, U. Köster, B. A. Marsh, C. Raison, J. P. Ramos, R. E. Rossel, S. Rothe, K. Wendt, S. G. Wilkins, *In-source laser spectroscopy of dysprosium isotopes at the ISOLDE-RILIS*, Nucl. Instrum. Methods Phys. Res. B **463**, 472–475 (2020). doi:10.1016/j.nimb.2019.04.021.

[100] S. Rothe, A. N. Andreyev, S. Antalic, A. Borschevsky, L. Capponi, T. E. Cocolios, H. de Witte, E. Eliav, D. V. Fedorov, V. N. Fedosseev, D. A. Fink, S. Fritzsche, L. Ghys, M. Huyse, N. Imai, U. Kaldor, Y. Kudryavtsev, U. Köster, J. F. W. Lane, J. Lassen, V. Liberati, K. M. Lynch, B. A. Marsh, K. Nishio, D. Pauwels, V. Pershina, L. Popescu, T. J. Procter, D. Radulov, S. Raeder, M. M. Rajabali, E. Rapisarda, R. E. Rossel, K. Sandhu, M. D. Seliverstov, A. M. Sjödin, P. van den Bergh, P. van Duppen, M. Venhart, Y. Wakabayashi, K. D. A. Wendt, *Measurement of the first ionization potential of astatine by laser ionization spectroscopy*, Nat. Commun. **4**, 1835 (2013). doi:10.1038/ncomms2819.

[101] R. Neugart, *Collinear laser spectroscopy on unstable isotopes: A tool of nuclear physics*, Hyperfine Interact. **24**, 159–180 (1985). doi:10.1007/BF02354810.

[102] R. Neugart, J. Billowes, M. L. Bissell, K. Blaum, B. Cheal, K. T. Flanagan, G. Neyens, W. Nörtershäuser, D. T. Yordanov, *Collinear laser spectroscopy at ISOLDE: new methods and highlights*, J. Phys. G: Nucl. Part. Phys. **44**, 064002 (2017). doi:10.1088/1361-6471/aa6642.

[103] T. E. Cocolios, H. H. Al Suradi, J. Billowes, I. Budinčević, R. P. de Groote, S. de Schepper, V. N. Fedosseev, K. T. Flanagan, S. Franchoo, R. F. Garcia Ruiz, H. Heylen, F. Le Blanc, K. M. Lynch, B. A. Marsh, P. Mason, G. Neyens, J. Papuga, T. J. Procter, M. M. Rajabali, R. E. Rossel, S. Rothe, G. S. Simpson, A. J. Smith, I. Strashnov, H. H. Stroke, D. Verney, P. M. Walker, K. Wendt, R. T. Wood, *The Collinear Resonance Ionization Spectroscopy (CRIS) experimental setup at CERN-ISOLDE*, Nucl. Instrum. Methods Phys. Res. B **317**, 565–569 (2013). doi:10.1016/j.nimb.2013.05.088.

[104] T. E. Cocolios, R. P. de Groote, J. Billowes, M. L. Bissell, I. Budinčević, T. Day Goodacre, G. J. Farooq-Smith, V. N. Fedosseev, K. T. Flanagan, S. Franchoo, R. F. Garcia Ruiz, W. Gins, H. Heylen, T. Kron, R. Li, K. M. Lynch, B. A. Marsh, G. Neyens, R. E. Rossel, S. Rothe, A. J. Smith, H. H. Stroke, K. Wendt, S. G. Wilkins, X. Yang, *High-resolution laser spectroscopy with the Collinear Resonance Ionisation Spectroscopy (CRIS) experiment at CERN-ISOLDE*, Nucl. Instrum. Methods Phys. Res. B **376**, 284–287 (2016). doi:10.1016/j.nimb.2015.11.024.

[105] T. Mayer-Kuckuk, *Atomphysik*, 5th Edition, Teubner Verlag, Wiesbaden, 1997. doi:10.1007/978-3-663-01606-9.

[106] W. Demtröder, *Atome, Moleküle und Festkörper*, 4th Edition, Springer, Berlin, 2010.

[107] I. V. Hertel, C.-P. Schulz, *Atome, Moleküle und optische Physik 1*, Springer, Berlin, Heidelberg, 2008. doi:10.1007/978-3-662-46808-1.

[108] M. Mohan (Ed.), *New trends in atomic and molecular physics: Advanced technological applications*, Vol. 76 of Springer Series on Atomic, Optical, and Plasma Physics, Springer, Berlin, 2013.

[109] A. Kramida, Y. Ralchenko, J. Reader, NIST ASD Team, *NIST Atomic Spectra Database (version 5.7), NIST Standard Reference Database 78*. doi:10.18434/T4W30F,
URL https://www.nist.gov/pml/atomic-spectra-database

[110] T. F. Gallagher, *Rydberg atoms*, Rep. Prog. Phys. **51**, 143–188 (1988). doi:10.1088/0034-4885/51/2/001.

[111] K. D. A. Wendt, K. Blaum, C. Geppert, P. Müller, W. Nörtershäuser, A. Schmitt, P. Schumann, N. Trautmann, B. A. Bushaw, *Laser Based Techniques*

for Ultra Trace Isotope Production, Spectroscopy and Detection, Hyperfine Interact. **162**, 147–157 (2006). doi:10.1007/s10751-005-9219-8.

[112] H. Friedrich, *Theoretische Atomphysik*, Springer, Berlin, Heidelberg, 1994. doi:10.1007/978-3-642-85161-2.

[113] P. Dyrauf, *Resonanzionisation und Rydbergspektroskopie an Dysprosium*, Master thesis, Johannes Gutenberg-Universität, Mainz (2015).

[114] D. Studer, *Resonanzionisationsspektroskopie hochliegender Zustände in Dysprosium und Erbium zur Entwicklung effizienter Anregungsschemata und Bestimmung des ersten Ionisationspotentials*, Diploma thesis, Johannes Gutenberg-Universität, Mainz (2015).

[115] N. Petersen, M. Trümper, P. Windpassinger, *Spectroscopy of the 1001 nm transition in atomic dysprosium*, Preprint (v2) (2019).
URL https://arxiv.org/abs/1907.05754v2

[116] M. Wickliffe, J. Lawler, G. Nave, *Atomic transition probabilities for Dy I and Dy II*, J. Quant. Spectrosc. Radiat. Transf. **66**, 363–404 (2000). doi:10.1016/S0022-4073(99)00173-9.

[117] G. C. King, F. H. Read, R. E. Imhof, *The measurement of molecular lifetimes by the photon-photon delayed coincidence method*, J. Phys. B: At. Mol. Phys. **8**, 665–673 (1975). doi:10.1088/0022-3700/8/4/027.

[118] T. Day Goodacre, J. Billowes, C. L. Binnersley, M. L. Bissell, K. Chrysalidis, T. E. Cocolios, R. P. de Groote, G. J. Farooq-Smith, D. V. Fedorov, V. N. Fedosseev, K. T. Flanagan, S. Franchoo, R. F. Garcia Ruiz, W. Gins, R. Heinke, Á. Koszorús, K. M. Lynch, B. A. Marsh, P. L. Molkanov, P. Naubereit, G. Neyens, C. M. Ricketts, S. Rothe, C. Seiffert, M. D. Seliverstov, H. H. Stroke, D. Studer, A. R. Vernon, S. G. Wilkins, K. Wendt, X. F. Yang, *Radium ionization scheme development: The first observed autoionizing states and optical pumping effects in the hot cavity environment*, Spectrochim. Acta B **150**, 99–104 (2018). doi:10.1016/j.sab.2018.10.002.

[119] R. Heinke, V. Fedosseev, T. Kieck, T. Kron, B. Marsh, S. Raeder, S. Richter, S. Rothe, K. Wendt, *Atom beam emersion from hot cavity laser ion sources*, Nucl. Instrum. Methods Phys. Res. B **463**, 449–454 (2020). doi:10.1016/j.nimb.2019.04.026.

[120] Y. Liu, J. Lin, G. Huang, Y. Guo, C. Duan, *Simple empirical analytical approximation to the Voigt profile*, J. Opt. Soc. Am. B **18**, 666–672 (2001). doi:10.1364/JOSAB.18.000666.

[121] W. Gins, R. P. de Groote, M. L. Bissell, C. Granados Buitrago, R. Ferrer, K. M. Lynch, G. Neyens, S. Sels, *Analysis of counting data: Development of the SATLAS Python package*, Comput. Phys. Commun. **222**, 286–294 (2018). doi:10.1016/j.cpc.2017.09.012.

[122] R. P. de Groote, M. Verlinde, V. Sonnenschein, K. T. Flanagan, I. Moore, G. Neyens, *Efficient, high-resolution resonance laser ionization spectroscopy using weak transitions to long-lived excited states*, Phys. Rev. A **95**, 031693 (2017). doi:10.1103/PhysRevA.95.032502.

[123] B. H. Isselhardt, S. G. Prussin, M. R. Savina, D. G. Willingham, K. B. Knight, I. D. Hutcheon, *Rate equation model of laser induced bias in uranium isotope ratios measured by resonance ionization mass spectrometry*, J. Anal. At. Spectrom. **31**, 666–678 (2016). doi:10.1039/c5ja00249d.

[124] U. Fano, *Effects of Configuration Interaction on Intensities and Phase Shifts*, Phys. Rev. **124**, 1866–1878 (1961). doi:10.1103/PhysRev.124.1866.

[125] P. Chhetri, D. Ackermann, H. Backe, M. Block, B. Cheal, C. Droese, C. E. Düllmann, J. Even, R. Ferrer, F. Giacoppo, S. Götz, F. P. Heßberger, M. Huyse, O. Kaleja, J. Khuyagbaatar, P. Kunz, M. Laatiaoui, F. Lautenschläger, W. Lauth, N. Lecesne, L. Lens, E. Minaya Ramirez, A. K. Mistry, S. Raeder, P. van Duppen, T. Walther, A. Yakushev, Z. Zhang, *Precision Measurement of the First Ionization Potential of Nobelium*, Phys. Rev. Lett. **120**, 263003 (2018). doi:10.1103/PhysRevLett.120.263003.

[126] I. Pohjalainen, *Gas-phase chemistry, recoil source characterization and in-gas-cell resonance ionization of actinides at IGISOL*, Dissertation, University of Jyväskylä, Jyväskylä (2018).
URL http://urn.fi/URN:ISBN:978-951-39-7477-0

[127] R. S. Mulliken, *A New Electroaffinity Scale; Together with Data on Valence States and on Valence Ionization Potentials and Electron Affinities*, J. Chem. Phys. **2**, 782–793 (1934). doi:10.1063/1.1749394.

[128] T. Gottwald, *Studium hochkomplexer atomarer Spektren mittels Methoden der Laserresonanzionisation*, Dissertation, Johannes Gutenberg-Universität, Mainz (2011).
URL https://d-nb.info/1010738534/34

[129] A. Schmitt, *Hochauflösende Resonanzionisationsspektroskopie an Samarium und Gadolinium*, Dissertation, Johannes Gutenberg-Universität, Mainz (2004).
URL https://publications.ub.uni-mainz.de/theses/frontdoor.php?source_opus=546

[130] M. J. Seaton, *Quantum defect theory*, J. Chem. Phys. **46**, 167–257 (1983). doi:10.1088/0034-4885/46/2/002.

[131] M. G. Littman, M. M. Kash, D. Kleppner, *Field-Ionization Processes in Excited Atoms*, Phys. Rev. Lett. **41**, 103–107 (1978). doi:10.1103/PhysRevLett.41.103.

[132] T. F. Gallagher, L. M. Humphrey, W. E. Cooke, R. M. Hill, S. A. Edelstein, *Field ionization of highly excited states of sodium*, Phys. Rev. A **16**, 1098–1108 (1977). doi:10.1103/PhysRevA.16.1098.

[133] T. F. Gallagher, L. M. Humphrey, R. M. Hill, S. A. Edelstein, *Resolution of $|m_l|$ and $|m_j|$ Levels in the Electric Field Ionization of Highly Excited d States of Na*, Phys. Rev. Lett. **37**, 1465–1467 (1976). doi:10.1103/PhysRevLett.37.1465.

[134] V. A. Dzuba, V. V. Flambaum, *Theoretical study of some experimentally relevant states of dysprosium*, Phys. Rev. A **81**, 052515 (2010). doi:10.1103/PhysRevA.81.052515.

[135] M. Lu, S. H. Youn, B. L. Lev, *Spectroscopy of a narrow-line laser-cooling transition in atomic dysprosium*, Phys. Rev. A **83**, 012510 (2011). doi:10.1103/PhysRevA.83.012510.

[136] L. Maske, *Spektroskopie des 1001 nm Übergangs von Dysprosium*, Master thesis, Johannes Gutenberg-Universität, Mainz (2018).

[137] H. Dorrer, K. Chrysalidis, T. D. Goodacre, C. E. Düllmann, K. Eberhardt, C. Enss, L. Gastaldo, R. Haas, J. Harding, C. Hassel, K. Johnston, T. Kieck, U. Köster, B. Marsh, C. Mokry, S. Rothe, J. Runke, F. Schneider, T. Stora, A. Türler, K. Wendt, *Production, isolation and characterization of radiochemically pure ^{163}Ho samples for the ECHo-project*, Radiochim. Acta **106**, 535–547 (2018). doi:10.1515/ract-2017-2877.

[138] K. Wendt, T. Gottwald, C. Mattolat, S. Raeder, *Ionization potentials of the lanthanides and actinides – towards atomic spectroscopy of super-heavy elements*, Hyperfine Interact. **227**, 55–67 (2014). doi:10.1007/s10751-014-1041-8.

[139] M. G. Mayer, *Nuclear Configurations in the Spin-Orbit Coupling Model: I. Empirical Evidence*, Phys. Rev. **78**, 16–21 (1950). doi:10.1103/PhysRev.78.16.

[140] M. G. Mayer, *The Shell Model*, Science **145**, 999–1006 (1964). doi:10.1126/science.145.3636.999.

[141] R. D. Woods, D. S. Saxon, *Diffuse Surface Optical Model for Nucleon-Nuclei Scattering*, Phys. Rev. **95**, 577–578 (1954). doi:10.1103/PhysRev.95.577.

[142] S. G. Nilsson, I. Ragnarsson, *Shapes and shells in nuclear structure*, Cambridge Univ. Press, Cambridge, 2005. doi:10.1017/CBO9780511563973.

[143] P. F. A. Klinkenberg, *Tables of Nuclear Shell Structure*, Rev. Mod. Phys. **24**, 63–73 (1952). doi:10.1103/RevModPhys.24.63.

[144] H. Kopferman, E. E. Schneider, H. S. W. Massey, *Nuclear Moments*, 2nd Edition, Elsevier Science, Burlington, 1958.

[145] A. Bohr, B. R. Mottelson, *Nuclear structure: Volume II: Nuclear deformations*, 2nd Edition, World Scientific, Singapore, 1998. doi:10.1142/3530.

[146] Thomas P. D. Swan, *High-K Structure in the ^{164}Er Region*, Dissertation, University of Surrey, Guildford (2011). doi:10.13140/RG.2.2.30586.75200.

[147] A. J. Buchmann, E. M. Henley, *Intrinsic quadrupole moment of the nucleon*, Phys. Rev. C **63**, 015202 (2000). doi:10.1103/PhysRevC.63.015202.

[148] E. W. Otten, *Nuclear Radii and Moments of Unstable Isotopes*, in: D. A. Bromley (Ed.), Treatise on Heavy Ion Science, Vol. 248, Springer US, Boston, MA, 1989, pp. 517–638. doi:10.1007/978-1-4613-0713-6.

[149] A. Bohr, B. R. Mottelson, *Nuclear structure: Vol. I: Single-Particle motion*, 2nd Edition, World Scientific, Singapore, 1998. doi:10.1142/3530.

[150] W. Nörtershäuser, C. Geppert, *Nuclear Charge Radii of Light Elements and Recent Developments in Collinear Laser Spectroscopy*, in: C. Scheidenberger, M. Pfützner (Eds.), The Euroschool on Exotic Beams, Vol. IV, Vol. 879 of Lecture Notes in Physics, Springer, Berlin, Heidelberg, 2014, pp. 233–292. doi:10.1007/978-3-642-45141-6.

[151] Margraf, Heil, Kneissl, Maier, Pitz, Friedrichs, Lindenstruth, Schlitt, Wesselborg, P. von Brentano, Herzberg, Zilges, *Deformation dependence of low lying M1 strengths in even Nd isotopes*, Phys. Rev. C **47**, 1474–1477 (1993). doi:10.1103/PhysRevC.47.1474.

[152] R. Otto, H. Hühnermann, J. Reader, J.-F. Wyart, *Hyperfine structure investigations and identification of new energy levels in the ionic spectrum of ^{147}Pm*, J. Phys. B: At. Mol. Opt. Phys. **28**, 3615–3627 (1995). doi:10.1088/0953-4075/28/16/014.

[153] G. D. Alkhazov, A. E. Barzakh, V. A. Bolshakov, V. P. Denisov, V. S. Ivanov, Y. Y. Sergeyev, I. Y. Chubukov, V. I. Tikhonov, V. S. Letokhov, V. I. Mishin, S. K. Sekatsky, V. N. Fedoseyev, *Odd-even staggering in nuclear charge radii of neutron-rich europium isotopes*, Z. Physik A **337**, 257–259 (1990). doi:10.1007/BF01289691.

[154] R. A. Sorensen, *Odd-even staggering in the isotope shift of the nuclear radius*, Phys. Lett. **21**, 333–334 (1966). doi:10.1016/0031-9163(66)90839-0.

[155] B. S. Reehal, R. A. Sorensen, *Odd-even staggering of nuclear radii*, Nucl. Phys. A **161**, 385–400 (1971). doi:10.1016/0375-9474(71)90376-9.

[156] G. Ulm, S. K. Bhattacherjee, P. Dabkiewicz, G. Huber, H. J. Kluge, T. Kühl, H. Lochmann, E. W. Otten, K. Wendt, S. A. Ahmad, W. Klempt, R. Neugart, *Isotope shift of ^{182}Hg and an update of nuclear moments and charge radii in the isotope range ^{181}Hg-^{206}Hg*, Z. Physik A **325**, 247–259 (1986). doi:10.1007/BF01294605.

[157] A. E. Barzakh, J. G. Cubiss, A. N. Andreyev, M. D. Seliverstov, B. Andel, S. Antalic, P. Ascher, D. Atanasov, D. Beck, J. Bieroń, K. Blaum, C. Borgmann, M. Breitenfeldt, L. Capponi, T. E. Cocolios, T. Day Goodacre, X. Derkx, H. de Witte, J. Elseviers, D. V. Fedorov, V. N. Fedosseev, S. Fritzsche, L. P. Gaffney, S. George, L. Ghys, F. P. Heßberger, M. Huyse, N. Imai, Z. Kalaninová, D. Kisler, U. Köster, M. Kowalska, S. Kreim, J. F. W. Lane, V. Liberati, D. Lunney, K. M. Lynch, V. Manea, B. A. Marsh, S. Mitsuoka, P. L. Molkanov, Y. Nagame, D. Neidherr, K. Nishio, S. Ota, D. Pauwels, L. Popescu, D. Radulov, E. Rapisarda, J. P. Revill, M. Rosenbusch, R. E. Rossel, S. Rothe, K. Sandhu, L. Schweikhard, S. Sels, V. L. Truesdale, C. van Beveren, P. van den Bergh, P. van Duppen, Y. Wakabayashi, K. D. A. Wendt, F. Wienholtz, B. W. Whitmore, G. L. Wilson, R. N. Wolf, K. Zuber, *Inverse odd-even staggering in nuclear charge radii and possible octupole collectivity in ^{217,218,219}At revealed by in-source laser spectroscopy*, Phys. Rev. C **99**, 054317 (2019). doi:10.1103/PhysRevC.99.054317.

[158] E. Verstraelen, A. Teigelhöfer, W. Ryssens, F. Ames, A. Barzakh, M. Bender, R. Ferrer, S. Goriely, P.-H. Heenen, M. Huyse, P. Kunz, J. Lassen, V. Manea, S. Raeder, P. van Duppen, *Search for octupole-deformed actinium isotopes using resonance ionization spectroscopy*, Phys. Rev. C **100**, 044321 (2019). doi:10.1103/PhysRevC.100.044321.

[159] K. Blaum, J. Dilling, W. Nörtershäuser, *Precision atomic physics techniques for nuclear physics with radioactive beams*, Phys. Scr. **T152**, 014017 (2013). doi:10.1088/0031-8949/2013/T152/014017.

[160] P. C. Magnante, H. H. Stroke, *Isotope Shift between ^{209}Bi and 63-day ^{206}Bi*, J. Opt. Soc. Am. **59**, 836–841 (1969). doi:10.1364/JOSA.59.000836.

[161] J. R. Persson, *Table of hyperfine anomaly in atomic systems*, At. Data Nucl. Data Tables **99**, 62–68 (2013). doi:10.1016/j.adt.2012.04.002.

[162] V. A. Dzuba, V. V. Flambaum, B. M. Roberts, *Calculations of the atomic structure for the low-lying states of actinium*, Phys. Rev. A **100**, 022504 (2019). doi:10.1103/PhysRevA.100.022504.

[163] S. Raeder, T. Kron, R. Heinke, J. L. Henares, N. Lecesne, P. Schönberg, M. Trümper, K. Wendt, *High resolution spectroscopy of the hyperfine struc-*

ture splitting in $^{97,99}Tc$, Hyperfine Interact. **238**, 15 (2017). doi:10.1007/s10751-016-1389-z.

[164] P. Naubereit, T. Gottwald, D. Studer, K. Wendt, *Excited atomic energy levels in protactinium by resonance ionization spectroscopy*, Phys. Rev. A **98**, 022505 (2018). doi:10.1103/PhysRevA.98.022505.

Acknowledgements

People always say you will miss your final years in school when starting with a regular job or studies at the university. While I agree with this, I must say it wasn't so bad. In fact, I very much enjoyed the many years of being a student at Mainz University. Eventually ending up in the LARISSA group, I was surprised by the great atmosphere and teamwork. Starting completely clueless about almost any device you can possibly find in the lab was not so much of an issue, since I never had the feeling of being lost or left alone with the many problems one is facing in experimental physics. With this in mind I would like to thank my colleagues from the first hour, Tobi, Fabian, Sven, Pascal, Tom, Michael, Reinhard, Katerina, Marcel and Patrick, who gave me a warm welcome and great support during my work. Since then the group has changed a bit, but fortunately not for the worse. In this sense I thank Vadim, Nina, Felix, Vlad and Johannes as the newer members of the LARISSA family. The four o'clock tea and countless rounds of after-lunch kicker, when normal people have coffee, brighten up the daily routine (despite struggling to stay above the "Guest" player in my personal ranking). And of course, not to forget about the many successful and not-so-successful Pub-Quiz evenings featuring Larissa-(Z)User. We all miss you as our team captain, Reinhard.
A special thanks goes to my mentor Klaus. I really appreciated the encouragement towards independent work, leaving room for initiative and creativity, while I could always count on advice and interest in details. Moreover, the introduction to the international RIMS community was strongly supported by Klaus. The many exciting experiments at CERN, GANIL or LLNL, and participation in international conferences and meetings have been of great value to me. Apart from that, being the guy responsible for any spontaneously upcoming projects, I enjoyed the collaboration within the QUANTUM group. Searching for the mysterious dysprosium-1000 line with Lena and trapping beryllium ions with Sebastian was something refreshingly different.
Since I will stay in Mainz for a bit longer, this is not a goodbye and I am looking forward to continue research without a PhD thesis looming on the horizon.

In addition to my closer colleagues, I would like to thank Seppl for the great support during almost any experiment and the target production team of PSI, Jiri, Stephan, Rugard and Dorothea for supplying me with these valuable Pm samples, rendering our measurements possible in the first place.
Another special thanks goes to Dr. James for proofreading.

Finally, I thank my family and Sarah. I would not have made it here without you ♡☺.